

Micro/hydro coupling for the simulation of detonation and shock waves

Gérôme Faure

▶ **To cite this version:**

Gérôme Faure. Micro/hydro coupling for the simulation of detonation and shock waves. Numerical Analysis [math.NA]. Université Paris-Est, 2017. English. NNT : 2017PESC1063 . tel-01789719

HAL Id: tel-01789719
https://pastel.hal.science/tel-01789719

Submitted on 11 May 2018

HAL is a multi-disciplinary open access archive for the deposit and dissemination of scientific research documents, whether they are published or not. The documents may come from teaching and research institutions in France or abroad, or from public or private research centers.

L'archive ouverte pluridisciplinaire **HAL**, est destinée au dépôt et à la diffusion de documents scientifiques de niveau recherche, publiés ou non, émanant des établissements d'enseignement et de recherche français ou étrangers, des laboratoires publics ou privés.

UNIVERSITÉ PARIS-EST

Thèse présentée pour obtenir le grade de

Docteur de l'Université Paris-Est

École doctorale MSTIC
spécialité Mathématiques appliquées

Gérôme Faure

Couplage micro/hydro pour la simulation d'ondes de choc et de détonation

Thèse dirigée par
Gabriel Stoltz et Jean-Bernard Maillet

Soutenue le 29 novembre 2017 devant un jury composé de

Rapporteurs	Mme Mireille Bossy	INRIA
	M. Florian De Vuyst	Université de Technologie de Compiègne
Examinateurs	M. Pep Español	UNED
	M. Kurt Kremer	Max-Planck Institut
	M. Mathias Rousset	INRIA
Directeur de thèse	M. Gabriel Stoltz	Ecole des Ponts ParisTech
Encadrant	M. Jean-Bernard Maillet	CEA/DAM

Couplage micro/hydro pour la simulation d'ondes de choc et de détonation

Résumé : Cette thèse étudie des modèles mésoscopiques adaptés à la simulation d'ondes de choc et de détonation dans des fluides. Ces phénomènes mettent en jeu des processus complexes et nécessitent des systèmes de taille suffisante pour les observer. L'enjeu est ainsi de gagner en échelle par rapport aux méthodes microscopiques, précises mais coûteuses, tout en conservant les propriétés essentielles. Dans cette optique, le développement de méthodes multi-échelles couplant différentes résolutions au sein d'une même simulation permet d'adopter une description plus fine dans certaines régions.

Nous étudions plus particulièrement la SDPD (*Smoothed Dissipative Particle Dynamics*) qui couple une discrétisation particulaire des équations de Navier-Stokes et des fluctuations thermiques variant avec la résolution. La reformulation de la SDPD en terme d'énergie interne, en plus de la position et de la quantité de mouvement, permet de rapprocher structurellement la SDPD et la DPDE (*Dissipative Particle Dynamics with Energy conservation*). Des schémas numériques conçus pour la DPDE sont adaptés à la SDPD afin d'assurer la conservation de l'énergie et la stabilité de la dynamique. Nous étudions également les propriétés statistiques de la SDPD et établissons des estimateurs de la température et de la pression. La cohérence multi-échelle de la SDPD est démontrée par des simulations à l'équilibre et pour des ondes de choc et nous proposons un couplage entre la SDPD à différentes résolutions. Enfin, la pertinence physique de la méthode est illustrée par la simulation d'ondes de détonation et d'éjection de matière.

Mots clés : Modèles multi-échelles, Smoothed Dissipative Particle Dynamics, Equations Différentielles Stochastiques, Ondes de choc

---

Micro/macro coupling for the simulation of shock and detonation waves

Abstract: This thesis studies mesoscopic models adapted to the simulation of shock and detonation waves in fluids. These phenomena require systems sufficiently large to observe the complex processes occurring in this context. The aim is thus to increase the accessible time and length scales of microscopic methods, accurate but expensive, while preserving their essential properties. To this end, the multiscale coupling of methods at different resolutions allows to finely describe a specific region, limiting the computational cost.

In particular, we study Smoothed Dissipative Particle Dynamics (SDPD) which couples a particle discretization of the Navier-Stokes equations and thermal fluctuations that scale consistently with the resolution. The SDPD equations are reformulated in terms of internal energies, which increases the structural similarity with Dissipative Particle Dynamics with Energy conservation (DPDE). We adapt numerical schemes for DPDE to the context of SDPD in order to ensure energy conservation and stability. We study the statistical properties of SDPD and determine estimators for temperature and pressure. The size consistency in SDPD is established for equilibrium and shock waves, which leads us to propose a multiscale coupling of SDPD at different resolutions. Finally, its physical relevance is illustrated by simulating micro-jetting and detonation waves.

Keywords: Multiscale models, Smoothed Dissipative Particle Dynamics, Stochastic Differential Equations, Shock waves

Remerciements

Je tiens à remercier Gabriel et Jean-Bernard qui m'ont accompagné au cours de ces 3 années Vous avez toujours su être présents et votre aide m'a été précieuse pour mener à bien cette thèse. J'ai été ravi de l'avoir effectué avec vous. Elle a été, grâce à vous, très enrichissante.

I also wish to thank Pep Español. It has been a pleasure to work with you for two months at UNED and share very interesting discussions on coarse-graining.

Merci également à tous ceux qui m'ont aidé par vos conseils, votre expertise en maths, physique ou informatique. Je pense notamment à Laurent qui a suivi ma thèse, et à bien d'autres aussi. Je me dois bien sûr de mentionner Sandra et Isabelle pour tous les aspects administratifs.

Je souhaite bien entendu remercier mes collègues au CEA comme au CERMICS qui m'auront permis de passer de bons moments au cours de ma thèse, en particulier Alexandre, Jordan et Xavier avec qui j'ai partagé mon bureau. Et je n'oublie pas les autres thésards, post-docs ou stagiaires : Jean-Charles, Ahmed, Emmanuel, Estelle, Richard, Lucas, David, Aude, Paul, Jean-Baptiste, Thibaut, Giovanni, Raphael, Luc, Julien, Sami, Grégoire, François, Yannick, Athmane, Boris, Laurent, Pierre, Henri, Laura, Alexandre, Frédéric.

Enfin un grand merci à ma famille présente depuis toujours et dont le soutien m'est indispensable.

Liste des publications

Articles de journaux scientifiques

- G. Faure, J. Roussel, J.-B. Maillet, G. Stoltz. Size consistency in smoothed dissipative particle dynamics. *Physical Review E*, **94**, 043305 (2016).
- G. Faure, R. Delgado-Buscalioni, P. Español. The entropy of a complex molecule. *Journal of Chemical Physics*, **146**, 224106 (2017).
- G. Faure, G. Stoltz. Stable and accuracte schemes for smoothed dissipative particle dynamics. *Soumis à Applied Mathematics and Mechanics*. Preprint: arXiv:1707.04232.
- G. Faure, J.-B. Maillet. Simulation of detonation waves with smoothed dissipative particle dynamics. *Soumis à Physical Review E*. Preprint: arXiv:1709.03890.

Publications antérieures à la thèse

- G. Faure, J.-B. Maillet, G. Stoltz. Local density dependent potential for compressible mesoparticles. *Journal of Chemical Physics*, **140**, 114105, 2014.

Posters et présentations

- *Mainz Materials Simulation Days*, Mayence, Mai 2015 (poster)
- *Discrete Simulation of Fluid Dynamics*, Edimbourg, Juillet 2015 (exposé)
- *CCP5 DPD Workshop*, Manchester, Janvier 2016 (exposé)
- *Computational Statistics and Molecular Simulations*, Paris, Février 2016 (poster)
- *Hydrodynamic Fluctuation in Soft-Matter Simulations*, Prato, Février 2016 (poster)
- *New Models in Hydrocodes (PETER)*, Saint-Malo, Juin 2016 (exposé)
- *Non-Equlibrium Simulations Conference*, Sheffield, Juillet 2016 (poster)
- *Congrès de la SMAI*, Ronce-les-Bains, Juin 2017 (poster)
- *European Congress on Advanced Materials*, Thessalonique, Septembre 2017 (exposé)

Résumé substantiel

L'étude du comportement de la matière sous choc est l'un des objectifs du CEA/DAM. Pour cela, il a notamment recours à la simulation numérique. La prise en compte des processus complexes intervenant à des échelles de temps et d'espace très diverses est un enjeu majeur pour la simulation d'ondes de choc et de détonation dans les fluides. La dynamique moléculaire (DM) est très utilisée pour étudier précisément le comportement des matériaux à l'échelle microscopique. La DM consiste à suivre les déplacements atomiques et à évaluer l'énergie du système en décrivant les interactions entre atomes à l'aide d'un potentiel. Cela en fait une méthode précise mais fortement limitée en terme d'échelles spatiales et temporelles accessibles. A l'autre extrémité du spectre, les modèles hydrodynamiques adoptent une représentation continue de la matière et décrivent l'évolution de quantités macroscopiques par des lois de conservation. Bien qu'il soit possible d'adopter des approches multi-échelles avec des méthodes hydrodynamiques tels l'AMR (*Adpative Mesh Refinement*), la validité de ces modèles macroscopiques n'est pas établie lorsque l'on s'approche des domaines microscopiques.

Certaines méthodes, dites « gros grains », se proposent de travailler à une échelle intermédiaire en supprimant des degrés de liberté par rapport à la DM mais en gardant les ingrédients pertinents pour une description précise de phénomènes complexes. On peut notamment citer la DPD (*Dissipative Particle Dynamics* [81, 44]) adaptée aux systèmes à température fixée et la DPDE (*Dissipative Particle Dynamics with Energy conservation* [7, 43]) qui étend la DPD aux situations non isothermes. Dans le cadre de la DPDE, un groupe d'atomes, typiquement une molécule, est représenté par la position et la vitesse de leur centre de masse. Les degrés de liberté internes, non décrits explicitement, sont pris en compte par une énergie interne. Une équation d'état interne permet d'associer une température interne à chaque particule. L'équilibre entre températures internes et cinétiques est garantie par des forces de fluctuation et dissipation occasionnant un échange entre énergies internes et cinétiques.

Cette thèse s'attache à étudier des modèles mésoscopiques capables de simuler des ondes de choc et de détonation dans les fluides pour une large gamme de résolution. Une attention particulière est apportée au lien avec les systèmes microscopiques et à la cohérence de la méthode lorsque la résolution varie. Cela doit nous permettre de proposer un couplage multi-échelle mais également de valider les lois d'échelles habituellement postulées pour étendre les résultats de DM aux échelles expérimentales. Une méthode particulièrement intéressante au vu de ces critères est la SDPD (*Smoothed Dissipative Particle Dynamics* [40]). Elle couple en effet une discrétisation particulaire des équations de Navier-Stokes qui régissent le comportement hydrodynamique de la

matière et des fluctuations thermiques dont l'amplitude varie avec la résolution adoptée.

Discrétisation particulaire des équations de Navier-Stokes

La méthode de discrétisation particulaire utilisée pour obtenir les équations de la SPH (*Smoothed Particle Hydrodyanmics* [123, 62]) repose sur deux approximations qui sont détaillées dans la section 1.2.3. Dans un premier temps, la fonction ϕ est remplacée par sa convolution ϕ_h avec un noyau régulier W_h :

$$\phi_h(\boldsymbol{x}) = \int_\Omega \phi(\boldsymbol{x}')W_h(|\boldsymbol{x} - \boldsymbol{x}'|)\,\mathrm{d}\boldsymbol{x}'. \tag{1}$$

La longueur de régularisation h est telle que $W_h(r) = 0$ si $|r| > h$. Par ailleurs, le noyau W_h doit satisfaire une condition de normalisation :

$$\int_\Omega W_h(|\boldsymbol{x}|)\,\mathrm{d}\boldsymbol{x} = 1.$$

Un exemple de noyau fréquemment utilisé est la fonction de Lucy [123] :

$$W_{\text{Lucy}}(r) = \frac{105}{16\pi h^3}\left(1 + 3\frac{r}{h}\right)\left(1 - \frac{r}{h}\right)^3 1_{0\leq r\leq h}.$$

La seconde étape consiste à remplacer l'intégrale dans l'équation (1) par une somme sur un nombre fini $N \in \mathbb{N}$ de particules situés aux positions $\boldsymbol{q}_i$ dans le domaine Ω. La fonction ϕ est finalement approchée par

$$\tilde{\phi}_h(\boldsymbol{x}) = \sum_{i=1}^{N} \frac{m_i}{\rho_i}\phi(\boldsymbol{q}_i)W_h(|\boldsymbol{x} - \boldsymbol{q}_i|), \tag{2}$$

où nous avons exprimé la pondération de chaque particule dans la somme en fonction de leur masse m_i et de leur densité ρ_i. Cela revient à considérer qu'une particule n'est pas seulement un nœud d'interpolation mais également une petite portion du fluide de masse m_i. Au vu de (2), la densité ρ_i d'une particule est donnée par

$$\rho_i(\boldsymbol{q}) = \sum_{j=1}^{N} m_j W_h(r_{ij}), \tag{3}$$

avec $\boldsymbol{r}_{ij} = \boldsymbol{q}_i - \boldsymbol{q}_j$ et $r_{ij} = \left|\boldsymbol{r}_{ij}\right|$. L'approximation de la dérivée d'une fonction peut être obtenue en appliquant l'équation (1) à la dérivée puis en effectuant une intégration par partie. Ainsi l'approximation particulaire du gradient $\boldsymbol{\nabla}\phi$ fait intervenir le gradient du noyau avec

$$\widetilde{\boldsymbol{\nabla}\phi}_h(\boldsymbol{x}) = -\sum_{i=1}^{N} \frac{m_i}{\rho_i}\phi(\boldsymbol{q}_i)\boldsymbol{\nabla}W_h(|\boldsymbol{x} - \boldsymbol{q}_i|).$$

Pour alléger les futures notations, la quantité F_{ij} est définie par

$$\boldsymbol{\nabla}_{\boldsymbol{q}_i} W_h(r_{ij}) = -F_{ij}\boldsymbol{r}_{ij}.$$

L'erreur d'approximation globale $\left\|\phi - \tilde{\phi}_h\right\|$ peut ainsi être bornée par deux termes : l'approximation du noyau $\|\phi - \phi_h\|$ intervenant dans (1) et l'approximation particulaire $\left\|\phi_h - \tilde{\phi}_h\right\|$ introduite dans (2). Cette dernière est particulièrement délicate à appréhender puisque les positions des

particules sont amenées à évoluer au cours d'une dynamique. On peut notamment observer, suivant le noyau employé, la formation de groupements de particules qui augmentent considérablement les erreurs de discrétisation.

Cette méthode d'approximation particulaire peut être appliquée aux équations de Navier-Stokes qui traduisent la conservation de la masse, de la quantité de mouvement et de l'énergie à l'échelle hydrodynamique. On obtient alors la SPH [123, 62] en suivant la dérivation exposée dans la section 1.2.3. Ce type de méthode adopte un point de vue Lagrangien puisque l'on suit le mouvement des particules de fluide utilisées dans la discrétisation. La SDPD [40] consiste à ajouter des fluctuations thermiques aux équations du mouvement de la SPH. Ces fluctuations varient avec la résolution, diminuant lorsque la masse des particules augmente. Dans la formulation originelle détaillée dans la section 2.1, les particules SDPD sont décrites par leur position $\boldsymbol{q}_i$, leur quantité de mouvement $\boldsymbol{p}_i$ et leur entropie S_i. Une équation d'état relie leur énergie interne ε_i à leur entropie S_i et leur densité $\rho_i(\boldsymbol{q})$.

Nous reformulons ces équations dans la section 2.2 en remplaçant les entropies par les énergies internes et en proposant une forme plus simple pour les forces de fluctuation et dissipation. Cela permet de rapprocher structurellement la SDPD et la DPDE en vue d'un possible couplage multi-échelle entre les deux méthodes. Cela facilite aussi la construction de schémas numériques conservant l'énergie en SDPD. Si une équation d'état est toujours nécessaire, elle donne à présent l'entropie en fonction de l'énergie interne et de la densité. La température T_i, la pression P_i et la capacité calorifique C_i d'une particule peuvent alors s'exprimer en fonction des dérivées de l'entropie S_i. Nous écrivons les équations de la SDPD comme la superposition de deux sous-dynamiques : une dynamique conservatrice

$$\begin{cases} \mathrm{d}\boldsymbol{q}_i = \dfrac{\boldsymbol{p}_i}{m_i}\,\mathrm{d}t, \\ \mathrm{d}\boldsymbol{p}_i = \displaystyle\sum_{j\neq i} \boldsymbol{\mathscr{F}}_{\mathrm{cons},ij}\,\mathrm{d}t, \\ \mathrm{d}\varepsilon_i = -\displaystyle\sum_{j\neq i} \frac{m_i m_j P_i}{\rho_i(\boldsymbol{q})^2} F_{ij}\boldsymbol{r}_{ij}\cdot\boldsymbol{v}_{ij}\,\mathrm{d}t, \end{cases} \tag{4}$$

et une dynamique de fluctuation/dissipation pour chaque paire (i, j)

$$\begin{cases} \mathrm{d}\boldsymbol{p}_i = -\boldsymbol{\Gamma}_{ij}\boldsymbol{v}_{ij}\,\mathrm{d}t + \Sigma_{ij}\mathrm{d}\boldsymbol{B}_{ij}, \\ \mathrm{d}\boldsymbol{p}_j = \boldsymbol{\Gamma}_{ij}\boldsymbol{v}_{ij}\,\mathrm{d}t - \Sigma_{ij}\mathrm{d}\boldsymbol{B}_{ij}, \\ \mathrm{d}\varepsilon_i = \dfrac{1}{2}\left[\boldsymbol{v}_{ij}^T\boldsymbol{\Gamma}_{ij}\boldsymbol{v}_{ij} - \dfrac{\mathrm{Tr}(\Sigma_{ij}\Sigma_{ij}^T)}{m_{ij}}\right]\mathrm{d}t - \dfrac{1}{2}\boldsymbol{v}_{ij}^T\Sigma_{ij}\mathrm{d}\boldsymbol{B}_{ij}, \\ \mathrm{d}\varepsilon_j = \dfrac{1}{2}\left[\boldsymbol{v}_{ij}^T\boldsymbol{\Gamma}_{ij}\boldsymbol{v}_{ij} - \dfrac{\mathrm{Tr}(\Sigma_{ij}\Sigma_{ij}^T)}{m_{ij}}\right]\mathrm{d}t - \dfrac{1}{2}\boldsymbol{v}_{ij}^T\Sigma_{ij}\mathrm{d}\boldsymbol{B}_{ij}. \end{cases} \tag{5}$$

Ces dynamiques font intervenir les forces conservatrices

$$\boldsymbol{\mathscr{F}}_{\mathrm{cons},ij} = m_i m_j\left(\frac{P_i}{\rho_i^2} + \frac{P_j}{\rho_j^2}\right)F_{ij}\boldsymbol{r}_{ij},$$

des mouvements Browniens indépendants $\boldsymbol{B}_{ij}$ vérifiant $\boldsymbol{B}_{ij} = -\boldsymbol{B}_{ji}$ et la vitesse relative $\boldsymbol{v}_{ij} = \dfrac{\boldsymbol{p}_i}{m_i} - \dfrac{\boldsymbol{p}_j}{m_j}$. Nous choisissons des coefficients de friction Γ_{ij} et de fluctuation Σ_{ij} sous la forme

$$\boldsymbol{\Gamma}_{ij} = \gamma_{ij}^{\parallel}\boldsymbol{P}_{ij}^{\parallel} + \gamma_{ij}^{\perp}\boldsymbol{P}_{ij}^{\perp}, \quad \boldsymbol{\Sigma}_{ij} = \sigma_{ij}^{\parallel}\boldsymbol{P}_{ij}^{\parallel} + \sigma_{ij}^{\perp}\boldsymbol{P}_{ij}^{\perp},$$

où $\boldsymbol{P}_{ij}^{\parallel}$ est la matrice de projection sur la ligne des centres de masse et $\boldsymbol{P}_{ij}^{\perp}$ dans le plan orthogonal. Les coefficients γ_{ij}^{θ} et σ_{ij}^{θ} pour $\theta \in \{\parallel, \perp\}$ dépendent des énergies internes $\varepsilon_i, \varepsilon_j$ et doivent satisfaire la relation de fluctuation/dissipation

$$\gamma_{ij}^{\theta} = \frac{1}{4}\left(T_iT_j(\partial_{\varepsilon_i} + \partial_{\varepsilon_j})\left[\frac{(\sigma_{ij}^{\theta})^2}{T_iT_j}\right] + \frac{(\sigma_{ij}^{\theta})^2}{k_{\mathrm{B}}}\frac{T_i + T_j}{T_iT_j}\right),$$

afin de garantir l'invariance de mesures de la forme

$$\mu(\mathrm{d}\boldsymbol{q}\,\mathrm{d}\boldsymbol{p}\,\mathrm{d}\varepsilon) = g\left(E(\boldsymbol{q},\boldsymbol{p},\varepsilon), \sum_{i=1}^{N}\boldsymbol{p}_i\right)\prod_{i=1}^{N}\frac{\exp\left(\frac{S_i(\varepsilon_i,\boldsymbol{q})}{k_{\mathrm{B}}}\right)}{T_i(\varepsilon_i,\boldsymbol{q})}\,\mathrm{d}\boldsymbol{q}\,\mathrm{d}\boldsymbol{p}\,\mathrm{d}\varepsilon,$$

pour g une fonction de l'énergie totale $E(\boldsymbol{q},\boldsymbol{p},\varepsilon) = \displaystyle\sum_{i=1}^{N}\varepsilon_i + \frac{\boldsymbol{p}_i^2}{2m}$ et de la quantité de mouvement totale $\displaystyle\sum_{i=1}^{N}\boldsymbol{p}_i$. Nous établissons également l'expression d'estimateurs pour la température grâce à la température cinétique

$$T_{\mathrm{kin}}(\boldsymbol{q},\boldsymbol{p},\varepsilon) = \frac{1}{N}\sum_{i=1}^{N}\frac{\boldsymbol{p}_i^2}{3mk_{\mathrm{B}}},$$

et à la température interne

$$T_{\mathrm{int}}(\boldsymbol{q},\boldsymbol{p},\varepsilon) = \frac{1}{N}\sum_{i=1}^{N}T_i,$$

ainsi que pour la pression estimée par

$$\mathscr{P} = \frac{N}{\beta\mathscr{V}} + \frac{1}{3\mathscr{V}}\left\langle\sum_{1\le i<j\le N}\boldsymbol{\mathscr{F}}_{\mathrm{cons},ij}\cdot\boldsymbol{r}_{ij}\right\rangle_{\mu_\beta}.$$

Le détail des calculs est effectué dans les sections 2.4.2 et 2.4.3.

Paramétrisation de modèles gros-grains à partir de la DM

La dérivation de modèles gros grains à partir de la description microscopique de la matière est essentielle afin d'établir leur justification théorique. Cela permet en outre d'obtenir des paramétrisations de ces méthodes à partir de simulations microscopiques. Cette démarche a récemment conduit à la dérivation d'un modèle semblable à la DPDE pour décrire un système de molécules pour lequel l'énergie totale est conservée [41]. Pour ce faire, une hypothèse a dû être formulée et nous nous attachons à la valider pour un système modèle. Nous renvoyons au chapitre 3 pour une approche plus détaillée de ces aspects.

Nous considérons un système de polymères étoilés composés d'un monomère central auquel sont attachés N_b branches de N_m monomères chacune. Les interactions entre monomères liés sont décrites par un potentiel quadratique tandis qu'un potentiel de Lennard-Jones est utilisé entre les monomères non liés. L'énergie potentielle entre deux atomes i et j sera dénotée par φ_{ij}. Dans la description gros grains, chaque molécule est représentée par la position $\boldsymbol{R}_\mu$ et la vitesse $\boldsymbol{V}_\mu$ de leur centre de masse ainsi que par une énergie interne $\mathfrak{E}_\mu$ qui sont des fonctions de l'état microscopique z du système (positions $\boldsymbol{q}_i$ et vitesse $\boldsymbol{v}_i$ des atomes). En particulier, l'énergie interne s'écrit comme

$$\mathfrak{E}_\mu(z) = U_\mu(z) + \Phi_\mu(z),$$

où l'énergie intrinsèque

$$U_\mu(z) = \sum_i^N \frac{m_i}{2}(\boldsymbol{v}_i - \boldsymbol{V}_\mu(z))^2 \delta_\mu(i) + \frac{1}{2}\sum_{ij} \varphi_{ij}^{\mathrm{intra}} \delta_\mu(i)\delta_\mu(j)$$

ne comprend que des termes internes à la molécule μ et l'énergie d'interaction

$$\Phi_\mu(z) = \frac{1}{2}\sum_\nu \sum_{ij} \varphi_{ij}^{\mathrm{intra}} \delta_\mu(i)\delta_\nu(j)$$

décrit son interaction avec les autres molécules. L'indicatrice $\delta_\mu(i)$ vaut 1 si l'atome i appartient à la molécule μ et 0 sinon. L'hypothèse cruciale pour mener à bien les calculs dans [41] est que le potentiel d'interaction intermoléculaire $\Phi_\mu(z)$ ne dépend en réalité que des positions $\boldsymbol{R}_\nu$ des centres de masse des molécules. Cette hypothèse permet à la dynamique gros grains d'admettre des mesures invariantes factorisées, par exemple sous une forme canonique :

$$P^{\mathrm{eq}}(\boldsymbol{R}, \boldsymbol{P}, U) = \frac{1}{Z}\exp\left(-\beta_0 \sum_\mu \left[\frac{\boldsymbol{P}_\mu^2}{2M_\mu} + U_\mu - T_0 S_\mu(U_\mu) + \Phi_\mu(\boldsymbol{R})\right]\right),$$

dans laquelle l'entropie S_μ associée à la molécule μ ne dépend que de son énergie intrinsèque U_μ.

Afin de valider cette hypothèse, nous effectuons des simulations de DM pour des systèmes de polymères étoilés (avec $N_\mathrm{b} = 6$ et $N_\mathrm{m} = 6$) et vérifions l'indépendance des variables gros grains. La figure 1 illustre par exemple l'indépendance entre les énergies intrinsèques U_μ et les densités évaluées pour chaque particule avec (3). Nous observons également sur la figure 2 que l'entropie d'une molécule dans un système dense coïncide avec l'entropie d'une molécule isolée (dans le vide). Cela nous fournit un moyen de paramétriser l'équation d'état en DPDE en estimant l'entropie d'une molécule isolée par des simulations de DM.

Discrétisation temporelle de la SDPD

La reformulation de la SDPD en énergies internes permet d'augmenter la similarité structurelle avec la DPDE et par conséquent d'adapter des schémas numériques initialement introduits pour la DPDE dans le cadre de la SDPD. L'étude de la discrétisation temporelle de la SDPD est effectuée dans le chapitre 4 et nous en présentons ici les grandes lignes.

Les schémas décrits dans cette section repose sur une technique de *splitting* [168, 163] qui consiste à diviser la dynamique en sous-dynamiques intégrées successivement. Pour la SDPD,

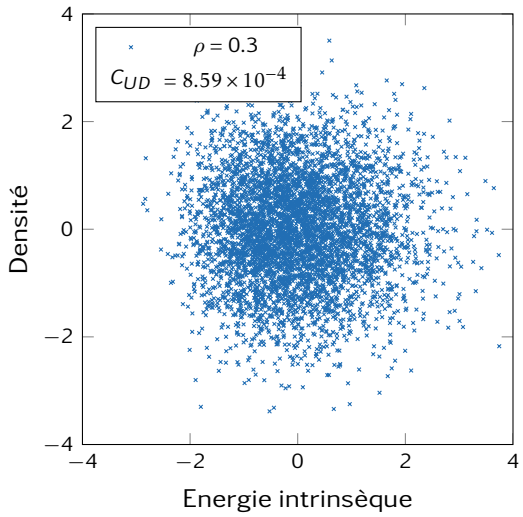


Figure 1 | Valeurs instantanées de la densité et de l'énergie intrinsèque pour chaque particule. Ces quantités sont normalisées pour garantir une moyenne nulle et une variance égale à 1.

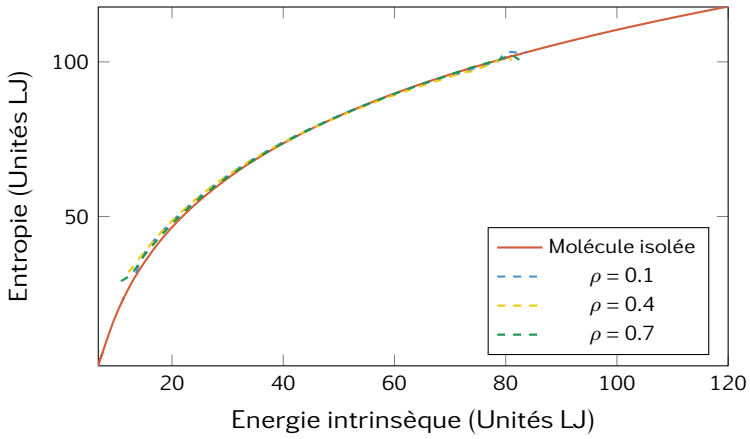


Figure 2 | Comparaison entre l'entropie d'une molécule isolée et d'une molécule dans un milieu dense (pour plusieurs densités).

cela revient à considérer, d'une part, la dynamique conservatrice (4) et d'autre part, la dynamique de fluctuation/dissipation (5).

Comme précisé dans le chapitre 2, la dynamique conservatrice est en réalité Hamiltonienne et il est donc naturel de recourir à un schéma symplectique pour son intégration, par exemple le schéma de Verlet-Vitesse [172] :

$$\begin{cases} \boldsymbol{p}_i^{n+\frac{1}{2}} = \boldsymbol{p}_i^n + \sum_{j \neq i} \mathscr{F}_{\text{cons},ij}^n \dfrac{\Delta t}{2}, \\ \boldsymbol{q}_i^{n+1} = \boldsymbol{q}_i^n + \dfrac{\boldsymbol{p}_i^{n+\frac{1}{2}}}{m_i} \Delta t, \\ \boldsymbol{p}_i^{n+1} = \boldsymbol{p}_i^{n+\frac{1}{2}} + \sum_{j \neq i} \mathscr{F}_{\text{cons},ij}^{n+1} \dfrac{\Delta t}{2}, \end{cases} \tag{6}$$

qui assure la conservation en moyenne de l'énergie en temps long [67].

L'enjeu majeur des schémas de discrétisation pour ce type de dynamiques stochastiques est de proposer une intégration de la partie de fluctuation et dissipation qui puisse à la fois garantir la conservation de l'énergie et la stabilité et être aisément parallélisable. Le premier schéma que nous considérons, dénommé SSA (*Shardlow-like Splitting Algorithm* [156, 160]), consiste à intégrer successivement la fluctuation/dissipation pour chaque paire de particules, assurant la conservation exacte de l'énergie lors de cette étape. Pour une paire (i, j) intégrée pendant un pas de temps Δt, le schéma s'écrit

$$\begin{cases} \boldsymbol{p}_i^{n+1} = \boldsymbol{p}_i^n + \left(\dfrac{1}{m_i} + \dfrac{1}{m_j}\right)^{-1} \displaystyle\sum_{\theta\in\{\parallel,\perp\}} \boldsymbol{P}_{ij}^{\theta} \left[\left(\alpha_{ij}^{\theta}(\varepsilon_i^n, \varepsilon_j^n, \boldsymbol{q}^n) - 1\right) \boldsymbol{v}_{ij}^n + \zeta_{ij}^{\theta}(\varepsilon_i^n, \varepsilon_j^n, \boldsymbol{q}^n) \boldsymbol{G}_{ij}^n\right], \\ \boldsymbol{p}_j^{n+1} = \boldsymbol{p}_j^n - \left(\dfrac{1}{m_i} + \dfrac{1}{m_j}\right)^{-1} \displaystyle\sum_{\theta\in\{\parallel,\perp\}} \boldsymbol{P}_{ij}^{\theta} \left[\left(\alpha_{ij}^{\theta}(\varepsilon_i^n, \varepsilon_j^n, \boldsymbol{q}^n) - 1\right) \boldsymbol{v}_{ij}^n + \zeta_{ij}^{\theta}(\varepsilon_i^n, \varepsilon_j^n, \boldsymbol{q}^n) \boldsymbol{G}_{ij}^n\right], \\ \varepsilon_i^{n+1} = \varepsilon_i^n - \dfrac{1}{2}\left[\dfrac{\left(\boldsymbol{p}_i^{n+1}\right)^2}{2m_i} + \dfrac{\left(\boldsymbol{p}_j^{n+1}\right)^2}{2m_j} - \dfrac{\left(\boldsymbol{p}_i^{n}\right)^2}{2m_i} - \dfrac{\left(\boldsymbol{p}_j^{n}\right)^2}{2m_j}\right], \\ \varepsilon_j^{n+1} = \varepsilon_j^n - \dfrac{1}{2}\left[\dfrac{\left(\boldsymbol{p}_i^{n+1}\right)^2}{2m_i} + \dfrac{\left(\boldsymbol{p}_j^{n+1}\right)^2}{2m_j} - \dfrac{\left(\boldsymbol{p}_i^{n}\right)^2}{2m_i} - \dfrac{\left(\boldsymbol{p}_j^{n}\right)^2}{2m_j}\right]. \end{cases} \tag{7}$$

Nous testons la conservation de l'énergie pour SSA en utilisant l'équation d'état du gaz parfait donné par

$$\mathcal{S}_{\text{ideal}}(\varepsilon, \rho) = \frac{3}{2}(K-1)k_{\text{B}} \ln(\varepsilon) - \frac{1}{2}(K-1)\ln(\rho), \tag{8}$$

où K est la taille d'une particule, c'est-à-dire le rapport entre la masse d'une particule SDPD et la masse d'une particule microscopique (par exemple d'une molécule). Des simulations pour différents K sont menées à l'équilibre et décrites dans la section 4.1. Nous pouvons observer que l'énergie dérive linéairement au cours du temps, ce qui est similaire au comportement du schéma en DPDE [125, 79]. La figure 3 compare la pente de la dérive relative de l'énergie totale en fonction du pas de temps pour plusieurs tailles de particule. L'augmentation de la taille des particules

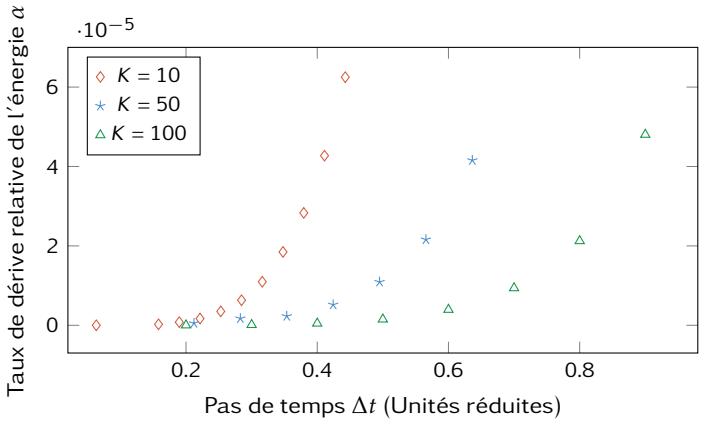


Figure 3 | Taux $\alpha_{\Delta t,K}$ de la dérive relative de l'énergie en fonction du pas de temps Δt pour SSA. Les pas de temps sont donnés dans les unités réduites définies dans la section 2.3.

permet en pratique d'utiliser des pas de temps plus grands pour un taux de dérive donné.

Pour de petites particules ($K < 10$), les pas de temps sont limités de façon prépondérante par des problèmes d'instabilité dus à l'apparition d'énergies internes négatives. Dans la section 4.3, nous adaptons pour la SDPD la procédure de Métropolisation de SSA introduite pour la DPDE [161]. Elle consiste, pour chaque paire, à calculer un taux d'acceptation des nouvelles quantités de mouvement et énergies données par (7), vue comme une proposition pour l'algorithme de Metropolis. Le taux est estimé conformément à la mesure invariante de la dynamique. En particulier, les propositions conduisant à une énergie négative sont rejetées. Une version simplifiée et moins coûteuse est également considérée où seule la vérification sur les énergies internes est effectuée sans nécessiter le calcul du taux d'acceptation. Nous observons, pour $K = 5$, une forte augmentation de la stabilité pour la Métropolisation exacte comme approchée lors de simulations à l'équilibre et dans le cas d'une onde de choc.

Les schémas précédents restent toutefois très compliqués à paralléliser (voir [104]) puisque SSA considère chaque paire séquentiellement. Une alternative a été proposée pour la DPDE avec le schéma SER [79] et adaptée ici pour la SDPD. Les forces de fluctuation et dissipation sont calculées globalement avant la mise à jour des vitesses. Les énergies internes sont finalement calculées en redistribuant symétriquement les variations d'énergies cinétiques. L'algorithme pour l'intégration de la fluctuation/dissipation s'écrit

$$\begin{cases} \boldsymbol{p}_i^{n+1} = \boldsymbol{p}_i^n + \displaystyle\sum_{j\neq i} \boldsymbol{\Gamma}_{ij}^n \boldsymbol{v}_{ij}^n \Delta t + \boldsymbol{\Sigma}_{ij}^n \boldsymbol{G}_{ij}^n \sqrt{\Delta t}, \\ \varepsilon_i^{n+1} = \varepsilon_i^n + \displaystyle\sum_{j\neq i} \frac{1}{2} \left(\boldsymbol{\Gamma}_{ij}^n \boldsymbol{v}_{ij}^n \Delta t - \boldsymbol{\Gamma}_{ij}^n \boldsymbol{G}_{ij}^n \sqrt{\Delta t} \right) \cdot \left(\boldsymbol{v}_{ij}^n + \frac{\delta \boldsymbol{p}_i^n}{2m_i} - \frac{\delta \boldsymbol{p}_j^n}{2m_j} \right). \end{cases}$$

Cela garantit une parallélisation plus immédiate au détriment de la conservation de l'énergie et de la stabilité qui sont fortement détériorées par rapport à SSA. L'amélioration de ces aspects pour des schémas parallèles demeure ainsi un enjeu majeur pour l'intégration de ces modèles mésoscopiques stochastiques.

Cohérence et couplage multi-échelle

La SDPD présente l'avantage de pouvoir décrire le comportement d'un fluide pour une large gamme de résolution en choisissant la masse m_i des particules. Nous résumons ici le contenu du chapitre 5 qui étudie les propriétés multi-échelles de la SDPD et son couplage à différentes résolutions. Nous vérifions que les propriétés prédites à l'aide de simulations en SDPD sont effectivement cohérentes avec la description microscopique du système et ce quelque soit la résolution. Pour cela, il nous faut recourir à une équation d'état ajustée à partir de simulations microscopiques.

Par la suite, nous considérons un fluide dont les interactions sont modélisées par un potentiel de Lennard-Jones :

$$\mathscr{U}_{\mathrm{LJ}}(r) = 4\varepsilon_{\mathrm{LJ}} \left[\left(\frac{\sigma_{\mathrm{LJ}}}{r} \right)^{12} - \left(\frac{\sigma_{\mathrm{LJ}}}{r} \right)^{6} \right].$$

et utilisons une équation d'état introduite dans [90] optimisées sur des résultats de DM. Afin de tester la cohérence multi-échelle de la SDPD, nous effectuons des simulations à l'équilibre pour différentes tailles de particules ($5 \leq K \leq 25000$). Le système de $N = 1000$ particules est initialisé à une densité $\rho = 1150$ kg.m^{-3} et une température $T = 1000$ K (voir la section 5.1). Il apparaît

dans la figure 4 que les valeurs moyennes sont en bon accord entre elles dès $K = 50$ En revanche, si les deux estimateurs de la température sont très proches de la prédiction de l'équation d'état, une différence de 5% est observée pour la pression. L'équation (3) conduit en effet à un biais dans l'estimation de la densité qui influe sur la pression. Par ailleurs, nous pouvons vérifier que

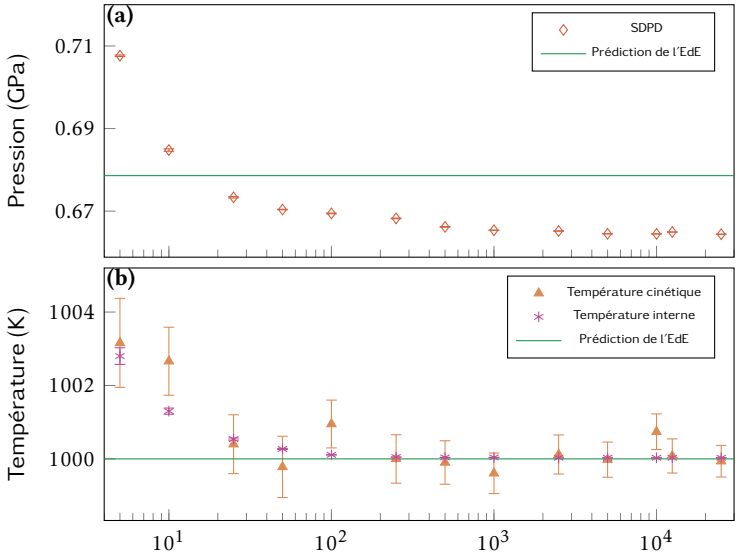


Figure 4 | Estimations de (a) la pression et (b) la température en fonction de la taille K des particules SDPD (en échelle logarithmique) comparées a la prédiction de l'équation d'état.

la variance de ces quantités est proportionnelle à K^{-1}. Un tel résultat est cohérent avec l'idée que les variables associées à une particule de taille K représentent les moyennes effectuées sur K particules microscopiques indépendantes.

Ces résultats s'avèrent également valables pour des simulations hors équilibre, en particulier dans le cas des ondes de choc. Le système est à présent initialisé sur un réseau cubique simple de taille $16 \times 16 \times 212$. Des conditions périodiques sont appliquées en x et y. Un mur est placé à chaque extrémité du système dans la direction z. Les murs sont constitués de particules SDPD « virtuelles »qui permettent d'évaluer correctement la densité et les forces conservatrices. Par ailleurs une interaction de type Lennard-Jones garantit l'imperméabilité des murs. Le mur inférieur est mis en mouvement à une vitesse $v_P = 500$ m.s^{-1} et crée un choc dans le système. Nous comparons dans la figure 5 les profils moyens de densité dans le référentiel du front de choc pour la DM, la SDPD à différentes résolutions et un modèle hydrodynamique simplifié en 1D. Les propriétés thermodynamiques dans l'état choqué sont en très bon accord avec les prévisions de la DM et de l'hydrodynamique. Nous observons toutefois la présence, pour de faibles valeurs de la viscosité, de fortes oscillations après le passage du choc. L'augmentation artificielle de ce paramètre permet d'éviter ce phénomène mais accroît la largeur du front de choc.

L'assurance de la cohérence multi-échelle de la SDPD aussi bien à l'équilibre que pour les ondes de choc nous permet de proposer un couplage multi-échelle de la SDPD à différentes résolutions à l'image de ceux proposés dans le cas isotherme [98, 145]. Le domaine est partagé en deux sous-domaines : l'un contient des particules de taille plus grande K_0, l'autre de taille plus petite K_1. Le rapport $\mathscr{R} = \dfrac{K_0}{K_1}$ définit le taux de raffinement lors du passage de l'un à l'autre. Les deux sous-domaines sont séparés par une zone tampon dans laquelle les deux résolutions peuvent coexister. Lorsqu'une grande particule (de taille K_0) quitte la zone tampon pour entrer dans le

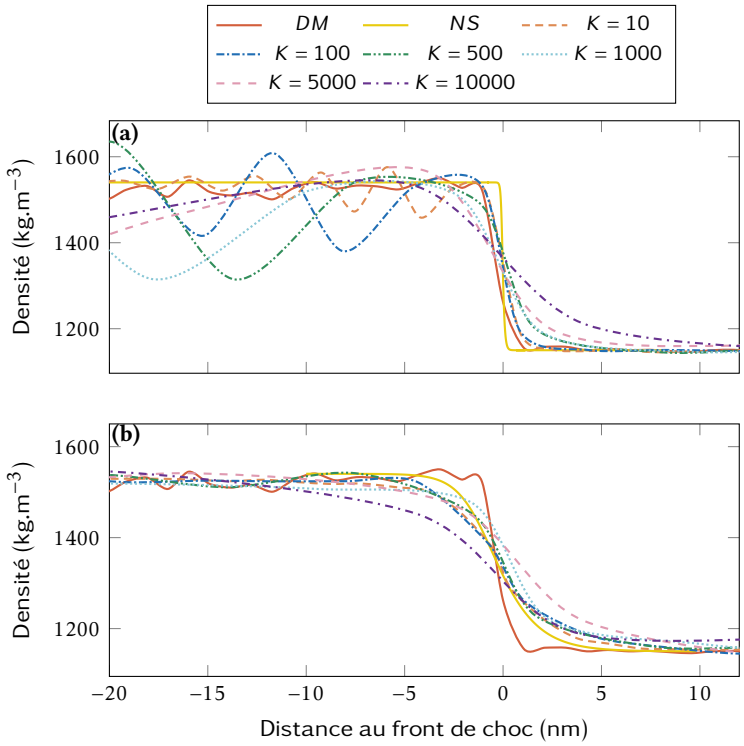


Figure 5 | Profils de densité dans le référentiel du front de choc pour $10 \leq K \leq 10000$ comparés à la DM et au modèle hydrodynamique (NS).

domaine raffiné, elle est divisée en $\mathscr{R}$ petites particules (de taille K_1). A l'inverse, le déraffinement se produit lorsqu'une petite particule entre dans la région de plus faible résolution. Elle est alors fusionnée avec ses $\mathscr{R}-1$ plus proches voisins de tailles K_1 pour former une seule grande particule de taille K_0. Les positions, vitesses et énergies internes des nouvelles particules sont déterminées pour conserver le centre de masse, la quantité de mouvement totale et l'énergie totale. Ce couplage est illustré par une simulation à l'équilibre dans la figure 6 avec $K_0 = 100$ et $K_1 = 50$. Le biais entre les deux régions pour l'estimation de la pression est faible, de l'ordre de $0,5\%$. En revanche, la transition provoque l'apparition de pics plus importants, de l'ordre de $2,5\%$, aux interfaces avec les zones tampons. D'autres mécanismes permettant un changement de résolution plus doux pourraient être envisagés pour diminuer ces perturbations.

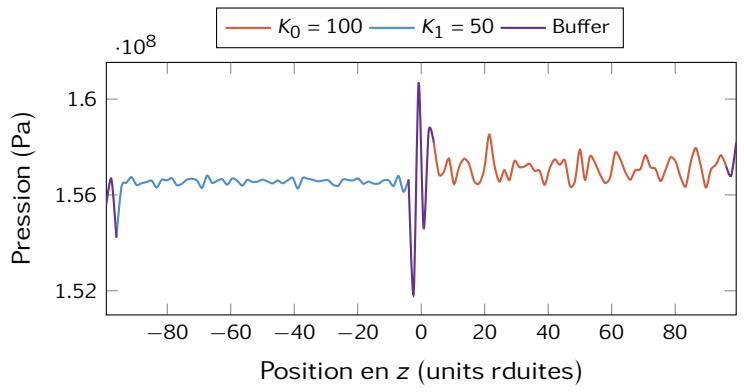


Figure 6 | Profil moyen de pression avec la SDPD multi-échelle ($K_0 = 100$ and $K_1 = 50$).

Applications physiques

Finalement, la pertinence physique de la SDPD est illustrée par la simulation de phénomènes physiques complexes liés aux ondes de choc dans le chapitre 6. Nous nous intéressons plus particulièrement à l'éjection de matière et aux ondes de détonation.

La réflexion d'une onde de choc sur une surface libre provoque une éjection de matière en présence de défauts. Ce phénomène fait intervenir des propriétés d'origine microscopique comme les fluctuations ou la tension superficielle. Les simulations de DM (voir [61, 35, 70] par exemple) qui les prennent naturellement en compte sont limitées à des échelles de temps et d'espace inférieures aux observations expérimentales. La comparaison entre les deux s'effectuent donc en postulant des lois d'échelle. La validation de ces dernières est une application possible de la SDPD qui peut simuler l'éjection de matière à des résolutions différentes. Nos résultats présentés dans la section 6.2 et illustrés par la figure 7 pour l'étain montrent un accord qualitatif avec la DM. L'ajout des effets de la tension superficielle à la SDPD permettrait une description plus précise du phénomène et une comparaison plus avancée avec les données microscopiques.

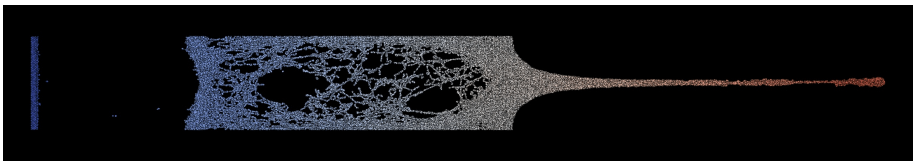


Figure 7 | Ejection de matière suite à la réflexion d'un choc sur une surface libre présentant un défaut sinusoïdale.

Une onde de détonation consiste en une onde de choc soutenue par des réactions chimiques exothermiques qui se produisent à l'arrière du front de choc, dans le matériau choqué. Pour pouvoir simuler ce phénomène avec la SDPD, nous introduisons un mécanisme réactif inspiré de l'extension de la DPDE aux matériaux réactifs [127]. Une variable d'avancement λ_i est associée à chaque particule et représente la partie qui a réagi et s'est transformée en produit. L'évolution de la variable d'avancement est décrite par une cinétique chimique, par exemple :

$$\frac{\mathrm{d}\lambda_i}{\mathrm{d}t} = \sum_{j\neq i} \mathscr{K}_{0\to 1}\left(T_{ij}\right)(1-\lambda_i)(1-\lambda_j)W_h(r_{ij})$$

qui fait intervenir des interactions avec les particules voisines pondérées par le noyau W_h. La constante de réaction $\mathscr{K}_{0\to 1}$ est donnée par une loi d'Arrhénius

$$\mathscr{K}_{0\to 1}(T) = Z_{0\to 1}\exp\left(-\frac{E_{0\to 1}}{k_\mathrm{B}T}\right),$$

avec une énergie d'activation $E_{0\to 1}$ et un préfacteur $Z_{0\to 1}$. Au cours de la réaction exothermique, de l'énergie est libérée et transférée dans l'énergie interne. Nous modifions donc l'énergie totale du système pour prendre en compte cette énergie chimique :

$$E(\boldsymbol{q},\boldsymbol{p},\varepsilon,\lambda) = \sum_{i=1}^{N}\varepsilon_i + \frac{\boldsymbol{p}_i^2}{2m} + (1-\lambda_i)KE_\mathrm{exo},$$

où l'exothermicité E_{exo} est l'énergie libérée par la réaction d'une molécule. La conservation de l'énergie est assurée en en mettant à jour les énergies internes lors de la cinétique chimique avec

$$\mathrm{d}\varepsilon_i = KE_{\text{exo}}\,\mathrm{d}\lambda_i.$$

Par ailleurs, les équations d'état pour le réactif et le produit sont différentes. Aussi, lorsque $0 < \lambda_i < 1$, une loi de mélange permet de déterminer l'état thermodynamique de la particule, qui contient à la fois du réactif et du produit. La description précise du mécanisme réactif et des simulations pour les ondes de détonation est effectuée dans la section 6.3.

Après avoir provoqué un choc dans du nitrométhane non réagi, nous observons l'initiation de réactions chimiques dans le matériau choqué de plus en plus proche du front de choc. Lorsque les réactions chimiques se produisent au niveau du front, l'onde se transforme en onde de détonation qui se propage plus vite que l'onde de choc initiale. Cette transition similaire à celle observée en DPDE [126] ne dépend pas de la résolution choisie en SDPD. La figure 8 représente l'évolution de la température dans un diagramme espace-temps pour différentes tailles de particule. Par ailleurs, nous vérifions que le régime stationnaire est établi à partir de $0,1$ nanosecondes avec une vitesse d'onde constante très proche des prédictions théoriques hydrodynamiques (6646 m.s^{-1} pour $K = 100$ comparé à 6620 m.s^{-1} pour la valeur théorique). La SDPD se montre donc capable de simuler des ondes de détonation et le gain dans les échelles de temps et d'espace accessibles ouvrent la voie à leur simulation dans des géométries plus complexes difficilement traitées aujourd'hui.

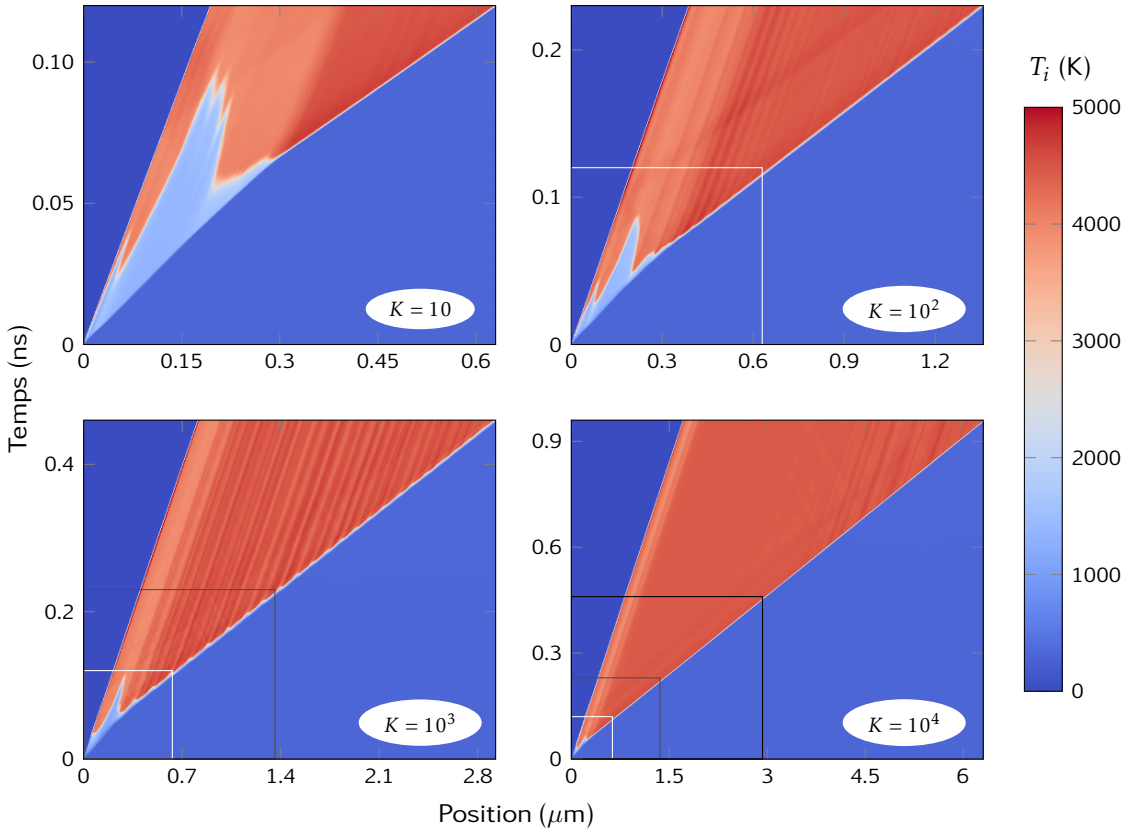


Figure 8 | Diagramme espace-temps de la température pour $10 \leq K \leq 10000$. La taille du domaine spatio-temporel simulé pour chaque résolution est représentée dans les diagrammes à plus haute échelle par un cadre blanc ($K = 10$), gris ($K = 100$) ou noir ($K = 1000$).

Contents

Remerciements iii

Liste des publications v

Résumé substantiel vii

Contents xxi

Context 1

1 Introduction 5
- 1.1 Molecular Dynamics . . . 5
  - 1.1.1 Potential energy . . . 6
  - 1.1.2 Thermodynamic ensembles . . . 8
    - Microcanonical ensemble . . . 8
    - Canonical ensemble . . . 9
  - 1.1.3 Coarse-grained models . . . 11
    - Dissipative Particle Dynamics . . . 11
    - Dissipative Particle Dynamics with Energy conservation . . . 12
- 1.2 Hydrodynamics . . . 14
  - 1.2.1 Navier-Stokes equations . . . 14
  - 1.2.2 Equations of state . . . 15
  - 1.2.3 Particular discretization of Navier-Stokes . . . 15
    - Kernel approximation . . . 16
    - Particle approximation . . . 17
    - Smoothed Particle Hydrodynamics . . . 19

2 Smoothed Dissipative Particle Dynamics 25
- 2.1 Original formulation of Smoothed Dissipative Particle Dynamics . . . 25
- 2.2 Reformulation of SDPD in terms of the internal energies . . . 30
  - 2.2.1 Equation of state . . . 30
  - 2.2.2 Energy reformulation of SDPD . . . 31
    - Elementary conservative dynamics . . . 31

Elementary fluctuation-dissipation dynamics . . . 32
Equations of motion . . . 33
2.2.3 Conservation properties . . . 34
Conservation of the energy by the conservative part of the dynamics . . . 34
Conservation of the energy by the fluctuation and dissipation part of the dynamics . . . 34
2.3 Reduced units for SDPD . . . 35
2.4 Thermodynamic properties of the reformulated SDPD . . . 35
2.4.1 Stochastic dynamics and the Fokker-Plank equation . . . 35
2.4.2 Invariant measure . . . 36
Evaluation of the derivatives of the density function . . . 36
Invariance by the conservative part of the dynamics . . . 38
Invariance by the fluctuation/dissipation part of the dynamics . . . 40
2.4.3 Estimators . . . 43
Estimators for temperature . . . 44
Estimator for pressure . . . 45

3 Parametrization of coarse-grained models from microscopic simulations 49
3.1 The coarse-grained description of star polymers . . . 50
3.2 Validation of the key approximation for star polymers . . . 52
3.2.1 Momentum and energy correlations . . . 53
3.2.2 The blob entropy . . . 55
3.2.3 Position and energy correlations . . . 57
3.2.4 Extension to larger molecules . . . 61
3.3 Coarse-grained interaction potential . . . 61

4 Integration of SDPD with accurate and stable schemes 65
4.1 Shardlow-like Splitting Algorithm . . . 66
4.1.1 Integrating the Hamiltonian part of the dynamics . . . 66
4.1.2 SSA integration of the fluctuation/dissipation part . . . 67
Reformulation in terms of the relative velocity . . . 67
Integration as Ornstein-Uhlenbeck process . . . 67
4.1.3 Analysis of the energy drift for SSA . . . 69
4.2 Splitting with Energy Reinjection . . . 71
4.2.1 SER integration of fluctuation/dissipation . . . 71
4.2.2 Energy drift and stability with SER . . . 72
4.3 Metropolization of the numerical schemes . . . 73
4.3.1 Integration of the fluctuation/dissipation part with Metropolized schemes 73
Reformulation as an overdamped Langevin dynamics . . . 74
Metropolis ratio . . . 75
4.3.2 Approximate Metropolized scheme . . . 77
4.3.3 Stability and energy conservation with the Metropolized schemes . . . 78
Integrating the fluctuation/dissipation dynamics . . . 78
Integrating the full SDPD . . . 79
Simulation of non-equilibrium systems . . . 82

5 A mutliple resolution method **85**
5.1 Size consistency for SDPD . . . 85
5.1.1 Ideal gas . . . 85
5.1.2 Lennard-Jones fluid . . . 86
5.1.3 Shock waves . . . 90
5.2 Multiscale SDPD . . . 93
5.2.1 Splitting and merging particles . . . 94
Splitting . . . 95
Merging . . . 95
5.2.2 Numerical illustration . . . 96
5.2.3 Possible improvements . . . 98

6 Applications to shock and detonation waves **101**
6.1 Shock and detonation waves . . . 101
6.2 Micro-jetting . . . 103
6.2.1 Simulation setting . . . 104
6.2.2 Results . . . 105
6.2.3 Surface tension in SDPD . . . 107
6.3 Detonation wave . . . 108
6.3.1 Reactive SDPD . . . 108
Kinetics of the chemical reaction . . . 109
Reactive equation of state . . . 109
Exothermicity . . . 110
6.3.2 Simulation of a detonation wave for nitromethane . . . 111
Shock to detonation transition . . . 113
Steady detonation wave . . . 115
Influence of the Arrhenius prefactor . . . 118

Conclusion **121**

A ExaStamp **125**
A.1 The architecture . . . 125
A.2 Implementation of mesoscopic models . . . 127

B Surface tension **129**

Bibliography **133**

Context

Numerical simulations

Physical sciences aim at understanding natural phenomena and their direct observations constitute the primary source of knowledge. These experiments sustain the development of theoretical models able to explain them and to predict new properties not yet observed. These theoretical properties in turn foster the design of experiments to validate, or maybe more importantly, stress the limits of such models and highlight the important physical processes that should be taken into account in an improved model.

Most models rely on mathematical equations that govern the behavior of the system they represent. Apart from some very simplified models, the corresponding equations are too complex to be solved analytically. The development of computer sciences has provided a way to construct approximate solutions to these equations through numerical simulations. Since physical experiments can be quite expensive or very difficult to perform, numerical simulations may also be considered as numerical experiments allowing to validate or calibrate simpler models.

At CEA/DAM, the study of the behavior of shocked materials is a major topic of interest. This proves particularly challenging both on the experimental side and for numerical simulations due to the extreme thermodynamic conditions and complex phenomena that may occur under shock. Some examples of these situations include micro-jetting, which relies to the ejection of particles when a shock wave is reflected on a rough free surface, or detonation waves, where exothermic chemical reactions occur in the shocked material and drive the shock wave. There exists a number of simulation methods to study the physical properties of such systems that range from microscopic methods to macroscopic models.

Molecular Dynamics (MD) is a microscopic method that follows the movement of atoms in a material. Since the first numerical simulations of MD for hard spheres [4] or Lennard-Jones fluids [148] that could handle only a few hundred atoms, there has been a massive increase in the computational power that progressively extended the range of the possible applications, for instance shock waves [75], while the most recent works are able to reach billions of atoms [64, 93] and study complex phenomena such as hydrodynamic instabilities. To further extend the accessible time and length scales, the current and future supercomputers rely on a massively parallel architecture with less powerful but more numerous computing units. This means that dedicated algorithms and codes need to be designed to take full advantage of these architectures. At CEA/DAM, this led in particular to the development of the massively parallel code ExaStamp [21,

20] devoted to MD simulations. With the next generation of supercomputers expected to reach the exaflop (*i.e.* 10^{18} floating point operations per second), specific codes like ExaStamp will allow the simulation of very large systems. However it does not seem currently possible to reach, with MD simulations, the time and length scales at which experimental observations are performed.

On the other hand, the equations of hydrodynamics describe the behavior of the fluid at a much more macroscopic scale. They consist in conservation laws for macroscopic variables such as fluid density, momenta or energy (see for instance [99]). A number of computational methods have been developed to solve these partial differential equations. They usually rely on a mesh on which the derivative operators are discretized [6, 53]. Mesh-free methods like SPH [123, 62] have been introduced to deal more easily with large deformation. Adaptive Mesh Refinement techniques [13, 12] enable to solve hydrodynamics at different scales in the same simulation, enlarging the range of tractable problems for hydrodynamics. The validity of the hydrodynamic conservation laws remains however questionable as the scale of the system or the discretization decreases. Indeed, at the nanoscale, atomistic details such as fluctuations gain importance and their inclusion is required to properly describe complex processes.

Traditional simulation methods such as Molecular Dynamics at the microscopic scale or hydrodynamics at a macroscopic scale have been applied successfully to simulate shock waves [75]. However, the need for larger systems to deal with more complex geometry along with the need to retain some microscopic accuracy to correctly describe complex phenomena are strong incentives to develop mesoscopic models displaying both desired properties. Coarse-grained dynamics where several atoms are represented by a single particle provide a way to decrease the number of degrees of freedom explicitly simulated and hence the computational cost. Dissipative Particle Dynamics with Energy conservation (DPDE) [7, 43] is one such coarse-grained model where several atoms are represented with a single particle. In particular, it has been adapted to the context of shock waves [160] and detonation waves [127, 126]. Nevertheless, DPDE remains atomistic in its validity domain and does not allow to freely choose the level of resolution adopted in the simulation.

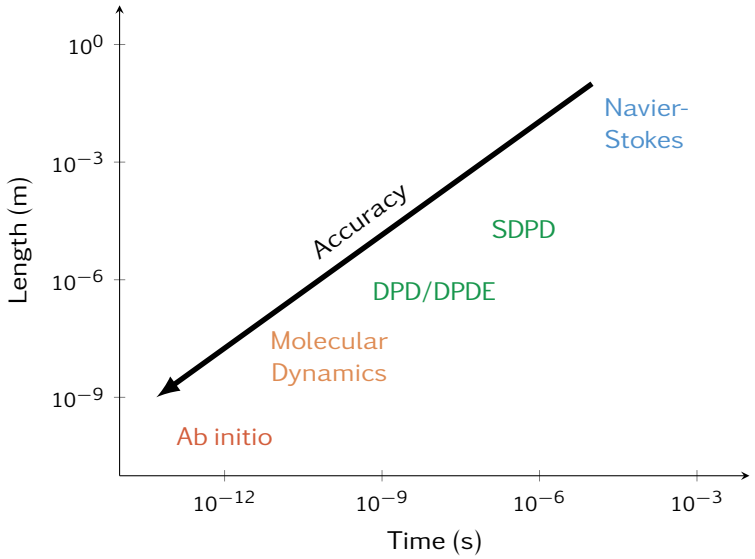


Figure 9 | Validity domains of microscopic to macroscopic models. On top of the usual classification in terms of accessible time and length scales, it should be noted that the physical accuracy decreases as the description becomes more macroscopic.

Since the atomistic behavior at the microscopic scale and the hydrodynamic properties at the

macroscopic scale are governed by very different equations, deciding what are the key ingredients to describe the material at a mesoscopic scale is one of the main challenge in the design of methods able to bridge the gap between microscopic and macroscopic models. As a result, these methods aim at including the relevant microscopic features in a coarser description, which allows to deal with more complex systems at an increased accuracy. Figure 9 shows the accessible time and length scales for microscopic and macroscopic models. As a coarser description of matter is adopted, the accuracy of the methods also decreases. Modeling efforts, for instance more involved potentials in MD, are then needed in order to enhance the accuracy of these methods by providing more faithful descriptions of the material behavior at the time and length scale under consideration. Mesoscopic models such as DPDE or SDPD (see below) are naturally found in between and represent a good compromise between cost and accuracy.

It is also essential in many situations that the mesoscopic model remains valid for a wide range of time and length scales and offers a way to select the resolution at which matter is described. The interest is twofold. First, results from MD simulations are often extrapolated with some scaling law to explain the observations at a macroscopic level. A mesoscopic method that enables the simulation of the same phenomena at different resolutions would allow to check and validate these scaling laws and provide another link between the microscopic and macroscopic models. Second, many physical situations actually involve phenomena that occur at very different time and length scales. For instance, the simulation of a shock wave requires to track with a high accuracy the propagation of the shock front, which is a very narrow region with strong gradients, while the remainder of the domain is mainly at equilibrium. With traditional methods, the resolution of the simulation method is usually governed by the highest accuracy needed even if only a very small part of the domain is concerned. It is thus very tempting to resort to a concurrent multiscale coupling of different resolutions adapted to the local accuracy requirement. In the case of a shock wave, this would mean that a microscopic model would be used for the shock front, like MD or DPDE, while a hydrodynamic method would suffice for the rest of the system. This requires to provide a consistent and rigorous link between the involved simulation methods from the microscopic scale to the macroscopic one. This has triggered the development of many coupling schemes between MD and coarse-grained models [147, 146], between MD and continuum [23, 24, 59] or even between all three of these methods within the same simulation [25]. These models are designed so that the resolution may change adaptively during the simulation and more accurate methods are used in the zone of interest.

In this work, we focus on Smoothed Dissipative Particle Dynamics (SDPD) [40]. This mesoscopic method couples a particle discretization of the Navier-Stokes equations with thermal fluctuations scaling with the resolution. One of the main improvement of SDPD over microscopic models is the ability to select the desired level of resolution in the model by playing with a parameter fixing the number of molecules one mesoparticle stands for. This paves the way for multiscale simulations based on a concurrent coupling between models at different coarse-grained level, such as MD and SDPD [144], SDPD and Navier-Stokes [137] or even SDPD at various resolutions [98, 145]. In the context of CEA/DAM, the close structural similarity between SDPD and DPDE, which is successfully used for the simulation of shock and detonation waves [160, 127], is a promising feature for a future coupling between these two methods. Apart from physical considerations, the particle nature of the SDPD method also has the practical advantage of making it suitable for an implementation in the massively parallel MD code ExaStamp [21].

Outline

In this thesis, we aim at studying mesoscopic models for the simulation of shock waves in fluids over a wide range of resolutions, from the microscopic to the macroscopic scale. We pay a particular attention to the link with microscopic properties and to the consistency of the method when we change the resolution at which the fluid is described. This last feature is crucial for the ability of the method to study scaling laws in complex physical processes and to include it in a concurrent multiscale coupling. The thesis is organized as follows:

Chapter 1 introduces some fundamental concepts on existing simulation methods, both microscopic and macroscopic. At the atomistic scale, we gather the main principles underlying Molecular Dynamics and coarse graining methods, in particular Dissipative Particle Dynamics and Dissipative Particle Dynamics with Energy conservation. We then turn to the Navier-Stokes equations that model the hydrodynamic behavior of a fluid and focus on their particle discretization with Smoothed Particle Hydrodynamics, from which SDPD is derived.

In Chapter 2, we reformulate the equations of Smoothed Dissipative Particle Dynamics (SDPD) in order to increase their structural similarities with DPDE and allow for a better control of the dynamical invariant in the numerical integration of SDPD. We also determine the form of invariant measures for SDPD and deduce estimators for thermodynamic properties such as temperature or pressure. We follow the work published in [48].

In order for coarse-grained models to be physically relevant, it is essential to know how to parametrize them based on microscopic methods. Chapter 3 is based on article [46] and focuses on the link established between atomistic computations and the behavior of coarse-grained molecules in terms of their equation of state in the DPDE model.

Chapter 4 is devoted to the numerical integration of SDPD with schemes preserving the invariants and especially the energy of the system. We take advantage of the similarities between SDPD and DPDE to adapt numerical schemes first introduced for DPDE [160, 79, 161] with a focus on stability and/or parallelizability. We first formulate the SSA scheme for SDPD that is based on a splitting between the conservative part and the fluctuation/dissipation one, following [48]. A Metropolization procedure, published in [50], then allows to increase the stability of the integration schemes for SDPD.

The interest of SDPD resides in its ability to choose the level of resolution at which the fluid is described. We check in Chapter 5 the size consistency of SDPD, that is how the estimations of physical properties it provides scale with the particle size. This corresponds to the work published in [48]. We also investigate the possibilities to couple different resolutions of SDPD in the same simulation.

To assess the ability of SDPD to give a real physical insight, we present in Chapter 6 some applications to physical systems in shock related phenomena, namely micro-jetting, which consists in the ejection of matter after a shock is reflected on a free surface, and detonation waves, which are shock waves driven by exothermic chemical reactions occurring behind the shock front. These results are gathered in [47].

1 Introduction

The simulation of shock and detonation waves is a challenging problem involving strong heterogeneities and complex phenomena. We first introduce some existing simulation methods. Molecular Dynamics consists in studying the evolution of the atomic configuration over time. This makes it an accurate but expensive model and limits its scope to the microscopic scale. We review its principles and coarse-grained methods that aim at extending the time and length scales in Section 1.1. On the other hand, the macroscopic description of fluid dynamics is governed by the conservation laws of hydrodynamics. In Section 1.2, we introduce the Navier-Stokes equations along with Smoothed Particle Hydrodynamics (SPH) which is a particle discretization to solve them numerically.

1.1 Molecular Dynamics

Molecular Dynamics (MD) is a major method to study the behavior of a material by means of numeric computations. It relies on a microscopic description of matter where the atoms are explicitly described. The principle of MD is to follow the atomic trajectories along time. This requires to solve differential equations, the so-called equations of motions, with a numerical scheme that approximates the real solution. We can thus acquire detailed information on processes occurring at a microscopic scale: structural properties, diffusion, defects in a crystalline structure,...

The information contained in the trajectories of all the considered atoms is however very rich and we are often more interested in extracting macroscopic properties such as pressure or temperature from these high dimensional data. These physical properties can be determined within the framework of statistical physics which introduces the notion of thermodynamic ensembles. Such an ensemble corresponds to a probability measure on the atomic configurations. The macroscopic properties are then computed as averages of some observables according to the ensemble probability measure.

In the following, we consider systems of N atoms indexed by an integer $i \in [\![1, N]\!]$. The atoms are represented by their positions $\boldsymbol{q} = (\boldsymbol{q}_i)_{i\in[\![1,N]\!]} \in \Omega^N \subset \mathbb{R}^{Nd}$ and momenta $\boldsymbol{p} = (\boldsymbol{p})_{i\in[\![1,N]\!]} \in \mathbb{R}^{Nd}$, where d is the dimension of the physical space (typically $d = 3$) and Ω is the physical domain, a subset of $\mathbb{R}^d$. In practice periodic boundary conditions are often used in order to study bulk properties and avoid surface effects. Their mass is denoted by $m_i \in \mathbb{R}_+$.

In classical physics, MD does not account for the quantum effects occurring in the electronic structure of the atoms. The total energy of the system $E(\boldsymbol{q}, \boldsymbol{p})$ is given as a sum between a kinetic

term

$$E_{\text{kin}}(\boldsymbol{p}) = \sum_{i=1}^{N} \frac{\boldsymbol{p}_i^2}{2m_i},$$

and a potential energy $E_{\text{pot}}(\boldsymbol{q})$ which stands for the interactions between the atoms. Therefore

$$E(\boldsymbol{q}, \boldsymbol{p}) = E_{\text{kin}}(\boldsymbol{p}) + E_{\text{pot}}(\boldsymbol{q}).$$

The physical behavior of the system is characterized by the modeling of the interactions through a potential energy (which is the focus of Section 1.1.1) and by the statistical ensemble that is sampled. This latter notion is developed in Section 1.1.2. We refer to [5, 56] for a more detailed presentation of molecular simulations. Due to its microscopic nature, MD is an expensive method and coarse-grained models have been developed to decrease the computational cost by focusing on some relevant variables, thus increasing the accessible time and length scales. We introduce some of them: Dissipative Particle Dynamics (DPD) and DPD with energy conservation (DPDE) in Section 1.1.3.

1.1.1 Potential energy

The key ingredient governing the physics in MD is how the atoms interact. This is generally prescribed through a potential that associates an energy to an atomic configuration. Ideally the energy is directly obtained from ab-initio computations that do not rely on any empirical parameters. In ab-initio molecular dynamics, the electronic configuration is treated with quantum mechanics while nuclei are treated as classical particles. These methods (see [106, 18, 140] for instance) provide a good accuracy in the estimation of the energy and the forces acting on the atoms. However, they require expensive computations that effectively limit the range of tractable problems to systems of a few hundred particles.

In order for MD to deal with larger systems required for the simulation of more complex phenomena such as diffusion process or shocks, we need to resort to much simpler potentials, *i.e.* a functional form whose parameters are fitted to reproduce properties computed with ab-initio methods or observed experimentally.

A standard and simple example is the Lennard-Jones potential [92]. It belongs to a general class of potentials that are called pairwise since they consider the total potential energy in the system to be the sum of pair interactions:

$$E_{\text{pot}}(\boldsymbol{q}) = \sum_{1 \le i < j \le N} U(\left|\boldsymbol{q}_i - \boldsymbol{q}_j\right|).$$

Here the potential function U only depends on the distance between the atoms, denoted as $r_{ij} = \left|\boldsymbol{r}_{ij}\right|$ with $\boldsymbol{r}_{ij}$ the inter-atomic vector. The Lennard-Jones potential consists in a long-range attractive part and a short-range repulsive part that diverges at $r_{ij} = 0$. Its expression is given by

$$U_{\text{LJ}}(r) = 4\varepsilon \left(\left(\frac{\sigma}{r}\right)^{12} - \left(\frac{\sigma}{r}\right)^{6} \right), \tag{1.1}$$

with two parameters: σ, such that $U'_{\text{LJ}}(2^{1/6}\sigma) = 0$, controls the distance at which the potential energy is minimum while ε fixes the depth of the energy well. The Lennard-Jones potential energy U_{LJ} is plotted in Figure 1.1.

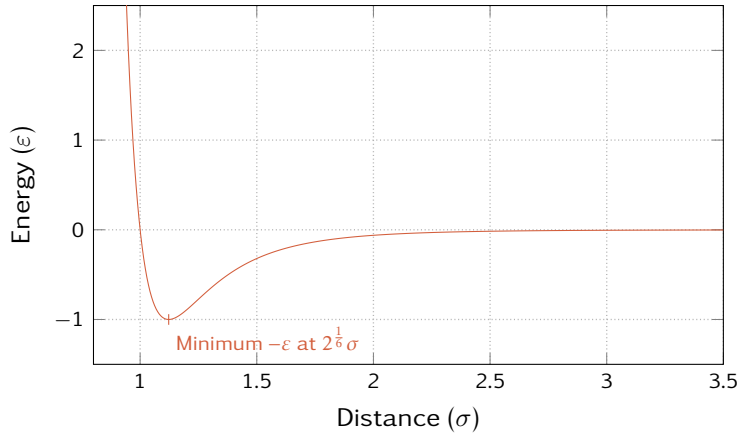


Figure 1.1 | Energy for the Lennard-Jones potential.

The Lennard-Jones potential is rather simple and mostly adapted to noble gases like Argon (with typical parameters: $\sigma = 3.405$ and $\varepsilon = 120k_B$, see [5] for instance). Here k_B is the Boltzmann constant. More complex potentials have been developed to represent different and more complex physics. For instance, EAM [22] and MEAM [11] potentials are well suited to the simulation of metal while the REBO potential [166] or the ReaxFF force field [171] are designed for the simulation of molecules and chemical reactions.

For pair potentials in the most general setting, the force for each pair of particles needs to be computed, which results in a quadratic complexity of the MD algorithm. It is also problematic when periodic boundary conditions are used since an infinite number of interactions would be required. In order to retrieve a linear complexity and hence limit the computational cost, short range potentials are usually truncated at a distance r_{cut}, called the cut-off radius, where the interaction energy becomes negligible. Since the energy at the cut-off radius is not exactly zero, corrections can be included to maintain the regularity of the potential. For instance, a simple shift allows to restore the continuity of the function.

With truncated potentials, a particle only needs to know its neighbors located at a distance smaller than r_{cut}. To fully take advantage of this finite interaction range, specific strategies need to be implemented to search for neighboring particles. The Verlet list [172] consists in storing for each particle all its neighbors within a given radius $r_V > R_{\text{cut}}$ in a list. If the Verlet radius is large enough, the Verlet list contains all the neighbors that are at distance smaller than r_{cut} of the particle after integrating the dynamics during a time step. Hence, we may keep the same lists for several time steps and update it only when the maximum displacement of a particle reaches $r_V - r_{\text{cut}}$. The choice of the Verlet radius is a trade-off between the number of particles included in the Verlet list and the rate at which it must be updated. Another technique consists in splitting the domain into cells of dimension r_{cut} (or larger). Thanks to this spatial decomposition, all the neighbors of a particle are located in the particle's cell or in the neighboring cells. In 3 dimensions, this means that we only need to loop over particles in 27 cells instead of the whole domain. This strategy may be used to compute the Verlet lists to further decrease the computational cost of the neighbor search. Possible improvements and more details about the implementation of such techniques in MD simulations may be found in [56] for instance.

1.1.2 Thermodynamic ensembles

In order to get macroscopic properties from the atomic trajectories computed with MD, we rely on the principles of statistical physics. Indeed a great deal of information is produced when explicitly tracking all the atoms in the system but they are not individually significant to understand the physics of the system at a macroscopic scale. The extraction of relevant properties such as temperature or pressure is performed by computing expectations according to probability measures called thermodynamic ensembles. In statistical physics, the state of a system is thus characterized by means of a probability distribution π in the phase space $\mathscr{E} = \Omega^N \times \mathbb{R}^{Nd}$.

A macroscopic property is the average value $\langle A \rangle_\pi$ of a microscopic observable $A(\boldsymbol{q}, \boldsymbol{p})$, a function of the atomic configuration, in a given thermodynamic ensemble:

$$\langle A \rangle_\pi = \int_{\mathscr{E}} A(\boldsymbol{q}, \boldsymbol{p}) \pi(\mathrm{d}\boldsymbol{q}\mathrm{d}\boldsymbol{p}).$$

In practice, the phase space is of very high dimension and thus a direct numeric approach to evaluate this average is not tractable. There exist several methods aimed at sampling a thermodynamic ensemble. Metropolis-Hastings [132, 69] is a Monte-Carlo method where atomic configurations are sampled by successive random perturbations of the atomic configurations that are accepted or rejected according to the desired probability measure It is also possible to find some dynamics that are ergodic for the thermodynamics measure π, meaning that the integration in the phase space can be replaced by an integration along trajectories. Denoting by $(\boldsymbol{q}(t), \boldsymbol{p}(t))$ the trajectory generated by this dynamics, the ensemble average is then reformulated as

$$\langle A \rangle_\pi = \lim_{t \to \infty} \frac{1}{t} \int_0^t A(\boldsymbol{q}(t), \boldsymbol{p}(t)) \, \mathrm{d}t.$$

These dynamics are then usually discretized in time by means of a numerical scheme.

There exist several standard thermodynamic ensembles describing various conditions for the system. We will focus mainly on the microcanonical ensemble, also denoted NVE since the number of atoms, the volume and the total energy are kept constant, and on the canonical ensemble that fixes the temperature instead of the energy and is thus denoted NVT. Note that other ensembles exist with constant pressure or allowing the number of atoms to vary while maintaining the chemical potential constant. We refer to [30, 169] for a detailed presentation of the concepts of physical statistics and thermodynamic ensembles.

Microcanonical ensemble

The microcanonical ensemble corresponds to an isolated system whose energy is constant. It is characterized by the microcanonical measure at the energy E_0:

$$\mu_{NVE,E_0}(\boldsymbol{q}, \boldsymbol{p}) = Z^{-1} \delta_{E(\boldsymbol{q},\boldsymbol{p}) - E_0},$$

where all states having the energy E_0 are equally likely. The normalization constant Z is chosen such that $\mu_{NVE,E_0}(\mathscr{E}) = 1$.

It can be shown that this measure is invariant for the Hamiltonian dynamics

$$\begin{cases} \mathrm{d}\boldsymbol{q}_i = \dfrac{\boldsymbol{p}_i}{m_i}, \\ \mathrm{d}\boldsymbol{p}_i = -\boldsymbol{\nabla}_{\boldsymbol{q}_i} E_{\mathrm{pot}}(\boldsymbol{q}). \end{cases} \tag{1.2}$$

The first equation acting on the positions simply represents the movement of the atoms with velocities $\boldsymbol{v}_i = \frac{\boldsymbol{p}_i}{m_i}$. The second equation lets the momenta evolve according to Newton's laws of motion. This dynamics preserve the total energy $E(\boldsymbol{q}, \boldsymbol{p})$ that is called the Hamiltonian of the system.

A typical way to numerically integrate the Hamiltonian dynamics (1.2) is to use a symplectic scheme. A widely used integration scheme is the Velocity-Verlet scheme [172]. It is based on a Strang splitting [163] of the Hamiltonian dynamics (1.2) and consists in integrating the momenta equation for a half time step Δt before updating the positions for a full time step and finally integrating again the momenta equation for a half time step. It reads

$$\begin{cases} \boldsymbol{p}_i^{n+\frac{1}{2}} = \boldsymbol{p}_i^n - \boldsymbol{\nabla}_{\boldsymbol{q}_i} E_{\mathrm{pot}}(\boldsymbol{q}^n) \dfrac{\Delta t}{2}, \\ \boldsymbol{q}_i^{n+1} = \boldsymbol{q}_i^n + \dfrac{\boldsymbol{p}_i^{n+\frac{1}{2}}}{m_i} \Delta t, \\ \boldsymbol{p}_i^{n+1} = \boldsymbol{p}_i^{n+\frac{1}{2}} - \boldsymbol{\nabla}_{\boldsymbol{q}_i} E_{\mathrm{pot}}(\boldsymbol{q}^{n+1}) \dfrac{\Delta t}{2} \end{cases} \tag{1.3}$$

The Verlet scheme allows for a good preservation of the energy in the long term [67, 68].

Canonical ensemble

In many physical or chemical contexts, the systems of interest are not isolated but interact with a much larger system imposing some constraints on it. The canonical ensemble represents a system that may exchange energy with a thermostat fixing its temperature T. The corresponding canonical measure associated with the inverse temperature $\beta = \dfrac{1}{k_{\mathrm{B}} T}$ is given by

$$\mu_{NVT,\beta}(\mathrm{d}\boldsymbol{q}, \mathrm{d}\boldsymbol{p}) = Z^{-1} \int \exp\left(-\beta E(\boldsymbol{q}, \boldsymbol{p})\right) \, \mathrm{d}\boldsymbol{q} \, \mathrm{d}\boldsymbol{p},$$

where Z is a normalization constant chosen so that $\mu_{NVT,\beta}(\mathscr{E}) = 1$. The temperature is fixed in the canonical ensemble in the sense that the ensemble average of the kinetic temperature, defined for a configuration $\boldsymbol{q}, \boldsymbol{p}$ as

$$T_{\mathrm{kin}}(\boldsymbol{p}, \boldsymbol{q}) = \frac{1}{N} \sum_{i=1}^{N} \frac{\boldsymbol{p}_i^2}{3 m_i},$$

is equal to the prescribed temperature:

$$\langle T_{\mathrm{kin}} \rangle_{\mu_{NVT,\beta}} = T.$$

Unlike the microcanonical ensemble, the energy of the system varies according to the canonical measure.

In the thermodynamic limit, that is when the number of particles is infinitely large ($N \to +\infty$), it can be shown that the microcanonical ensemble at energy E_0 and the corresponding canonical ensemble, *i.e.* for a temperature β_0 such that $\langle E \rangle_{\mu_{NVT,\beta_0}} = E_0$, are equivalent. This means that average values of observables that depend on a finite number of variables coincide in both ensembles., *i.e.*

$$\lim_{N \to +\infty} \left(\langle A \rangle_{NVT,\beta_0} - \langle A \rangle_{NVE,E_0} \right) = 0,$$

for A an observable depending on $(\boldsymbol{q}_1, \cdot, \boldsymbol{q}_k, \boldsymbol{p}_1, \cdot, \boldsymbol{p}_k)$ and k a fixed integer. A rigorous proof can be found in [155]. In particular, this holds for the kinetic temperature T_{kin} and, when finite range potentials are used, the energy $E(\boldsymbol{q}, \boldsymbol{p})$ or the virial pressure

$$P_{\text{virial}} = \frac{1}{3\,|\Omega|} \sum_{1 \leq i < j \leq N} \boldsymbol{r}_{ij} \cdot \boldsymbol{\nabla}_{\boldsymbol{q}_i} U(r_{ij})$$

which can actually be written as a sum of terms depending only on a finite number of variables.

To sample the canonical ensemble, we can resort to the Langevin dynamics [101] which is ergodic for the canonical measure [96, 151, 108]. It consists in adding a fluctuation and dissipation force allowing to explore different levels of energy. The resulting equations of motion are stochastic differential equations (SDE) since the fluctuation term is modeled thanks to a Brownian motion $\boldsymbol{B}_i$. The Langevin dynamics reads

$$\begin{cases} \mathrm{d}\boldsymbol{q}_i = \dfrac{\boldsymbol{p}_i}{m_i}\,\mathrm{d}t, \\ \mathrm{d}\boldsymbol{p}_i = -\boldsymbol{\nabla}_{\boldsymbol{q}_i} E_{\text{pot}}(\boldsymbol{q})\,\mathrm{d}t - \dfrac{\gamma}{m_i}\boldsymbol{p}_i\,\mathrm{d}t + \sigma \mathrm{d}\boldsymbol{B}_i. \end{cases} \tag{1.4}$$

The amplitudes of the dissipation $\gamma > 0$ and of the fluctuation $\sigma \in \mathbb{R}$ are balanced so that the canonical measure at the desired temperature is invariant for the Langevin dynamics. This is the so-called fluctuation-dissipation relation and it holds

$$\gamma = \frac{1}{2}\beta\sigma^2.$$

By considering the Langevin dynamics as a superposition of a Hamiltonian dynamics with fluctuation and dissipation terms, it is possible to use a Trotter splitting [168] to obtain a numerical scheme for its integration. The Hamiltonian dynamics can be integrated by a Velocity-Verlet scheme (see Equation (1.3)). The remaining fluctuation/dissipation part is the following Ornstein-Uhlenbeck process

$$\mathrm{d}\boldsymbol{p}_i = -\frac{\gamma}{m_i}\boldsymbol{p}_i\,\mathrm{d}t + \sigma \mathrm{d}\boldsymbol{B}_i,$$

that may be integrated during a time step Δt exactly in law as

$$\boldsymbol{p}_i(\Delta t) = \alpha_{\Delta t}\boldsymbol{p}_i + \zeta_{\Delta t}\boldsymbol{G}_i,$$

with $\boldsymbol{G}_i$ a standard Gaussian random variable and the quantities

$$\alpha_{\Delta t} = \exp\left(-\frac{\gamma \Delta t}{m_i}\right), \quad \zeta_{\Delta t} = \sqrt{\frac{1 - \alpha_{\Delta t}^2}{\beta}}.$$

1.1.3 Coarse-grained models

Molecular Dynamics is a powerful tool to study physical systems with a good accuracy. The increase in computing power in the last decades has allowed to tackle systems of growing sizes (up to a micrometer) and to reach longer times (a few nanoseconds). However, the accessible time and length scales remain several orders of magnitude below experimental observations and some complex phenomena would require much larger and longer simulations to be considered. In order to account for the atomic vibrations, time steps of the order of the femtosecond (10^{-15} s) need to be chosen, effectively limiting the time scale that can be reached.

There is a great interest in developing methods able to increase the simulated time and length scales while retaining the essential microscopic details. A usual route is to reduce the number of degrees of freedom explicitly handled by representing a complex molecule by one or several blobs. The idea is to take advantage of the separation in timescales between "slow" variables like the movement of the center of mass of a molecule and "fast" variables such as the vibration of intra-molecular bonds to integrate over the latter and obtain effective evolution equations on the slow variables.

The theory of coarse-graining [65, 176, 138] provides a firm theoretical foundation for these models. Its application in a fixed temperature setting [3, 73] leads to dynamics very similar to Dissipative Particle Dynamics (DPD) [81]. It represents the motion of molecules only through the movement of their centers of mass, in terms of positions and momenta. The blobs interact with a coarse-grained potential along with fluctuation/dissipation modeling the coarse-grained degrees of freedom.

An adaptation of DPD in an energy conserving setting is DPD with Energy conservation (DPDE) [7, 43]. It also reduces molecules to their centers of mass but an additional variable, the internal energy, is introduced to take into account the coarse-grained degrees of freedom. These internal energies and their ability to exchange energy with the external degrees of freedom through fluctuation/dissipation are essential for the simulation of shock waves where the energy behind the shock front needs to be distributed among all degrees of freedom [162] and the total energy to be preserved.

Dissipative Particle Dynamics

Dissipative Particle Dynamics (DPD) has been introduced as a coarse-grained mesoscopic model [81] which represents groups of atoms, for instance forming one or several molecules, by a single particle described by its center of mass in terms of position $\boldsymbol{q}_i$ and momentum $\boldsymbol{p}_i$. DPD particles interact through some potential energy (usually, a soft potential) while dissipative and stochastic forces are added to take into account the missing degrees of freedom.

We introduce the relative velocity between two particles as

$$\boldsymbol{v}_{ij} = \frac{\boldsymbol{p}_i}{m_i} - \frac{\boldsymbol{p}_j}{m_j}.$$

On top of the regular potential interaction, each pair of DPD particles interact through a fluctuation and dissipation force that takes the form of a friction proportional to their relative velocity and of a Brownian motion. A cut-off function χ, depending on the inter-particle distance r_{ij} is introduced in both terms to limit the range of these fluctuation-dissipation interactions. A usual choice for

the cut-off function is a quadratic spline:

$$\chi(r) = \left(1 - \frac{r}{r_{\text{cut}}}\right)^2 1_{r<r_{\text{cut}}}.$$

By adding the fluctuation/dissipation terms to the Hamiltonian dynamics for the potential, we obtain the equations of motion for DPD:

$$\begin{cases} \mathrm{d}\boldsymbol{q}_i = \dfrac{\boldsymbol{p}_i}{m_i}\,\mathrm{d}t \\ \mathrm{d}\boldsymbol{p}_i = -\boldsymbol{\nabla}_{\boldsymbol{q}_i} E_{\text{pot}}(\boldsymbol{q})\,\mathrm{d}t + \displaystyle\sum_{j\neq i} -\gamma\,\chi(r_{ij})^2 \boldsymbol{v}_{ij}\,\mathrm{d}t + \sigma\,\chi(r_{ij})\mathrm{d}\boldsymbol{B}_{ij}, \end{cases} \tag{1.5}$$

with the friction coefficient $\gamma > 0$ and fluctuation amplitude $\sigma \in \mathbb{R}$ related by a fluctuation/dissipation relation:

$$\gamma = \frac{1}{2}\beta\sigma^2,$$

to ensure the sampling of the canonical ensemble [44]. These coefficient can be more generally expressed as matrices Γ and Σ with different values along different directions. Structurally the equations of motion 1.5 are very closed to the Langevin dynamics (1.4) except that the fluctuation/dissipation in DPD is pairwise. The Brownian motion is antisymmetric and thus verifies $B_{ij} = -B_{ji}$. Thanks to this property, the pairwise fluctuation/dissipation interactions are also antisymmetric, which ensures that $\mathrm{d}\left(\sum_{i=1}^N \boldsymbol{p}_i\right) = 0$. Hence the total momentum is preserved by DPD. The integration of the equations of motion 1.5 is usually performed thanks to a splitting strategy where DPD is seen as the superposition of a Hamiltonian part (see Equation (1.2)) and a fluctuation/dissipation part. A popular scheme introduced by Shardlow [156] uses a Velocity-Verlet algorithm for the conservative part (see Equation (1.3)) and then integrates successively the fluctuation/dissipation part for each pair of particles.

DPD is well suited for isothermal settings but cannot be used in non-equilibrium situations where there exist strong spatial heterogeneities (*e.g.* shock waves). It also does not account for the energy stored in the coarse-grained degrees of freedom. This shortcoming has been answered in DPDE.

Dissipative Particle Dynamics with Energy conservation

At the microscopic level, non-equilibrium phenomena such as shock waves, which are characterized by conservation laws, are simulated with Hamiltonian dynamics (1.2) which correctly describes the exchange of energy between the different degrees of freedom. This motivated the introduction of an energy preserving DPD (DPDE) [7, 43] in order to extend DPD to non isothermal situations and ensure the conservation of the energy in the system. The coarse-grained internal degrees of freedom in DPD are represented in this model by a single variable, called internal energy $\varepsilon_i \in \mathbb{R}_+^*$, which exchanges energy with the external degrees of freedom through a dissipation and fluctuation mechanism. This ensures the overall conservation of the total energy in the system and allows for its use in non-equilibrium situations such as the simulation of shock waves [162, 160, 115]. DPDE was extended to reactive materials [127, 17] and proved able to simulate the transition from a shock to a detonation wave [126]. The theoretical link between

DPDE and the underlying microscopic system has recently been established through the rigorous derivation of a DPDE-like model with the theory of coarse-graining [41].

With the addition of the internal energy variables, the total energy in the system is given by

$$E(\boldsymbol{q},\boldsymbol{p},\varepsilon) = E_{\mathrm{kin}}(\boldsymbol{p}) + E_{\mathrm{pot}}(\boldsymbol{q}) + \sum_{i=1}^{N} \varepsilon_i.$$

An internal entropy S_i can be defined for each particle by means of an equation of state as $S_i = \mathcal{S}(\varepsilon_i)$, and consequently an internal temperature $T_i = (\mathcal{S}'(\varepsilon_i))^{-1}$. This internal equation of state represents the behavior of the internal degrees of freedom and may include quantum effects at low energy. The fluctuation and dissipation terms for DPDE aim at thermalizing the internal and external degrees of freedom. This is achieved by using friction and fluctuation coefficients γ_{ij}, σ_{ij} that depends on the internal energies ε_i, ε_j and are related through a fluctuation/dissipation relation. If we choose the fluctuation amplitude to be constant ($\sigma_{ij} = \sigma$ for any pair of particles), this relation reads

$$\gamma_{ij} = \frac{\sigma^2}{4}\left(\frac{1}{k_{\mathrm{B}}T_i} + \frac{1}{k_{\mathrm{B}}T_j}\right). \tag{1.6}$$

Compared to DPD, an additional equation is also introduced to follow the evolution of the internal energy. This equation is determined by Itô calculus in order for the total energy $E(\boldsymbol{q},\boldsymbol{p},\varepsilon)$ to be preserved:

$$\begin{cases} \mathrm{d}\boldsymbol{q}_i = \dfrac{\boldsymbol{p}_i}{m_i}\,\mathrm{d}t, \\ \mathrm{d}\boldsymbol{p}_i = -\boldsymbol{\nabla}_{\boldsymbol{q}_i} E_{\mathrm{pot}}(\boldsymbol{q})\,\mathrm{d}t + \displaystyle\sum_{j\neq i} -\gamma_{ij}\chi(r_{ij})^2 \boldsymbol{v}_{ij}\,\mathrm{d}t + \sigma_{ij}\chi(r_{ij})\mathrm{d}\boldsymbol{B}_{ij}, \\ \mathrm{d}\boldsymbol{\varepsilon}_i = \dfrac{1}{2}\displaystyle\sum_{j\neq i}\chi(r_{ij})^2\left(\gamma_{ij}\boldsymbol{v}_{ij} - 3\frac{\sigma_{ij}^2}{2}\left[\frac{1}{m_i}+\frac{1}{m_j}\right]\right)\mathrm{d}t + \sigma_{ij}\chi(r_{ij})\mathrm{d}\boldsymbol{B}_{ij}. \end{cases} \tag{1.7}$$

These equations of motion with fluctuation and dissipation coefficients related through the relation (1.6) preserve measures of the form

$$\mu_{DPDE}(\mathrm{d}\boldsymbol{q}\,\mathrm{d}\boldsymbol{p}\,\mathrm{d}\varepsilon) = g\left(E(\boldsymbol{q},\boldsymbol{p},\varepsilon), \sum_{i=1}^{N}\boldsymbol{p}_i\right)\prod_{i=1}^{N}\exp\left(\frac{\mathcal{S}(\varepsilon_i)}{k_{\mathrm{B}}}\right)\,\mathrm{d}\boldsymbol{q}\,\mathrm{d}\boldsymbol{p}.$$

This measure can be viewed as the product between any function g of the two invariants of the dynamics: $E(\boldsymbol{q},\boldsymbol{p},\varepsilon)$ and $\sum_{i=1}^{N}\boldsymbol{p}_i$ and a reference measure $\exp\left(\frac{1}{k_{\mathrm{B}}}\sum_{i=1}^{N} S_i\right)$ depending on the entropy of the coarse-grained variables.

The integration of DPDE may be performed with a Shardlow-like Splitting Algorithm (SSA) [160, 125] adapted from the Shardlow scheme [156] developed for DPD. As in the DPD version, SSA relies on a Velocity-Verlet algorithm for the conservative part (see Equation (1.3)) coupled with a pairwise integration of the fluctuation/dissipation part that reads:

$$\begin{cases} \mathrm{d}\boldsymbol{p}_i = \displaystyle\sum_{j\neq i} -\gamma_{ij}\chi(r_{ij})^2 \boldsymbol{v}_{ij}\,\mathrm{d}t + \sigma_{ij}\chi(r_{ij})\mathrm{d}\boldsymbol{B}_{ij} \\ \mathrm{d}\boldsymbol{\varepsilon}_i = \dfrac{1}{2}\displaystyle\sum_{j\neq i}\chi(r_{ij})^2\left(\gamma_{ij}\boldsymbol{v}_{ij} - 3\frac{\sigma_{ij}^2}{2}\left[\frac{1}{m_i}+\frac{1}{m_j}\right]\right)\mathrm{d}t + \sigma_{ij}\chi(r_{ij})\mathrm{d}\boldsymbol{B}_{ij} \end{cases} \tag{1.8}$$

For each pair of particles, the integration of the fluctuation/dissipation can be performed for instance by updating the velocities by analytically integrating the equations on the momenta in Equation (1.8) at fixed energies ε_i, ε_j. The variation in the kinetic energy generated by this update is then redistributed symmetrically in the internal energies ε_i, ε_j, in order to conserve the energy in this step. The improvement of numerical schemes for DPDE is however still an open topic of research with works on accuracy, parallelization [104, 79] and stability [161].

The coarse-grained methods described in these sections still remain atomistic in nature as the fluctuations in DPD or DPDE do not scale with the level of coarse-graining chosen to model the system. While it is possible to freely choose the friction parameters without perturbing the equilibrium properties, as long as an appropriate fluctuation-dissipation relation is satisfied, it is still unclear whether it is possible to retrieve various dynamical properties such as the equilibration time between the internal and external degrees of freedom, and transport coefficients of the fluid, *e.g.* self-diffusion, thermal conductivity, or shear viscosity (see [97]). It is also questionable if a single coarse-grained particle may satisfactorily represent several non-bonded particles [15].

The parametrization of coarse-grained models, in terms of coarse-grained potential, equation of state or transport coefficient, is also attracting more attention as it determines their physical relevance. The theoretical foundations of such models from their underlying microscopic description, such as [73, 41], help establishing links between the coarse-grained parameters and the atomistic systems, hence providing a sound way to capture the relevant microscopic properties.

1.2 Hydrodynamics

1.2.1 Navier-Stokes equations

The Navier-Stokes equations are a set of conservation equations, for mass, momentum and energy, that govern the dynamics of a fluid at the hydrodynamic scale. There are two main approaches to formulate the Navier-Stokes equation. In the Eulerian perspective, the positions $\boldsymbol{x}$ of the computational nodes are fixed in the domain $\Omega \subset \mathbb{R}^3$ and we observe the flux of the physical quantities at these positions. The Lagrangian description lets the computational nodes move along with the material motion and naturally takes into account the convection.

When the heat conduction is neglected, the Navier-Stokes equations (1.9) in their Lagrangian form read, for time $t \geq 0$ and position $\boldsymbol{x}$ in the domain Ω:

$$\begin{cases} \mathrm{D}_t \rho + \rho \operatorname{div}_{\boldsymbol{x}} \boldsymbol{v} = 0, \\ \rho \mathrm{D}_t \boldsymbol{v} = \operatorname{div}_{\boldsymbol{x}} (\boldsymbol{\sigma}), \\ \rho \mathrm{D}_t \left(u + \dfrac{1}{2} \boldsymbol{v}^2 \right) = \operatorname{div}_{\boldsymbol{x}} (\boldsymbol{\sigma} \boldsymbol{v}). \end{cases} \tag{1.9}$$

The material derivative used in the Lagrangian description is defined as

$$D_t f(t, \boldsymbol{x}) = \partial_t f(t, \boldsymbol{x}) + \boldsymbol{v}(t, \boldsymbol{x}) \boldsymbol{\nabla}_{\boldsymbol{x}} f(t, \boldsymbol{x}),$$

which is the sum of the usual partial derivative with respect to time and of the convective term. The unknowns are $\rho(t, \boldsymbol{x}) \in \mathbb{R}$ the density of the fluid, $\boldsymbol{v}(t, \boldsymbol{x}) \in \mathbb{R}^3$ its velocity, $u(t, \boldsymbol{x}) \in \mathbb{R}$ its

internal energy. The stress tensor $\boldsymbol{\sigma}(t, \boldsymbol{x}) \in \mathbb{R}^{3\times3}$ gives the pressure in the fluid as

$$\boldsymbol{\sigma}(t, \boldsymbol{x}) = -P(t, \boldsymbol{x})\boldsymbol{I} + \eta \left(\boldsymbol{\nabla}_{\boldsymbol{x}} \boldsymbol{v}(t, \boldsymbol{x}) + (\boldsymbol{\nabla}_{\boldsymbol{x}} \boldsymbol{v})^T(t, \boldsymbol{x}) \right) + \left(\zeta - \frac{2}{3}\eta \right) \operatorname{div}_{\boldsymbol{x}}(\boldsymbol{v})(t, \boldsymbol{x})\boldsymbol{I}, \tag{1.10}$$

where $P(t, \boldsymbol{x}) \in \mathbb{R}$ is the hydrostatic pressure of the fluid. The shear viscosity $\eta > 0$ and the bulk viscosity $\zeta > 0$ are independent of time and position..

1.2.2 Equations of state

An equation of state is needed to close the system of equations (1.9) by relating different thermodynamic variables. In the following, we will be most interested by equations of states linking the internal energy u with the density ρ and the entropy S or conversely the entropy with density and energy. Usually a functional form is fitted using data from microscopic simulations or experimental observations.

A particularly simple equation of state is the ideal gas equation of state that models a gas with no interaction between particles. It reads

$$S(u, \rho) = \frac{3}{2} k_{\mathrm{B}} \log(u) - \frac{1}{2} k_{\mathrm{B}} \log(\rho). \tag{1.11}$$

The other thermodynamic properties can then be written in terms of derivatives of the entropy. For instance, the temperature and pressure are given by

$$T(u, \rho) = \left[\frac{1}{\partial_u \mathcal{S}} \right](u, \rho), \quad P(u, \rho) = -\frac{\rho^2}{m} \left[\frac{\partial_\rho \mathcal{S}}{\partial_u \mathcal{S}} \right](u, \rho).$$

For the ideal gas, it holds

$$T(u, \rho) = \frac{2\varepsilon}{3k_{\mathrm{B}}}, \quad P(u, \rho) = \frac{1}{3} \frac{\rho u}{m}.$$

In particular the temperature does not depend on the density.

The equation of state characterizes the physical behavior of the material and numerous models have been developed: for instance the Mie-Grüneisen equation of state [111, 72] most suited for condensed matter under shock or the Jones-Wilkins-Lee equation of state [31] for explosives.

1.2.3 Particular discretization of Navier-Stokes

In order to numerically solve the Navier-Stokes equations, one usually resorts to meshing the spatial domain. Methods such as Finite Differences [6], Finite Elements [63] and Finite Volumes [45, 112] may then be used to discretize the spatial derivatives in the conservation laws. Lagrangian models suffer from a loss of accuracy as the material is subject to large deformations since the mesh becomes highly distorted. On the other hand, it is difficult to track interfaces with Eulerian formulations. Techniques like Arbitrary Lagrangian-Eulerian (ALE) methods [141, 55, 32] aim at taking advantages of the two approaches by letting the mesh evolve during the simulation but not necessarily by following the material motion.

In the presence of multiscale phenomena, a part of the domain often requires to be resolved with a higher accuracy. With uniform meshes, this means that the whole domain needs to be handled with a fine mesh, which is computationally expensive. Adaptive Mesh Refinement (AMR) [13, 12] consists in adapting the spatial grid to the local physical variables. For instance a

finer mesh can be used near discontinuities while the remainder of the domain is handled with a coarser resolution. This allows to concentrate the computational power where it is actually needed and makes possible the simulation of complex problems, which would be intractable with a uniform grid.

Besides mesh-based methods, mesh-free methods relying on a set of discrete particles have been introduced to deal more easily with large deformations and interfaces. Smoothed Particle Hydrodynamics (SPH) [123, 62] is such a technique. It is particularly popular in the field of astrophysics. The particular discretization of the Navier-Stokes equations, from which SPH is derived, relies on two major principles used to evaluate field variables: the kernel approximation, which consists in approximating a function by a smoothing convolution, and the particle approximation which amounts to replacing the convolution integral by a sum on a finite number of particles. We follow the presentation of the key steps in the derivation of the SPH discretization in [119].

Kernel approximation

First let us note that, for a smooth function ϕ with support in a domain Ω, we may evaluate its value at some point $\boldsymbol{x} \in \Omega$ through the Dirac distribution $\delta_{\boldsymbol{x}}$ defined as

$$\langle \delta_{\boldsymbol{x}}, \phi \rangle_{\mathscr{D}',\mathscr{D}} = \phi(\boldsymbol{x}),$$

where $< \cdot >_{\mathscr{D}',\mathscr{D}}$ is the duality pairing between a distribution in $\mathscr{D}'(\Omega)$ and a test function in $\mathscr{D}(\Omega)$. The idea of the kernel approximation is to replace the Dirac distribution by smooth functions $\mathscr{W}_{\boldsymbol{x},h}$, called kernel functions, such that

$$\left\langle \mathscr{W}_{\boldsymbol{x},h}, \phi \right\rangle_{\mathscr{D}',\mathscr{D}} \underset{h\to 0}{\to} \phi(\boldsymbol{x}). \tag{1.12}$$

We can now define the approximated function ϕ_h as

$$\phi_h(\boldsymbol{x}) = \int_\Omega \phi(\boldsymbol{x}')\mathscr{W}_{\boldsymbol{x},h}(\boldsymbol{x}')\,\mathrm{d}\boldsymbol{x}'. \tag{1.13}$$

We will actually require $\mathscr{W}_{\boldsymbol{x},h}$ to be even, positive, normalized and with compact support ($\mathscr{W}_{\boldsymbol{x},h}(\boldsymbol{x}') = 0$ if $|\boldsymbol{x}'| > h$), which implies property (1.12). For example, considering kernel functions of the form

$$\mathscr{W}_{\boldsymbol{x},h}(\boldsymbol{x}') = \frac{W_h(|\boldsymbol{x}' - \boldsymbol{x}|)}{\int_\Omega W_h(|\boldsymbol{x}'|)\,\mathrm{d}\boldsymbol{x}'},$$

with W_h a smooth and positive function such that $W_h(r) = 0$ if $r > h$ ensures that all the required properties for $\mathscr{W}_{\boldsymbol{x},h}$ are satisfied. The Lucy function, introduced in [123], is a typical choice for the kernel function:

$$W_{\mathrm{Lucy}}(r) = \frac{105}{16\pi h^3}\left(1 + 3\frac{r}{h}\right)\left(1 - \frac{r}{h}\right)^3 1_{0\le r\le h}. \tag{1.14}$$

Alternative forms of the kernel function may be used: for instance a cubic spline [120] whose expression reads

$$W_{\text{cubic}}(\boldsymbol{r}) = \begin{cases} \dfrac{8}{\pi h^3}\left(1 - 6\dfrac{r^2}{h^2} + 6\dfrac{r^3}{h^3}\right) & \text{if } r \leq \dfrac{h}{2}, \\ \dfrac{16}{\pi h^3}\left(1 - \dfrac{r}{h}\right)^3 & \text{if } \dfrac{h}{2} \leq r \leq h, \\ 0 & \text{if } r \geq h. \end{cases} \tag{1.15}$$

We can easily check that W_{Lucy} and W_{cubic} are smooth, positive and with compact support. Moreover, $\int_\Omega W_h(|\boldsymbol{x}'|)\,\mathrm{d}\boldsymbol{x}' = 1$ for both kernels. These two examples of smoothing functions are plotted in Figure 1.2.

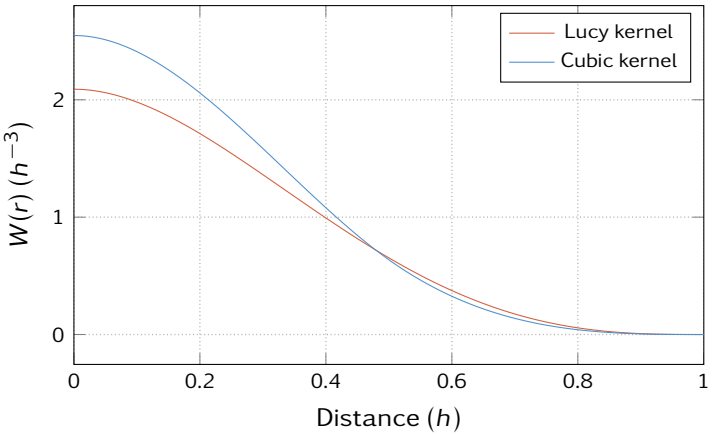


Figure 1.2 | Lucy and cubic kernels

The quality of the kernel approximation may be estimated by measuring the consistency error $\|\phi_h - \phi\|$. In the $L^\infty(\Omega)$ norm and for polynomials of degree k, this actually amounts, for $j \in [\![1, k]\!]$ to

$$\int_\Omega (\boldsymbol{x}')^j \mathscr{W}_{\boldsymbol{x},h}(\boldsymbol{x}')\,\mathrm{d}\boldsymbol{x}' = 0, \quad \forall \boldsymbol{x} \in \Omega.$$

These relations may be used to construct high order kernels (see [120] for instance) so that the consistency error $\|\phi_h - \phi\|_{L_\infty(\Omega)}$ vanishes for polynomials of a given order. However, the positivity condition may be lost, which may cause instabilities and lead to the appearance of unphysical situations.

Particle approximation

The particle approximation consists in discretizing the integral in Equation (1.13) on a finite number N of nodes called particles at positions $\boldsymbol{q}_i$ and associated with some weight $\mathscr{V}_i$. This enables us to further approximate ϕ as

$$\tilde{\phi}_h(\boldsymbol{x}) = \sum_{i=1}^{N} \phi(\boldsymbol{q}_i)\mathscr{W}_{\boldsymbol{x},h}(\boldsymbol{q}_i)\mathscr{V}_i,$$

or, upon rewriting $\mathscr{V}_i = \frac{m_i}{\rho_i}$,

$$\tilde{\phi}_h(\boldsymbol{x}) = \sum_{i=1}^{N} \frac{m_i}{\rho_i} \phi(\boldsymbol{q}_i) \mathscr{W}_{\boldsymbol{x},h}(\boldsymbol{q}_i). \tag{1.16}$$

The latter expression is motivated by seeing $\mathscr{V}_i$ as the volume of particle i, m_i and ρ_i being its mass and density. Another interpretation of the volume $\mathscr{V}_i$ (or the mass m_i) is to consider that each particle is a small portion of the studied fluid. To get a good approximation of ϕ, we need a sufficiently high number of particles in the support of $\mathscr{W}_{\boldsymbol{x},h}$. This means that, for a coarser resolution (with large particle masses m_i), we will need a larger smoothing length h to ensure the number of neighbors to remain constant. Indeed, if we want approximately N_n neighbors in the support domain with particles of mass $m_i = m$ at average density ρ, we need to choose

$$h = \left(\frac{3 N_n m}{4\pi\rho} \right)^{\frac{1}{3}}. \tag{1.17}$$

The error caused by the particle approximation $\left\| \tilde{\phi}_h - \phi_h \right\|$ depends by nature on the particle positions $\boldsymbol{q}_i$. As a consequence, it is difficult to assess the quality of a kernel when using both the kernel and the particle approximations in an actual simulation where particles move. Some criteria have been proposed to compare kernels when the particles are organized on a regular lattice [58, 80]. They consist in evaluating the global error $\left\| \tilde{\phi}_h - \phi \right\|$ for some specific functions ϕ in the L^∞, L^1 and L^2 norms. Actually, if we want to ensure that polynomials of a given order are exactly reproduced, *i.e.* the global error vanishes, we need to adapt the kernel to each specific particle configuration with techniques such as renormalized kernels [89], renormalized derivatives [102, 103] or reproducing kernels particle methods [121]. The particle approximation can also lead to undesired behaviors and instabilities such as particle clustering [164, 133, 149]. This is particularly problematic as it may cause metastability issues.

To use the kernel and particle approximations in the discretization of a differential equation, it is necessary to present the approximation of the derivatives $\psi_i = \partial_i \phi$ of function ϕ. We can integrate by part the kernel approximation (1.13) used with ψ_i and obtain:

$$\psi_{i,h}(\boldsymbol{x}) = \int_\Omega \partial_i \phi(\boldsymbol{x}') \mathscr{W}_{\boldsymbol{x},h}(\boldsymbol{x}') \, \mathrm{d}\boldsymbol{x}' = - \int_\Omega \phi(\boldsymbol{x}') \partial_i \mathscr{W}_{\boldsymbol{x},h}(\boldsymbol{x}') \, \mathrm{d}\boldsymbol{x}'.$$

Upon replacing the integral by a finite summation, the particle approximation finally gives

$$\widetilde{\psi_{i,h}}(\boldsymbol{x}) = - \sum_{j=1}^{N} \frac{m_j}{\rho_j} \phi(\boldsymbol{q}_j) \partial_i \mathscr{W}_{\boldsymbol{x},h}(\boldsymbol{q}_j).$$

Introducing the function F_h such that

$$\boldsymbol{\nabla}_{\boldsymbol{x}} \mathscr{W}_{\boldsymbol{x},h}(\boldsymbol{x}) = -F_h(|\boldsymbol{x}|)\boldsymbol{x}, \tag{1.18}$$

it is possible to rewrite the approximation of the derivatives of ϕ as

$$\widetilde{\boldsymbol{\nabla}_{\boldsymbol{x}} \phi}(\boldsymbol{x}) = - \sum_{j=1}^{N} \frac{m_j}{\rho_j} \phi(\boldsymbol{q}_j) F_h(\left|\boldsymbol{x} - \boldsymbol{q}_j\right|)(\boldsymbol{x} - \boldsymbol{q}_j). \tag{1.19}$$

Using Equation (1.16), we can approximate the variables in the Navier-Stokes equations. For instance, we evaluate the density field as

$$\tilde{\rho}(\boldsymbol{x}) = \sum_{i=1}^{N} m_i \mathscr{W}_{\boldsymbol{x},h}(\boldsymbol{x}_i).$$

Thus, the density ρ_i and volume $\mathscr{V}_i$ associated with the particle i are given by

$$\rho_i(\boldsymbol{q}) = \sum_{j=1}^{N} m_j W_h(r_{ij}), \quad \mathscr{V}_i(\boldsymbol{q}) = \frac{m_i}{\rho_i(\boldsymbol{q})}. \tag{1.20}$$

The corresponding approximations of the density gradient evaluated at the particle points read

$$\boldsymbol{\nabla}_{\boldsymbol{q}_j} \rho_i = \begin{cases} m_j F_{ij} \boldsymbol{r}_{ij} & \text{if } j \neq i, \\ -\displaystyle\sum_{j=1}^{N} m_j F_{ij} \boldsymbol{r}_{ij} & \text{if } j = i, \end{cases} \tag{1.21}$$

which will be most useful in the SPH and SDPD equations.

Smoothed Particle Hydrodynamics

Smoothed Particle Hydrodynamics [123, 62] is a Lagrangian discretization of the Navier-Stokes equations (1.9) based on the kernel and particle approximations. A finite number N of fluid particles are inserted in the domain to play the role of interpolation nodes. These fluid particles are associated with a portion of fluid of mass m_i. They are located at positions $\boldsymbol{q}_i \in \Omega$ and have a momentum $\boldsymbol{p}_i \in \mathbb{R}^3$. The internal degrees of freedom are represented by an entropy $S_i \in \mathbb{R}$.

In this setting, we may consider particle quantities as the approximation of the variables appearing in the Navier-Stokes equations at point $\boldsymbol{q}_i$. For instance. the internal energy ε_i associated with particle i stands for the internal energy u in (1.9) evaluated at position $\boldsymbol{q}_i$. Here, we relate the internal energy ε_i with the entropy S_i and the density $\rho_i(\boldsymbol{q})$, computed with (1.20), by evaluating the equation of state in Section 1.2.2 with the particle quantities:

$$\varepsilon_i(S_i, \boldsymbol{q}) = \mathscr{E}(S_i, \rho_i(\boldsymbol{q})). \tag{1.22}$$

Accordingly we define a temperature T_i, pressure P_i and heat capacity at constant volume C_i for each particle as derivatives of the internal energy:

$$\begin{aligned} T_i(S_i, \boldsymbol{q}) &= \partial_S \mathscr{E}(S_i, \rho_i(\boldsymbol{q})), \\ P_i(S_i, \boldsymbol{q}) &= \frac{\rho_i(\boldsymbol{q})^2}{m_i} \partial_\rho \mathscr{E}(S_i, \rho_i(\boldsymbol{q})), \\ C_i(S_i, \boldsymbol{q}) &= \left[\frac{\partial_S \mathscr{E}}{\partial_S^2 \mathscr{E}} \right] (S_i, \rho_i(\boldsymbol{q})). \end{aligned} \tag{1.23}$$

To simplify the notation, we omit in the following the dependence of T_i, P_i and C_i on the variables S_i and $\boldsymbol{q}$.

The SPH discretization can be split into two elementary dynamics. The first one is a conservative dynamics derived from the pressure gradient in the stress tensor (1.10) and the second one a dissipative dynamics stemming from the viscous terms in (1.10). Rather than discretizing the energy conservation in the Navier-Stokes equations (third equation in (1.9)), we consider the evolution of the entropy $s(t, \boldsymbol{x})$ as it was done in the original SDPD model [40]:

$$T\rho \mathrm{D}_t s = \rho \mathrm{D}_t u + P\rho \mathrm{D}_t \left(\frac{1}{\rho}\right).$$

Using the conservation of mass and momentum, this can be rewritten as

$$\begin{aligned} T\rho \mathrm{D}_t s &= \rho \mathrm{D}_t \left(u + \frac{1}{2}\boldsymbol{v}^2\right) - \boldsymbol{v}\,\mathrm{div}_{\boldsymbol{x}}\boldsymbol{\sigma} - P\,\mathrm{div}_{\boldsymbol{x}}\boldsymbol{v} \\ &= \boldsymbol{\sigma} : \boldsymbol{\nabla}_{\boldsymbol{x}}\boldsymbol{v} - P\,\mathrm{div}_{\boldsymbol{x}}\boldsymbol{v}, \end{aligned}$$

where the contraction operation for two matrices $\boldsymbol{A}$ and $\boldsymbol{B}$ of size $d \times d$ is defined as

$$\boldsymbol{A} : \boldsymbol{B} = \sum_{1 \le \alpha, \beta \le d} A_{\alpha\beta} B_{\alpha\beta}.$$

By further developing the stress tensor with Equation (1.10), the terms depending on the pressure vanish while the viscosity terms may be reorganized as follows:

$$T\rho \mathrm{D}_t s = 2\eta \overline{\boldsymbol{\nabla}_{\boldsymbol{x}}\boldsymbol{v}} : \overline{\boldsymbol{\nabla}_{\boldsymbol{x}}\boldsymbol{v}} + \zeta \left(\mathrm{div}_{\boldsymbol{x}}\boldsymbol{v}\right)^2, \tag{1.24}$$

where we introduced the symmetric traceless part of a matrix A as

$$\overline{\boldsymbol{A}} = \frac{1}{2}\left(\boldsymbol{A} + \boldsymbol{A}^T\right) - \frac{1}{3}\mathrm{Tr}\left(\boldsymbol{A}\right).$$

The mass conservation in the Navier-Stokes equation (first equation in (1.9)) is automatically ensured by computing the particle densities with Equation (1.20). Indeed if we use the identity:

$$\rho\,\mathrm{div}_{\boldsymbol{x}}\boldsymbol{v} = \mathrm{div}_{\boldsymbol{x}}(\rho\boldsymbol{v}) - \boldsymbol{v}\,\mathrm{div}_{\boldsymbol{x}}\rho$$

and apply the SPH approximation (1.19), the mass conservation is discretized as

$$\begin{aligned} \mathrm{d}\rho_i &= \sum_{j \neq i} F_{ij} \boldsymbol{p}_j^T \boldsymbol{r}_{ij}\,\mathrm{d}t - \sum_{j \neq i} \frac{m_j}{m_i} F_{ij} \boldsymbol{p}_i^T \boldsymbol{r}_{ij}\,\mathrm{d}t \\ &= -\sum_{j \neq i} m_j F_{ij} \boldsymbol{v}_{ij}^T \boldsymbol{r}_{ij}\,\mathrm{d}t. \end{aligned}$$

This is equivalent to the derivation of Equation (1.20) with respect to time when the positions are evolved with their velocities:

$$\mathrm{d}\boldsymbol{q}_i = \frac{\boldsymbol{p}_i}{m_i}\mathrm{d}t$$

In order to discretize the momentum conservation in the Navier-Stokes equation (second equation in (1.9)), we first derive the elementary force between particles i and j due to the hydrostatic pressure, *i.e.* with no viscosity ($\eta = 0$ and $\nu = 0$). The momentum equations then

amounts only to

$$\rho \mathrm{D}_t \boldsymbol{v} = \boldsymbol{\nabla}_{\boldsymbol{x}} P(t, \boldsymbol{x}). \tag{1.25}$$

A direct application of Equation (1.19) yields:

$$\mathrm{d}\boldsymbol{p}_i = \sum_{j \neq i} \frac{m_i m_j}{\rho_i \rho_j} P_j F_{ij} \boldsymbol{r}_{ij} \, \mathrm{d}t.$$

However this formulation is not symmetric and thus does not preserve the total momentum. Following [119], we may obtain a symmetric SPH discretization by using the following identity:

$$\frac{1}{\rho} \boldsymbol{\nabla}_{\boldsymbol{x}} P = \boldsymbol{\nabla}_{\boldsymbol{x}} \left[\frac{P}{\rho} \right] + \frac{P}{\rho^2} \boldsymbol{\nabla}_{\boldsymbol{x}} \rho, \tag{1.26}$$

in Equation (1.25). Now, the approximation (1.19) leads to a symmetric form that conserves the total momentum:

$$\begin{aligned} \mathrm{d}\boldsymbol{p}_i &= \sum_{j \neq i} m_i m_j \frac{P_j}{\rho_j^2} F_{ij} \boldsymbol{r}_{ij} + m_i \frac{P_i}{\rho_i^2} \sum_{j \neq i} m_j F_{ij} \boldsymbol{r}_{ij} \\ &= \sum_{j \neq i} \boldsymbol{\mathcal{F}}_{\mathrm{cons},ij}, \end{aligned}$$

where we introduce the notation

$$\boldsymbol{\mathcal{F}}_{\mathrm{cons},ij} = m_i m_j \left(\frac{P_i}{\rho_i^2} + \frac{P_j}{\rho_j^2} \right) F_{ij} \boldsymbol{r}_{ij}. \tag{1.27}$$

When the viscosities are not considered, the entropy is constant as can be seen in Equation (1.24). This allows us to write this part of the dynamics as

$$\begin{cases} \mathrm{d}\boldsymbol{q}_i = \dfrac{\boldsymbol{p}_i}{m_i} \, \mathrm{d}t, \\ \mathrm{d}\boldsymbol{p}_i = \displaystyle\sum_{j \neq i} \boldsymbol{\mathcal{F}}_{\mathrm{cons},ij} \, \mathrm{d}t, \\ \mathrm{d}S_i = 0. \end{cases} \tag{1.28}$$

It is actually possible to view Equation (1.28) as the conservative part of the SPH dynamics since it can be rewritten in a Hamiltonian form. Indeed,

$$\sum_{j \neq i} \boldsymbol{\mathcal{F}}_{\mathrm{cons},ij} = -\boldsymbol{\nabla}_{\boldsymbol{q}_i} H(\boldsymbol{q}, \boldsymbol{p}, S),$$

where the energy of the system is given by

$$H(\boldsymbol{q}, \boldsymbol{p}, S) = \sum_{i=1}^{N} \varepsilon_i(S_i, \boldsymbol{q}) + \sum_{i=1}^{N} \frac{\boldsymbol{p}_i^2}{2m_i}. \tag{1.29}$$

The conservation of the Hamiltonian H follows directly from the application of the relations (1.21) and (1.23). This dynamics preserves by construction the total momentum $\displaystyle\sum_{i=1}^{N} \frac{\boldsymbol{p}_i^2}{2m_i}$ and the total energy $H(\boldsymbol{q}, \boldsymbol{p}, S)$. Another interesting property is that the entropies S_i are left unchanged by the

conservative dynamics.

We now discretize the momentum equation when only the viscous terms are considered, *i.e.* $P = 0$. To this end, we follow the derivation introduced in [40]. The conservation of momentum is then given by

$$\rho \, \mathrm{D}_t \boldsymbol{v} = \eta \boldsymbol{\Delta}_{\boldsymbol{x}} \boldsymbol{v} + \left(\zeta + \frac{\eta}{3}\right) \boldsymbol{\nabla}_{\boldsymbol{x}} \mathrm{div}_{\boldsymbol{x}} \boldsymbol{v}. \tag{1.30}$$

Here, the Laplacian $\boldsymbol{\Delta}_{\boldsymbol{x}}$ of the velocity vector is defined as the vector of the Laplacian applied to each component of $\boldsymbol{v}$:

$$\boldsymbol{\Delta}_{\boldsymbol{x}} \boldsymbol{v} = \left(\sum_{\beta} \partial^2_{x_\beta} \boldsymbol{v}_\alpha \right)_{1 \leq \alpha \leq 3}.$$

In order to obtain discretized equations, we need to approximate the second derivatives of the velocity field. A possible route is to use the identity for a scalar function f:

$$\int \left(f(\boldsymbol{r} + \boldsymbol{\delta}) - f(\boldsymbol{r})\right) F_h(|\boldsymbol{\delta}|) \left(5 \frac{\boldsymbol{\delta} \otimes \boldsymbol{\delta}}{\boldsymbol{\delta}^2} - \boldsymbol{I}\right) \mathrm{d}\boldsymbol{\delta} = \boldsymbol{\nabla}^2_{\boldsymbol{x}} f(\boldsymbol{r}) + \mathcal{O}(|\boldsymbol{\delta}|^3) \mathrm{d}t. \tag{1.31}$$

This can be obtained by plugging a Taylor expansion on f at position $\boldsymbol{r}$:

$$f(\boldsymbol{r} + \boldsymbol{\delta}) = f(\boldsymbol{r}) + \boldsymbol{\nabla}_{\boldsymbol{x}} f(\boldsymbol{r}) \cdot \boldsymbol{\delta} + \frac{1}{2} \boldsymbol{\nabla}^2_{\boldsymbol{x}} f(\boldsymbol{r}) : (\boldsymbol{\delta} \otimes \boldsymbol{\delta}) + \mathcal{O}(|\boldsymbol{\delta}|^3),$$

in the integral and noticing that the terms involving first derivatives vanish due to the symmetry of F_h. The second order terms that remain read

$$\begin{aligned} &\int \left(f(\boldsymbol{r} + \boldsymbol{\delta}) - f(\boldsymbol{r})\right) F_h(|\boldsymbol{\delta}|) \left(5 \frac{\boldsymbol{\delta} \otimes \boldsymbol{\delta}}{\boldsymbol{\delta}^2} - \boldsymbol{I}\right) \mathrm{d}\boldsymbol{\delta} \\ &\quad = \frac{1}{2} \sum_{\alpha,\beta} \partial_{x_\alpha} \partial_{x_\beta} f(\boldsymbol{r}) \int F_h(|\boldsymbol{\delta}|) \delta_\alpha \delta_\beta \left(5 \frac{\boldsymbol{\delta} \otimes \boldsymbol{\delta}}{\boldsymbol{\delta}^2} - \boldsymbol{I}\right) \mathrm{d}\boldsymbol{\delta} + \mathcal{O}(|\boldsymbol{\delta}|^3). \end{aligned}$$

In order to further develop this expression, we may check, by integrating by part and using the normalization property of the kernel W_h and the definition of F_h in Equation (1.18), that F_h verifies the following properties

$$\int F_h(|r|) \boldsymbol{r} \otimes \boldsymbol{r} \, \mathrm{d}\boldsymbol{r} = \boldsymbol{I},$$

and

$$\int F_h(|r|) \frac{r_a r_b r_c r_d}{|r|^2} \, \mathrm{d}\boldsymbol{r} = \begin{cases} \dfrac{3}{5} & \text{if } a = b = c = d, \\ \dfrac{1}{5} & \text{if } a, b, c \text{ and } d \text{ are equal by pairs,} \\ 0 & \text{otherwise.} \end{cases}$$

This allows to retrieve the identity (1.31) after bounding $|\boldsymbol{\delta}|$ by the smoothing length h (since $F_h(r) = 0$ for $r > h$). We can finally approximate the second order derivatives by the integral in (1.31) and discretize it with the particle approximation. For the α-th component of the velocity,

$$\boldsymbol{\nabla}^2_{\boldsymbol{x}} v_\alpha(t, \boldsymbol{q}_i) \approx - \sum_{j \neq i} \frac{m_j}{\rho_j} [\boldsymbol{v}_{ij}]_\alpha F_{ij} \left(5 \boldsymbol{e}_{ij} \otimes \boldsymbol{e}_{ij} - \boldsymbol{I}\right),$$

with

$$\boldsymbol{e}_{ij} = \frac{\boldsymbol{r}_{ij}}{\left|\boldsymbol{r}_{ij}\right|}.$$

This discretization may be applied to the derivatives appearing in Equation (1.30) to obtain discrete expressions for the viscous terms:

$$\Delta_{\boldsymbol{x}} \boldsymbol{v}(t, \boldsymbol{q}_i) = \left(\mathrm{Tr}\left(\boldsymbol{\nabla}_{\boldsymbol{x}}^2 v_\alpha(t, \boldsymbol{q}_i)\right)\right)_{1 \leq \alpha \leq 3} \approx -2 \sum_{j \neq i} \frac{m_j}{\rho_j} F_{ij} \boldsymbol{v}_{ij},$$

and

$$\boldsymbol{\nabla}_{\boldsymbol{x}} \mathrm{div}_{\boldsymbol{x}} \boldsymbol{v}(t, \boldsymbol{q}_i) \approx -\sum_{j \neq i} \frac{m_j}{\rho_j} F_{ij} \left[5\left(\boldsymbol{v}_{ij} \cdot \boldsymbol{e}_{ij}\right) \boldsymbol{e}_{ij} - \boldsymbol{v}_{ij}\right].$$

By plugging the latter approximations in Equation (1.30), we obtain the discretized momentum equation

$$\frac{\rho_i}{m_i} \mathrm{d}\boldsymbol{p}_i = -\sum_{j \neq i} \frac{m_j F_{ij}}{\rho_j} \left[2\eta \boldsymbol{v}_{ij} + \left(\zeta + \frac{\eta}{3}\right)\left((\boldsymbol{e}_{ij} \cdot \boldsymbol{v}_{ij})\boldsymbol{e}_{ij} - \boldsymbol{v}_{ij}\right)\right].$$

In order to simplify the notation, we introduce the elementary pairwise dissipative force

$$\boldsymbol{\mathcal{F}}_{\mathrm{diss},ij} = -a_{ij} \boldsymbol{v}_{ij} - \left(\frac{a_{ij}}{3} + b_{ij}\right)(\boldsymbol{e}_{ij} \cdot \boldsymbol{v}_{ij})\boldsymbol{e}_{ij}, \tag{1.32}$$

where the friction coefficients are defined from the fluid viscosities η and ζ appearing in the stress tensor (1.10) as

$$a_{ij} = \left(\frac{5\eta}{3} - \zeta\right) \frac{m_i m_j F_{ij}}{\rho_i \rho_j}, \quad b_{ij} + \frac{a_{ij}}{3} = 5\left(\frac{\eta}{3} + \zeta\right) \frac{m_i m_j F_{ij}}{\rho_i \rho_j}. \tag{1.33}$$

Instead of discretizing the terms in the entropy equation (1.24), it is possible, as in [40], to find the evolution of the entropies S_i so that the total energy $H(\boldsymbol{q}, \boldsymbol{p}, S)$ is preserved by the viscous part of the dynamics. When the positions are not evolved, the variation of the total energy is given by

$$\mathrm{d}H = \sum_{i=1}^{N} \frac{\boldsymbol{p}_i}{m_i} \mathrm{d}\boldsymbol{p}_i + T_i \mathrm{d}S_i.$$

It follows from a simple reorganization that choosing

$$T_i \mathrm{d}S_i = \sum_{j \neq i} \boldsymbol{\mathcal{F}}_{\mathrm{diss},ij} \boldsymbol{v}_{ij} \, \mathrm{d}t,$$

ensures the conservation of the energy. Finally, the pairwise dissipative elementary dynamics can be written as

$$\begin{cases} \mathrm{d}\boldsymbol{q}_i = 0, \\ \mathrm{d}\boldsymbol{p}_i = \displaystyle\sum_{j \neq i} \boldsymbol{\mathcal{F}}_{\mathrm{diss},ij} \, \mathrm{d}t, \\ T_i \mathrm{d}S_i = \dfrac{1}{2} \displaystyle\sum_{j \neq i} \boldsymbol{v}_{ij} \cdot \boldsymbol{\mathcal{F}}_{\mathrm{diss},ij} \, \mathrm{d}t. \end{cases} \tag{1.34}$$

The dynamics (1.34) also satisfies Galilean invariance since $\sum_{i=1}^{N} \mathrm{d}\boldsymbol{p}_i = 0$.

Gathering all the discretized terms (Equations (1.28) and (1.34)), the equations of motion for SPH finally read:

$$\begin{cases} \mathrm{d}\boldsymbol{q}_i = \dfrac{\boldsymbol{p}_i}{m_i}\,\mathrm{d}t, \\ \mathrm{d}\boldsymbol{p}_i = \displaystyle\sum_{j\neq i} \boldsymbol{\mathcal{F}}_{\mathrm{cons},ij}\,\mathrm{d}t + \sum_{j\neq i} \boldsymbol{\mathcal{F}}_{\mathrm{diss},ij}\,\mathrm{d}t, \\ \mathrm{d}S_i = \dfrac{1}{2}\displaystyle\sum_{j\neq i} \boldsymbol{v}_{ij}\cdot\boldsymbol{\mathcal{F}}_{\mathrm{diss},ij}\,\mathrm{d}t. \end{cases} \tag{1.35}$$

One of the main issue in SPH is the poor stability of the method [57, 164]. This may result in particles clumping together while other regions contain very few of them. These large perturbations in the particle configuration decrease the accuracy of the SPH approximations. Some improvements have been proposed through other derivations of the SPH discretization: with a Galerkin approximation [29] or by introducing Riemann solvers [83, 19]. The spatial convergence [129, 57, 116] of SPH has been shown when the smoothing length vanishes ($h \to 0$) while keeping the typical number of neighbors constant thanks to Equation (1.17). This convergence result has been extended to take into account the time discretization (for instance with an explicit Euler scheme), see [139].

SPH is a particle discretization of the Navier-Stokes equations, *i.e.* a macroscopic model. In particular it does not account for thermal fluctuations which can be of importance for phenomena such as hydrodynamic instabilities [94] or for small fluid particles. As such it lacks the microscopic details to accurately describe some complex processes. Furthermore, its validity domain, which is that of hydrodynamics, does not overlap with that of MD. As a macroscopic method, it lacks the ability to justify the scaling laws used to extrapolate the properties observed in atomistic simulations to the hydrodynamic scale.

In the following chapters, we focus on a mesoscopic model, called Smoothed Dissipative Particle Dynamics (SDPD), that adds to the SPH discretization of the Navier-Stokes equations thermal fluctuations similar to the ones considered in coarse-grained methods like DPD or DPDE (see Section 1.1.3). The crucial point is that the fluctuations in SDPD scale consistently with the resolution. The inclusion of these two ingredients makes it a good candidate to accurately describe complex systems through a wide range of resolutions, hence establishing a clearer and firmer link between atomistic and macroscopic models.

2 Smoothed Dissipative Particle Dynamics

Smoothed Dissipative Particle Dynamics [40] is a top-down mesoscopic method relying on the SPH discretization of the Navier-Stokes equations to which thermal fluctuations, modeled by a stochastic force, are incorporated. This allows to deal with hydrodynamics at the nanoscale. Some examples of SDPD applications cover the study of colloids [173, 14] or polymer suspensions [118].

It was first formulated in [40] in terms of the positions $\boldsymbol{q}_i \in \Omega \subset \mathbb{R}^3$, the momenta $\boldsymbol{p}_i \in \mathbb{R}^3$ and the entropies $S_i \in \mathbb{R}$ for $i = 1 \dots N$. This original model is introduced in Section 2.1. One should note that SDPD structure is similar to that of DPDE and this analogy is further enhanced by adopting a simpler expression for the fluctuation term in Section 2.2. The equations of motion are also reformulated in terms of the internal energy variables ε_i instead of the entropies. This allows for a better control of the energy conservation in the integration scheme and a close structural resemblance with DPDE. We introduce reduced units for SDPD that scale with the resolution in Section 2.3. In Section 2.4, we study the existence of invariant measures for SDPD and determine estimators for thermodynamic properties such as temperature and pressure.

2.1 Original formulation of Smoothed Dissipative Particle Dynamics

In its original formulation, SDPD is a set of stochastic differential equations for the positions $\boldsymbol{q}_i \in \Omega \subset \mathbb{R}^3$, the momenta $\boldsymbol{p}_i \in \mathbb{R}^3$ and the entropies $S_i \in \mathbb{R}$ for $i = 1 \dots N$. SDPD consists in the superposition of the SPH equations of motion, discretizing the Navier-Stokes equations (1.9) as established in Section 1.2.3, and of fluctuation terms, which are determined in [40] through the GENERIC framework [66]. The idea of the GENERIC framework is to express the random process $\boldsymbol{X}_t = (\boldsymbol{q}, \boldsymbol{p}, S)$ under the form:

$$d\boldsymbol{X}_t = \left[\boldsymbol{L}\boldsymbol{\nabla}_{\boldsymbol{X}} E + \boldsymbol{M}\boldsymbol{\nabla}_{\boldsymbol{X}} \left(\sum_{i=1}^{N} S_i \right) + k_{\mathrm{B}} \mathrm{div}_{\boldsymbol{X}} \boldsymbol{M} \right] \mathrm{d}t + \mathrm{d}\boldsymbol{Y}_t, \tag{2.1}$$

where $\boldsymbol{L}$ and $\boldsymbol{M}$ are $7N \times 7N$ matrices and $\boldsymbol{Y}_t$ a stochastic process with quadratic variation given by $\mathrm{d}\langle \boldsymbol{Y} \rangle_t = 2k_{\mathrm{B}}\boldsymbol{M}\mathrm{d}t$. The entropy S_i are related to the energy ε_i and the density $\rho_i(\boldsymbol{q})$ with the equation of state (1.22).

The first term of Equation (2.1) is the conservative part of the dynamics. The matrix $\boldsymbol{L}$ can be identified by comparing the GENERIC expression

$$d\boldsymbol{X}_t = \boldsymbol{L}\boldsymbol{\nabla}_{\boldsymbol{X}} E \mathrm{d}t$$

with the conservative dynamics derived for SPH in Equation (1.28). It comes straightforwardly that

$$\boldsymbol{L} = \begin{pmatrix} 0 & \mathscr{M}^{-1} & 0 \\ -\mathscr{M}^{-1} & 0 & 0 \\ 0 & 0 & 0 \end{pmatrix},$$

where $\mathscr{M}$ is the $3N \times 3N$ diagonal matrix such that $\mathscr{M}_{3i+k,3i+k} = m_i$ for $k \in \{0, 1, 2\}$.

In order to find an expression for the matrix $\boldsymbol{M}$, pairwise fluctuation terms were introduced in [40] under the form

$$\mathrm{d}\boldsymbol{\mathscr{F}}_{\mathrm{fluct},ij} = \left(A_{ij} \mathrm{d}\overline{\boldsymbol{W}}_{ij} + \frac{1}{3} B_{ij} \mathrm{Tr}(\mathrm{d}\boldsymbol{W}_{ij}) \boldsymbol{I} \right) \boldsymbol{e}_{ij}, \tag{2.2}$$

with coefficients A_{ij} and B_{ij} symmetric in i and j. Here, for $1 \leq i, j \leq N$, $\boldsymbol{W}_{ij}$ are 3×3 matrices of independent standard Brownian motions such that $\boldsymbol{W}_{ij} = -\boldsymbol{W}_{ji}$. We denote by $\overline{\boldsymbol{W}}_{ij} = \frac{1}{2}\left(\boldsymbol{W}_{ij} + \boldsymbol{W}_{ij}^T\right) - \frac{1}{3}\mathrm{Tr}\left(\boldsymbol{W}_{ij}\right)\boldsymbol{I}$ the symmetric traceless part of $\boldsymbol{W}_{ij}$. These fluctuation terms correspond in the momentum and entropy equations in the GENERIC formulation (2.1) to

$$\mathrm{d}\boldsymbol{Y}_t = \begin{pmatrix} 0 \\ \displaystyle\sum_{j \neq i} \mathrm{d}\boldsymbol{\mathscr{F}}_{\mathrm{fluct},ij} \\ \displaystyle\frac{1}{T_i} \sum_{j \neq i} \mathrm{d}\boldsymbol{\mathscr{F}}_{\mathrm{fluct},ij} \cdot \boldsymbol{v}_{ij} \end{pmatrix}.$$

Note that no fluctuation was assumed for the positions whose evolution is completely described by the conservative part (1.28). Using the relation $\mathrm{d}\langle \boldsymbol{Y} \rangle_t = 2k_{\mathrm{B}}\boldsymbol{M}\mathrm{d}t$, we can determine the matrix $\boldsymbol{M}$ as

$$\boldsymbol{M} = \begin{pmatrix} 0 & 0 & 0 \\ 0 & \widetilde{\boldsymbol{M}}_{pp} & \widetilde{\boldsymbol{M}}_{sp} \\ 0 & \widetilde{\boldsymbol{M}}_{sp}^T & \widetilde{\boldsymbol{M}}_{ss} \end{pmatrix},$$

with the covariance matrices defined as

$$\begin{aligned} 2k_{\mathrm{B}}[\widetilde{\boldsymbol{M}}_{pp}]_{ij}\mathrm{d}t &= \mathrm{d}\left\langle \boldsymbol{p}_i, \boldsymbol{p}_j \right\rangle_t, \\ 2k_{\mathrm{B}}[\widetilde{\boldsymbol{M}}_{ps}]_{ij}\mathrm{d}t &= \mathrm{d}\left\langle \boldsymbol{p}_i, S_j \right\rangle_t, \\ 2k_{\mathrm{B}}[\widetilde{\boldsymbol{M}}_{ss}]_{ij}\mathrm{d}t &= \mathrm{d}\left\langle S_i, S_j \right\rangle_t. \end{aligned}$$

From the expression (2.2) of the fluctuation forces, the latter covariances can be formulated in terms of the covariances between the Brownian motions $\boldsymbol{W}_{ij}$ and $\boldsymbol{W}_{i'j'}$. The independence of the Brownian motions makes all covariances vanish except for $i = i'$ and $j = j'$, or $i = j'$ and $j = i'$

(using the symmetry $\boldsymbol{W}_{ij} = -\boldsymbol{W}_{ji}$). Furthermore it holds

$$\mathrm{d}\left\langle [\boldsymbol{W}_{ij}]_{\alpha\beta} [\boldsymbol{W}_{ij}]_{\alpha'\beta'} \right\rangle_t = \begin{cases} \mathrm{d}t & \text{if } \alpha = \alpha' \text{ and } \beta = \beta' \\ 0 & \text{otherwise.} \end{cases}$$

Using these properties, it follows from straightforward but cumbersome calculations that

$$\frac{\mathrm{d}\left\langle \boldsymbol{p}_i, \boldsymbol{p}_j \right\rangle_t}{\mathrm{d}t} = \begin{cases} -\dfrac{A_{ij}^2}{2}\left(\boldsymbol{I} + \boldsymbol{e}_{ij} \otimes \boldsymbol{e}_{ij}\right) - \dfrac{B_{ij}^2 - A_{ij}^2}{3} \boldsymbol{e}_{ij} \otimes \boldsymbol{e}_{ij} & \text{if } i \neq j, \\ \displaystyle\sum_{k \neq i} \frac{A_{ik}^2}{2} \left(\boldsymbol{I} + \boldsymbol{e}_{ik} \otimes \boldsymbol{e}_{ik}\right) + \frac{B_{ik}^2 - A_{ik}^2}{3} \boldsymbol{e}_{ik} \otimes \boldsymbol{e}_{ik} & \text{if } i = j, \end{cases}$$

for the momenta covariance,

$$\frac{T_j \mathrm{d}\left\langle \boldsymbol{p}_i, S_j \right\rangle_t}{\mathrm{d}t} = \begin{cases} -\dfrac{A_{ij}^2}{4}\left(\boldsymbol{v}_{ij} + \left(\boldsymbol{e}_{ij} \cdot \boldsymbol{v}_{ij}\right) \boldsymbol{e}_{ij}\right) - \dfrac{B_{ij}^2 - A_{ij}^2}{6} \left(\boldsymbol{e}_{ij} \cdot \boldsymbol{v}_{ij}\right) \boldsymbol{e}_{ij} & \text{if } i \neq j \\ \displaystyle\sum_{k \neq i} \frac{A_{ik}^2}{4} \left(\boldsymbol{v}_{ik} + \left(\boldsymbol{e}_{ik} \cdot \boldsymbol{v}_{ik}\right) \boldsymbol{e}_{ik}\right) + \frac{B_{ik}^2 - A_{ik}^2}{6} \left(\boldsymbol{e}_{ik} \cdot \boldsymbol{v}_{ik}\right) \boldsymbol{e}_{ik} & \text{if } i = j \end{cases}$$

for the mixed covariance and

$$\frac{T_i T_j \mathrm{d}\left\langle S_i, S_j \right\rangle_t}{\mathrm{d}t} = \begin{cases} \dfrac{A_{ij}^2}{8}\left(\boldsymbol{v}_{ij}^2 + \left(\boldsymbol{e}_{ij} \cdot \boldsymbol{v}_{ij}\right)^2\right) + \dfrac{B_{ij}^2 - A_{ij}^2}{12} \left(\boldsymbol{e}_{ij} \cdot \boldsymbol{v}_{ij}\right)^2 & \text{if } i \neq j \\ \displaystyle\sum_{k \neq i} \frac{A_{ik}^2}{8} \left(\boldsymbol{v}_{ik}^2 + \left(\boldsymbol{e}_{ik} \cdot \boldsymbol{v}_{ik}\right)^2\right) + \frac{B_{ik}^2 - A_{ik}^2}{6} \left(\boldsymbol{e}_{ik} \cdot \boldsymbol{v}_{ik}\right)^2 & \text{if } i = j \end{cases}$$

for the entropy covariance.

The second term in the GENERIC equation (2.1) is responsible for the dissipative part of the dynamics:

$$\mathrm{d}\boldsymbol{X}_t = \boldsymbol{M} \begin{pmatrix} 0 \\ 0 \\ 1 \end{pmatrix} \mathrm{d}t.$$

In particular, the momentum equation for particle i reads

$$\begin{aligned} \mathrm{d}\boldsymbol{p}_i &= \sum \frac{1}{2k_\mathrm{B}} \mathrm{d}\left\langle \boldsymbol{p}_i, S_j \right\rangle_t \\ &= \sum_{j \neq i} \frac{A_{ij}^2}{8k_\mathrm{B}} \left[\frac{1}{T_i} + \frac{1}{T_j}\right] \left(\boldsymbol{v}_{ij} + \left(\boldsymbol{e}_{ij} \cdot \boldsymbol{v}_{ij}\right) \boldsymbol{e}_{ij}\right) \mathrm{d}t + \frac{B_{ij}^2 - A_{ij}^2}{12k_\mathrm{B}} \left[\frac{1}{T_i} + \frac{1}{T_j}\right] \left(\boldsymbol{e}_{ij} \cdot \boldsymbol{v}_{ij}\right) \boldsymbol{e}_{ij} \mathrm{d}t \end{aligned}$$

Compared to the dissipative part of SPH (see Equation (1.34)), this allows to identify the fluctuation amplitudes

$$A_{ij}^2 = 8k_\mathrm{B} a_{ij} \frac{T_i T_j}{T_i + T_j}, \quad B_{ij}^2 = 12k_\mathrm{B} b_{ij} \frac{T_i T_j}{T_i + T_j}, \tag{2.3}$$

with the viscous coefficients a_{ij} and b_{ij} defined by Equation (1.33).

The last remaining term is an extra dissipative force balancing the addition of thermal fluctuations. From Equation (2.1), it reads

$$\mathrm{d}\boldsymbol{X}_t = k_\mathrm{B}\mathrm{div}_{\boldsymbol{X}}\boldsymbol{M}\mathrm{d}t,$$

or more explicitly for particle i

$$\begin{cases} \mathrm{d}\boldsymbol{q}_i = 0, \\ \mathrm{d}\boldsymbol{p}_i = \dfrac{1}{2}\displaystyle\sum_{j=1}^{N} \mathrm{div}_{\boldsymbol{p}_j}\mathrm{d}\left\langle \boldsymbol{p}_i, \boldsymbol{p}_j \right\rangle_t + \partial_{S_j}\mathrm{d}\left\langle \boldsymbol{p}_i, S_j \right\rangle_t, \\ T_i\mathrm{d}\boldsymbol{S}_i = \dfrac{T_i}{2}\displaystyle\sum_{j=1}^{N} \mathrm{div}_{\boldsymbol{p}_j}\mathrm{d}\left\langle S_i, \boldsymbol{p}_j \right\rangle_t + \partial_{S_j}\mathrm{d}\left\langle S_i, S_j \right\rangle_t. \end{cases} \tag{2.4}$$

In order to further evaluate the equation of motions (2.4), we need to compute the following derivatives with respect to momentum

$$\mathrm{div}_{\boldsymbol{p}_j}\boldsymbol{v}_{ij} = -\frac{3}{m_j},$$

$$\mathrm{div}_{\boldsymbol{p}_j}\left[(\boldsymbol{e}_{ij}\cdot\boldsymbol{v}_{ij})\boldsymbol{e}_{ij}\right] = -\frac{1}{m_j}.$$

and with respect to entropy

$$\partial_{S_j}\left(\frac{1}{T_i+T_j}\right) = -\frac{T_j}{C_j}\frac{1}{(T_i+T_j)^2},$$

$$\partial_{S_j}\left(\frac{T_j}{T_i+T_j}\right) = \frac{1}{C_j}\frac{T_iT_j}{(T_i+T_j)^2},$$

$$\partial_{S_j}\left(\frac{1}{T_j(T_i+T_j)}\right) = -\frac{1}{C_j}\left(\frac{1}{T_i(T_i+T_j)} + \frac{1}{(T_i+T_j)^2}\right).$$

This allows to rewrite the momentum equation in (2.4) as

$$\begin{aligned}\mathrm{d}\boldsymbol{p}_i &= k_\mathrm{B}\sum_{j\neq i}\left(\partial_{S_i}\left(\frac{T_i}{T_i+T_j}\right) + \partial_{S_j}\left(\frac{T_j}{T_i+T_j}\right)\right)\left[a_{ij}\boldsymbol{v}_{ij} + \left(b_{ij}+\frac{a_{ij}}{3}\right)\left(\boldsymbol{e}_{ij}\cdot\boldsymbol{v}_{ij}\right)\boldsymbol{v}_{ij}\right]\mathrm{d}t \\ &= \sum_{j\neq i}\widetilde{\boldsymbol{\mathcal{F}}}_{\mathrm{diss},ij}\mathrm{d}t,\end{aligned}$$

where we introduce the additional dissipative force

$$\widetilde{\boldsymbol{\mathcal{F}}}_{\mathrm{diss},ij} = d_{ij}\boldsymbol{\mathcal{F}}_{\mathrm{diss},ij},$$

that is related to the SPH dissipative force (1.32) through the coefficient

$$d_{ij} = k_\mathrm{B}\frac{T_iT_j}{(T_i+T_j)^2}\left(\frac{1}{C_i}+\frac{1}{C_j}\right).$$

Lastly the entropy equation in (2.4) becomes

$$\begin{aligned}
T_i \mathrm{d}\boldsymbol{S}_i &= k_{\mathrm{B}} \sum_{j\neq i} \frac{T_i T_j}{T_i+T_j} \left(a_{ij} \left[\mathrm{div}_{\boldsymbol{p}_i} + \mathrm{div}_{\boldsymbol{p}_j} \right] \boldsymbol{v}_{ij} + \left(b_{ij} + \frac{a_{ij}}{3} \right) \left[\mathrm{div}_{\boldsymbol{p}_i} + \mathrm{div}_{\boldsymbol{p}_j} \right] \left((\boldsymbol{e}_{ij} \cdot \boldsymbol{v}_{ij}) \boldsymbol{e}_{ij} \right) \right) \mathrm{d}t \\
&\quad + \frac{k_{\mathrm{B}} T_i}{2} \sum_{j\neq i} \left[\partial_{S_i} \left(\frac{T_j}{T_i(T_i+T_j)} \right) + \partial_{S_j} \left(\frac{1}{T_i+T_j} \right) \right] \left[a_{ij} \boldsymbol{v}_{ij}^2 + \left(b_{ij} + \frac{a_{ij}}{3} \right) \left(\boldsymbol{e}_{ij} \cdot \boldsymbol{v}_{ij} \right)^2 \right] \mathrm{d}t \\
&= -4 \sum_{j\neq i} \left[\frac{1}{m_i} + \frac{1}{m_j} \right] k_{\mathrm{B}} \frac{T_i T_j}{T_i+T_j} \left(b_{ij} + \frac{10}{3} a_{ij} \right) \mathrm{d}t \\
&\quad - \frac{1}{2} \sum_{j\neq i} \left[\frac{k_{\mathrm{B}}}{C_i} \frac{T_j}{T_i+T_j} + d_{ij} \right] \left[a_{ij} \boldsymbol{v}_{ij}^2 + \left(b_{ij} + \frac{a_{ij}}{3} \right) \left(\boldsymbol{e}_{ij} \cdot \boldsymbol{v}_{ij} \right)^2 \right] \mathrm{d}t.
\end{aligned}$$

In order to simplify the notation, we introduce the coefficient $\mathscr{D}_{ij} = 1 - d_{ij} + \frac{T_i}{T_i+T_j} \frac{k_{\mathrm{B}}}{C_i}$ and the reduced mass $m_{ij} = \frac{1}{2} \left(\frac{1}{m_i} + \frac{1}{m_j} \right)^{-1}$. Gathering all the terms from the GENERIC equation (2.1), the elementary fluctuation/dissipation dynamics reads

$$\begin{cases}
\mathrm{d}\boldsymbol{q}_i = 0, \\
\mathrm{d}\boldsymbol{p}_i = \displaystyle\sum_{j\neq i} (1-d_{ij}) \boldsymbol{\mathscr{F}}_{\mathrm{diss},ij} \, \mathrm{d}t + \mathrm{d}\boldsymbol{\mathscr{F}}_{\mathrm{fluct},ij}, \\
T_i \mathrm{d}S_i = \displaystyle\sum_{j\neq i} \frac{1}{2} \mathscr{D}_{ij} \boldsymbol{v}_{ij}^T \boldsymbol{\mathscr{F}}_{\mathrm{diss},ij} \, \mathrm{d}t - \frac{8 k_{\mathrm{B}}}{m_{ij}} \frac{T_i T_j}{T_i+T_j} \left(\frac{10}{3} a_{ij} + b_{ij} \right) \mathrm{d}t
\end{cases} \tag{2.5}$$

The dynamics (2.5) replaces the dissipative dynamics (1.34) of the SPH discretization. It can be shown that it preserves the energy $H(\boldsymbol{q}, \boldsymbol{p}, S)$ (defined in Equation (1.29)) and the total momentum. The equation of state (1.23) allows to estimate the thermodynamic properties (ε_i, P_i, T_i and C_i) for each particle.

Finally, the complete set of equations of motion for the original SDPD [40] is obtained by concatenating the conservative dynamics (1.28) and the fluctuation/dissipation dynamics (2.5) as

$$\begin{cases}
\mathrm{d}\boldsymbol{q}_i = \dfrac{\boldsymbol{p}_i}{m_i} \mathrm{d}t, \\
\mathrm{d}\boldsymbol{p}_i = \displaystyle\sum_{j\neq i} m_i m_j \left(\frac{P_i}{\rho_i^2} + \frac{P_j}{\rho_j^2} \right) F_{ij} \boldsymbol{r}_{ij} \, \mathrm{d}t - (1-d_{ij}) \left[a_{ij} \boldsymbol{v}_{ij} + \left(\frac{a_{ij}}{3} + b_{ij} \right) (\boldsymbol{v}_{ij}^T \boldsymbol{e}_{ij}) \boldsymbol{e}_{ij} \right] \mathrm{d}t \\
\qquad\qquad + \left(A_{ij} \mathrm{d}\overline{\boldsymbol{W}}_{ij} + \dfrac{1}{3} B_{ij} \mathrm{Tr}(\mathrm{d}\boldsymbol{W}_{ij}) \boldsymbol{I} \right) \boldsymbol{e}_{ij}, \\
T_i \mathrm{d}S_i = \displaystyle\sum_{j\neq i} \frac{1}{2} \mathscr{D}_{ij} \left(a_{ij} \boldsymbol{v}_{ij}^2 + \left(\frac{a_{ij}}{3} + b_{ij} \right) (\boldsymbol{v}_{ij}^T \boldsymbol{e}_{ij})^2 \right) \mathrm{d}t - \frac{8 k_{\mathrm{B}}}{m_{ij}} \frac{T_i T_j}{T_i+T_j} \left(\frac{10}{3} a_{ij} + b_{ij} \right) \mathrm{d}t \\
\qquad\qquad - \dfrac{1}{2} \boldsymbol{v}_{ij}^T \left(A_{ij} \mathrm{d}\overline{\boldsymbol{W}}_{ij} + \dfrac{1}{3} B_{ij} \mathrm{Tr}(\mathrm{d}\boldsymbol{W}_{ij}) \boldsymbol{I} \right) \boldsymbol{e}_{ij}.
\end{cases} \tag{2.6}$$

The dynamics (2.6) preserve the total momentum $\sum_{i=1}^{N} \boldsymbol{p}_i$ and the total energy $H(\boldsymbol{q}, \boldsymbol{p}, S)$ since the elementary dynamics (1.28) and (2.5) conserve these invariants. The GENERIC framework [66]

ensures that measures of the form

$$\nu(\mathrm{d}\boldsymbol{q}\,\mathrm{d}\boldsymbol{p}\,\mathrm{d}S) = g\left(H(\boldsymbol{q},\boldsymbol{p},S),\sum_{i=1}^{N}\boldsymbol{p}_i\right)\prod_{i=1}^{N}\frac{\exp\left(\frac{S_i}{k_\mathrm{B}}\right)}{T_i(S_i,\boldsymbol{q})}\,\mathrm{d}\boldsymbol{q}\,\mathrm{d}\boldsymbol{p}\,\mathrm{d}S, \tag{2.7}$$

for any function g, are invariant for the dynamics (2.6).

The dynamics (2.6) has mainly been used in a simplified form when internal temperatures are kept fixed at $T_i = T$, which is enough to describe isothermal situations. The whole set of equations is however needed when we consider systems for which the energy is conserved. For such situations, the formulation of SDPD in the entropy variables is not very practical from a numerical point of view. More microscopic models, like DPDE, tend to focus on the energies, which enables to devise conservative numerical schemes more easily. Furthermore, the expression of the fluctuations in (2.6) is quite complex and requires to draw a matrix of random variables for each pair. These remarks lead us to reformulate the equations of motion for SDPD with internal energies instead of entropies. This allows to increase the similarities between SDPD and DPDE, notably for the fluctuation/dissipation terms.

2.2 Reformulation of SDPD in terms of the internal energies

We propose in this section a reformulation of the original SDPD equations (2.6) in terms of positions, momenta and internal energies ε_i. In general, the energies are bounded below. Upon shifting the minimum of the internal energy, we may consider that the energies remain positive ($\varepsilon_i \geq 0$). The corresponding phase space is denoted by $\mathscr{E} = \Omega^N \times \mathbb{R}^{3N} \times \mathbb{R}_+^N$. We also propose a somewhat simpler expression for the fluctuation term in analogy with the stochastic term used in DPDE [7, 43]. The new expressions for the fluctuation/dissipation forces are chosen to ensure the same invariant measure as in the original SDPD equations. Moreover, the same friction forces appear in both formulations. The interest of this reformulation is twofold: first, it allows for a better control of the energy conservation in the integration scheme; second, it is a first step towards a more straightforward coupling with DPDE thanks to the increased structural similarity between the two methods.

2.2.1 Equation of state

As in Section 1.2.3, we need an input equation of state in order to close the equations and characterize the physical behavior of the material. In the energy formulation, the equation of state links the entropy S_i with the internal energy ε_i and the density $\rho_i(\boldsymbol{q})$ of the particles as

$$S_i(\varepsilon_i,\boldsymbol{q}) = \mathscr{S}(\varepsilon_i,\rho_i(\boldsymbol{q})). \tag{2.8}$$

The pressure, temperature and heat capacity are then determined accordingly as

$$\begin{aligned}\mathscr{T}(\varepsilon,\rho) &= \left[\frac{1}{\partial_\varepsilon \mathscr{S}}\right](\varepsilon,\rho),\\ \mathscr{P}(\varepsilon,\rho) &= -\frac{\rho^2}{m}\left[\frac{\partial_\rho \mathscr{S}}{\partial_\varepsilon \mathscr{S}}\right](\varepsilon,\rho),\\ \mathscr{C}(\varepsilon,\rho) &= -\left[\frac{(\partial_\varepsilon \mathscr{S})^2}{\partial_\varepsilon^2 \mathscr{S}}\right](\varepsilon,\rho),\end{aligned} \tag{2.9}$$

and assigned to each particle as

$$\begin{aligned}T_i(\varepsilon_i,\boldsymbol{q}) &= \mathscr{T}(\varepsilon_i,\rho_i(\boldsymbol{q})),\\ P_i(\varepsilon_i,\boldsymbol{q}) &= \mathscr{P}(\varepsilon_i,\rho_i(\boldsymbol{q})),\\ C_i(\varepsilon_i,\boldsymbol{q}) &= \mathscr{C}(\varepsilon_i,\rho_i(\boldsymbol{q})).\end{aligned}$$

As in the previous sections, we omit from now on the dependence of T_i, P_i and C_i on the variables ε_i and $\boldsymbol{q}$.

2.2.2 Energy reformulation of SDPD

In its energy reformulation, SDPD can still be split in two main elementary sub-dynamics. We first review the adaptation of the conservative part to the formulation in the internal energy variable before introducing a new expression for the fluctuation/dissipation part inspired by DPDE. We finally give the overall equations of motion for SDPD formulated in the position, momentum and energy variables.

Elementary conservative dynamics

We keep the conservative part of the dynamics (1.28). In order to reformulate it in terms of internal energies, we compute the associated variation in the energy, expressed in the new set of independent variables $(\boldsymbol{q},\boldsymbol{p},\varepsilon)$ as

$$E(\boldsymbol{q},\boldsymbol{p},\varepsilon) = \sum_{i=1}^{N} \varepsilon_i + \frac{\boldsymbol{p}_i^2}{2m}. \tag{2.10}$$

Since a change of variables should not change the energy, H defined by Equation (1.29) and E are related by

$$E(\boldsymbol{q},\boldsymbol{p},\varepsilon) = H\Big(\boldsymbol{q},\boldsymbol{p},\mathscr{S}(\varepsilon_1,\rho_i(\boldsymbol{q})),\dots,\mathscr{S}(\varepsilon_N,\rho_i(\boldsymbol{q}))\Big).$$

The dynamics (1.28) being isentropic, the induced energy variation is simply given by

$$\mathrm{d}\varepsilon_i = -P_i \mathrm{d}\mathscr{V}_i. \tag{2.11}$$

From the definition (1.20) of the density and volume of a particle, the infinitesimal volume variation reads $\mathrm{d}\mathscr{V}_i = -\dfrac{m_i}{\rho_i^2}\mathrm{d}\rho_i$ with $\mathrm{d}\rho_i$ given by

$$\mathrm{d}\rho_i = -\sum_{j\neq i} m_j F_{ij} \boldsymbol{r}_{ij}\cdot\boldsymbol{v}_{ij}\,\mathrm{d}t.$$

Therefore, the conservative part of the dynamics can be rewritten as

$$\begin{cases} \mathrm{d}\boldsymbol{q}_i = \dfrac{\boldsymbol{p}_i}{m_i}\,\mathrm{d}t, \\ \mathrm{d}\boldsymbol{p}_i = \displaystyle\sum_{j\neq i} \boldsymbol{\mathscr{F}}_{\mathrm{cons},ij}\,\mathrm{d}t, \\ \mathrm{d}\varepsilon_i = -\displaystyle\sum_{j\neq i} \frac{m_i m_j P_i}{\rho_i(\boldsymbol{q})^2} F_{ij}\boldsymbol{r}_{ij}\cdot\boldsymbol{v}_{ij}\,\mathrm{d}t. \end{cases} \tag{2.12}$$

Let us emphasize that the indices i and j do not play a symmetrical role in the evolution of the internal energies, although the conservative forces are symmetric. This asymmetry is a consequence of the fact that the energy variation (2.11) for a given particle only involves the volume variation of this particle. This formulation preserves the total momentum since the forces are antisymmetric and we check in Section 2.2.3 that the total energy is conserved by the dynamics (2.12).

Elementary fluctuation-dissipation dynamics

In the spirit of DPDE (see Equation (1.7)), we choose a pairwise fluctuation and dissipation term for $i < j$ of the following form:

$$\begin{cases} \mathrm{d}\boldsymbol{p}_i = -\boldsymbol{\Gamma}_{ij}\boldsymbol{v}_{ij}\,\mathrm{d}t + \Sigma_{ij}\mathrm{d}\boldsymbol{B}_{ij}, \\ \mathrm{d}\boldsymbol{p}_j = \boldsymbol{\Gamma}_{ij}\boldsymbol{v}_{ij}\,\mathrm{d}t - \Sigma_{ij}\mathrm{d}\boldsymbol{B}_{ij}, \\ \mathrm{d}\varepsilon_i = \dfrac{1}{2}\left[\boldsymbol{v}_{ij}^T\boldsymbol{\Gamma}_{ij}\boldsymbol{v}_{ij} - \dfrac{\mathrm{Tr}(\Sigma_{ij}\Sigma_{ij}^T)}{m_{ij}}\right]\mathrm{d}t - \dfrac{1}{2}\boldsymbol{v}_{ij}^T\Sigma_{ij}\mathrm{d}\boldsymbol{B}_{ij}, \\ \mathrm{d}\varepsilon_j = \dfrac{1}{2}\left[\boldsymbol{v}_{ij}^T\boldsymbol{\Gamma}_{ij}\boldsymbol{v}_{ij} - \dfrac{\mathrm{Tr}(\Sigma_{ij}\Sigma_{ij}^T)}{m_{ij}}\right]\mathrm{d}t - \dfrac{1}{2}\boldsymbol{v}_{ij}^T\Sigma_{ij}\mathrm{d}\boldsymbol{B}_{ij}, \end{cases} \tag{2.13}$$

where $\boldsymbol{B}_{ij}$ is a 3-dimensional vector of standard Brownian motions, instead of the 6-dimensional Brownian motion $\overline{\boldsymbol{W}}_{ij}$ appearing in the original dynamics (2.5). The friction and diffusion coefficients $\boldsymbol{\Gamma}_{ij}$ and Σ_{ij} are 3×3 symmetric matrices. In the dynamics (2.13), the equations acting on the momenta preserve the total momentum in the system. Furthermore, as in DPDE, the equations for the energy variables are determined to ensure the conservation of the total energy $E(\boldsymbol{q},\boldsymbol{p},\varepsilon)$. As $\mathrm{d}\varepsilon_i = -\dfrac{1}{2}\mathrm{d}\left(\dfrac{\boldsymbol{p}_i^2}{2m_i} + \dfrac{\boldsymbol{p}_j^2}{2m_j}\right)$, Itô calculus yields the resulting equations in (2.13).

For the friction and fluctuation coefficients, we consider matrices of the form

$$\boldsymbol{\Gamma}_{ij} = \gamma_{ij}^{\parallel}\boldsymbol{P}_{ij}^{\parallel} + \gamma_{ij}^{\perp}\boldsymbol{P}_{ij}^{\perp}, \quad \Sigma_{ij} = \sigma_{ij}^{\parallel}\boldsymbol{P}_{ij}^{\parallel} + \sigma_{ij}^{\perp}\boldsymbol{P}_{ij}^{\perp}, \tag{2.14}$$

with the projection matrices $\boldsymbol{P}_{ij}^{\parallel}$, on the line of the centers of mass, and $\boldsymbol{P}_{ij}^{\perp}$, in the orthogonal plane, given by

$$\boldsymbol{P}_{ij}^{\parallel} = \boldsymbol{e}_{ij}\otimes\boldsymbol{e}_{ij}, \quad \boldsymbol{P}_{ij}^{\perp} = \boldsymbol{I} - \boldsymbol{P}_{ij}^{\parallel}.$$

This amounts to considering non isotropic friction and fluctuation coefficients in the directions parallel and orthogonal to the line defined by $\boldsymbol{q}_i$ and $\boldsymbol{q}_j$.

Equations of motion

Using the decomposition (2.14) for the friction and fluctuation matrices, the dynamics (2.13) is obtained by superposing the following dynamics for $\theta \in \{\parallel, \perp\}$:

$$\begin{cases} \mathrm{d}\boldsymbol{p}_i = -\gamma_{ij}^{\theta}\boldsymbol{P}_{ij}^{\theta}\boldsymbol{v}_{ij}\mathrm{d}t + \sigma_{ij}^{\theta}\boldsymbol{P}_{ij}^{\theta}\mathrm{d}\boldsymbol{B}_{ij}, \\ \mathrm{d}\boldsymbol{p}_j = \gamma_{ij}^{\theta}\boldsymbol{P}_{ij}^{\theta}\boldsymbol{v}_{ij}\mathrm{d}t - \sigma_{ij}^{\theta}\boldsymbol{P}_{ij}^{\theta}\mathrm{d}\boldsymbol{B}_{ij}, \\ \mathrm{d}\varepsilon_i = \dfrac{1}{2}\left[\gamma_{ij}^{\theta}\boldsymbol{v}_{ij}^T\boldsymbol{P}_{ij}^{\theta}\boldsymbol{v}_{ij} - \dfrac{(\sigma_{ij}^{\theta})^2}{m}\mathrm{Tr}(\boldsymbol{P}_{ij}^{\theta})\right]\mathrm{d}t - \dfrac{1}{2}\sigma_{ij}^{\theta}\boldsymbol{v}_{ij}^T\boldsymbol{P}_{ij}^{\theta}\mathrm{d}\boldsymbol{B}_{ij}, \\ \mathrm{d}\varepsilon_j = \dfrac{1}{2}\left[\gamma_{ij}^{\theta}\boldsymbol{v}_{ij}^T\boldsymbol{P}^{\theta}\boldsymbol{v}_{ij} - \dfrac{(\sigma_{ij}^{\theta})^2}{m}\mathrm{Tr}(\boldsymbol{P}_{ij}^{\theta})\right]\mathrm{d}t - \dfrac{1}{2}\sigma_{ij}^{\theta}\boldsymbol{v}_{ij}^T\boldsymbol{P}_{ij}^{\theta}\mathrm{d}\boldsymbol{B}_{ij}. \end{cases} \tag{2.15}$$

The choice

$$\begin{aligned} \gamma_{ij}^{\parallel} &= \left(\frac{4}{3}a_{ij} + b_{ij}\right)\left(1 - d_{ij}\right), \\ \gamma_{ij}^{\perp} &= a_{ij}\left(1 - d_{ij}\right), \\ \sigma_{ij}^{\theta} &= 2\sqrt{\frac{\gamma_{\theta}}{1 - d_{ij}}k_{\mathrm{B}}\frac{T_iT_j}{T_i + T_j}}, \end{aligned} \tag{2.16}$$

with the coefficients a_{ij} and b_{ij} defined by Equation (1.33), ensures that measures of the form

$$\mu(\mathrm{d}\boldsymbol{q}\,\mathrm{d}\boldsymbol{p}\,\mathrm{d}\varepsilon) = g\left(E(\boldsymbol{q},\boldsymbol{p},\varepsilon), \sum_{i=1}^{N}\boldsymbol{p}_i\right)\prod_{i=1}^{N}\frac{\exp\left(\frac{S_i(\varepsilon_i,\boldsymbol{q})}{k_{\mathrm{B}}}\right)}{T_i(\varepsilon_i,\boldsymbol{q})}\,\mathrm{d}\boldsymbol{q}\,\mathrm{d}\boldsymbol{p}\,\mathrm{d}\varepsilon \tag{2.17}$$

are left invariant by the elementary dynamics (2.13) (see Section 2.4.2 for the proof). Note that μ is just obtained from the measure ν defined in (2.7) by the change of variables $(\boldsymbol{q},\boldsymbol{p},S) \to (\boldsymbol{q},\boldsymbol{p},\varepsilon)$. As our derivation shows, other choices are possible for the coefficients γ_{ij}^{θ} and σ_{ij}^{θ} (see Equation (2.30) in Section 2.4.2). This may be of interest since it is possible to choose a constant fluctuation magnitude σ_{ij}^{θ} while the friction coefficient γ_{ij}^{θ} still depends on the configuration of the system through the positions $\boldsymbol{q}$ and the internal energies ε_i and ε_j as

$$\gamma_{ij}^{\theta} = \frac{1}{4}\left(\sigma_{ij}^{\theta}\right)^2\left[\left(\frac{1}{k_{\mathrm{B}}} - \frac{1}{C_i}\right)\frac{1}{T_i} + \left(\frac{1}{k_{\mathrm{B}}} - \frac{1}{C_j}\right)\frac{1}{T_j}\right],$$

following Equation (2.30). Such a choice would further increase the similarity with DPDE and simplify the numerical discretization. However, in this work, we stick to the choice (2.16) which yields the same friction terms as in the original SDPD equations (2.6).

As a result, the SDPD equations of motion reformulated in the position, momentum and internal energy variables read

$$\begin{cases} \mathrm{d}\boldsymbol{q}_i = \dfrac{\boldsymbol{p}_i}{m_i}\,\mathrm{d}t, \\ \mathrm{d}\boldsymbol{p}_i = \displaystyle\sum_{j\neq i} m_im_j\left(\frac{P_i}{\rho_i^2} + \frac{P_j}{\rho_j^2}\right)F_{ij}\boldsymbol{r}_{ij}\,\mathrm{d}t - \boldsymbol{\Gamma}_{ij}\boldsymbol{v}_{ij}\,\mathrm{d}t + \boldsymbol{\Sigma}_{ij}\mathrm{d}\boldsymbol{B}_{ij}, \\ \mathrm{d}\varepsilon_i = \displaystyle\sum_{j\neq i} -\frac{m_im_jP_i}{\rho_i^2}F_{ij}\boldsymbol{r}_{ij}^T\boldsymbol{v}_{ij}\,\mathrm{d}t + \frac{1}{2}\left[\boldsymbol{v}_{ij}^T\boldsymbol{\Sigma}_{ij}\boldsymbol{v}_{ij} - \frac{1}{m_{ij}}\mathrm{Tr}(\boldsymbol{\Sigma}_{ij}\boldsymbol{\Sigma}_{ij}^T)\right]\mathrm{d}t - \frac{1}{2}\boldsymbol{v}_{ij}^T\boldsymbol{\Sigma}_{ij}\mathrm{d}\boldsymbol{B}_{ij}, \end{cases} \tag{2.18}$$

with Σ_{ij} and $\mathbf{\Gamma}_{ij}$ given by (2.14) and (2.16).

2.2.3 Conservation properties

By construction, the dynamics (2.18) preserves the total momentum $\sum_{i=1}^{N} \boldsymbol{p}_i$. It can also be checked that the total energy $E(\boldsymbol{q}, \boldsymbol{p}, \varepsilon)$ defined in Equation (2.10) is conserved by showing that each elementary dynamics (2.12) and (2.13) independently preserves the total energy $E(\boldsymbol{q}, \boldsymbol{p}, \varepsilon)$. The variation of the energy along the trajectory is given by

$$\mathrm{d}E(\boldsymbol{q}, \boldsymbol{p}, \varepsilon) = \sum_{i=1}^{N} \frac{1}{2m} \mathrm{d}\left(\boldsymbol{p}_i^2\right) + \mathrm{d}\varepsilon_i. \tag{2.19}$$

We next evaluate this variation for the sub-dynamics under consideration.

Conservation of the energy by the conservative part of the dynamics

We first study the conservative dynamics (2.12). Since it is a deterministic dynamics, the energy variation simply reads

$$\mathrm{d}E(\boldsymbol{q}, \boldsymbol{p}, \varepsilon) = \sum_{i=1}^{N} \frac{1}{m_i} \boldsymbol{p}_i^T \mathrm{d}\boldsymbol{p}_i + \mathrm{d}\varepsilon_i.$$

In view of the equations of motion (2.12), we get

$$\mathrm{d}E(\boldsymbol{q}, \boldsymbol{p}, \varepsilon) = \sum_{i=1}^{N} \frac{1}{m_i} \boldsymbol{p}_i^T \left[\sum_{j \neq i} m_i m_j \left(\frac{P_i}{\rho_i^2} + \frac{P_j}{\rho_j^2} \right) F_{ij} \boldsymbol{r}_{ij} \, \mathrm{d}t \right] - \sum_{i=1}^{N} \sum_{j \neq i} m_i m_j \frac{P_i}{\rho_i^2} F_{ij} \boldsymbol{r}_{ij}^T \boldsymbol{v}_{ij} \, \mathrm{d}t.$$

A final reorganization of the second term makes it clear that the right hand side vanishes and proves the conservation of the energy by the elementary dynamics (2.12).

Conservation of the energy by the fluctuation and dissipation part of the dynamics

We now focus on the elementary pairwise fluctuation and dissipation dynamics (2.13) for a given pair (i, j). Since this is a stochastic dynamics, we resort to Itô calculus to further evaluate the energy variation as:

$$\begin{aligned} \mathrm{d}\left[\frac{\boldsymbol{p}_i^2}{2m_i} + \frac{\boldsymbol{p}_j^2}{2m_j} \right] &= \frac{1}{m_i} \boldsymbol{p}_i^T \mathrm{d}\boldsymbol{p}_i + \frac{1}{m_j} \boldsymbol{p}_j^T \mathrm{d}\boldsymbol{p}_j + \frac{\mathrm{Tr}\left(\Sigma_{ij} \Sigma_{ij}^T\right)}{m_{ij}} \mathrm{d}t \\ &= \boldsymbol{v}_{ij}^T \mathrm{d}\boldsymbol{p}_i + \frac{1}{m_{ij}} \mathrm{Tr}\left(\Sigma_{ij} \Sigma_{ij}^T\right) \mathrm{d}t. \end{aligned}$$

In view of the equations of motion (2.13), the variation of the internal energies can be rewritten as

$$\mathrm{d}\left(\varepsilon_i + \varepsilon_j\right) = -\boldsymbol{v}_{ij}^T \mathrm{d}\boldsymbol{p}_i - \frac{1}{m_{ij}} \mathrm{Tr}\left(\Sigma_{ij} \Sigma_{ij}^T\right) \mathrm{d}t.$$

This proves that $\mathrm{d}E(\boldsymbol{q}, \boldsymbol{p}, \varepsilon) = 0$. The energy is thus conserved by the pairwise dynamics (2.13).

Since all the elementary dynamics preserve the energy, the global dynamics (2.18) obtained by the superposition of (2.12) and (2.13) also preserves the energy $E(\boldsymbol{q}, \boldsymbol{p}, \varepsilon)$.

2.3 Reduced units for SDPD

One of the important feature of SDPD is that it is possible to prescribe a size for the particles, which leads us to study the effect of the resolution and enables a multiscale approach (see Chapter 5). In this perspective, the mass of the fluid particles is given by $m_K = Km_0$, where m_0 is the mass of one microscopic particle (*i.e.* a molecule). It is in fact convenient to define a system of reduced units for each size K:

$$\begin{aligned} \widetilde{m}_K &= m_K, \\ \widetilde{l}_K &= \left(\frac{m_K}{\rho}\right)^{\frac{1}{3}}, \\ \widetilde{\varepsilon}_K &= Kk_{\mathrm{B}}T, \end{aligned} \tag{2.20}$$

where $\widetilde{m}_K$ is the mass unit, $\widetilde{l}_K$ the length unit, $\widetilde{\varepsilon}_K$ the energy unit and ρ the average density of the fluid. With such a set of reduced units, the time unit is

$$\widetilde{t}_K = \widetilde{l}_K \sqrt{\frac{\widetilde{m}_K}{\widetilde{\varepsilon}_K}} = \frac{m_0^{\frac{5}{6}} K^{\frac{1}{3}}}{\rho^{\frac{1}{3}} \sqrt{k_{\mathrm{B}}T}}.$$

The smoothing length h_K defining the cut-off radius in (1.14) and (1.15) also needs to be adapted to the size of the SDPD particles so that the particle approximation (see Equation (1.16)) continues to make sense. In order to keep the average number of neighbors roughly constant in the smoothing sum, h_K should be rescaled as

$$h_K = h\left(\frac{m_K}{\rho}\right)^{\frac{1}{3}},$$

following the relation (1.17). In this work, we have taken $h = 2.5$, which correspond to a typical number of 60-70 neighbors, a commonly accepted number [120].

2.4 Thermodynamic properties of the reformulated SDPD

We now turn to the analysis of the thermodynamic properties of SDPD. In order to check that measures μ of the form (2.17) are left invariant by the SDPD dynamics (2.18), we first introduce some standard tools to study stochastic dynamics in Section 2.4.1 We then proceed in Section 2.4.2 to show that measures given by Equation (2.17) are left invariant by each sub-dynamics: the conservative part (see Equation (2.12)) and the pairwise fluctuation/dynamics parts (see Equation (2.13)). Finally, we determine estimators for temperature and pressure in the context of SDPD in Section 2.4.3

2.4.1 Stochastic dynamics and the Fokker-Plank equation

In this section, we present some standard tools (see [108] for instance) which we use in the following sections to study the SDPD stochastic differential equations and prove the invariance of (2.17). We consider stochastic dynamics of the form

$$\mathrm{d}X_t = b(X_t)\,\mathrm{d}t + \mathscr{S}(X_t)\mathrm{d}\mathscr{W}_t, \tag{2.21}$$

where the variable X_t is of dimension d, the drift coefficient b is a vector of dimension d, the diffusion coefficient $\mathscr{S}$ a matrix of dimension $d \times n$ and $\mathscr{W}$ a standard Brownian motion of dimension n. The solutions X_t of such stochastic differential equations (SDE) are Markov processes and are characterized by their transition function defined, for times $0 \leq s < t$ and smooth test functions ϕ, as

$$P_{s,t}(\phi)(x) = \mathbb{E}(\phi(x_t)|x_s = x).$$

We can also associate to these stochastic dynamics an operator $\mathscr{L}$, called the infinitesimal generator, defined as the following limit:

$$\mathscr{L} = \lim_{s \to 0} \frac{P_{t,t+s} - \boldsymbol{I}}{s}.$$

In particular, for SDE of the form (2.21), the infinitesimal generator reads

$$\mathscr{L} = b \cdot \boldsymbol{\nabla}_X + \frac{1}{2} \mathscr{S}\mathscr{S}^T : \boldsymbol{\nabla}_X^2.$$

We define the adjoint $\mathscr{A}^*$ of an operator $\mathscr{A}$ as the operator such that, for any ϕ and ψ, smooth and compactly supported test functions,

$$\int_{\mathscr{E}} (\mathscr{A}\phi)\, \psi = \int_{\mathscr{E}} \phi\, (\mathscr{A}^*\psi)\,.$$

The adjoint $\mathscr{L}^*$ of the generator governs the evolution of the law of the process X_t characterized by its density $\psi(t)$ at times $t > 0$, solution of (2.21) through the well-known Fokker-Plank equation as

$$\partial_t \psi = \mathscr{L}^* \psi.$$

Thus ψ is a stationary solution of the Fokker-Plank equation if and only if

$$\mathscr{L}^* \psi = 0, \tag{2.22}$$

which we use in the following to prove the invariance of measures given by Equation (2.17) for SDPD.

2.4.2 Invariant measure

We check that measures μ of the form (2.17) are left invariant by the SDPD dynamics (2.18). To that end, we study the elementary sub-dynamics by writing the associated infinitesimal generators $\mathscr{L}_{\text{cons}}$ and $\mathscr{L}_{\text{fd},ij}$ along with their adjoints. In order to prove the invariance of (2.17), we introduce f_μ the density of the measure μ (see Equation (2.23) below) and compute $\mathscr{L}^*_{\text{cons}} f_\mu$ and $\mathscr{L}^*_{\text{fd},ij} f_\mu$. Since these operators are differential operators, we first need to evaluate the derivatives of the density function f_μ.

Evaluation of the derivatives of the density function

We first do some preliminary calculations and estimate derivatives of the density function f_μ that will be required in the next sections to prove the invariance of the measure μ. We introduce a

smooth function $g(E, \mathscr{P})$ (with $E \in \mathbb{R}$ and $\mathscr{P} \in \mathbb{R}^3$) and the function

$$h(\rho, \varepsilon) = \prod_{i=1}^{N} \frac{1}{\mathscr{T}(\varepsilon_i, \rho_i)} \exp\left(\frac{\mathscr{S}(\varepsilon_i, \rho_i)}{k_\mathrm{B}}\right) = \prod_{i=1}^{N} \partial_\varepsilon \mathscr{S}(\varepsilon_i, \rho_i) \exp\left(\frac{\mathscr{S}(\varepsilon_i, \rho_i)}{k_\mathrm{B}}\right),$$

where we made use of the relations (2.9). We introduce the following notation:

$$\mathfrak{h}(\boldsymbol{q}, \boldsymbol{p}, \varepsilon) = h(\rho_1(\boldsymbol{q}), \dots, \rho_N(\boldsymbol{q}), \varepsilon),$$
$$\mathfrak{g}(\boldsymbol{q}, \boldsymbol{p}, \varepsilon) = g\left(E(\boldsymbol{q}, \boldsymbol{p}, \varepsilon), \sum_{i=1}^{N} \boldsymbol{p}_i\right),$$

so that we can write the measure μ in (2.17) as

$$\mu(\mathrm{d}\boldsymbol{q}\, \mathrm{d}\boldsymbol{p}\, \mathrm{d}\varepsilon) = f_\mu(\boldsymbol{q}, \boldsymbol{p}, \varepsilon)\, \mathrm{d}\boldsymbol{q}\, \mathrm{d}\boldsymbol{p}\, \mathrm{d}\varepsilon,$$

with

$$f_\mu(\boldsymbol{q}, \boldsymbol{p}, \varepsilon) = \mathfrak{g}(\boldsymbol{q}, \boldsymbol{p}, \varepsilon)\mathfrak{h}(\boldsymbol{q}, \boldsymbol{p}, \varepsilon). \tag{2.23}$$

In order to compute the derivatives of f_μ with respect to the variables $\boldsymbol{q}_i, \boldsymbol{p}_i$ and ε_i, we first evaluate the derivatives of $\mathfrak{g}$ and $\mathfrak{h}$ with respect to these variables. Since the total energy $E(\boldsymbol{q}, \boldsymbol{p}, \varepsilon) = \sum_{i=1}^{N} \frac{\boldsymbol{p}_i^2}{2m_i} + \varepsilon_i$ does not depend on $\boldsymbol{q}$, the derivatives of $\mathfrak{g}$ read

$$\begin{aligned}
\boldsymbol{\nabla}_{\boldsymbol{q}_i} \mathfrak{g}\left(E(\boldsymbol{q}, \boldsymbol{p}, \varepsilon), \sum_{i=1}^{N} \boldsymbol{p}_i\right) &= 0, \\
\boldsymbol{\nabla}_{\boldsymbol{p}_i} \mathfrak{g}\left(E(\boldsymbol{q}, \boldsymbol{p}, \varepsilon), \sum_{i=1}^{N} \boldsymbol{p}_i\right) &= \frac{1}{m_i} \boldsymbol{p}_i \partial_E g + \boldsymbol{\nabla}_{\mathscr{P}} g, \\
\partial_{\varepsilon_i} \mathfrak{g}\left(E(\boldsymbol{q}, \boldsymbol{p}, \varepsilon), \sum_{i=1}^{N} \boldsymbol{p}_i\right) &= \partial_E g.
\end{aligned} \tag{2.24}$$

We note that $\mathfrak{h}$ does not depend on the momenta $\boldsymbol{p}_i$ and actually only depends on the positions $\boldsymbol{q}_i$ through the densities ρ_i. We therefore first compute the derivatives of h with respect to the density ρ_i:

$$\begin{aligned}
\partial_{\rho_i} h(\rho, \varepsilon) &= \left[\partial_{\varepsilon_i} \mathscr{S}(\varepsilon_i, \rho_i) \partial_{\rho_i} \left(\exp\left(\frac{\mathscr{S}(\varepsilon_i, \rho_i)}{k_\mathrm{B}}\right)\right) + \partial_{\rho_i} \partial_{\varepsilon_i} \mathscr{S}(\varepsilon_i, \rho_i) \exp\left(\frac{\mathscr{S}(\varepsilon_i, \rho_i)}{k_\mathrm{B}}\right)\right] \\
&\quad \times \prod_{j \neq i} \partial_\varepsilon \mathscr{S}(\varepsilon_i, \rho_i) \exp\left(\frac{\mathscr{S}(\varepsilon_i, \rho_i)}{k_\mathrm{B}}\right) \\
&= \left(\frac{\partial_{\rho_i} \mathscr{S}(\varepsilon_i, \rho_i)}{k_\mathrm{B}} + \frac{\partial_{\rho_i} \partial_{\varepsilon_i} \mathscr{S}(\varepsilon_i, \rho_i)}{\partial_{\varepsilon_i} \mathscr{S}(\varepsilon_i, \rho_i)}\right) h(\rho, \varepsilon),
\end{aligned} \tag{2.25}$$

along with the derivative of h with respect to the internal energy ε_i:

$$\begin{aligned}\partial_{\varepsilon_i} h(\rho,\varepsilon) &= \left[\partial_{\varepsilon_i}\mathcal{S}(\varepsilon_i,\rho_i)\partial_{\varepsilon_i}\left(\exp\left(\frac{\mathcal{S}(\varepsilon_i,\rho_i)}{k_\mathrm{B}}\right)\right) + \partial^2_{\varepsilon_i} S(\rho_i,\varepsilon_i)\exp\left(\frac{\mathcal{S}(\varepsilon_i,\rho_i)}{k_\mathrm{B}}\right)\right] \\ &\quad\times\prod_{j\neq i}\partial_\varepsilon\mathcal{S}(\varepsilon_i,\rho_i)\exp\left(\frac{\mathcal{S}(\varepsilon_i,\rho_i)}{k_\mathrm{B}}\right) \\ &= \left(\frac{\partial_{\varepsilon_i}\mathcal{S}(\varepsilon_i,\rho_i)}{k_\mathrm{B}} + \frac{\partial^2_{\varepsilon_i}\mathcal{S}(\varepsilon_i,\rho_i)}{\partial_{\varepsilon_i}\mathcal{S}(\varepsilon_i,\rho_i)}\right)h(\rho,\varepsilon).\end{aligned} \tag{2.26}$$

Equation (1.21) allows us to express the derivatives of $\mathfrak{h}$ with respect to the positions in terms of the derivatives of h with respect to the densities ρ_i as

$$\begin{aligned}\boldsymbol{\nabla}_{\boldsymbol{q}_i}\mathfrak{h}(\boldsymbol{q},\boldsymbol{p},\varepsilon) &= \left(\boldsymbol{\nabla}_{\boldsymbol{q}_i}\rho_i\right)\partial_{\rho_i}h + \sum_{j\neq i}\left(\boldsymbol{\nabla}_{\boldsymbol{q}_i}\rho_j\right)\partial_{\rho_j}h \\ &= -\sum_{j\neq i}(m_j\partial_{\rho_i}h + m_i\partial_{\rho_j}h)F_{ij}\boldsymbol{r}_{ij}.\end{aligned} \tag{2.27}$$

Using Equations (2.24), (2.25), (2.26) and (2.27), we are finally able to write the derivatives of f_μ with respect to the positions $\boldsymbol{q}_i$ as

$$\boldsymbol{\nabla}_{\boldsymbol{q}_i} f_\mu = \mathfrak{g}\left(\boldsymbol{q},\boldsymbol{p},\varepsilon\right)\boldsymbol{\nabla}_{\boldsymbol{q}_i}\mathfrak{h}(\boldsymbol{q},\boldsymbol{p},\varepsilon) = -\mathfrak{g}\left(\boldsymbol{q},\boldsymbol{p},\varepsilon\right)\sum_{j\neq i} m_j F_{ij}\boldsymbol{r}_{ij}(\partial_{\rho_j}h + \partial_{\rho_i}h);$$

the derivatives of f_μ with respect to the momenta $\boldsymbol{p}_i$ as

$$\boldsymbol{\nabla}_{\boldsymbol{p}_i} f_\mu = \mathfrak{h}(\boldsymbol{q},\boldsymbol{p},\varepsilon)\left[\boldsymbol{\nabla}_{\mathscr{p}} g + \frac{\boldsymbol{p}_i}{m_i}\partial_E g\right],$$

and the derivatives with respect to the energies ε_i as

$$\partial_{\varepsilon_i} f_\mu = \mathfrak{g}\left(\boldsymbol{q},\boldsymbol{p},\varepsilon\right)\partial_{\varepsilon_i}h + \mathfrak{h}(\boldsymbol{q},\boldsymbol{p},\varepsilon)\partial_E g.$$

Invariance by the conservative part of the dynamics

Now that we have determined some relations for the derivatives of the density function f_μ, we turn our attention to the conservative part of SDPD defined by Equation (2.12). The generator $\mathscr{L}_\mathrm{cons}$ associated with the dynamics (2.12) reads

$$\mathscr{L}_\mathrm{cons} = \sum_{i=1}^{N}\frac{\boldsymbol{p_i}}{m_i}\cdot\boldsymbol{\nabla}_{\boldsymbol{q}_i} - \sum_{i=1}^{N}\sum_{j\neq i} m_i m_j\frac{P_i}{\rho_i^2}F_{ij}\boldsymbol{r}_{ij}\cdot\boldsymbol{v}_{ij}\partial_{\varepsilon_i} + \sum_{1\leq i<j\leq N} m_i m_j\left[\frac{P_i}{\rho_i^2}+\frac{P_j}{\rho_j^2}\right]F_{ij}\boldsymbol{r}_{ij}\cdot(\boldsymbol{\nabla}_{\boldsymbol{p}_i}-\boldsymbol{\nabla}_{\boldsymbol{p}_j}).$$

In order to simplify the notation, we introduce

$$\mathfrak{F}_i = \sum_{j\neq i} m_j F_{ij}\boldsymbol{r}_{ij}\cdot\boldsymbol{v}_{ij}.$$

The adjoint of the generator $\mathscr{L}_{\text{cons}}$ is readily given by

$$\mathscr{L}^*_{\text{cons}}\phi = \sum_{i=1}^{N}\left(-\frac{\boldsymbol{p_i}}{m_i}\cdot\boldsymbol{\nabla}_{\boldsymbol{q}_i}\phi + \frac{\partial_{\varepsilon_i}[P_i\phi]}{\rho_i^2}m_i\mathfrak{F}_i - \sum_{j=i+1}^{N} m_i m_j\left[\frac{P_i}{\rho_i^2}+\frac{P_j}{\rho_j^2}\right]F_{ij}\boldsymbol{r}_{ij}\cdot(\boldsymbol{\nabla}_{\boldsymbol{p}_i}-\boldsymbol{\nabla}_{\boldsymbol{p}_j})\phi\right).$$

For $\phi = f_\mu$, we have $\partial_{\varepsilon_i}(P_i f_\mu) = \partial_{\varepsilon_i}(P_i\mathfrak{h})\mathfrak{g} + (P_i\mathfrak{h})(\partial_{\varepsilon_i}\mathfrak{g})$. As all the other terms in $\mathscr{L}^*_{\text{cons}}$ are first order linear differential operators, it holds

$$\mathscr{L}^*_{\text{cons}} f_\mu = (\mathscr{L}^*_{\text{cons}}\mathfrak{h})\mathfrak{g} + \mathfrak{h}(\mathscr{L}^*_{\text{cons}} + \mathfrak{L})\mathfrak{g},$$

where

$$\mathfrak{L}\phi = -\sum_{i=1}^{N}\frac{m_i}{\rho_i^2}\mathfrak{F}_i\partial_{\varepsilon_i}(P_i)\phi.$$

We first check that $\mathscr{L}^*_{\text{cons}}\mathfrak{h} = 0$. Since $\mathfrak{h}$ does not depend on $\boldsymbol{p}_i$ and thanks to the relations (2.27), (2.25) and (2.26), we may rewrite the generator as a sum of differential operators $\mathscr{A}^i_{\text{cons}}$ depending only on a single particle:

$$\begin{aligned}\mathscr{L}^*_{\text{cons}}\mathfrak{h} &= -\sum_{i=1}^{N}\frac{\boldsymbol{p_i}}{m_i}\cdot\boldsymbol{\nabla}_{\boldsymbol{q}_i}\mathfrak{h} + \sum_{i=1}^{N}\frac{1}{\rho_i^2}\partial_{\varepsilon_i}(P_i\mathfrak{h})m_i\mathfrak{F}_i\\ &= \sum_{i=1}^{N}\left(\partial_{\rho_i}h + m_i\frac{P_i}{\rho_i^2}\partial_{\varepsilon_i}h + m_i h\frac{\partial_{\varepsilon_i}P_i}{\rho_i^2}\right)\mathfrak{F}_i\\ &= \sum_{i=1}^{N}\mathfrak{F}_i\mathscr{A}^i_{\text{cons}}h.\end{aligned}$$

The expression of $\mathscr{A}^i_{\text{cons}}h$ only involves derivatives of h with respect to the density and energy of particle i:

$$\mathscr{A}^i_{\text{cons}}h = \partial_{\rho_i}h + m_i\frac{P_i}{\rho_i^2}\partial_{\varepsilon_i}h + m_i h\frac{\partial_{\varepsilon_i}P_i}{\rho_i^2}$$

Using again Equations (2.25) and (2.26), we can expand this expression as

$$\begin{aligned}\mathscr{A}^i_{\text{cons}}h &= \left[\frac{1}{k_{\text{B}}}(\partial_{\rho_i}S_i)(\partial_{\varepsilon_i}S_i) + \partial_{\rho_i}\partial_{\varepsilon_i}S_i + \frac{m_i}{k_{\text{B}}}\frac{P_i}{\rho_i^2}(\partial_{\varepsilon_i}S_i)^2 + m_i\frac{P_i}{\rho_i^2}\partial^2_{\varepsilon_i}S_i + \frac{m_i}{\rho_i^2}(\partial_{\varepsilon_i}P_i)(\partial_{\varepsilon_i}S_i)\right]\frac{h}{\partial_{\varepsilon_i}S_i}\\ &= \left[\left(\partial_{\rho_i}S_i + m_i\frac{P_i}{\rho_i^2}\partial_{\varepsilon_i}S_i\right)\frac{\partial_{\varepsilon_i}S_i}{k_{\text{B}}} + \partial_{\rho_i}\partial_{\varepsilon_i}S_i + m_i\frac{P_i}{\rho_i^2}\partial^2_{\varepsilon_i}S_i + \frac{m_i}{\rho_i^2}(\partial_{\varepsilon_i}P_i)(\partial_{\varepsilon_i}S_i)\right]\frac{h}{\partial_{\varepsilon_i}S_i}.\end{aligned} \tag{2.28}$$

We can now make use of the relations (2.9) to get

$$\partial_{\rho_i}S_i + m_i\frac{P_i}{\rho_i^2}\partial_{\varepsilon_i}S_i = 0,$$

and

$$\begin{aligned} m_i \frac{\partial_{\varepsilon_i} P_i}{\rho_i^2} &= -\partial_{\varepsilon_i}\left(\frac{\partial_{\rho_i} S_i}{\partial_{\varepsilon_i} S_i}\right) \\ &= \partial_{\rho_i} S_i \frac{\partial^2_{\varepsilon_i} S_i}{(\partial_{\varepsilon_i} S_i)^2} - \frac{\partial_{\varepsilon_i}\partial_{\rho_i} S_i}{\partial_{\varepsilon_i} S_i}, \\ &= -m_i \frac{P_i}{\rho_i^2}\frac{\partial^2_{\varepsilon_i} S_i}{\partial_{\varepsilon_i} S_i} - \frac{\partial_{\varepsilon_i}\partial_{\rho_i} S_i}{\partial_{\varepsilon_i} S_i}. \end{aligned}$$

A simple substitution in Equation 2.28 shows that $\mathscr{A}^i_{\text{cons}} h = 0$.

Now, for a general function $g(E, \boldsymbol{P})$, we compute the remaining term

$$\begin{aligned} (\mathscr{L}^*_{\text{cons}} + \mathfrak{L})\mathfrak{g} = &\sum_{1\le i<j\le N} m_i m_j \left(\frac{P_i}{\rho_i^2} + \frac{P_j}{\rho_j^2}\right) F_{ij}\boldsymbol{r}_{ij}\left(\boldsymbol{\nabla}_{\boldsymbol{p}} g + \frac{\boldsymbol{p}_j}{m_i}\partial_E g\right) + \sum_{i=1}^{N} m_i m_j \frac{P_i}{\rho_i^2}\partial_E g \sum_{j\neq i} F_{ij}\boldsymbol{r}_{ij}\cdot\boldsymbol{v}_{ij} \\ &- \sum_{1\le i<j\le N} m_i m_j \left(\frac{P_i}{\rho_i^2} + \frac{P_j}{\rho_j^2}\right) F_{ij}\boldsymbol{r}_{ij}\left(\boldsymbol{\nabla}_{\boldsymbol{p}} g + \frac{\boldsymbol{p}_i}{m_i}\partial_E g\right), \end{aligned}$$

which clearly vanishes upon a simple reorganization of the sums.

Hence, the elementary conservative dynamics (2.12) verifies relation (2.22) and keeps the measure (2.17) invariant.

Invariance by the fluctuation/dissipation part of the dynamics

We now check that Equation (2.22) holds for the fluctuation/dissipation part defined by Equation (2.13). We follow here the same proof as for DPDE [7, 43]. In order to better identify the terms in Equation (2.21) we rewrite the elementary dynamics (2.13) using the variable $X_t = (\boldsymbol{v}_i^T, \boldsymbol{v}_j^T, \varepsilon_i, \varepsilon_j)^T$:

$$dX_t = b(X_t)\,\mathrm{d}t + \mathscr{S}(X_t)\,\mathrm{d}\boldsymbol{W}_t$$

with the drift

$$b(X) = \begin{pmatrix} -\boldsymbol{\Gamma}_{ij}\boldsymbol{v}_{ij} \\ \boldsymbol{\Gamma}_{ij}\boldsymbol{v}_{ij} \\ \frac{1}{2}\left(\boldsymbol{v}_{ij}^T\boldsymbol{\Gamma}_{ij}\boldsymbol{v}_{ij} - \frac{1}{m_{ij}}\mathrm{Tr}(\Sigma_{ij}\Sigma_{ij}^T)\right) \\ \frac{1}{2}\left(\boldsymbol{v}_{ij}^T\boldsymbol{\Gamma}_{ij}\boldsymbol{v}_{ij} - \frac{1}{m_{ij}}\mathrm{Tr}(\Sigma_{ij}\Sigma_{ij}^T)\right) \end{pmatrix},$$

and the diffusion matrix

$$\mathscr{S}(X) = \begin{pmatrix} \Sigma_{ij} \\ -\Sigma_{ij} \\ -\frac{1}{2}\boldsymbol{v}_{ij}^T\Sigma_{ij} \\ -\frac{1}{2}\boldsymbol{v}_{ij}^T\Sigma_{ij} \end{pmatrix}.$$

The generator for the dynamics (2.13) is then given by

$$\mathscr{L}_{\mathrm{fd},ij} = b \cdot \nabla_X + \frac{1}{2}\mathscr{S}\mathscr{S}^T : \nabla_X^2.$$

The matrix $\mathscr{S}\mathscr{S}^T$ reads

$$\mathscr{S}\mathscr{S}^T = \begin{pmatrix} \Sigma\Sigma^T & -\Sigma\Sigma^T & -\frac{1}{2}\Sigma\Sigma^T\boldsymbol{v} & \frac{1}{2}\Sigma\Sigma^T\boldsymbol{v} \\ -\Sigma\Sigma^T & \Sigma\Sigma^T & \frac{1}{2}\Sigma\Sigma^T\boldsymbol{v} & -\frac{1}{2}\Sigma\Sigma^T\boldsymbol{v} \\ -\frac{1}{2}\boldsymbol{v}^T\Sigma\Sigma^T & \frac{1}{2}\boldsymbol{v}^T\Sigma\Sigma^T & \frac{1}{4}\boldsymbol{v}^T\Sigma\Sigma^T\boldsymbol{v} & \frac{1}{4}\boldsymbol{v}^T\Sigma\Sigma^T\boldsymbol{v} \\ \frac{1}{2}\boldsymbol{v}^T\Sigma\Sigma^T & -\frac{1}{2}\boldsymbol{v}^T\Sigma\Sigma^T & \frac{1}{4}\boldsymbol{v}^T\Sigma\Sigma^T\boldsymbol{v} & \frac{1}{4}\boldsymbol{v}^T\Sigma\Sigma^T\boldsymbol{v} \end{pmatrix}$$

where we omitted the indices (i, j). More explicitly, assuming Γ_{ij} to be symmetric,

$$\begin{aligned}\mathscr{L}_{\mathrm{fd},ij} =& -\boldsymbol{v}_{ij}\Gamma_{ij}(\boldsymbol{\nabla}_{\boldsymbol{p}_i} - \boldsymbol{\nabla}_{\boldsymbol{p}_j}) + \frac{1}{2}\left[\boldsymbol{v}_{ij}^T\Gamma_{ij}\boldsymbol{v}_{ij} - \frac{1}{m_{ij}}\mathrm{Tr}\left(\Sigma_{ij}\Sigma_{ij}^T\right)\right](\partial_{\varepsilon_i} + \partial_{\varepsilon_j}) \\ &+ \frac{1}{2}(\boldsymbol{\nabla}_{\boldsymbol{p}_i} - \boldsymbol{\nabla}_{\boldsymbol{p}_j})^T\Sigma_{ij}\Sigma_{ij}^T(\boldsymbol{\nabla}_{\boldsymbol{p}_i} - \boldsymbol{\nabla}_{\boldsymbol{p}_j}) - \frac{1}{2}\boldsymbol{v}_{ij}^T\Sigma_{ij}\Sigma_{ij}^T(\boldsymbol{\nabla}_{\boldsymbol{p}_i} - \boldsymbol{\nabla}_{\boldsymbol{p}_j})(\partial_{\varepsilon_i} + \partial_{\varepsilon_j}) \\ &+ \frac{1}{8}\boldsymbol{v}_{ij}^T\Sigma_{ij}\Sigma_{ij}^T\boldsymbol{v}_{ij}(\partial_{\varepsilon_i} + \partial_{\varepsilon_j})^2.\end{aligned}$$

Introducing

$$\boldsymbol{A}_{ij} = \boldsymbol{\nabla}_{\boldsymbol{p}_i} - \boldsymbol{\nabla}_{\boldsymbol{p}_j} - \frac{1}{2}\boldsymbol{v}_{ij}(\partial_{\varepsilon_i} + \partial_{\varepsilon_j}),$$

the generator can be rewritten as

$$\mathscr{L}_{\mathrm{fd},ij} = -\boldsymbol{v}_{ij}^T\Gamma_{ij}\boldsymbol{A}_{ij} + \frac{1}{2}\Sigma_{ij}\Sigma_{ij}^T : \boldsymbol{A}_{ij}\boldsymbol{A}_{ij}^T.$$

We now consider matrices of the form (2.14), which are indeed symmetric, and use the following relations

$$\Gamma_{ij} = \gamma_{ij}^{\parallel}\boldsymbol{P}_{ij}^{\parallel} + \gamma_{ij}^{\perp}\boldsymbol{P}_{ij}^{\perp}, \quad \Sigma_{ij}\Sigma_{ij}^T = (\sigma_{ij}^{\parallel})^2\boldsymbol{P}_{ij}^{\parallel} + (\sigma_{ij}^{\perp})^2\boldsymbol{P}_{ij}^{\perp},$$

to write the generator $\mathscr{L}_{\mathrm{fd},ij}$ as a sum of two operators $\mathscr{L}_{\perp,ij}$ and $\mathscr{L}_{\parallel,ij}$. More precisely $\mathscr{L}_{\mathrm{fd},ij} = \mathscr{L}_{\perp,ij} + \mathscr{L}_{\parallel,ij}$ where

$$\mathscr{L}_{\theta,ij} = -\gamma_{ij}^{\theta}\boldsymbol{v}_{ij}^T\boldsymbol{P}_{ij}^{\theta}\boldsymbol{A}_{ij} + \frac{1}{2}\left(\sigma_{ij}^{\theta}\right)^2\boldsymbol{A}_{ij}^T\boldsymbol{P}_{ij}^{\theta}\boldsymbol{A}_{ij},$$

for $\theta \in \{\perp, \parallel\}$. Since $\boldsymbol{A}_{ij}^* = -\boldsymbol{A}_{ij}$, the adjoint of the generator applied to f_μ reads

$$\mathscr{L}_{\theta,ij}^* f_\mu = \boldsymbol{A}_{ij}^T\boldsymbol{P}_{ij}^{\theta}\left(\gamma_{ij}^{\theta}\boldsymbol{v}_{ij}f_\mu + \frac{1}{2}\boldsymbol{A}_{ij}\left[\left(\sigma_{ij}^{\theta}\right)^2 f_\mu\right]\right).$$

A sufficient condition for the measure μ to be left invariant by (2.13) is then

$$\gamma_{ij}^{\theta}\boldsymbol{v}_{ij}f_\mu + \frac{1}{2}\boldsymbol{A}_{ij}[(\sigma_{ij}^{\theta})^2 f_\mu] = 0$$

for $\theta \in \{\perp, \parallel\}$. Since $\boldsymbol{A}_{ij}$ is a first order linear differential operator, we can write

$$\boldsymbol{A}_{ij}\left[\left(\sigma_{ij}^{\theta}\right)^2 f_\mu\right] = \boldsymbol{A}_{ij}\left[\left(\sigma_{ij}^{\theta}\right)^2 \mathfrak{g}\mathfrak{h}\right] = \left(\boldsymbol{A}_{ij}\left[\left(\sigma_{ij}^{\theta}\right)^2 \mathfrak{h}\right]\right)\mathfrak{g} + \left(\sigma_{ij}^{\theta}\right)^2 \mathfrak{h}\left(\boldsymbol{A}_{ij}\mathfrak{g}\right). \tag{2.29}$$

For any function $\mathfrak{g}$, it holds

$$\boldsymbol{A}_{ij}\mathfrak{g} = \left(\frac{\boldsymbol{p}_i}{m_i} - \frac{\boldsymbol{p}_j}{m_j}\right)\partial_E g - \boldsymbol{v}_{ij}\partial_E g = 0,$$

and the second term in Equation (2.29) vanishes. We assume that the fluctuation amplitude σ_{ij}^{θ} depends only on the positions $\boldsymbol{q}$ (through the cut-off function) and the internal energies ε_i and ε_j. We next compute the first term in Equation (2.29):

$$\begin{aligned}
\boldsymbol{A}_{ij}\left[(\sigma_{ij}^{\theta})^2\mathfrak{h}\right] &= \boldsymbol{A}_{ij}\left((\sigma_{ij}^{\theta})^2 \prod_{k=1}^{N} \frac{\exp\left(\frac{S_k(\varepsilon_k,\boldsymbol{q})}{k_{\mathrm{B}}}\right)}{T_k(\varepsilon_k,\boldsymbol{q})}\right) \\
&= -\frac{1}{2}\mathfrak{h}\boldsymbol{v}_{ij}\left(T_iT_j(\partial_{\varepsilon_i}+\partial_{\varepsilon_j})\left[\frac{(\sigma_{ij}^{\theta})^2}{T_iT_j}\right] + (\sigma_{ij}^{\theta})^2\left[\frac{\partial_{\varepsilon_i}S_i}{k_{\mathrm{B}}} + \frac{\partial_{\varepsilon_j}S_j}{k_{\mathrm{B}}}\right]\right) \\
&= -\frac{1}{2}\mathfrak{h}\boldsymbol{v}_{ij}\left(T_iT_j(\partial_{\varepsilon_i}+\partial_{\varepsilon_j})\left[\frac{(\sigma_{ij}^{\theta})^2}{T_iT_j}\right] + \frac{(\sigma_{ij}^{\theta})^2}{k_{\mathrm{B}}}\frac{T_i+T_j}{T_iT_j}\right).
\end{aligned}$$

This leads us to the following sufficient condition on γ_{ij}^{θ} and σ_{ij}^{θ}:

$$\gamma_{ij}^{\theta} = \frac{1}{4}\left(T_iT_j(\partial_{\varepsilon_i}+\partial_{\varepsilon_j})\left[\frac{(\sigma_{ij}^{\theta})^2}{T_iT_j}\right] + \frac{(\sigma_{ij}^{\theta})^2}{k_{\mathrm{B}}}\frac{T_i+T_j}{T_iT_j}\right). \tag{2.30}$$

There are many possible solutions to this equation. Actually any choice for σ_{ij}^{θ} (for example σ_{ij}^{θ} constant as in DPDE) yields a corresponding expression for γ_{ij}^{θ}.

The expression of the fluctuation amplitude in the original SDPD (2.3) suggests taking

$$\sigma^{\theta} = \sqrt{\kappa_{ij}^{\theta}k_{\mathrm{B}}\frac{T_iT_j}{T_i+T_j}},$$

with κ_{ij}^{θ} a positive constant. We can then further evaluate the friction coefficient as

$$\begin{aligned}
\gamma_{ij}^{\theta} &= \frac{1}{4}\left(T_iT_j(\partial_{\varepsilon_i}+\partial_{\varepsilon_j})\left[\frac{\kappa_{ij}^{\theta}k_{\mathrm{B}}}{T_i+T_j}\right] + \kappa_{ij}^{\theta}\right) \\
&= \frac{1}{4}\kappa_{ij}^{\theta}\left(1 - k_{\mathrm{B}}\left(\frac{1}{C_i}+\frac{1}{C_j}\right)\frac{T_iT_j}{(T_i+T_j)^2}\right),
\end{aligned}$$

by using the expressions of the heat capacities (see Equation (2.9)). More precisely,

$$\partial_{\varepsilon_i}\left(\frac{1}{T_i+T_j}\right) = -\frac{\partial_{\varepsilon_i}T_i}{(T_i+T_j)^2} = -\frac{1}{C_i}\frac{1}{(T_i+T_j)^2}.$$

In order to retrieve the friction term of the original SDPD dynamics (2.6), we choose

$$\kappa_{ij}^{\perp} = 4a_{ij}, \quad \text{and} \quad \kappa_{ij}^{\parallel} = \frac{4}{3}a_{ij} + b_{ij}.$$

This choice for the friction and fluctuation coefficients ensures that each pairwise elementary dynamics leaves the measure (2.17) invariant.

By gathering the results for both the conservative and the fluctuation/dissipation parts of the dynamics, this concludes the proof of the invariance of measures of the form (2.17) for SDPD.

2.4.3 Estimators

We present in this section expressions for the estimators of thermodynamic quantities like temperature and pressure. Following the same ideas as for DPDE [79], we rely on a thermodynamic equivalence with an appropriate canonical measure to make the computations tractable.

Although the dynamics (2.18) leaves any measure of the form (2.17) invariant, there is no mathematical result about its ergodicity since the fluctuation may be degenerate. Even for DPD, ergodicity is known to hold only for simple one-dimensional systems [157]. Since the total energy and the total momentum are conserved, we assume the ergodicity of the dynamics (2.18) with respect to the measure

$$\mu_{E_0,\boldsymbol{\mathscr{P}}_0}(\mathrm{d}\boldsymbol{q}\mathrm{d}\boldsymbol{p}\mathrm{d}\varepsilon) = Z_{E_0,\boldsymbol{\mathscr{P}}_0}^{-1}\,\delta\left(E(\boldsymbol{q},\boldsymbol{p},\varepsilon) - E_0\right)\delta\left(\sum_{i=1}^{N}\boldsymbol{p}_i - \boldsymbol{\mathscr{P}}_0\right)\prod_{i=1}^{N}\frac{\exp\left(\frac{S_i(\varepsilon_i,\boldsymbol{q})}{k_\mathrm{B}}\right)}{T_i(\varepsilon_i,\boldsymbol{q})}\,\mathrm{d}\boldsymbol{q}\,\mathrm{d}\boldsymbol{p}\,\mathrm{d}\varepsilon,$$

with E_0 the initial total energy, $\boldsymbol{\mathscr{P}}_0$ the initial momentum and $Z_{E_0,\boldsymbol{\mathscr{P}}_0}^{-1}$ a normalization constant. As stated in Section 1.1.2, under this ergodic assumption, the average of some observable A can be estimated as an average along a trajectory:

$$\langle A\rangle_{E_0,\boldsymbol{\mathscr{P}}_0} = \int_{\mathscr{E}} A\,\mathrm{d}\mu_{E_0,\boldsymbol{\mathscr{P}}_0} = \lim_{t\to+\infty}\frac{1}{t}\int_0^t A(q_s,p_s,\varepsilon_s)\mathrm{d}s,$$

where (q_s,p_s,ε_s) is the solution at time s of the dynamics (2.18). We assume in the following that $\boldsymbol{\mathscr{P}}_0 = 0$, which can be achieved by adopting the center of mass reference frame.

To justify the expressions of thermodynamic estimators of temperature, it is convenient to introduce the canonical measure

$$\mu_\beta(\mathrm{d}\boldsymbol{q}\,\mathrm{d}\boldsymbol{p}\,\mathrm{d}\varepsilon) = Z_\beta^{-1}\prod_{i=1}^{N}\frac{\exp\left(-\beta\left[\frac{\boldsymbol{p}_i^2}{2m_i}+\varepsilon_i\right]+\frac{S_i(\varepsilon_i,\boldsymbol{q})}{k_\mathrm{B}}\right)}{T_i(\varepsilon_i,\boldsymbol{q})}\,\mathrm{d}\boldsymbol{q}\,\mathrm{d}\boldsymbol{p}\,\mathrm{d}\varepsilon, \tag{2.31}$$

where β is chosen such that $\langle E\rangle_{\mu_\beta} = E_0$ and Z_β^{-1} a normalization constant. In the thermodynamic limit, μ_β and $\mu_{E_0,0}$ are expected to be equivalent in the same way that the microcanonical and canonical measures are equivalent for systems described only in terms of $\boldsymbol{q}$ and $\boldsymbol{p}$.

Estimators for temperature

Under the canonical measure (2.31), the thermodynamic temperature $T_\beta = \dfrac{1}{k_\mathrm{B}\beta}$ can be estimated from the kinetic energy as

$$T_\beta = \left\langle \frac{\boldsymbol{p}_i^2}{3m_i k_\mathrm{B}} \right\rangle_{\mu_\beta},$$

which motivates the use of the kinetic temperature

$$T_{\mathrm{kin}}(\boldsymbol{q},\boldsymbol{p},\varepsilon) = \frac{1}{N}\sum_{i=1}^{N} \frac{\boldsymbol{p}_i^2}{3m_i k_\mathrm{B}} \tag{2.32}$$

as an estimator of T_β. Under some assumptions on the equation of state (2.8), which hold for instance for the ideal gas equation of state (see Equation (1.11) in Section 1.2.2), namely

$$\begin{aligned} \forall \rho \in \mathbb{R}_+, \quad & \mathcal{S}(\rho,\varepsilon) \xrightarrow[\varepsilon\to 0]{} -\infty, \\ & \mathcal{S}(\rho,\varepsilon) - k_\mathrm{B}\beta\varepsilon \xrightarrow[\varepsilon\to+\infty]{} -\infty, \end{aligned} \tag{2.33}$$

the internal temperature also provides an estimator of the thermodynamic temperature since

$$T_\beta = \langle T_i \rangle_{\mu_\beta}.$$

The temperature T_β can therefore be estimated from the average of the internal temperatures in the system as

$$T_{\mathrm{int}}(\boldsymbol{q},\boldsymbol{p},\varepsilon) = \frac{1}{N}\sum_{i=1}^{N} T_i. \tag{2.34}$$

Let us stress that the internal temperature estimator for SDPD relies on an arithmetic average in contrast to DPDE where an harmonic mean should be used [160].

We now prove that the average internal temperature indeed provides an estimator for the thermodynamic temperature. The ensemble average of the internal temperature under the canonical measure μ_β defined in Equation (2.31) is given by

$$\begin{aligned} \langle T_i \rangle_{\mu_\beta} &= Z_\beta^{-1} \int_{\mathscr{E}} T_i(\varepsilon_i,\boldsymbol{q}) \exp\left(-\beta \sum_{j=1}^{N} \frac{\boldsymbol{p}_j^2}{m_j}\right) \prod_{j=1}^{N} \frac{\exp\left(\frac{S_j(\varepsilon_j,\boldsymbol{q})}{k_\mathrm{B}} - \beta\varepsilon_j\right)}{T_j(\varepsilon_j,\boldsymbol{q})} \,\mathrm{d}\boldsymbol{q}\,\mathrm{d}\boldsymbol{p}\,\mathrm{d}\varepsilon, \\ &= \mathfrak{Z}_\beta^{-1} \int_{\boldsymbol{q}\in\Omega^N} \left[\int_{\mathbb{R}_+} \exp\left(\frac{S_i(\varepsilon_i,\boldsymbol{q})}{k_\mathrm{B}} - \beta\varepsilon_i\right) \mathrm{d}\varepsilon_i\right] \prod_{j\neq i} \mathscr{R}_j(\boldsymbol{q})\,\mathrm{d}\boldsymbol{q}, \end{aligned} \tag{2.35}$$

where we have integrated out the momenta and introduced

$$\mathscr{R}_j(\boldsymbol{q}) = \int_{\mathbb{R}_+} \frac{\exp\left(\frac{S_j(\varepsilon_j,\boldsymbol{q})}{k_\mathrm{B}} - \beta\varepsilon_j\right)}{T_j(\varepsilon_j,\boldsymbol{q})} \,\mathrm{d}\varepsilon_j,$$

along with the normalization constant $\mathfrak{Z}_\beta = \int_{\Omega^N} \prod_{j=1}^N \mathscr{R}_j(\boldsymbol{q})\,\mathrm{d}\boldsymbol{q}$. A simple computation based on (2.9) and an integration by part gives

$$\begin{aligned}\mathscr{R}_j(\boldsymbol{q}) &= \int_0^{+\infty} \exp\left(\frac{S_j(\varepsilon_j,\boldsymbol{q})}{k_\mathrm{B}} - \beta\varepsilon_j\right)(\partial_{\varepsilon_j} S_j)\,\mathrm{d}\varepsilon_j,\\ &= k_\mathrm{B}\left(\int_0^{+\infty} \partial_{\varepsilon_j}\left[\exp\left(\frac{S_j(\varepsilon_j,\boldsymbol{q})}{k_\mathrm{B}} - \beta\varepsilon_j\right)\right]\mathrm{d}\varepsilon_j + \beta\int_0^{+\infty}\exp\left(\frac{S_j(\varepsilon_j,\boldsymbol{q})}{k_\mathrm{B}} - \beta\varepsilon_j\right)\mathrm{d}\varepsilon_j\right).\end{aligned}$$

Under the assumptions (2.33), the first integral vanishes and hence

$$\mathscr{R}_j(\boldsymbol{q}) = k_\mathrm{B}\beta\int_0^{+\infty}\exp\left(\frac{S_j(\varepsilon_j,\boldsymbol{q})}{k_\mathrm{B}} - \beta\varepsilon_j\right)\mathrm{d}\varepsilon_j. \tag{2.36}$$

Plugging this result in (2.35) leads to the desired results:

$$\langle T_i\rangle_{\mu_\beta} = \frac{1}{k_\mathrm{B}\beta} = T_\beta.$$

Estimator for pressure

The thermodynamic pressure in the system is defined as the derivative of the free energy $\mathscr{F}$ with respect to the total volume $\mathscr{V} = |\Omega|$ of the system. With the previous ergodicity assumption, the pressure can be estimated as a sum of two terms

$$\mathscr{P} = -\partial_{\mathscr{V}}\mathscr{F} = \mathscr{P}_\mathrm{kin} + \mathscr{P}_\mathrm{virial}, \tag{2.37}$$

where $\mathscr{P}_\mathrm{kin}$ is the kinetic pressure

$$\mathscr{P}_\mathrm{kin} = \frac{N}{\mathscr{V}\beta},$$

and $\mathscr{P}_\mathrm{virial}$ is the virial pressure

$$\mathscr{P}_\mathrm{virial} = \frac{1}{3\mathscr{V}}\left\langle \sum_{1\le i<j\le N} \boldsymbol{\mathcal{F}}_{\mathrm{cons},ij}\cdot\boldsymbol{r}_{ij}\right\rangle_{\mu_\beta}.$$

We now prove that the relation (2.37) holds for SDPD. To evaluate the pressure in the SDPD system, we first compute the partition function of the canonical measure μ_β defined by Equation (2.31):

$$\begin{aligned}Z_\beta &= \int_{\mathscr{E}} \frac{\exp\left(\sum_{i=1}^N -\beta\left[\frac{\boldsymbol{p}_i^2}{2m_i} + \varepsilon_i\right] + \frac{S_i(\varepsilon_i,\boldsymbol{q})}{k_\mathrm{B}}\right)}{\prod_{i=1}^N T_i(\varepsilon_i,\boldsymbol{q})}\,\mathrm{d}\boldsymbol{q}\,\mathrm{d}\boldsymbol{p}\,\mathrm{d}\varepsilon\\ &= \int_{\mathbb{R}^{3N}}\exp\left(-\beta\sum_{i=1}^N\frac{\boldsymbol{p}_i^2}{2m_i}\right)\mathrm{d}\boldsymbol{p}\times\int_{\Omega^N}\prod_{i=1}^N\left[\int_{\mathbb{R}_+}\frac{\exp\left(-\beta\varepsilon_i + \frac{S_i(\varepsilon_i,\boldsymbol{q})}{k_\mathrm{B}}\right)}{T_i(\varepsilon_i,\boldsymbol{q})}\,\mathrm{d}\varepsilon_i\right]\mathrm{d}\boldsymbol{q}.\end{aligned}$$

We use again the relation (2.36) previously introduced to obtain an estimator for the temperature and rewrite the partition function as

$$Z_\beta = \mathscr{Z}_\beta \int_{\Omega^N} \prod_{i=1}^{N} \left[\int_{\mathbb{R}_+} \exp\left(-\beta\varepsilon_i + \frac{S_i(\varepsilon_i, \boldsymbol{q})}{k_\mathrm{B}} \right) \mathrm{d}\varepsilon_i \right] \mathrm{d}\boldsymbol{q},$$

where the normalization constant $\mathscr{Z}_\beta = k_\mathrm{B}^N \beta^{5N/2} (2\pi)^{-3N/2} \left(\prod_{i=1}^{N} m_i \right)^{-3/2}$ does not depend on the volume $\mathscr{V}$ of the domain.

The free energy is given by

$$\mathscr{F}(\beta, \mathscr{V}) = -\frac{1}{\beta} \log Z_\beta(\beta, \mathscr{V})$$

and the thermodynamic pressure by

$$\mathscr{P} = -\partial_{\mathscr{V}} \mathscr{F} = \frac{1}{\beta} \frac{\partial_{\mathscr{V}} Z_\beta}{Z_\beta}. \tag{2.38}$$

In order to compute the derivative of Z_β with respect to the volume $\mathscr{V}$ of the system, we introduce a spatial dilation $\tilde{\boldsymbol{q}} = (1+\lambda)\boldsymbol{q}$ for $\lambda > -1$. We then consider the partition function associated with the domain $(1+\lambda)\Omega$:

$$\mathscr{Z}(\lambda) = \mathscr{Z}_\beta \int_{[(1+\lambda)\Omega]^N} \prod_{i=1}^{N} \left[\int_{\mathbb{R}_+} \exp\left(\frac{S_i(\varepsilon_i, \tilde{\boldsymbol{q}})}{k_\mathrm{B}} - \beta\varepsilon_i \right) \mathrm{d}\varepsilon_i \right] \mathrm{d}\tilde{\boldsymbol{q}}$$

which gives, after a change of variables allowing to map back the integration domain to Ω^N:

$$\mathscr{Z}(\lambda) = \mathscr{Z}_\beta (1+\lambda)^{3N} \times \int_{\Omega^N} \prod_{i=1}^{N} \left[\int_{\mathbb{R}_+} \exp\left(-\beta\varepsilon_i + \frac{S_i(\varepsilon_i, (1+\lambda)\boldsymbol{q})}{k_\mathrm{B}} \right) \mathrm{d}\varepsilon_i \right] \mathrm{d}\boldsymbol{q}.$$

Note that $\lambda = 0$ corresponds to no dilation and thus $\mathscr{Z}(0) = Z_\beta$. Since the volume of the dilated domain is given by

$$\mathscr{V}(\lambda) = (1+\lambda)^3 \mathscr{V}(0),$$

it holds $\mathscr{V}'(0) = 3\mathscr{V}(0)$. The derivative of the partition function Z_β with respect to the volume $\mathscr{V}$ can then be written as

$$\partial_{\mathscr{V}} Z_\beta = \frac{\mathscr{Z}'(0)}{\mathscr{V}'(0)} = \frac{\mathscr{Z}'(0)}{3\mathscr{V}(0)}.$$

We can now derive $\log(\mathscr{Z}(\lambda))$ with respect to λ at $\lambda = 0$ as

$$\frac{\mathscr{Z}'(0)}{\mathscr{Z}(0)} = 3N + \frac{\mathscr{Z}_\beta}{Z_\beta} \int_{\Omega^N \times \mathbb{R}_+^N} \partial_\lambda \left(\sum_{i=1}^{N} \frac{S_i(\varepsilon_i, (1+\lambda)\boldsymbol{q})}{k_\mathrm{B}} \right) \Bigg|_{\lambda=0} \exp\left(\sum_{i=1}^{N} -\beta\varepsilon_i + \frac{S_i(\varepsilon_i, \boldsymbol{q})}{k_\mathrm{B}} \right) \mathrm{d}\varepsilon \, \mathrm{d}\boldsymbol{q}. \tag{2.39}$$

In order to evaluate (2.39), we first need to compute the derivatives of the density ρ_i and of the entropy S_i with respect to λ. We have, by deriving Equation (1.20),

$$\partial_\lambda \left[\rho_i \left((1+\lambda)\boldsymbol{q}\right)\right] = \sum_{j\neq i} m_j \partial_\lambda [W((1+\lambda)\boldsymbol{r}_{ij})] = -(1+\lambda)\sum_{j\neq i} m_j F((1+\lambda)\boldsymbol{r}_{ij})\boldsymbol{r}_{ij}^2.$$

With this result and the equation of state (2.8), we can compute $\partial_\lambda S_i(\varepsilon_i, (1+\lambda)\boldsymbol{q})$ as

$$\partial_\lambda [S_i\left(\varepsilon_i, (1+\lambda)\boldsymbol{q}\right)] = \partial_\lambda[\rho_i((1+\lambda)\boldsymbol{q})]\partial_{\rho_i} S_i = (1+\lambda)\sum_{j\neq i}\frac{m_i m_j P_i}{\rho_i^2 T_i} F((1+\lambda)\boldsymbol{r}_{ij})\boldsymbol{r}_{ij}^2.$$

Finally, plugging these expressions evaluated at $\lambda = 0$ in equation (2.39) leads to

$$\begin{aligned}\frac{\mathscr{Z}'(0)}{\mathscr{Z}(0)} &= 3N + \frac{\mathscr{Z}_\beta}{Z_\beta}\int_{\Omega^N\times\mathbb{R}_+^N}\left[\sum_{i=1}^N\sum_{j\neq i} m_i m_j F_{ij}\boldsymbol{r}_{ij}^2\frac{P_i}{\rho_i^2 T_i}\right]\prod_{k=1}^N \exp\left(-\beta\varepsilon_k + \frac{S_k(\varepsilon_k,\boldsymbol{q})}{k_\mathrm{B}}\right)\mathrm{d}\varepsilon\,\mathrm{d}\boldsymbol{q}\\ &= 3N + \sum_{i=1}^N \beta Z_\beta^{-1}\int_{\mathscr{E}}\left[\frac{P_i}{\rho_i^2}\sum_{j\neq i} m_i m_j F_{ij}\boldsymbol{r}_{ij}^2\right]\exp\left(-\beta\sum_{k=1}^N\left[\frac{\boldsymbol{p}_k^2}{2m_k}+\varepsilon_k\right]\right)\frac{\exp\left(\frac{S_i}{k_\mathrm{B}}\right)}{T_i}\\ &\qquad\times\prod_{k\neq i}\frac{\exp\left(\frac{S_k}{k_\mathrm{B}}\right)}{T_\beta}\,\mathrm{d}\boldsymbol{q}\,\mathrm{d}\boldsymbol{p}\,\mathrm{d}\varepsilon.\end{aligned}$$

In each term of the sum, we use the relation (2.36) for all variables ε_k with $k \neq i$, which gives

$$\frac{\mathscr{Z}'(0)}{\mathscr{Z}(0)} = 3N + \beta\int_{\mathscr{E}}\left[\sum_{i=1}^N\sum_{j\neq i} m_i m_j F_{ij}\boldsymbol{r}_{ij}^2\frac{P_i}{\rho_i^2}\right]\mu_\beta(\mathrm{d}\boldsymbol{q}\,\mathrm{d}\boldsymbol{p}\,\mathrm{d}\varepsilon).$$

We can finally compute the thermodynamic pressure in a SDPD system using (2.38):

$$\mathscr{P} = \frac{1}{3\beta\mathscr{V}}\frac{\mathscr{Z}'(0)}{\mathscr{Z}(0)} = \mathscr{P}_\mathrm{kin} + \langle P_\mathrm{virial}\rangle_{\mu_\beta},$$

where we identify the usual expressions for the kinetic part of the pressure:

$$\mathscr{P}_\mathrm{kin} = \frac{N}{\beta\mathscr{V}},$$

and for the potential part of the pressure:

$$P_\mathrm{virial} = \frac{1}{3\mathscr{V}}\sum_{i=1}^N m_i m_j\frac{P_i}{\rho_i^2}\sum_{j\neq i} F_{ij}\boldsymbol{r}_{ij}^2 = \frac{1}{3\mathscr{V}}\sum_{1\leq i<j\leq N}\boldsymbol{\mathcal{F}}_{\mathrm{cons},ij}\cdot\boldsymbol{r}_{ij},$$

with the forces $\boldsymbol{\mathcal{F}}_{\mathrm{cons},ij}$ defined in Equation (1.27).

3 Parametrization of coarse-grained models from microscopic simulations

Most often, coarse-grained models depend on several parameters (*e.g.* coarse-grained potentials, friction coefficients, equations of state,...) that are optimized to retrieve some properties of the microscopic system under consideration. It is actually very appealing to express these parameters as functions of the microscopic description, which would justify their physical relevance. The theory of coarse-graining [65, 176, 138] allows to derive the dynamics of coarse-grained variables from the atomistic system. This has led to the development of isothermal models close to DPD [3, 73]. More recently it has been extended to non-isothermal situations [41], resulting in a sound theoretical foundation from first principles for the DPDE model. The resulting blobs are referred to as thermal blobs, which are characterized by the position and momenta of the center of mass of the atoms that make up the blob, and also its internal energy. This additional degree of freedom allows us in particular to handle systems with temperature gradients.

One crucial ingredient of the theory of coarse-graining [65, 176, 138] is the notion of entropy of the level of description, which is a function of the coarse-grained variables of that level. In [41], the calculation of the entropy of the level of description of thermal blobs relied on a key approximation (KA). The KA consists in assuming that the microscopic intermolecular potential of interaction between complex molecules can be approximated (in a statistical sense) by a function of the coordinates of the centers of mass alone. The main consequence of this KA is that we may speak of the blob entropy which is the thermodynamic entropy of a single molecule taken as an isolated thermodynamic system. This simplifies enormously the theory and is essential for the tractability of the calculations in [41].

In this chapter, we assess the validity of the key approximation in the derivation of DPDE from first principles for a model system. We first give in Section 3.1 the coarse-grained description for star polymers based on the formalism developed in [41]. In Section 3.2, we then check the KA by studying the independence of selected coarse-grained variables, such as positions, momenta and energies of molecules, and comparing the entropy of star polymers in a melt and in vacuum. This actually provides us a parametrization of the equation state needed for DPDE (see Section 1.1.3) based on MD simulations. We also briefly discuss in Section 3.3 the possible parametrizations of the coarse-grained interaction potential and the friction coefficients based on the microscopic description of the system.

3.1 The coarse-grained description of star polymers

We consider a melt of identical star polymer molecules (as shown in Figure 3.1) that have been already used in the isothermal coarse-grained (CG) version of star polymer molecules [73]. Each star polymer molecule is described at a coarse-level as a single thermal blob. The CG variables used to describe the blob are the position, $\boldsymbol{R}_\mu$, and momentum, $\boldsymbol{P}_\mu$, of the centers of mass of the blobs, together with the internal energy $\mathfrak{E}_\mu$ of the blob for molecules indexed by $\mu = 1 \dots M$. The coarse-variables are the following functions of the microstate $z = (\boldsymbol{q}, \boldsymbol{p})$ (coordinates and momenta of each atom in the system)

$$\begin{aligned} \boldsymbol{R}_\mu(z) &= \frac{1}{M_\mu} \sum_i^N m_i \boldsymbol{q}_i \delta_\mu(i) \\ \boldsymbol{P}_\mu(z) &= \sum_i^N \boldsymbol{p}_i \delta_\mu(i) \\ \mathfrak{E}_\mu(z) &= \sum_i^N \frac{1}{2m_i} \left(\boldsymbol{p}_i - \boldsymbol{P}_\mu(z)\right)^2 \delta_\mu(i) + \phi_\mu(z) \end{aligned} \tag{3.1}$$

The indicator symbol $\delta_\mu(i)$ takes the value 1 if the atom i belongs to the blob μ and zero otherwise. This indicator satisfies

$$\sum_\mu \delta_\mu(i) = 1, \quad \delta_\mu(i)\delta_\nu(i) = \delta_{\mu\nu}\delta_\mu(i) \tag{3.2}$$

These expressions reflect that the atom i belongs to one and only one blob. The mass, the velocity, and the potential energy of the μ-th blob are defined as

$$\begin{aligned} M_\mu &= \sum_i^N m_i \delta_\mu(i), \\ \boldsymbol{V}_\mu(z) &= \frac{\boldsymbol{P}_\mu(z)}{M_\mu}, \\ \phi_\mu(z) &= \frac{1}{2} \sum_{ij}^N \varphi_{ij} \delta_\mu(i), \end{aligned} \tag{3.3}$$

with φ_{ij} the pairwise potential energy between atoms i and j. The total energy and total momentum of the system can be expressed explicitly in terms of the CG variables as follows

$$\begin{aligned} E(\boldsymbol{q}, \boldsymbol{p}) &= \sum_\mu^M \left[\frac{\boldsymbol{P}_\mu^2(z)}{2M_\mu} + \mathfrak{E}_\mu(z) \right], \\ \mathscr{P}(z) &= \sum_\mu^M \boldsymbol{P}_\mu(z) \end{aligned}$$

as can be seen by using the definitions (3.1) and the properties (3.2).

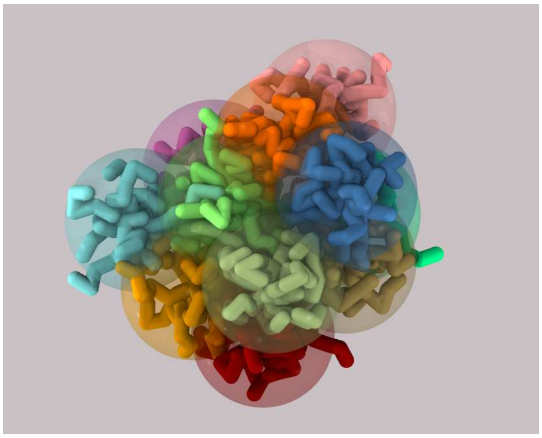


Figure 3.1 | Star polymer molecules (each molecule with a distinct color) are coarse-grained at the level of thermal blobs described by the position and momentum of the center of mass, plus the internal energy of the molecule with respect to the center of mass.

Another microscopic quantity that turns to be crucial in the formulation of the model is the intrinsic energy, defined in microscopic terms as

$$U_\mu(z) = \sum_i^N \frac{m_i}{2}(\boldsymbol{v}_i - \boldsymbol{V}_\mu(z))^2 \delta_\mu(i) + \frac{1}{2}\sum_{ij} \varphi_{ij}^{\text{intra}} \delta_\mu(i)\delta_\mu(j)$$

where the last contribution contains the potential φ^{intra} of interaction of atoms within the molecule. The difference between the internal energy $\mathfrak{E}_\mu(z)$ and the intrinsic energy $U_\mu(z)$ is the part of the potential energy of the molecule which is due to the interactions with other molecules. This intermolecular potential energy $\Phi_\mu = \mathfrak{E}_\mu - U_\mu$ is assumed, under the key approximation, to be a function of the microstate of the system only through the position $\boldsymbol{R} = \{\boldsymbol{R}_\mu\}_{\mu\in[\![1,M]\!]}$ of the centers of mass of the blobs. No pairwise assumption is made on the form of the interaction potential.

As shown in [41], under the KA the joint probability density of finding the values $\boldsymbol{R}, \boldsymbol{P}, U = \{\boldsymbol{R}_1, \cdots, \boldsymbol{R}_M, \boldsymbol{P}_1, \cdots, \boldsymbol{P}_M, U_1, \cdots, U_M\}$ has the following form

$$P^{\text{eq}}(\boldsymbol{R}, \boldsymbol{P}, U) = \frac{1}{\Omega}\delta\left(\sum_\mu \left[\frac{\boldsymbol{P}_\mu^2}{2M_\mu} + U_\mu + \phi_\mu(\boldsymbol{R})\right] - E_0\right) \times \delta\left(\sum_\mu \boldsymbol{P}_\mu - \boldsymbol{\mathcal{P}}_0\right) \exp\{S(\boldsymbol{R}, U)/k_B\} \quad (3.4)$$

under the understanding that we know with absolute certainty that the total energy of the system is E_0 and the total momentum is $\boldsymbol{\mathcal{P}}_0$, which is the case in usual MD simulations. Here $S(\boldsymbol{R}, U)$ is the entropy of the present level of description that depends, in principle, on all the CG variables. Due to Galilean invariance, in this level of description the entropy does not depend on momenta. As shown in [41], when the intermolecular potential can be approximated with a function of the position of the centers of mass of the blobs, the entropy becomes purely additive, and of the form

$$S(\boldsymbol{R}, U) = \sum_\mu S_\mu(U_\mu)$$

where the thermodynamic entropy of the blob $S_\mu(U)$ is the Boltzmann entropy of blob μ as a function of the intrinsic energy. The entropy S_μ follows the usual definition of the entropy of macroscopic thermodynamics. In the present case, the thermodynamic system is a single molecule.

Hence, S_μ is defined through the logarithm of the number of microstates compatible with the macrostate U, this is

$$S_\mu(U) = k_B \ln \int_{\mathscr{E}_\mu} \delta(\boldsymbol{R}_\mu)\delta(\boldsymbol{P}_\mu)\delta\left(U - \sum_i^N \frac{m_i}{2}\boldsymbol{v}_i^2\delta_\mu(i) - \phi_\mu^{\text{intra}}(z_\mu)\right)\mathrm{d}z_\mu \tag{3.5}$$

where the phase space integration is over the degrees of freedom z_μ (including positions and momenta) of a single isolated molecule μ.

The probability (3.4) is microcanonical in the total energy and momenta at the coarse-grained level. If we assume equivalence of ensembles for a sufficiently large number of molecules, we can approximate the microcanonical distribution with a canonical one, leading to

$$P^{\text{eq}}(\boldsymbol{R}, \boldsymbol{P}, U) = \frac{1}{Z} e^{-\beta_0 \sum_\mu \left[\frac{\boldsymbol{P}_\mu^2}{2M_\mu} + \mathscr{F}_\mu(U_\mu) + \Phi_\mu(\boldsymbol{R})\right]} \tag{3.6}$$

where Z stands for the normalization, and where we have introduced the free energy of blob μ as

$$\mathscr{F}_\mu(U_\mu) = U_\mu - T_0 S_\mu(U_\mu) \tag{3.7}$$

The temperature T_0, with $\beta_0 = (k_B T_0)^{-1}$, governs the overall thermodynamic point of the system and is related in a standard way with the total energy E_0 of the system.

The most salient feature of the probability distribution (3.6) is that positions, momenta, and intrinsic energies are statistically independent. We check in the following that the probability distribution (3.6) adequately describes the distribution of the coarse-grained variables for a system of star polymers in melt, by focusing on the statistical independence displayed. Because (3.6) is a joint probability in a multidimensional space it is not feasible to make histograms, and we need to select a number of observables out of this distribution function in order to validate the statistical independence of the variables.

3.2 Validation of the key approximation for star polymers

We consider a system of star polymers similar to the ones described in [73]. A number N_b of branches containing N_m identical monomers of mass m_0 are attached to a central monomer in order to construct a star polymer molecule. We will denote by a "N_b-N_m star polymer" such a molecule (*e.g.* a 6-3 star polymer has six branches with three monomers each). All monomers interact with a purely repulsive Lennard-Jones potential whose expression is given by

$$\mathscr{U}_{LJ,\text{rep}}(r) = \begin{cases} 4\varepsilon\left[\left(\frac{\sigma}{r}\right)^{12} - \left(\frac{\sigma}{r}\right)^{6} + \frac{1}{4}\right] \text{ if } r \le 2^{\frac{1}{6}}\sigma, \\ 0 \text{ if } r > 2^{\frac{1}{6}}\sigma, \end{cases}$$

In this chapter, all quantities will be given in Lennard-Jones reduced units where $\sigma = 1$, $\varepsilon = 1$ and $m_0 = 1$. The bonds are represented with a quadratic potential with stiffness $k = 20$:

$$\mathscr{U}_\text{bond}(r) = \frac{1}{2}k(r - l_\text{bond})^2.$$

The equilibrium bond length is set to $l_b = 1.147$ for monomers inside the branches and to $l_c = 1.615$ for bonds involving the central monomer.

Typically, we consider $N_{mol} = 1000$ star polymer molecules. The molecules are first set on a lattice and successive NVT simulations are carried for 25000 steps using a timestep $\Delta t = 0.001$ with a Langevin thermostat at a temperature $T = 1$ while the monomer density is progressively increased to reach the desired value. The Langevin friction is set to $\gamma = 1$. We then perform our simulations in the NVE ensemble using the Velocity-Verlet integration scheme with a timestep $\Delta t = 0.001$ during a total time $t_{sim} = 5000$.

In Sections 3.2.1 to 3.2.3 we focus on star polymers with 6 branches of 3 monomers each and study the independence of positions, momenta and intrinsic energy as well as the description of the blob entropy. We will extend the study to somewhat larger molecules in Section 3.2.4.

3.2.1 Momentum and energy correlations

In Figure 3.2 we plot the probability distribution of the momentum of the center of mass of a single molecule. According to the probability (3.6), the momenta are distributed according to a normal distribution. This is what is observed in our simulations. Note that the temperature is fixed to 1 on average during the thermostatting NVT process. When switching to NVE, the system may have a slightly different value of the average kinetic energy. The measured inverse thermal energy in the NVE simulation is $\beta = 1.05$. In Figure 3.3 we plot the distribution of the

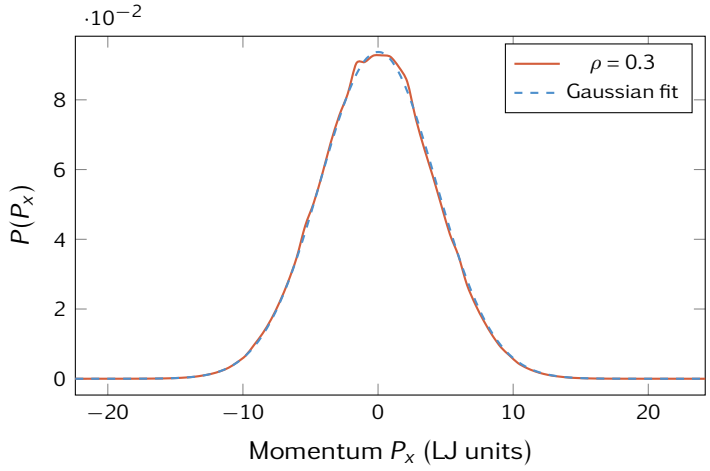


Figure 3.2 | The probability density $P(P_x)$ that the x component of the momentum of the center of mass of one given molecule is P_x. Also shown is a fit to a Maxwellian with temperature $\beta = 1.05$.

intrinsic energy of a single star polymer molecule.

In order to validate the independence of momentum and internal energy, we compute the covariance of the kinetic energy of the center of mass of a molecule with the intrinsic internal energy $\left\langle \Delta\left(\frac{\boldsymbol{P}_\mu^2}{2M_\mu}\right)\Delta U_\mu \right\rangle$. According to the form (3.6) this should be zero. Here and in what follows, we refer to $\Delta A = A - \langle A\rangle_{eq}$ as the fluctuations with respect to the equilibrium average. In order

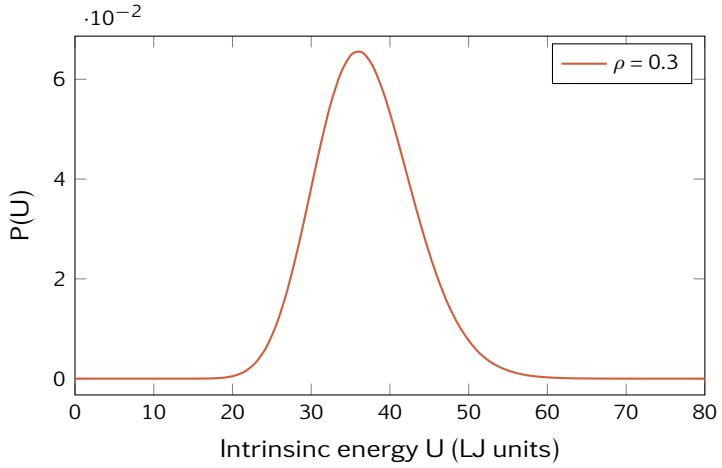


Figure 3.3 | The probability density $P(U)$ that the intrinsic energy of a molecule is U.

to check how small is this correlation we introduce the normalized covariance

$$C_{KU} \equiv \frac{\left\langle \Delta\left(\frac{\boldsymbol{P}_\mu^2}{2M_\mu}\right)\Delta U_\mu \right\rangle}{\sqrt{\left\langle \left(\Delta\left(\frac{\boldsymbol{P}_\mu^2}{2M_\mu}\right)\right)^2\right\rangle \left\langle (\Delta U_\mu)^2\right\rangle}}$$

The average correlation C_{KU} computed over all the molecules at a monomer density $\rho = 0.3$ is $C_{KU} = 5.08 \times 10^{-2}$, that we deem very small. Perhaps a more illustrative test is obtained from the scatter plot in Figure 3.4, where we plot the instantaneous kinetic energy and intrinsic energy for each blob at a given time. There is no particular trend, which indicates that the probability

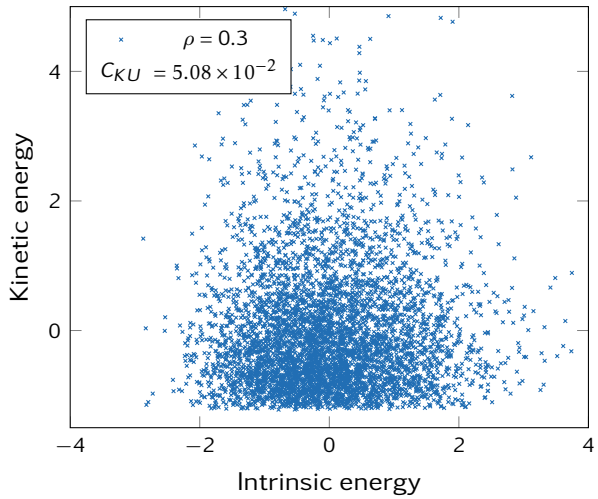


Figure 3.4 | Scatter plot of the value of instantaneous kinetic energy and intrinsic energy for each blob at a given time. These energies have been normalized to have 0 mean and a variance of 1.

factorizes $P(K,U) = P(K)P(U)$. Therefore, momentum and intrinsic energy are not correlated. A more quantitative test is by looking at the relative error $\left|\frac{(P(K,U)-P(K)P(U))}{P(K,U)}\right|$ that should vanish under statistical independence. In Figure 3.5 the relative error is plotted. In order to avoid spurious errors in regions with small values of $P(K,U)$ the error is not computed in those regions. We

observe that the relative error is very small in the region where the probability is appreciable, indicating a good degree of statistical independence.

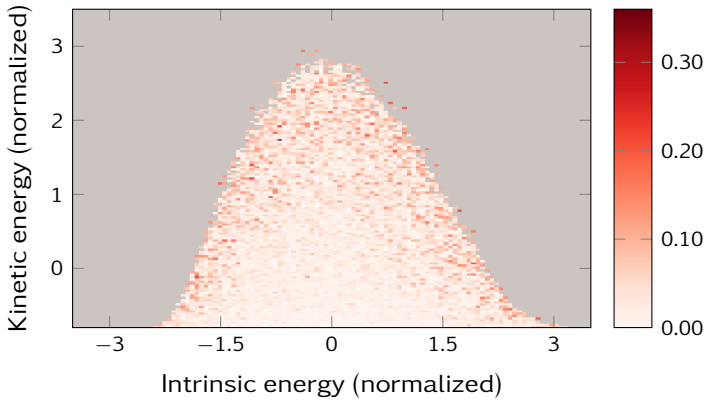


Figure 3.5 | Density plot colored with respect to the relative error $\left|\frac{(P(K,U)-P(K)P(U))}{P(K,U)}\right|$. If the value of $P(K,U)$ is too small, the relative error is not computed and displayed in gray. Note that in the region where the probability is noticeable different from 0, the relative error is very small.

3.2.2 The blob entropy

A very stringent test of the KA comes from the comparison of the two different and independent routes for computing the entropy of a molecule as a function of the intrinsic energy of the molecule. First, we consider the microscopic definition (3.5) in which an isolated molecule is considered as a thermodynamic system in its own right. With the equipartition of energy, it holds

$$\left\langle \sum_{i_\mu}^{N_\mu} \frac{\boldsymbol{p}_{i_\mu}^2}{2m_{i_\mu}} \right\rangle^U = \frac{3}{2} N_\mu k_B T(U) \tag{3.8}$$

where N_μ is the number of atoms of molecule μ, and the average $\langle \cdots \rangle^U$ is a microcanonical average of an isolated molecule at the energy U. By running MD simulations of an isolated molecule for different energies U we may plot the function $T(U)$ and, through integration, recover the entropy function

$$\frac{S_\mu(U)}{k_B} = \frac{S_\mu(U_0)}{k_B} + \int_{U_0}^{U} \frac{1}{k_B T(U')} \mathrm{d}U' \tag{3.9}$$

A second independent route to compute the entropy function of the blob is a consequence of the form (3.6) that implicitly assumes that the microscopic potential energy of interaction between molecules may be approximated by a function of the centers of mass of the blobs. If we integrate Equation (3.6) over all variables except the intrinsic energy of one blob we obtain the probability density $P(U)$ that one blob has a particular intrinsic energy U. This function is plotted in Figure 3.3. Using Equation (3.7) we obtain easily the identity

$$\frac{S_\mu(U)}{k_B} = \ln P(U) + \beta U \tag{3.10}$$

where β is obtained from fitting a Maxwellian to the momentum distribution of a single molecule. Note that while (3.9) is computed with a single isolated molecule in vacuum, (3.10) is computed

for the molecules in the melt. Both functions must be identical if the KA on the microscopic interaction potential is valid. Alternatively, and in order to avoid the integral, we may take the derivative of (3.10) in order to obtain the temperature

$$\frac{1}{k_B T(U)} = \frac{P'(U)}{P(U)} + \beta \tag{3.11}$$

and compare it with the temperature obtained from the equipartition theorem in Equation (3.8) for an isolated molecule.

In Figure 3.6 we plot the two entropy functions (3.9) and (3.10) as a function of the intrinsic energy, for different monomer densities. The agreement of the two curves for the entropy of a molecule in melt and in vacuum is quite remarkable. The temperature is the derivative of

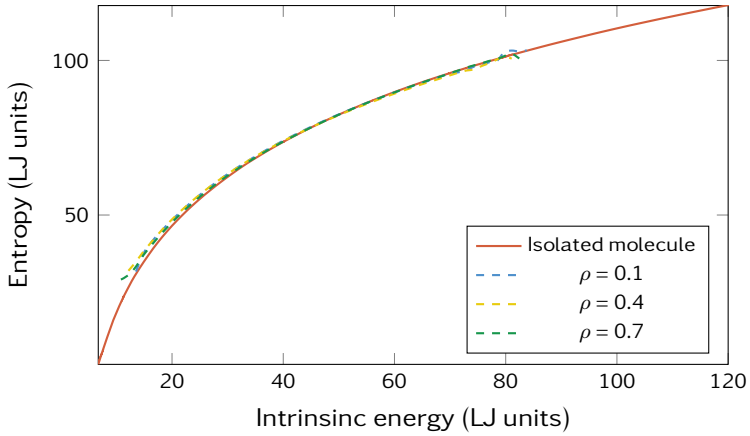


Figure 3.6 | The entropy of an isolated molecule from Eq. (3.9) (solid line) compared with the entropy of a molecule inside a melt, computed from Eq. (3.10) (dashed lines), for different monomer densities. The curves have been superimposed taking advantage of the fact that entropy is defined up to an additive constant.

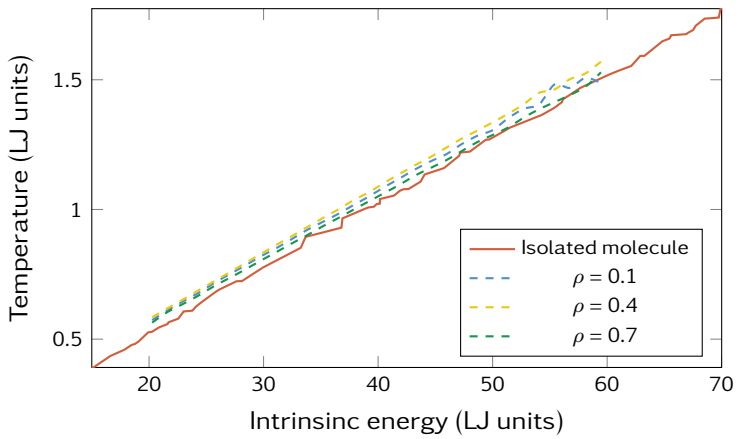


Figure 3.7 | Temperature of a single molecule in vacuum as a function of the intrinsic energy, computed from (3.8) (solid line). Temperature of a molecule in the melt as a function of the intrinsic energy, computed from (3.11) (dashed lines) for different monomer densities.

the entropy and it is practically linear, as shown in Figure 3.7. Under the approximation of a linear dependence of the temperature on the energy, the heat capacity of a molecule is constant and equal to the slope of the temperature function. In Figure 3.8 we plot the heat capacity of a

star polymer molecule in melt for different monomer densities, compared to the heat capacity of an isolated star polymer molecule. The heat capacity of a molecule in the melt is not strongly dependent on the monomer density and it is within a 5% difference from the heat capacity of a molecule in vacuum. It should be clear that the heat capacity of the whole sample of star polymers is not the sum of the heat capacity of each molecule. Energy can be stored in both the intrinsic energy of the molecules and also in the intermolecular potential energy between molecules.

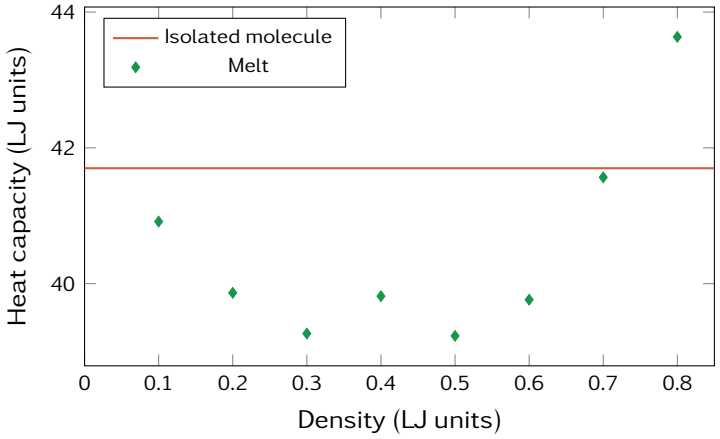


Figure 3.8 | The heat capacity of a molecule in melt for different monomer densities, and in vacuum (red line).

3.2.3 Position and energy correlations

We now consider the joint probability distribution $P(\boldsymbol{R}_\mu, \boldsymbol{R}_\nu, U_\mu, U_\nu)$ for two distinct molecules μ, ν that molecule μ has position and intrinsic energy $\boldsymbol{R}_\mu, U_\mu$ and ν has position and intrinsic energy $\boldsymbol{R}_\nu, U_\nu$. It is given by

$$P(\boldsymbol{R}_\mu, \boldsymbol{R}_\nu, U_\mu, U_\nu) = \int \delta(\boldsymbol{R}_\mu(z) - \boldsymbol{R}_\mu)\delta(\boldsymbol{R}_\nu(z) - \boldsymbol{R}_\nu)\delta(\hat{U}_\mu(z) - U_\mu)\delta(\hat{U}_\nu(z) - U_\nu)\rho_{\mathrm{eq}}(z)\mathrm{d}z$$

where $\rho_{\mathrm{eq}}(z)$ is the equilibrium ensemble. Translation and rotation invariance of the Hamiltonian, and hence of the equilibrium ensemble, implies that the above probability is, in fact, just a function of three variables

$$P(\boldsymbol{R}_\mu, \boldsymbol{R}_\nu, U_\mu, U_\nu) = P(R_{\mu\nu}, U_\mu, U_\nu)$$

where $R_{\mu\nu} = \left|\boldsymbol{R}_{\mu\nu}\right|$ is the distance between the centers of mass of molecule μ and ν. The above probability is defined on a three dimensional space and is too costly to evaluate by histograms. We may, therefore, look at the second moments with respect to intrinsic energy variables and at the following conditional covariance

$$\begin{aligned}\left\langle U_\mu U_\nu \right\rangle^{R_{\mu\nu}} &= \frac{\int U_\mu U_\nu P(R_{\mu\nu}, U_\mu, U_\nu)\mathrm{d}U_\mu \mathrm{d}U_\nu}{\int P(R_{\mu\nu}, U_\mu, U_\nu)\mathrm{d}U_\mu \mathrm{d}U_\nu} \\ &= \frac{\int U_\mu(z) U_\nu(z)\delta(\boldsymbol{R}_\mu)\delta(\boldsymbol{R}_\mu - \boldsymbol{R}_{\mu\nu})\rho_{\mathrm{eq}}(z)\mathrm{d}z}{\int \delta(\boldsymbol{R}_\mu)\delta(\boldsymbol{R}_\mu - \boldsymbol{R}_{\mu\nu})\rho_{\mathrm{eq}}(z)\mathrm{d}z}\end{aligned} \tag{3.12}$$

The intuitive meaning of this conditional correlation is that it gives the correlation of the intrinsic energies of two molecules separated by a distance $R_{\mu\nu}$. Clearly, if the position and intrinsic

energies are statistically independent, then $P(R_{\mu\nu}, U_\mu, U_\nu) = P(R_{\mu\nu})P(U_\mu, U_\nu)$, and the above covariance will be independent of $R_{\mu\nu}$. In order to increase statistics we will instead consider the following covariance

$$\langle U_1 U_2 \rangle^r = \frac{\sum_{\mu\neq\nu} \int U_\mu(z) U_\nu(z) \delta(r - \hat{R}_{\mu\nu}) \rho_{\text{eq}}(z) \mathrm{d}z}{\sum_{\mu\neq\nu} \int \delta(r - \hat{R}_{\mu\nu}) \rho_{\text{eq}}(z) \mathrm{d}z} \tag{3.13}$$

indexed by the distance r between the molecules. If the key approximation is valid, $P(R_{\mu\nu}, U_\mu, U_\nu) = P(R_{\mu\nu})P(U_\mu)P(U_\nu)$ and, from Equation (3.12) we should have that the conditional expectation in Equation (3.13) becomes identical to the unconditional expectation:

$$\langle U_1 U_2 \rangle^r = (\langle U \rangle)^2 \tag{3.14}$$

and, therefore, independent on the distance. If this is the case, we see that Equation (3.13) implies the identity

$$u(r) = g(r) \tag{3.15}$$

where the radial distribution function is

$$g(r) = \frac{1}{N_0} \sum_{\mu\neq\nu} \int \delta(r - \hat{R}_{\mu\nu}) \rho_{\text{eq}}(z) \mathrm{d}z \tag{3.16}$$

where N_0 is the usual normalization of the radial distribution function, and we introduce the following quantity

$$u(r) \equiv \frac{1}{N_0} \sum_{\mu\neq\nu} \int \frac{\hat{U}_\mu(z) \hat{U}_\nu(z)}{(\langle U \rangle)^2} \delta(r - \hat{R}_{\mu\nu}) \rho_{\text{eq}}(z) \mathrm{d}z \tag{3.17}$$

which is a sort of normalized covariance similar to the radial distribution function. Therefore, verification of the identity (3.15) is a proof of independence of intrinsic energy and positions of the blobs.

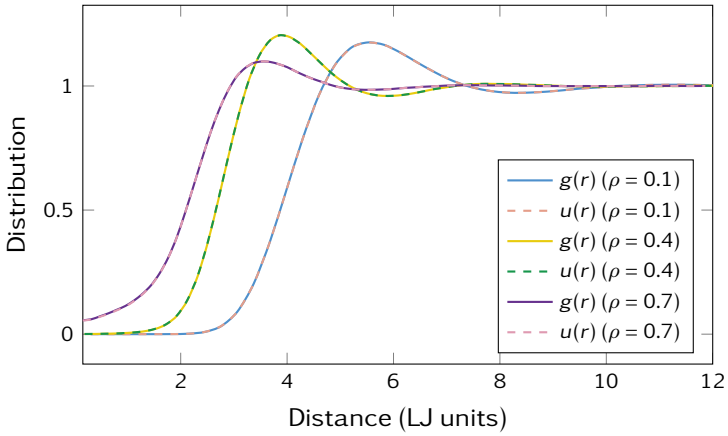


Figure 3.9 | Radial distribution function $g(r)$ of the centers of mass of the molecules for two different monomer densities. Also shown is the correlation $u(r)$ defined in (3.17). The identity (3.15) which is a consequence of the KA is satisfied very well.

We show in Figure 3.9 both functions $g(r)$ and $u(r)$ that turn out to be indistinguishable. It is

possible, however, to detect some differences at very short distances, by using Equation (3.14) directly. In Figure 3.10 we assess the validity of relation (3.14) by plotting Equation (3.13) normalized by the unconditional expectation $(\langle U \rangle)^2$ and the radial distribution function. We observe that when two molecules have their centers of mass "on top of each other", then the intrinsic energy of each molecule which is due entirely to self interaction, is affected by the presence of the other interdigitated molecule. This small effect occurs rarely, as can be seen from the fact that it occurs in the region where the radial distribution function is very small.

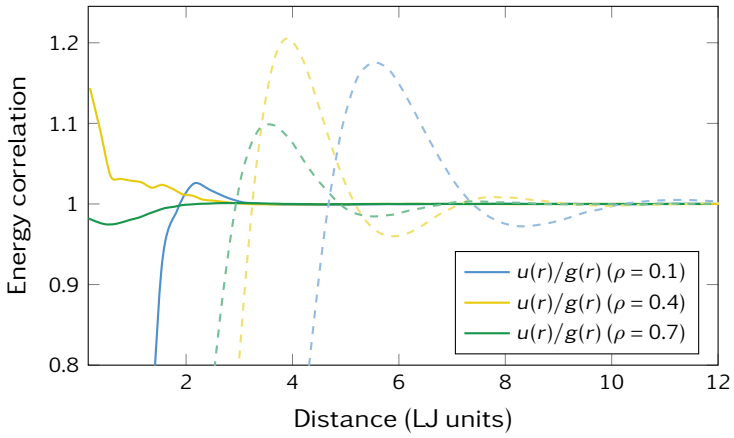


Figure 3.10 | The conditional covariance (3.13) normalized by the unconditional expectation $(\langle U \rangle)^2$ is plotted together with the radial distribution function, whose full curve is given in Figure 3.9.

Another illuminating criteria is the calculation of the correlations between the intrinsic energy U_μ of the blob and its "volume". The volume of a blob is defined as the inverse of the local density of molecules which, in turn is defined as

$$\rho_\mu(z) = \sum_{\nu \neq \mu} M_{nu} W(\hat{R}_{\mu\nu}(z))$$

which is the definition of the SPH interpolation of the density (see Equation (1.20)). When other molecules are close to molecule μ, the contribution to the sum is large and, consequently, the density of molecule μ is larger. We resort to the Lucy function defined in Equation (1.14) as the kernel function W with a smoothing length h that should be larger than the typical distance between blobs. In the following, we choose h such that the second peak of the radial distribution function is included in the kernel support (*i.e.* $h = 10$ for $\rho = 0.3$).

We will compute the following correlation

$$\left\langle \Delta\hat{U}_\mu \Delta\hat{\rho}_\mu \right\rangle^{\text{eq}} = \int \Delta U_\mu \Delta \left(\sum_{\nu \neq \mu} M_\nu W(R_{\mu\nu}) \right) P(R, P, U) \mathrm{d}R \mathrm{d}P \mathrm{d}U$$

and normalize it as

$$C_{UD} = \frac{\left\langle \Delta U_\mu \Delta \rho_\mu \right\rangle^{\text{eq}}}{\sqrt{\left\langle \left(\Delta U_\mu\right)^2 \right\rangle \left\langle \left(\Delta \rho_\mu\right)^2 \right\rangle}}$$

This correlation should vanish if positions and intrinsic energy of a molecule are statistically independent. At a monomer density $\rho = 0.3$, the average correlation computed over all particles

is indeed very small $C_{UD} = 8.59 \times 10^{-4}$. We also show in Figure 3.11 the scatter plot of the instantaneous density and intrinsic energy of each particle at a given time. As the plot shows no trend, we infer that these variables are statistically independent. A more stringent test in order to

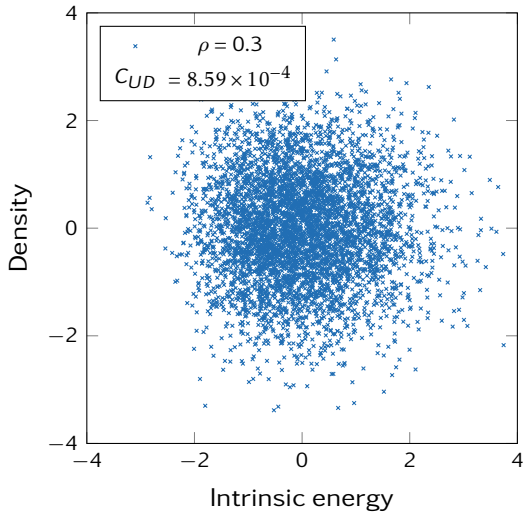


Figure 3.11 | Scatter plot of the value of instantaneous density and intrinsic energy for each particle at a given time. The density and energy have been normalized to have 0 mean and a variance of 1. The isotropy of the plot indicates that the probability factorizes $P(\rho, U) = P(\rho)P(U)$.

see that independence between intrinsic energy and local density can be obtained by looking at the following average

$$\langle U \rangle^{\rho} = \frac{\int UP(U, \rho) \mathrm{d}U}{\int P(U, \rho) \mathrm{d}U}$$

This gives the average of the intrinsic energy conditional to the value of the local density. We plot in Figure 3.12 the conditional expectation $\langle U \rangle^{\rho}$ as a function of the density. There are large errors, but no systematic trend, indicating that the intrinsic energy and the local density of a blob are uncorrelated.

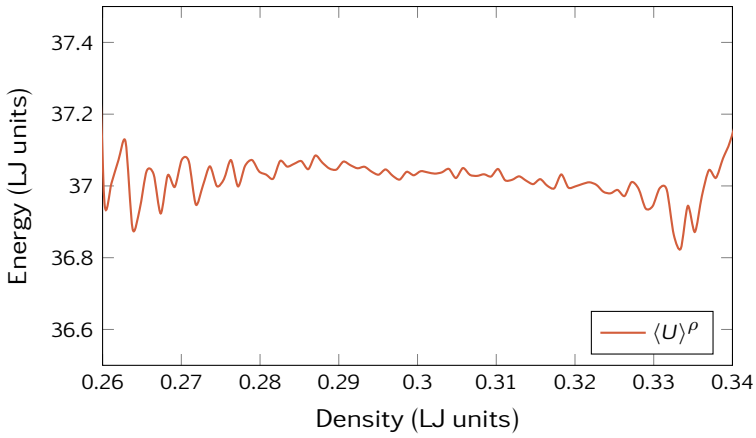


Figure 3.12 | The conditional expectation $\langle U \rangle^{\rho}$ of the intrinsic energy of a molecule, conditional to the value ρ of the local density of that molecule, at a global density $\rho = 0.3$. Within the large error, there is no systematic trend.

3.2.4 Extension to larger molecules

In order to further check the key approximation, we consider a few larger molecules, namely 6-6 star polymers and 6-12 star polymers. The results obtained for these molecules are very similar to what was observed for the 6-3 star polymers presented above.

Figure 3.13 shows the radial distribution function $g(r)$ along with the covariance function $u(r)$, similarly to Figure 3.9, but for these larger molecules. We observe that apart from the obvious fact that the peak of the radial distribution function is located at larger distances for larger molecules, the quantity defined by Equation (3.17) agrees very well with the radial distribution function g in Equation (3.16). Thus, the covariance $\langle U_1 U_2 \rangle^r$ defined by Equation (3.13) also appears to be independent of the distance r between these larger molecules.

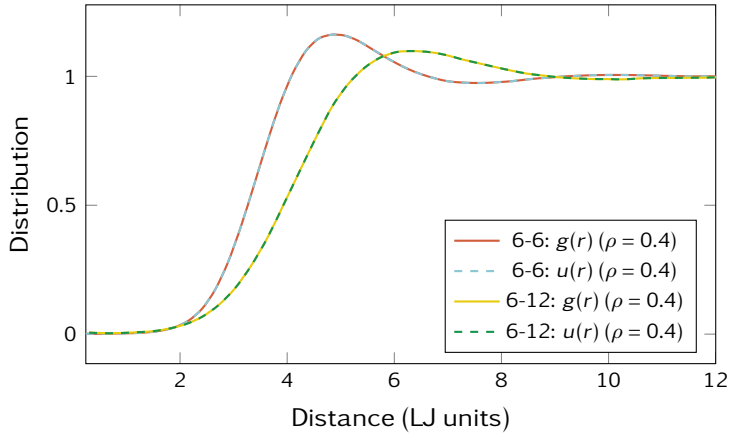


Figure 3.13 | Radial distribution function $g(r)$ of the centers of mass of the molecules for the 6-6 and 6-12 star polymers, compared to the correlation $u(r)$ defined in (3.17).

The entropy of a molecule in melt for these larger molecules agrees also quite well with the entropy of an isolated molecule. This appears clearly in Figure 3.14 for 6-6 and 6-12 star polymers.

This shows that the microscopic intermolecular interaction between those molecules is well approximated by a function of the positions of the centers of mass of the molecules only and effectively validates the key assumption for the derivation of DPDE from first principles [41] in the case of star polymers. It allows to express the entropy of this coarse-grained level of description as a sum of the entropies of each molecule, as if they were isolated thermodynamic subsystems of the whole system. Besides the validation of the thermal blob model based on the KA, this justifies the use of the entropy of a single isolated molecule to calibrate the equation of state in DPDE. This constitutes a preliminary and necessary step towards the construction and parametrization of coarse-grained models of complex molecules from first principles able to simulate thermal processes.

3.3 Coarse-grained interaction potential

Another step of paramount importance is to produce faithful interaction potentials between coarse-grained molecules. The equilibrium distribution of the coarse-grained potential is determined by the many-body Potential of Mean Force [142] However, it is in practice impossible to exactly compute it and use it to derive the interactions between the coarse-grained particles. Popular

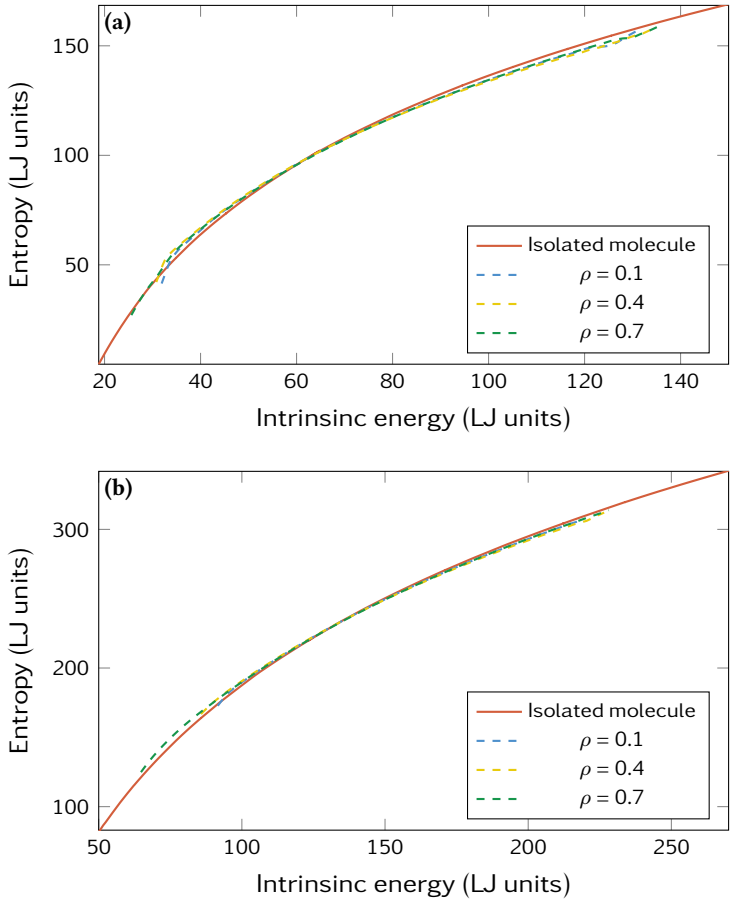


Figure 3.14 | The entropy of an isolated star polymer from Equation (3.9) (solid line) compared with the entropy of a molecule inside a melt, computed from Equation (3.10) (dashed lines), for different monomer densities, for (a) 6-6 star polymers and (b) 6-12 star polymers.

techniques to approximate the Potential of Mean Forces generally follow two different routes. Methods like Iterative Boltzmann Inversion [150] or Inverse Monte-Carlo [124] or Bayesian approaches [42, 26] based on the concept of relative entropy [158] are designed to reproduce structural properties of the microscopic system, *e.g.* the radial distribution function. Some corrections to retrieve the correct pressure may be included but it is unclear to what extent thermodynamic and structural properties can be recovered simultaneously [122, 91, 174]. This is known as the representability problems. Another route to obtain coarse-grained potential is through Force Matching [39, 86] which aims at recovering the forces in the system in average rather than the structure. Machine learning algorithms have been getting much attention in the recent years as a way to fit interaction potentials. They may be used in MD to recover the accuracy from ab-initio force calculations at a reduced cost [9, 10, 52]. It is a promising way to determine coarse-grained forces consistent with the atomistic configurations [88].

Another major issue in obtaining coarse-grained potentials is transferability, that is the ability of the potential to remain valid in a large range of thermodynamic states. While traditional methods usually perform the optimization at specific thermodynamic conditions, techniques such as multi-state Iterative Boltzmann Inversion [136] aim at taking into account a variety of thermodynamic states and improve the transferability of coarse-grained potentials. Another way consists in using multiple-body potentials instead of simple pair interactions. This may be done by

integrating a dependence of the potential function on the local density [85, 135]. In a work prior to this thesis [49], we established a model for compressible mesoparticle whose interaction potential was given by a functional form with parameters depending on a local density. This density may be defined with the SPH definition in Equation (1.20) or through a Voronoi tessellation. The dependence of the parameters on the density is fitted thanks to equilibrium MD simulations. The model was able to reproduce the Hugoniot curve of nitromethane with a good accuracy and over a large range of densities.

To complete the derivation of the CG model, the transport coefficients also need to be computed explicitly. In the context of DPD, it has been proposed to use constrained dynamics to compute the transport coefficients [73]. This approach has been successfully applied for star polymers [73, 113] and for other polymer chains [110]. In DPDE, as the intrinsic energy is non-linear in the degrees of freedom, as opposed to the positions and momenta of the centers of mass, the method proposed in [73] cannot be used. The Bayesian approach [42, 26] previously mentioned for the coarse-grained force-field also allows to determine the friction parameters and might be adapted to the DPDE model derived in [41].

4 Integration of SDPD with accurate and stable schemes

Most of the studies performed with SDPD resort to a simplified version of the dynamics where internal temperatures are kept fixed at $T_i = T_{\text{ref}}$. As a consequence, much simpler numerical schemes may be used without paying attention to the energy conservation. In this context, the equations of motion are integrated using a Verlet scheme or more specific splitting schemes designed for SDPD [117]. These schemes are very much inspired by integration schemes designed for DPD such as the Shardlow splitting scheme [156]. There are very few works providing numerical schemes for the integration of the full SDPD dynamics such as Gatsonis *et al.* [60] who mix a Velocity-Verlet scheme for the update of positions and momenta and a Runge-Kutta scheme for the entropy updates. In such works, no specific attention is devoted to the preservation of the invariants such as the energy since the applications are usually carried at constant temperature.

When considering the dynamics (2.6) or (2.18), the preservation of the invariants, especially the energy, requires some care in the design of the numerical scheme. Other desirable properties include stability, accuracy and parallelizability. Exhibiting a scheme satisfying all these constraints is not an easy task. The increased similarity of the reformulated dynamics (2.18) with DPDE makes it possible to resort to similar integration schemes in both methods. In this chapter, we adapt to the SDPD setting some numerical schemes introduced for the integration of DPDE.

In Section 4.1, we first formulate in the context of SDPD a Shardlow-like Splitting Algorithm (SSA) which is a popular scheme in DPDE [160, 125] inspired by the Shardlow scheme proposed for DPD [156]. We also provide an analysis of the energy drift observed in such schemes [125, 79]. Though quite satisfying in terms of energy conservation, SSA suffers from a major parallelization issue and requires a convoluted method [104] to run in a parallel application. We turn our attention in Section 4.2 to a scheme called Splitting with Energy Reinjection (SER) proposed in [79, 78] to be easily parallelized. Another major issue in the integration of stochastic dynamics like DPDE or SDPD is the stability of the fluctuation/dissipation part that may cause internal energies to become negative. It has been proposed in the context of DPDE [161] to add a Metropolis procedure to the integration of fluctuation/dissipation dynamics in order to reject in particular forbidden moves leading to negative energies. We derive in 4.3 Metropolized schemes for SDPD based on SSA to improve the stability especially for small particle sizes and evaluate its properties in terms of energy drift and stability by means of numerical computations.

4.1 Shardlow-like Splitting Algorithm

As all the numerical schemes presented below, the Shardlow-like Splitting Algorithm (SSA) rely on a splitting strategy [168, 163] where the full dynamics is divided in simpler elementary dynamics that are consecutively integrated. Since the conservative part of the dynamics (1.28) can be viewed as a Hamiltonian dynamics, it is natural to resort to a symplectic scheme such as the widely used Velocity-Verlet scheme [172] which ensures a good energy conservation in the long term [67, 68]. This algorithm is briefly described in Section 4.1.1.

There is however no definite way to deal with the fluctuation/dissipation part described in Section 2.2.2. The SSA approach, presented in Section 4.1.2, is based on the algorithm proposed by Shardlow [156] for DPD and its subsequent adaptations to DPDE [160]. The dynamics is split into a Hamiltonian dynamics, discretized through a Velocity-Verlet algorithm, and elementary pairwise fluctuation/dissipation dynamics that are successively integrated.

4.1.1 Integrating the Hamiltonian part of the dynamics

It is convenient to consider the conservative part of the dynamics (1.28) in its original formulation in the position, momentum and entropy variables [40] in order to take advantage of the conservation of the entropies S_i. The internal energies are related to the positions and entropies by an energy function $\mathscr{E}(S_i, \rho_i(\boldsymbol{q}))$, which allows us to write the Hamiltonian as

$$H(\boldsymbol{q}, \boldsymbol{p}, S) = \sum_{i=1}^{N} \frac{\boldsymbol{p}_i^2}{2m_i} + \mathscr{E}(S_i, \rho_i(\boldsymbol{q})).$$

The dynamics (1.28) can thus be recast in Hamiltonian form as

$$\begin{cases} \mathrm{d}\boldsymbol{q}_i = \dfrac{\boldsymbol{p}_i}{m_i}\,\mathrm{d}t, \\ \mathrm{d}\boldsymbol{p}_i = -\boldsymbol{\nabla}_{\boldsymbol{q}_i}\mathscr{H}(\boldsymbol{q}, \boldsymbol{p}, S) = \displaystyle\sum_{j\neq i} \boldsymbol{\mathscr{F}}_{\mathrm{cons},ij}\,\mathrm{d}t. \end{cases}$$

The Velocity-Verlet scheme [172], introduced in Section 1.1.2 allows to integrate such dynamics while preserving on average the Hamiltonian H. In the context of SDPD, this corresponds to the following integration scheme:

$$\begin{cases} \boldsymbol{p}_i^{n+\frac{1}{2}} = \boldsymbol{p}_i^n + \displaystyle\sum_{j\neq i} \boldsymbol{\mathscr{F}}_{\mathrm{cons},ij}^n \frac{\Delta t}{2}, \\ \boldsymbol{q}_i^{n+1} = \boldsymbol{q}_i^n + \dfrac{\boldsymbol{p}_i^{n+\frac{1}{2}}}{m_i}\Delta t, \\ \boldsymbol{p}_i^{n+1} = \boldsymbol{p}_i^{n+\frac{1}{2}} + \displaystyle\sum_{j\neq i} \boldsymbol{\mathscr{F}}_{\mathrm{cons},ij}^{n+1} \frac{\Delta t}{2}. \end{cases} \tag{4.1}$$

Since the entropy S_i of each particle is preserved by the integration of this reversible dynamics, the internal energy ε_i after this step can be computed by inverting the equation of state as

$$\tilde{\varepsilon}_i^{n+1} = \mathscr{E}\left(S_i^n, \rho_i(\boldsymbol{q}^{n+1})\right),$$

with the updated density $\rho_i(\boldsymbol{q}^{n+1})$. If no analytic form is available for $\mathscr{E}$, a numerical inversion may be required (see for instance the equation of state for Lennard-Jones fluid in Section 5.1.2).

4.1.2 SSA integration of the fluctuation/dissipation part

We present here a first possibility for the integration of the fluctuation/dissipation dynamics based on existing schemes for DPD [156] and DPDE [160]. The idea of Shardlow-like Splitting Algorithm is to consider the elementary fluctuation/dissipation part successively for each pair of particles.

Reformulation in terms of the relative velocity

In order to propose an integration of the elementary fluctuation-dissipation dynamics (2.13), we first show that it can be described only in terms of the relative velocity $\boldsymbol{v}_{ij}$.

Since the dynamics (2.13) preserve the momentum $\boldsymbol{p}_i + \boldsymbol{p}_j$, the momenta $\boldsymbol{p}_i$ and $\boldsymbol{p}_j$ can be rewritten as a function of $\boldsymbol{v}_{ij}$ as:

$$\boldsymbol{p}_i = \frac{m_{ij}}{2}\left[\frac{\boldsymbol{p}_i+\boldsymbol{p}_j}{m_j} + \frac{\boldsymbol{p}_i}{m_i} - \frac{\boldsymbol{p}_j}{m_j}\right] = \frac{m_{ij}}{2}\frac{\boldsymbol{p}_i^0+\boldsymbol{p}_j^0}{m_j} + \frac{m_{ij}}{2}\boldsymbol{v}_{ij} = \boldsymbol{p}_i^0 + \frac{m_{ij}}{2}(\boldsymbol{v}_{ij}-\boldsymbol{v}_{ij}^0), \tag{4.2}$$

and similarly

$$\boldsymbol{p}_j = \boldsymbol{p}_j^0 - \frac{m_{ij}}{2}(\boldsymbol{v}_{ij}-\boldsymbol{v}_{ij}^0).$$

This already shows how to express the momenta $\boldsymbol{p}_i$ and $\boldsymbol{p}_j$ in terms of $\boldsymbol{v}_{ij}$. In addition, the kinetic energy formulated in the relative velocity reads

$$\begin{aligned}\frac{\boldsymbol{p}_i^2}{2m_i} + \frac{\boldsymbol{p}_j^2}{2m_j} &= \frac{\left(\boldsymbol{p}_i^0\right)^2}{2m_i} + \frac{\left(\boldsymbol{p}_j^0\right)^2}{2m_j} + \frac{m_{ij}}{4}(\boldsymbol{v}_{ij}-\boldsymbol{v}_{ij}^0)^2 + \frac{m_{ij}}{2}(\boldsymbol{v}_{ij}-\boldsymbol{v}_{ij}^0)\boldsymbol{v}_{ij}^0 \\ &= \frac{\left(\boldsymbol{p}_i^0\right)^2}{2m_i} + \frac{\left(\boldsymbol{p}_j^0\right)^2}{2m_j} + \frac{m_{ij}}{4}\left(\left[\boldsymbol{v}_{ij}\right]^2 - \left[\boldsymbol{v}_{ij}^0\right]^2\right)\end{aligned}$$

The conservation of the energy $\frac{\boldsymbol{p}_i^2}{2m_i} + \frac{\boldsymbol{p}_j^2}{2m_j} + \varepsilon_i + \varepsilon_j$ and the fact that $\mathrm{d}\varepsilon_i = \mathrm{d}\varepsilon_j$ provides the expression of the internal energies as a function of the relative velocity as

$$\varepsilon_i = \varepsilon_i^0 - \frac{m_{ij}}{8}\left(\left[\boldsymbol{v}_{ij}\right]^2 - \left[\boldsymbol{v}_{ij}^0\right]^2\right), \quad \varepsilon_j = \varepsilon_j^0 - \frac{m_{ij}}{8}\left(\left[\boldsymbol{v}_{ij}\right]^2 - \left[\boldsymbol{v}_{ij}^0\right]^2\right). \tag{4.3}$$

Using this relation, the dynamics (2.13) can in fact be rewritten as an effective dynamics on the relative velocity only, since the positions $\boldsymbol{q}$ are left constant by the fluctuation/dissipation part, as

$$\mathrm{d}\boldsymbol{v}_{ij} = -\frac{2}{m_{ij}}\Gamma_{ij}\boldsymbol{v}_{ij}\mathrm{d}t + \frac{2}{m_{ij}}\Sigma_{ij}\mathrm{d}\boldsymbol{B}_{ij}, \tag{4.4}$$

where Γ_{ij}, Σ_{ij} are functions of the relative velocity through (4.3).

Integration as Ornstein-Uhlenbeck process

If we neglect the dependence of Γ and Σ on ε_i, the elementary dynamics (4.4) can be viewed as a standard Ornstein-Uhlenbeck process. In order to integrate it exactly during a time t, we consider

separately each direction $\theta \in \{\perp, \parallel\}$. The properties on the projection matrices $\boldsymbol{P}_{ij}^{\theta}$ imply that

$$\exp\left(\frac{2t}{m_{ij}}\boldsymbol{\Gamma}_{ij}^{\theta}\right) = \exp\left(\frac{2}{m_{ij}}\gamma_{ij}^{\theta}t\right)\boldsymbol{P}_{ij}^{\theta}. \tag{4.5}$$

Following the usual route for the analytic integration of Ornstein-Uhlenbeck processes, we introduce the process $\boldsymbol{Y}_t = \exp\left(\frac{2t}{m_{ij}}\boldsymbol{\Gamma}_{ij}^{\theta}\right)\boldsymbol{v}_{ij}$ and determine that it is a solution of the following SDE

$$\begin{aligned}\mathrm{d}\boldsymbol{Y}_t &= \frac{2}{m_{ij}}\exp\left(\frac{2t}{m_{ij}}\boldsymbol{\Gamma}_{ij}^{\theta}\right)\boldsymbol{\Sigma}_{ij}^{\theta}\mathrm{d}\boldsymbol{B}_{ij}\\ &= \frac{2\sigma_{ij}^{\theta}}{m_{ij}}\exp\left(\frac{2\gamma_{ij}^{\theta}t}{m_{ij}}\right)\boldsymbol{P}_{ij}^{\theta}\mathrm{d}\boldsymbol{B}_{ij}.\end{aligned}$$

This shows that $\boldsymbol{Y}_t$ is distributed along a normal distribution of mean $Y_0 = \boldsymbol{v}_{ij}^0$ and of variance $\frac{\left(\sigma_{ij}^{\theta}\right)^2}{m_{ij}\gamma_{ij}^{\theta}}\left[\exp\left(\frac{4\gamma_{ij}^{\theta}t}{m_{ij}}\right) - 1\right]$. Using the definition of $\boldsymbol{Y}$, we can finally conclude that Equation (4.4) is integrated analytically starting from step n and during a time step Δt as

$$\boldsymbol{v}_{ij}^{n+1} = \sum_{\theta\in\{\perp,\parallel\}}\boldsymbol{P}_{ij}^{\theta}\left[\alpha_{ij}^{\theta}(\varepsilon_i^n, \varepsilon_j^n, \boldsymbol{q}^n)\boldsymbol{v}_{ij}^n + \zeta_{ij}^{\theta}(\varepsilon_i^n, \varepsilon_j^n, \boldsymbol{q}^n)\boldsymbol{G}_{ij}^n\right],$$

where $\boldsymbol{G}_{ij}^n$ is a standard 3-dimensional Gaussian variable and for $\theta \in \{\parallel, \perp\}$

$$\begin{aligned}\alpha_{ij}^{\theta}(\varepsilon_i, \varepsilon_j, \boldsymbol{q}) &= \exp\left[-\frac{2\gamma_{ij}^{\theta}\Delta t}{m_{ij}}\right],\\ \zeta_{ij}^{\theta}(\varepsilon_i, \varepsilon_j, \boldsymbol{q}) &= \sigma_{ij}^{\theta}\sqrt{\frac{1}{m_{ij}\gamma_{ij}^{\theta}}\left(1 - \exp\left(-\frac{4\gamma_{ij}^{\theta}\Delta t}{m_{ij}}\right)\right)}.\end{aligned}$$

These coefficients depend on the internal energy ε_i, ε_j and on the positions $\boldsymbol{q}$ through the friction and fluctuation parameters γ_{ij}^{θ}, σ_{ij}^{θ}. Note however that the positions are left unchanged by the fluctuation/dissipation dynamics (2.15).

The momenta of particles i and j can be retrieved using Equation (4.2):

$$\begin{pmatrix}\boldsymbol{p}_i^{n+1}\\ \boldsymbol{p}_j^{n+1}\end{pmatrix} = \begin{pmatrix}\boldsymbol{p}_i^n\\ \boldsymbol{p}_j^n\end{pmatrix} + \frac{m_{ij}}{2}\sum_{\theta\in\{\parallel,\perp\}}\begin{pmatrix}\boldsymbol{I}\\ -\boldsymbol{I}\end{pmatrix}\boldsymbol{P}_{ij}^{\theta}\left[\left(\alpha_{ij}^{\theta}(\varepsilon_i^n, \varepsilon_j^n, \boldsymbol{q}^n) - 1\right)\boldsymbol{v}_{ij}^n + \zeta_{ij}^{\theta}(\varepsilon_i^n, \varepsilon_j^n, \boldsymbol{q}^n)\boldsymbol{G}_{ij}^n\right]. \tag{4.6}$$

The corresponding update for the internal energies is obtained through Equation (4.3). This is actually equivalent to the approach suggested in [128, 160] where the variation of the kinetic energy induced by the integration of the momenta with (4.6) is redistributed symmetrically in the

internal energies with

$$\begin{cases} \varepsilon_i^{n+1} = \varepsilon_i^n - \dfrac{1}{2}\left[\dfrac{\left(\boldsymbol{p}_i^{n+1}\right)^2}{2m_i} + \dfrac{\left(\boldsymbol{p}_j^{n+1}\right)^2}{2m_j} - \dfrac{\left(\boldsymbol{p}_i^{n}\right)^2}{2m_i} - \dfrac{\left(\boldsymbol{p}_j^{n}\right)^2}{2m_j}\right] \\ \varepsilon_j^{n+1} = \varepsilon_j^n - \dfrac{1}{2}\left[\dfrac{\left(\boldsymbol{p}_i^{n+1}\right)^2}{2m_i} + \dfrac{\left(\boldsymbol{p}_j^{n+1}\right)^2}{2m_j} - \dfrac{\left(\boldsymbol{p}_i^{n}\right)^2}{2m_i} - \dfrac{\left(\boldsymbol{p}_j^{n}\right)^2}{2m_j}\right] \end{cases}.$$

Thermodynamic variables like the temperatures T_i, T_j and heat capacities C_i, C_j are updated with the equation of state using the new internal energies, before turning to another pair of particles. This last step consisting in updating the thermodynamic variables may be expensive depending on the equation of state. It may be skipped at the expense of larger energy drifts and more frequent stability issues.

Let us however remark that the pairwise Shardlow-like algorithm is sequential by nature and its parallelization requires a convoluted method [104]. This is addressed by the SER scheme in Section 4.2. Moreover, and maybe more importantly, there is no mechanism preventing the appearance of negative internal energies during the simulation. This situation happens when the fluctuations are large with respect to the internal energies: typically at low temperature or when the particle sizes are small (so that their heat capacity are small as well). This leads to stability issues unless very small timesteps are used. The Metropolization procedure introduced in Section 4.3 aims at improving the stability of the SSA scheme.

4.1.3 Analysis of the energy drift for SSA

In the following, we test the accuracy of SSA for the ideal gas equation of state given, for particle of size K, by

$$\mathcal{S}_{\text{ideal}}(\varepsilon, \rho) = \frac{3}{2}(K-1)k_{\text{B}}\ln(\varepsilon) - \frac{1}{2}(K-1)\ln(\rho). \tag{4.7}$$

The interest of this model is that the marginal distribution for the internal energies ε_i has an analytic expression:

$$\overline{\mu}_{\beta,\varepsilon}(\mathrm{d}\varepsilon) = \frac{\beta^{\frac{C_K}{k_{\text{B}}}}}{\Gamma\left(\frac{C_K}{k_{\text{B}}}\right)}\varepsilon^{\frac{C_K}{k_{\text{B}}}-1}\exp\left(-\beta\varepsilon\right)\,\mathrm{d}\varepsilon, \tag{4.8}$$

where $C_K = \frac{3}{2}(K-1)k_{\text{B}}$ is the heat capacity in the equation of state (4.7) and Γ is the Gamma function. This distribution is plotted in Figure 4.1 for various particle sizes. As the size K decreases, very small internal energies become more likely and stability issues may arise (see Section 4.3).

Our simulations have been carried out on a 3-dimensional system of 1000 particles initialized on a simple cubic lattice with an initial temperature $T = 1000$ K. The internal energies are chosen so that $T_i(\varepsilon_i, \rho_i(\boldsymbol{q})) = T$ with the density $\rho_i(\boldsymbol{q})$ evaluated from the initial distribution of the positions; while the velocities are distributed along the Boltzmann distribution. We let the system evolve during a time $\tau_{\text{therm}} = 50$ to obtain an equilibrated initial configuration. The shear viscosity is set to $\eta = 2 \times 10^{-3}$ Pa.s and we neglect the bulk viscosity ζ.

The results have been obtained by averaging over $n_{\text{sim}} = 1000$ realizations of the dynamics for a total time $\tau_s = 50$ for each time step Δt and size K. Although each part in the splitting scheme preserve independently the energy, it has been observed that their coupling in SSA yields a linear drift in energy for stochastic dynamics like DPDE [125, 79, 78]. It proves to also be true for

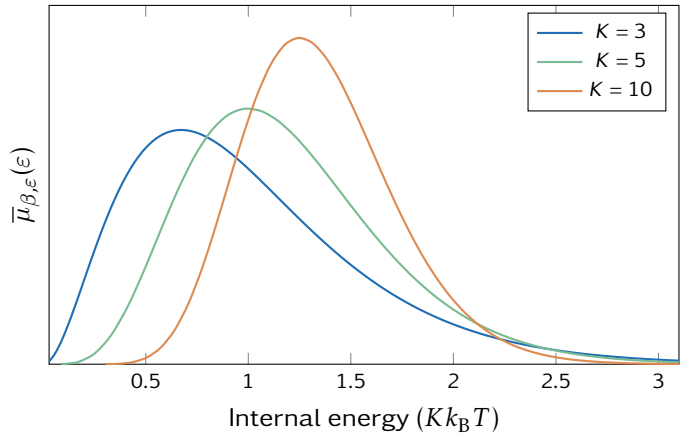


Figure 4.1 | Distribution of internal energies (in units of Kk_BT) with the ideal gas equation of state.

SDPD, which was expected since the structure of the dynamics is very similar. Figure 4.2 shows the relative error in energy for particle size $K = 100$ and highlights the linear drift. To analyze

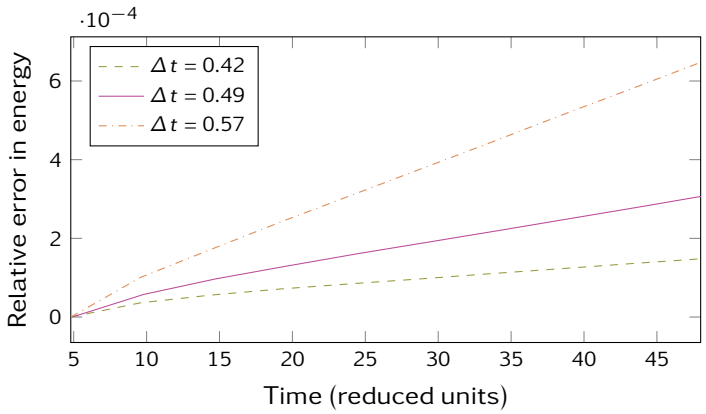


Figure 4.2 | Relative error in energy with respect to time for $K = 100$. A linear drift is observed.

the error in the energy conservation, we compute, for each timestep Δt and size K, the drift rate $\alpha_{\Delta t,K}$ defined as the slope of the relative energy drift $\frac{E(\boldsymbol{q}(t),\boldsymbol{p}(t),\varepsilon(t))-E_0}{E_0}$. We evaluate $\alpha_{\Delta t,K}$ by fitting a linear function on the relative error in energy with a least-square minimization. The drift rate $\alpha_{\Delta t,K}$ is represented in Figure 4.3 as a function of Δt for $K = 10$, $K = 50$ and $K = 100$. Assuming that the drift $\alpha_{\Delta t,K}$ can be written as

$$\alpha_{\Delta t,K} = \mathscr{C}_K \Delta t^{n_K},$$

we find, by performing a least-square fit in a log-log scale, that n_K is independent of K, with $n_K \approx 5.44$. The prefactor $\mathscr{C}_K$ varies with the mass of the particle. Here we estimate $\mathscr{C}_{10} = 9.50$, $\mathscr{C}_{50} = 181$ and $\mathscr{C}_{100} = 217$.

This suggests a way to choose the timestep to obtain a given drift rate: we perform a preliminary run with some timestep and measure the drift rate in this simulation. The power law, independent of K, then allows us to estimate the timestep needed to keep the energy drift below a given threshold. The results of Figure 4.2 also show that, for larger particle sizes K, we can increase the timestep in reduced units for a given drift rate, which allows us to integrate over

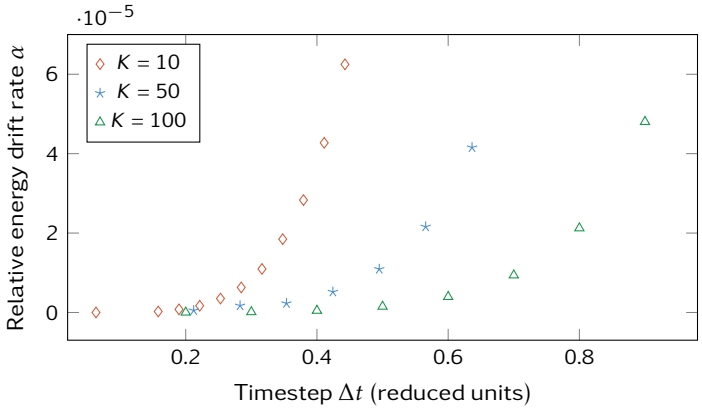


Figure 4.3 | Relative energy drift rate $\alpha_{\Delta t,K}$ as a function of the time step Δt for the SSA scheme.

longer times when using a coarse resolution.

4.2 Splitting with Energy Reinjection

In order to devise a naturally parallel scheme, we resort to global updates of the momenta and internal energies instead of pairwise steps. Such an approach was introduced for DPDE in [79] under the name Splitting with Energy Reinjection (SER). We adapt here this scheme in the SDPD setting in Section 4.2.1 and test its energy conservation and stability in Section 4.2.2.

4.2.1 SER integration of fluctuation/dissipation

While the conservative part is integrated by using the Verlet scheme (4.1), the fluctuation/dissipation part is now considered globally. The equations on momenta in Equation (2.13) are first integrated with an Euler-Maruyama scheme. The updated momenta are given by

$$\boldsymbol{p}_i^{n+1} = \boldsymbol{p}_i^n + \left[\sum_{j \neq i} -\boldsymbol{\Gamma}_{ij}^n \boldsymbol{v}_{ij}^n \Delta t + \Sigma_{ij}^n \boldsymbol{G}_{ij}^n \sqrt{\Delta t} \right] \tag{4.9}$$

We denote the corresponding momentum increment by

$$\delta \boldsymbol{p}_i^n = \sum_{j \neq i} -\boldsymbol{\Gamma}_{ij}^n \boldsymbol{v}_{ij}^n \Delta t + \Sigma_{ij}^n \boldsymbol{G}_{ij}^n \sqrt{\Delta t}$$

A simple reorganization of the sums allows to reformulate the induced kinetic energy variation in a pairwise way as

$$\begin{aligned} \Delta E_{\text{kin}}(\boldsymbol{p}^n, \boldsymbol{p}^{n+1}) &= \sum_{i=1}^{N} \frac{\left(\boldsymbol{p}_i^{n+1}\right)^2}{2m_i} - \frac{\left(\boldsymbol{p}_i^n\right)^2}{2m_i}, \\ &= \sum_{i=1}^{N} \frac{1}{2m_i} \delta \boldsymbol{p}_i^n \left(2\boldsymbol{p}_i^n + \delta \boldsymbol{p}_i^n\right), \\ &= \sum_{i=1}^{N} \sum_{j \neq i} \delta_{ij} E_{\text{kin}}^n, \end{aligned}$$

where we defined the pairwise symmetric energy variations

$$\delta_{ij}E^n_{\mathrm{kin}} = \frac{1}{2}\left(-\Gamma^n_{ij}\boldsymbol{v}^n_{ij}\Delta t + \Sigma^n_{ij}G^n_{ij}\sqrt{\Delta t}\right)\cdot\left(\boldsymbol{v}^n_{ij} + \frac{\delta\boldsymbol{p}^n_i}{2m_i} - \frac{\delta\boldsymbol{p}^n_j}{2m_j}\right).$$

We finally update the internal energies as

$$\varepsilon^{n+1}_i = \varepsilon^n_i - \sum_{j\neq i}\delta_{ij}E_{\mathrm{kin}} = \varepsilon^n_i + \sum_{j\neq i}\frac{1}{2}\left(\Gamma^n_{ij}\boldsymbol{v}^n_{ij}\Delta t - \Sigma^n_{ij}G^n_{ij}\sqrt{\Delta t}\right)\cdot\left(\boldsymbol{v}^n_{ij} + \frac{\delta\boldsymbol{p}^n_i}{2m_i} - \frac{\delta\boldsymbol{p}^n_j}{2m_j}\right), \tag{4.10}$$

to ensure the exact conservation of the total energy.

Gathering the updates in Equations (4.9) and (4.10), the overall SER integration of the fluctuation/dissipation dynamics read

$$\begin{cases} \boldsymbol{p}^{n+1}_i = \boldsymbol{p}^n_i + \displaystyle\sum_{j\neq i}\Gamma^n_{ij}\boldsymbol{v}^n_{ij}\Delta t + \Sigma^n_{ij}G^n_{ij}\sqrt{\Delta t}, \\ \varepsilon^{n+1}_i = \varepsilon^n_i + \displaystyle\sum_{j\neq i}\frac{1}{2}\left(\Gamma^n_{ij}\boldsymbol{v}^n_{ij}\Delta t - \Gamma^n_{ij}G^n_{ij}\sqrt{\Delta t}\right)\cdot\left(\boldsymbol{v}^n_{ij} + \frac{\delta\boldsymbol{p}^n_i}{2m_i} - \frac{\delta\boldsymbol{p}^n_j}{2m_j}\right). \end{cases} \tag{4.11}$$

The main advantage of this scheme is that it is far easier to parallelize than the SSA scheme given by Equation (4.6) since the pairs are not handled successively. A major requirement in the parallelization of the SER scheme is to draw the same random numbers for a given pair of particles belonging to different processors. This ensures that the same random force is computed if two interacting particles are handled by different processors while avoiding the communication cost. An example of pseudo-random generator that satisfies this property without additional communication is the SARU algorithm [2] that was introduced in the context of DPD.

4.2.2 Energy drift and stability with SER

We test the SER scheme with simulations using the ideal gas equation of state (see Equation (4.7)) with $K = 10$ initialized at $T = 1000$ K and $\rho = 1150$ kg.m^{-3} as specified in Section 4.1.3 for SSA. The system is first equilibrated during a time $\tau_{\mathrm{therm}} = 50$.

Despite its huge improvement in terms of parallelization, SER suffers from a poor stability. While SSA can use time steps up to $\Delta t = 0.3$ during a total time $\tau_s = 500$, negative internal energies may appear with SER for time steps as small as $\Delta t = 0.035$. In order to quantify the energy conservation, we perform simulations for several time steps during a total time $\tau_s = 500$. The energy trajectories are averaged over 10 realizations. Due to the stability issues previously discussed, the time steps used to evaluate the energy conservation with SER are small enough so that no significant drift are observed in SSA. The energy conservation is deteriorated when using SER compared to SSA and we still observe linear energy drifts. We plot in Figure 4.4 the drift rate $\alpha_{\Delta t,K}$ defined in Section 4.1.3 for the simulations integrated with SER.

The improvement of the stability and energy conservation of parallel schemes like SER is thus still a main challenge for the integration of stochastic dynamics like DPDE or SDPD. This is essential in order to carry efficiently and accurately large simulations and take profit of all the increase in time and length scales these mesoscopic methods can offer. It has been proposed in [79] to couple SSA and SER to integrate DPDE in parallel. In this scheme, SSA was used only for pairs of particles handled by the same processor while SER was applied to pairs shared by two

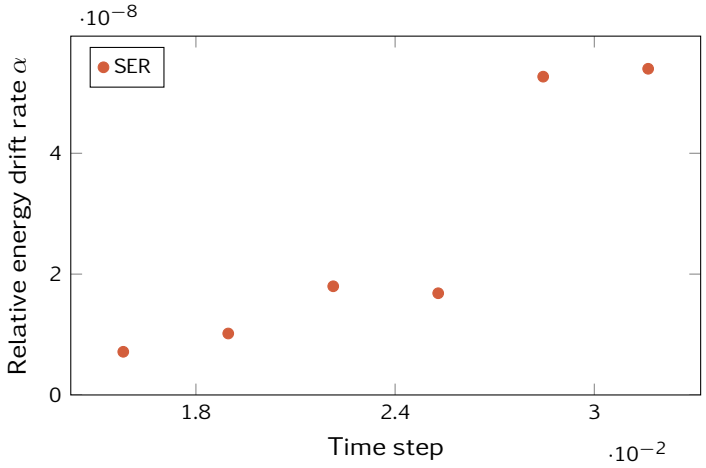


Figure 4.4 | Relative energy drift rate $\alpha_{\Delta t,10}$ as a function of the time step for the SER scheme.

processors. This allowed to increase the energy conservation compared to pure SER and provided an easier parallelization than pure SSA.

4.3 Metropolization of the numerical schemes

As seen in Section 4.1 and 4.2, the SSA and SER schemes are plagued with stability issues especially for small particles. These instabilities are related to internal energies becoming negative during the integration of the fluctuation/dissipation, requiring very small time steps to be used. To avoid them while keeping reasonable time steps, it has been proposed to use Monte Carlo principles sample the invariant measure of DPDE, by resampling the velocities along the lines of centers according to a Maxwell-Boltzmann distribution and redistributing the energy variation into internal energies according to some prescription [100]. This approach leads however to a dynamics which is not consistent with DPDE. It was proposed in [161] to correct discretization schemes for DPDE by rejecting unlikely or forbidden moves through a Metropolis procedure, which prevents the appearance of negative internal energies and improves the stability of the integration schemes. In the following, we show how this procedure can be used for SDPD. We first derive the expression of the Metropolis ratio in Section 4.3.1 In Section 4.3.2, we also proposed an approximated Metropolization where only moves leading to negative internal energies are rejected. This avoids the cumbersome calculation of the Metropolis ratio. Finally, we test the stability and energy conservation of the Metropolized scheme at equilibrium and for shock waves in Section 4.3.3.

4.3.1 Integration of the fluctuation/dissipation part with Metropolized schemes

As in Section 4.1, we reformulate the pairwise dynamics (2.13) in the relative velocity $\boldsymbol{v}_{ij}$ variable only. Furthermore, we show that it can be viewed as an overdamped Langevin dynamics. This allows us to construct proposed moves for the Metropolized scheme and compute the corresponding acceptance ratio.

Reformulation as an overdamped Langevin dynamics

In order to simplify the Metropolization of the integration scheme, we claim that the dynamics (4.4) formulated in the relative velocity can be written more explicitly as an overdamped Langevin dynamics under the form

$$\mathrm{d}\boldsymbol{v}_{ij} = \left(-\boldsymbol{M}(\boldsymbol{v}_{ij})\boldsymbol{\nabla}_{\boldsymbol{v}_{ij}}\mathscr{U}(\boldsymbol{v}_{ij}) + \mathrm{div}_{\boldsymbol{v}_{ij}}(\boldsymbol{M})(\boldsymbol{v}_{ij})\right)\mathrm{d}t + \sqrt{2}\boldsymbol{M}^{\frac{1}{2}}(\boldsymbol{v}_{ij})\mathrm{d}\boldsymbol{B}_{ij}, \tag{4.12}$$

with the diffusion matrix

$$\boldsymbol{M}(\boldsymbol{v}_{ij}) = \frac{2\left[\sigma^{\parallel}(\varepsilon_i,\varepsilon_j,\boldsymbol{q})\right]^2}{m_{ij}^2}\boldsymbol{P}_{ij}^{\parallel} + \frac{2\left[\sigma^{\perp}(\varepsilon_i,\varepsilon_j,\boldsymbol{q}))\right]^2}{m_{ij}^2}\boldsymbol{P}_{ij}^{\perp},$$

and the potential

$$\mathscr{U}(\boldsymbol{v}_{ij}) = U\left(\varepsilon_i^0 - \frac{m_{ij}}{8}\left([\boldsymbol{v}_{ij}]^2 - \left[\boldsymbol{v}_{ij}^0\right]^2\right),\boldsymbol{q}\right) + U\left(\varepsilon_j^0 - \frac{m_{ij}}{8}\left([\boldsymbol{v}_{ij}]^2 - \left[\boldsymbol{v}_{ij}^0\right]^2\right),\boldsymbol{q}\right),$$

where

$$U(\varepsilon_i,\boldsymbol{q}) = \log T_i(\varepsilon_i,\boldsymbol{q}) - \frac{1}{k_{\mathrm{B}}}S_i(\varepsilon_i,\boldsymbol{q}).$$

Let us emphasize that the reformulation (4.12) is the key element for the Metropolis stabilization. We now check that (4.12) holds. By definition

$$\boldsymbol{M}^{\frac{1}{2}}(\boldsymbol{v}_{ij}) = \frac{\sqrt{2}}{m_{ij}}\Sigma_{ij}.$$

It therefore suffices to check that

$$-\frac{2}{m_{ij}}\boldsymbol{\Gamma}_{ij}\boldsymbol{v}_{ij} = -\boldsymbol{M}(\boldsymbol{v}_{ij})\boldsymbol{\nabla}_{\boldsymbol{v}_{ij}}\mathscr{U}(\boldsymbol{v}_{ij}) + \mathrm{div}_{\boldsymbol{v}_{ij}}(\boldsymbol{M})(\boldsymbol{v}_{ij}).$$

We first compute the gradient of the potential $\mathscr{U}$ using the relations (2.9):

$$\begin{aligned}\boldsymbol{\nabla}_{\boldsymbol{v}_{ij}}\mathscr{U}(\boldsymbol{v}_{ij}) &= \left(\boldsymbol{\nabla}_{\boldsymbol{v}_{ij}}\varepsilon_i\right)\partial_\varepsilon U(\varepsilon_i,\boldsymbol{q}) + \left(\boldsymbol{\nabla}_{\boldsymbol{v}_{ij}}\varepsilon_j\right)\partial_\varepsilon U(\varepsilon_j,\boldsymbol{q})\\ &= -\frac{m_{ij}}{4}\boldsymbol{v}_{ij}\left(\frac{\partial_{\varepsilon_i}T_i}{T_i} - \frac{\partial_{\varepsilon_i}S_i}{k_{\mathrm{B}}} + \frac{\partial_{\varepsilon_j}T_j}{T_j} - \frac{\partial_{\varepsilon_j}S_j}{k_{\mathrm{B}}}\right)\\ &= -\frac{m_{ij}}{4}\boldsymbol{v}_{ij}\left(\frac{1}{T_i}\left[\frac{1}{C_i} - \frac{1}{k_{\mathrm{B}}}\right] + \frac{1}{T_j}\left[\frac{1}{C_j} - \frac{1}{k_{\mathrm{B}}}\right]\right).\end{aligned}$$

Upon application of the matrix $\boldsymbol{M}$,

$$\begin{aligned}\boldsymbol{M}(\boldsymbol{v}_{ij})\boldsymbol{\nabla}_{\boldsymbol{v}_{ij}}\mathscr{U}(\boldsymbol{v}_{ij}) &= -\frac{1}{2m_{ij}}\boldsymbol{v}_{ij}\sum_{\theta\in\{\parallel,\perp\}}\sigma^{\theta}(\varepsilon_i,\varepsilon_j,\boldsymbol{q})^2\left(\frac{1}{T_i}\left[\frac{1}{C_i} - \frac{1}{k_{\mathrm{B}}}\right] + \frac{1}{T_j}\left[\frac{1}{C_j} - \frac{1}{k_{\mathrm{B}}}\right]\right)\boldsymbol{P}_{ij}^{\theta}\boldsymbol{v}_{ij}\\ &= \frac{2}{m_{ij}}\boldsymbol{v}_{ij}\sum_{\theta\in\{\parallel,\perp\}}\kappa_{ij}^{\theta}\left(1 - \frac{k_{\mathrm{B}}}{T_i+T_j}\left(\frac{T_j}{C_i} + \frac{T_i}{C_j}\right)\right)\boldsymbol{P}_{ij}^{\theta}\boldsymbol{v}_{ij}.\end{aligned}$$

The divergence of $\boldsymbol{M}$ with respect to the relative velocity reads

$$\begin{aligned}\mathrm{div}_{\boldsymbol{v}_{ij}}(\boldsymbol{M})(\boldsymbol{v}_{ij}) &= \frac{2}{m_{ij}^2}\boldsymbol{P}_{ij}^{\parallel}\boldsymbol{\nabla}_{\boldsymbol{v}_{ij}}\left(\left[\sigma^{\parallel}(\varepsilon_i,\varepsilon_j,\boldsymbol{q})\right]^2\right)+\frac{2}{m_{ij}^2}\boldsymbol{P}_{ij}^{\perp}\boldsymbol{\nabla}_{\boldsymbol{v}_{ij}}\left(\left[\sigma^{\perp}(\varepsilon_i,\varepsilon_j,\boldsymbol{q})\right]^2\right)\\ &= -\frac{1}{2m_{ij}}\sum_{\theta\in\{\parallel,\perp\}}\left(\partial_{\varepsilon_i}+\partial_{\varepsilon_j}\right)\left(\left[\sigma^{\theta}(\varepsilon_i,\varepsilon_j,\boldsymbol{q})\right]^2\right)\boldsymbol{P}_{ij}^{\theta}\boldsymbol{v}_{ij}\\ &= -\frac{2}{m_{ij}}k_{\mathrm{B}}\sum_{\theta\in\{\parallel,\perp\}}\kappa_{ij}^{\theta}\left(\frac{T_j(\partial_{\varepsilon_i}T_i)}{T_i+T_j}-\frac{T_iT_j(\partial_{\varepsilon_i}T_i)}{(T_i+T_j)^2}+\frac{T_i(\partial_{\varepsilon_j}T_j)}{T_i+T_j}-\frac{T_iT_j(\partial_{\varepsilon_j}T_j)}{(T_i+T_j)^2}\right)\boldsymbol{P}_{ij}^{\theta}\boldsymbol{v}_{ij}.\end{aligned}$$

A final application of the thermodynamic relations (2.9) allows to simplify this expression as

$$\mathrm{div}_{\boldsymbol{v}_{ij}}(\boldsymbol{M})(\boldsymbol{v}_{ij}) = \frac{2}{m_{ij}}\sum_{\theta\in\{\parallel,\perp\}}\kappa_{ij}^{\theta}\left(d_{ij}-\frac{k_{\mathrm{B}}}{T_i+T_j}\left[\frac{T_j}{C_i}+\frac{T_i}{C_j}\right]\right)\boldsymbol{P}_{ij}^{\theta}\boldsymbol{v}_{ij}.$$

The desired result follows from

$$\begin{aligned}-\boldsymbol{M}(\boldsymbol{v}_{ij})\boldsymbol{\nabla}_{\boldsymbol{v}_{ij}}\mathscr{U}(\boldsymbol{v}_{ij})+\mathrm{div}_{\boldsymbol{v}_{ij}}(\boldsymbol{M})(\boldsymbol{v}_{ij}) &= -\frac{2}{m_{ij}}\left((1-d_{ij})\kappa_{ij}^{\parallel}\boldsymbol{P}_{ij}^{\parallel}+(1-d_{ij})\kappa_{ij}^{\perp}\boldsymbol{P}_{ij}^{\perp}\right)\boldsymbol{v}_{ij}\\ &= -\frac{2}{m_{ij}}\boldsymbol{\Gamma}_{ij}\boldsymbol{v}_{ij}.\end{aligned}$$

In view of (4.12), it can be immediately deduced that the measure (4.13) on the relative velocity, at fixed momenta $\boldsymbol{p}_i$, $\boldsymbol{p}_j$ and fixed internal energies ε_i, ε_j, is left invariant by the overdamped Langevin dynamics (4.4).

$$\nu(d\boldsymbol{v}_{ij}) = Z_{ij}^{-1}\exp\left(-\mathscr{U}(\boldsymbol{v}_{ij})\right)\mathrm{d}\boldsymbol{v}_{ij} = Z_{ij}^{-1}\frac{\exp\left(k_{\mathrm{B}}^{-1}\left[S_i\left(\varepsilon_i,\boldsymbol{q}\right)+S_j\left(\varepsilon_j,\boldsymbol{q}\right)\right]\right)}{T_i\left(\varepsilon_i,\boldsymbol{q}\right)T_j\left(\varepsilon_j,\boldsymbol{q}\right)}\mathrm{d}\boldsymbol{v}_{ij} \tag{4.13}$$

Metropolis ratio

We consider the SSA integration of the fluctuation/dissipation given by Equation (4.6) as the proposed move. In terms of the relative velocity, it reads

$$\begin{aligned}\boldsymbol{v}_{ij}^{n+1} &= \sum_{\theta\in\{\parallel,\perp\}}\alpha_{ij}^{\theta}(\varepsilon_i^n,\varepsilon_j^n,\boldsymbol{q}^n)\boldsymbol{P}_{ij}^{\theta}\boldsymbol{v}_{ij}^n+\zeta_{ij}^{\theta}(\varepsilon_i^n,\varepsilon_j^n,\boldsymbol{q}^n)\boldsymbol{P}_{ij}^{\theta}G^n\\ &= \boldsymbol{\mathscr{A}}(\boldsymbol{q}^n,\boldsymbol{v}_{ij}^n)\boldsymbol{v}_{ij}^n+\boldsymbol{\mathscr{B}}(\boldsymbol{q}^n,\boldsymbol{v}_{ij}^n)G_{ij}^n,\end{aligned} \tag{4.14}$$

with

$$\boldsymbol{\mathscr{A}}(\boldsymbol{q}^n,\boldsymbol{v}_{ij}^n) = \alpha_{ij}^{\parallel}(\varepsilon_i^n,\varepsilon_j^n,\boldsymbol{q}^n)\boldsymbol{P}_{ij}^{\parallel}+\alpha_{ij}^{\perp}(\varepsilon_i^n,\varepsilon_j^n,\boldsymbol{q}^n)\boldsymbol{P}_{ij}^{\perp},$$

and

$$\boldsymbol{\mathscr{B}}(\boldsymbol{q}^n,\boldsymbol{v}_{ij}^n) = \zeta_{ij}^{\parallel}(\varepsilon_i^n,\varepsilon_j^n,\boldsymbol{q}^n)\boldsymbol{P}_{ij}^{\parallel}+\zeta_{ij}^{\perp}(\varepsilon_i^n,\varepsilon_j^n,\boldsymbol{q}^n)\boldsymbol{P}_{ij}^{\perp},$$

The momenta and internal energies can then be updated as

$$\begin{cases} \boldsymbol{p}_i^{n+1} = \boldsymbol{p}_i^n + \dfrac{m_{ij}}{2}(\boldsymbol{v}_{ij}^{n+1} - \boldsymbol{v}_{ij}^n), \\ \boldsymbol{p}_j^{n+1} = \boldsymbol{p}_j^n - \dfrac{m_{ij}}{2}(\boldsymbol{v}_{ij}^{n+1} - \boldsymbol{v}_{ij}^n), \\ \varepsilon_i^{n+1} = \varepsilon_i^n - \dfrac{m_{ij}}{8}\left(\left[\boldsymbol{v}_{ij}^{n+1}\right]^2 - \left[\boldsymbol{v}_{ij}^n\right]^2\right), \\ \varepsilon_j^{n+1} = \varepsilon_j^n - \dfrac{m_{ij}}{8}\left(\left[\boldsymbol{v}_{ij}^{n+1}\right]^2 - \left[\boldsymbol{v}_{ij}^n\right]^2\right). \end{cases} \tag{4.15}$$

The internal energies T_i, T_j and heat capacities C_i, C_j are updated accordingly.

In order to decide whether we update the configuration with the proposed move or keep the current one, we first check whether ε_i^{n+1} and ε_j^{n+1} are negative, in which case the proposal is rejected. Otherwise, we compute a Metropolis ratio that is an acceptance probability. The probability to accept the proposed move from $\boldsymbol{v}$ to $\boldsymbol{v}'$ is $\min(1, A_{\Delta t}(\boldsymbol{v}, \boldsymbol{v}'))$ with

$$A_{\Delta t}(\boldsymbol{v}, \boldsymbol{v}') = \frac{\nu(\boldsymbol{v}')T_{\Delta t}(\boldsymbol{v}', \boldsymbol{v})}{\nu(\boldsymbol{v})T_{\Delta t}(\boldsymbol{v}, \boldsymbol{v}')},$$

where $T_{\Delta t}$ is the transition kernel associated with the proposal. In the following, we omit all the dependence on the positions $\boldsymbol{q}^n$, which remain constant in this subdynamics, to simplify the notation.

The probability that (4.14) proposes $\boldsymbol{v}'$ starting from $\boldsymbol{v}$ is given by

$$T_{\Delta t}(\boldsymbol{v}, \boldsymbol{v}') = \frac{1}{(2\pi)^{\frac{3}{2}}\,|\mathscr{B}(\boldsymbol{v})|} \exp\left(-\frac{1}{2}(\boldsymbol{v}' - \mathscr{A}(\boldsymbol{v})\boldsymbol{v})^T \mathscr{B}(\boldsymbol{v})^{-2}(\boldsymbol{v}' - \mathscr{A}(\boldsymbol{v})\boldsymbol{v})\right),$$

with the inverse matrix $\mathscr{B}(\boldsymbol{v})^{-1} = \dfrac{m_{ij}}{2\zeta_{ij}^{\parallel}(\boldsymbol{v})}\boldsymbol{P}_{ij}^{\parallel} + \dfrac{m_{ij}}{2\zeta_{ij}^{\perp}(\boldsymbol{v})}\boldsymbol{P}_{ij}^{\perp}$ and the determinant $|\mathscr{B}(\boldsymbol{v})| = \dfrac{8}{m_{ij}^3}\zeta_{ij}^{\parallel}(\boldsymbol{v})\zeta_{ij}^{\perp}(\boldsymbol{v})^2$. For the direct move, the transition probability simply reads

$$T_{\Delta t}(\boldsymbol{v}_{ij}^n, \boldsymbol{v}_{ij}^{n+1}) = \frac{1}{(2\pi)^{\frac{3}{2}}\left|\mathscr{B}(\boldsymbol{v}_{ij}^n)\right|} \exp\left(-\frac{(G^n)^T G^n}{2}\right),$$

while, for the reverse move,

$$T_{\Delta t}(\boldsymbol{v}_{ij}^{n+1}, \boldsymbol{v}_{ij}^n) = \frac{\exp\left(-\frac{1}{2}(\boldsymbol{v}_{ij}^n - \mathscr{A}(\boldsymbol{v}_{ij}^{n+1})\boldsymbol{v}_{ij}^{n+1})^T \mathscr{B}(\boldsymbol{v}_{ij}^{n+1})^{-2}(\boldsymbol{v}_{ij}^n - \mathscr{A}(\boldsymbol{v}_{ij}^{n+1})\boldsymbol{v}_{ij}^{n+1})\right)}{(2\pi)^{\frac{3}{2}}\left|\mathscr{B}(\boldsymbol{v}_{ij}^{n+1})\right|}.$$

Using (4.13) with the reference taken at iteration n,

$$\begin{aligned} \log\left(\frac{\nu(\boldsymbol{v}_{ij}^{n+1})}{\nu(\boldsymbol{v}_{ij}^n)}\right) = \sum_{k\in\{i,j\}} \frac{1}{k_{\mathrm{B}}}\left[S_k\left(\varepsilon_k^n - \frac{m_{ij}}{8}\left(\left[\boldsymbol{v}_{ij}^{n+1}\right]^2 - \left[\boldsymbol{v}_{ij}^n\right]^2\right)\right) - S_k(\varepsilon_k^n)\right] \\ - \log\left[T_k\left(\varepsilon_k^n - \frac{m_{ij}}{8}\left(\left[\boldsymbol{v}_{ij}^{n+1}\right]^2 - \left[\boldsymbol{v}_{ij}^n\right]^2\right)\right)\right] + \log[T_k(\varepsilon_k^n)]. \end{aligned}$$

Finally, the acceptance ratio is given by

$$A_{\Delta t}(\boldsymbol{v}_{ij}^n, \boldsymbol{v}_{ij}^{n+1}) = \exp(a(\boldsymbol{v}_{ij}^n, \boldsymbol{v}_{ij}^{n+1})), \tag{4.16}$$

with

$$\begin{aligned} a(\boldsymbol{v}_{ij}^n, \boldsymbol{v}_{ij}^{n+1}) &= -\log\left(T_{\Delta t}(\boldsymbol{v}_{ij}^n, \boldsymbol{v}_{ij}^{n+1})\right) + \log\left(T_{\Delta t}(\boldsymbol{v}_{ij}^{n+1}, \boldsymbol{v}_{ij}^n)\right) + \log\left(\frac{\nu(\boldsymbol{v}_{ij}^{n+1})}{\nu(\boldsymbol{v}_{ij}^n)}\right) \\ &= \frac{(G^n)^T G^n}{2} + \log\left|\mathscr{B}(\boldsymbol{v}_{ij}^n)\right| - \log\left|\mathscr{B}(\boldsymbol{v}_{ij}^{n+1})\right| \\ &\quad - \frac{1}{2}(\boldsymbol{v}_{ij}^n - \mathscr{A}(\boldsymbol{v}_{ij}^{n+1})\boldsymbol{v}_{ij}^{n+1})^T \mathscr{B}(\boldsymbol{v}_{ij}^{n+1})^{-2}(\boldsymbol{v}_{ij}^n - \mathscr{A}(\boldsymbol{v}_{ij}^{n+1})\boldsymbol{v}_{ij}^{n+1}) \\ &\quad + \frac{1}{k_B}\left(S_i(\varepsilon_i^{n+1}) - S_i(\varepsilon_i^n) + S_j(\varepsilon_j^{n+1}) - S_j(\varepsilon_j^n)\right) \\ &\quad - \log\left(T_i(\varepsilon_i^{n+1})\right) + \log(T_i(\varepsilon_i^n)) - \log\left(T_j(\varepsilon_j^{n+1})\right) + \log(T_j(\varepsilon_j^n)). \end{aligned}$$

Starting from a configuration $(\boldsymbol{p}_i^n, \boldsymbol{p}_j^n, \varepsilon_i^n, \varepsilon_j^n)$, the overall algorithm (Exact Metropolis Scheme or EMS) to integrate the fluctuation/dissipation for a pair (i, j) of particle is organized as follows:

1. Compute a proposed move for $\boldsymbol{v}_{ij}^{n+1}$ with (4.14).

2. If the following energy bound does not hold

$$\min\left(\varepsilon_i^n, \varepsilon_j^n\right) > \frac{m_{ij}}{8}\left([\boldsymbol{v}_{ij}^{n+1}]^2 - [\boldsymbol{v}_{ij}^n]^2\right), \tag{4.17}$$

   the move is rejected: $(\boldsymbol{p}_i^{n+1}, \boldsymbol{p}_j^{n+1}, \varepsilon_i^{n+1}, \varepsilon_j^{n+1}) = (\boldsymbol{p}_i^n, \boldsymbol{p}_j^n, \varepsilon_i^n, \varepsilon_j^n)$.
   If the bound is satisfied, the algorithm continues.

3. Compute the acceptance ratio with (4.16).

4. Draw $U_{ij}^n \sim \mathscr{U}[0, 1]$ and compare it with $A_{\Delta t}(\boldsymbol{v}_{ij}^n, \boldsymbol{v}_{ij}^{n+1})$. If $U_{ij}^n > A_{\Delta t}(\boldsymbol{v}_{ij}^n, \boldsymbol{v}_{ij}^{n+1})$, the move is rejected and $(\boldsymbol{p}_i^{n+1}, \boldsymbol{p}_j^{n+1}, \varepsilon_i^{n+1}, \varepsilon_j^{n+1}) = (\boldsymbol{p}_i^n, \boldsymbol{p}_j^n, \varepsilon_i^n, \varepsilon_j^n)$.
   Otherwise it is accepted and the momenta and internal energies are updated with (4.15), along with the internal temperatures T_i, T_j and heat capacities C_i, C_j.

4.3.2 Approximate Metropolized scheme

Since the computation of the Metropolis ratio may be cumbersome in practical simulations, we propose a simplified and approximate scheme where we only reject moves that cause internal energies to become negative. It avoids the need to actually compute the Metropolis acceptance ratio.

As for the complete Metropolized scheme, we use the expression (4.14) as the proposed evolution for the relative velocities. We then check whether the updated internal energies remain positive and reject the moves that do not satisfy this property. The current configuration at time is then used as the new configuration and counted as usual in the averages. Otherwise the move is accepted and the velocities and internal energies, along with the internal temperatures and heat capacities, are updated accordingly. When no stability issues, *i.e.* negative internal energies, appear, the Approximate Metropolis Scheme (AMS) is equivalent to SSA.

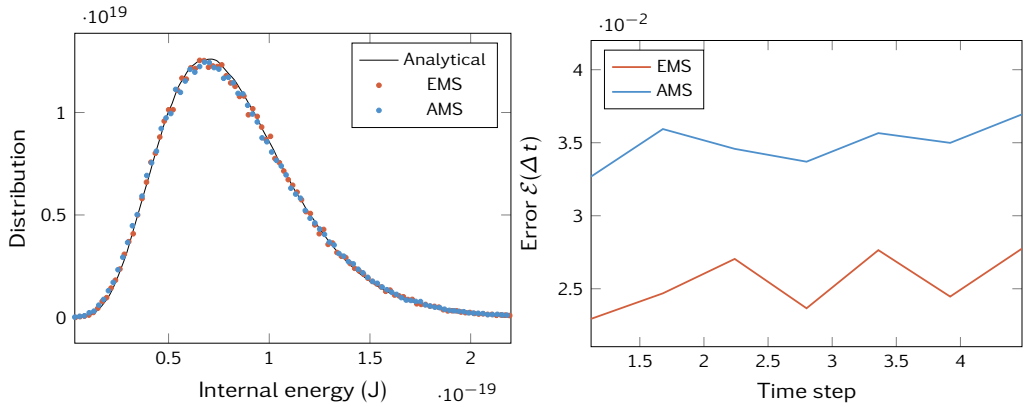
4.3.3 Stability and energy conservation with the Metropolized schemes

We assess the properties of both the exact and approximate Metropolized schemes below. We first consider only the integration of the fluctuation/dissipation part and compare the bias in the equilibrium distributions. The rejection ratio for EMS and AMS are also analyzed. We then turn to the full dynamics, with the conservative and fluctuation/dissipation part. We study the energy conservation and introduce a multiple time step strategy to take profit of the increased stability. Lastly we demonstrate the ability of the Metropolized schemes to handle non-equilibrium situations with a shock wave simulation.

Integrating the fluctuation/dissipation dynamics

We first investigate the properties of the integration schemes for the fluctuation/dissipation part only and do not couple SSA and the Metropolized schemes with Velocity Verlet. While SSA is quite stable for large particles ($K > 10$) for which time steps as large as $\Delta t = 5$ can be used with no occurrence of a negative internal energy during a simulation time τ_{sim}, stability issues arise for smaller particles. At $K = 5$, we need a time step $\Delta t < 0.025$ to avoid the appearance of negative internal energies with SSA. As a comparison, the stability limit for the Verlet scheme at $K = 5$ is $\Delta t = 0.8$. As the particle size decreases further, it becomes impossible to run simulations and no admissible time step has been found for $K = 2$. With the rejection of moves provoking negative energies, the Metropolized schemes are stable at any time step for every particle sizes.

When they are not coupled to Velocity Verlet, the SSA and Metropolized schemes preserve exactly the energy by construction. We can however compare the bias in the distributions of internal energies for the different schemes. Figure 4.5 shows the distributions of internal energy for the exact and approximate Metropolized scheme using the ideal gas equation of state (4.7) with $K = 5$ obtained with a simulation time $\tau_{\text{sim}} = 20000$, compared with the analytic distribution (4.8). In practice, the distributions $\nu_{\Delta t}$ obtained from the numerical simulations are approximated using histograms computed on 50 configurations extracted at regular time intervals from the simulations. This ensures a constant number of sampling points for all time steps. The histograms consist in $N_{\text{bins}} = 150$ bins uniformly distributed between $\varepsilon_{\min} = 0.1 k_{\text{B}} T$ and $\varepsilon_{\max} = 20 k_{\text{B}} T$. A



(a) Distributions at $\Delta t = 1$.

(b) Bias with respect to the time step

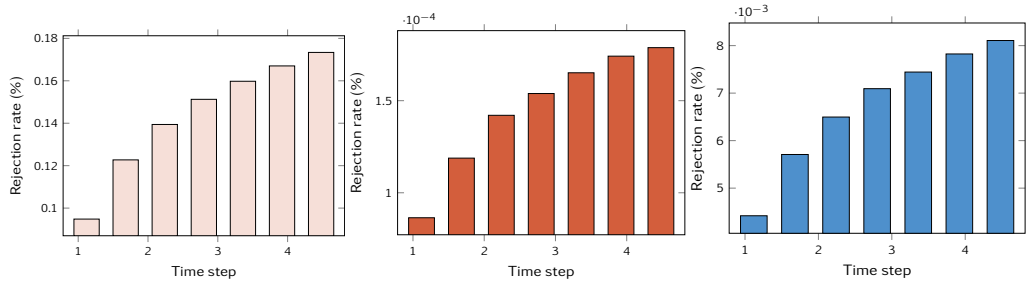
Figure 4.5 | Comparisons of the internal energy distributions with the ideal gas equation of state for the exact (EMS) and approximate (AMS) Metropolized algorithms: for $\Delta t = 1$ in (a) and with the error (4.18) with respect to the time step in (b).

more quantitative measurement of the bias is to evaluate the quadratic error with respect to the theoretical distribution

$$\mathscr{E}(\Delta t) = \sqrt{\frac{\int_0^{+\infty} \left[\nu_{\Delta t}(\varepsilon) - \overline{\mu}_{\beta,\varepsilon}(\varepsilon)\right]^2 \, \mathrm{d}\varepsilon}{\int_0^{+\infty} \overline{\mu}_{\beta,\varepsilon}(\varepsilon)^2 \, \mathrm{d}\varepsilon}}, \tag{4.18}$$

Due to the Metropolis procedure, the only source of error for EMS is of statistical nature. This is not guaranteed for AMS but no systematic bias is apparent up to $\Delta t = 5$, with errors of the same order as the exact Metropolization.

We also observe the scaling of the rejection rate with the time step in Figure 4.6. The Metropolized scheme displays rejection rates between 0.1% and 0.2% for time steps between $\Delta t = 1$ and $\Delta t = 5$. For our system size (1000 particles), it means that in average several fluctuation/dissipation interactions are rejected each time step. Most of these rejections are due to the Metropolis ratio and not to the appearance of negative internal energies which accounts for approximately one rejection every thousand pairs. When we only reject forbidden moves that would cause negative energies, the rejection rate of this approximate Metropolization is between 0.005% and 0.01%, which is about 20 times smaller than the overall rejection rate of the exact Metropolization. This is however two orders of magnitude larger than the occurrence of negative internal energies with the exact Metropolis scheme. By rejecting authorized but unlikely moves (leading to small energies for instance), EMS is less prompt to the appearance of negative internal energies. A linear fit in log scale shows that the total rejection rate for both the exact and approximate Metropolization scales as $\Delta t^{0.42}$. The rejection of negative energies with the exact Metropolis schemes roughly follows the same scaling with $\Delta t^{0.5}$.



(a) EMS (Total) **(b)** EMS (Negative energies) **(c)** AMS

Figure 4.6 | Rejection rates for (a) the exact Metropolization and (c) the approximate Metropolization. The rejection rate due to negative internal energies in the exact Metropolis scheme is also displayed in (b).

Integrating the full SDPD

We now turn to the numerical integration of the full dynamics and study the behavior of the full schemes coupling the Velocity Verlet scheme for the integration of the conservative part of the dynamics and either SSA or its Metropolized versions for the fluctuation/dissipation dynamics.

To evaluate the energy conservation and the scheme stability, we run $n_{\mathrm{sim}} = 10$ independent simulations with $K = 5$ during a time $\tau_{\mathrm{sim}} = 1000$ for each time step Δt and average the results. The schemes obtained by superimposing (4.1) and either SSA or the Metropolized scheme lead to linear energy drifts which have already been observed in DPDE [125, 79] and in Section 4.1 for

SDPD. This is illustrated in Figure 4.7 where the total energy with respect to time is displayed for different time steps in the case of the Metropolized scheme. We characterize the energy drift

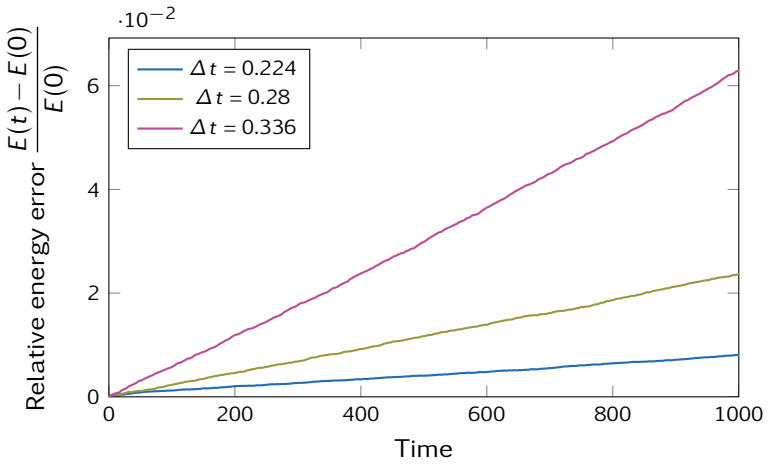


Figure 4.7 | Time evolution of the total energy with the Metropolized algorithm for different time steps. A linear drift in the energy is observed as is usual with such methods.

by fitting the time evolution of the energy on a linear function and plot the resulting slope in Figure 4.8 for SSA, Metropolis and its approximate version. We observe a similar energy drift for

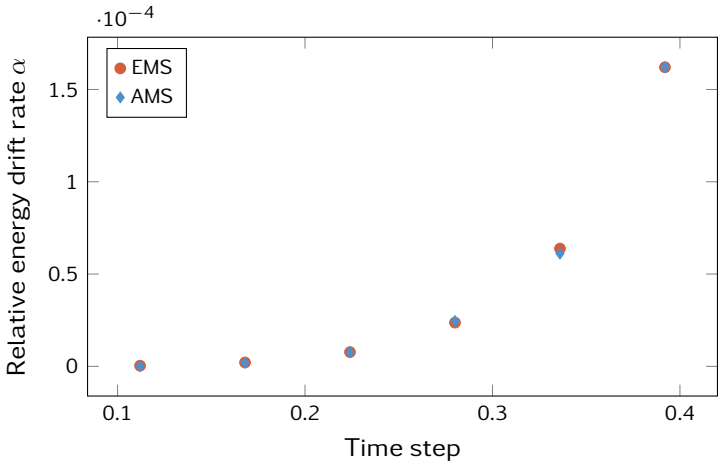


Figure 4.8 | Relative energy drift rate $\alpha_{\Delta t,5}$ with respect to the time step for the two Metropolized schemes (EMS and AMS).

all methods. As in the integration of the fluctuation/dissipation only, SSA is limited to small time steps to prevent stability issues to arise while the Metropolized schemes greatly increases the admissible time steps. However, the stable time steps are much smaller with the full dynamics than those reported in Section 4.3.3. Although the conservative interactions are bounded in SDPD unlike the DPDE simulations in [161], they still induce a stringent stability limit on the time steps. This observation leads us to consider multiple time step implementations (MTS) where the fluctuation/dissipation is integrated with a larger time step. We introduce an integer θ along with the time steps Δt_{VV} used to integrate the conservative part with the Velocity-Verlet scheme and $\Delta t_{\mathrm{FD}} = \theta \Delta t_{\mathrm{VV}}$ used for the discretization of the fluctuation/dissipation with a Metropolized scheme (EMS or AMS). We test this approach with $\theta = 5$ and $\theta = 10$. The algorithm then reads:

1. θ consecutive steps of Velocity Verlet with $\Delta t = \Delta t_{\mathrm{VV}}$.
2. One step of EMS or AMS with $\Delta t = \theta \Delta t_{\mathrm{VV}}$.

We plot in Figure 4.9 the slope of the energy drift compared to their single time step (STS) version (with a time step $\Delta t = \Delta t_{\mathrm{VV}}$). For both the exact and the approximate Metropolization, the energy drift rate is smaller for the multiple time step approach when the time step is large enough. Moreover, the reduction of the energy drift is enhanced for larger θ with a division by 6 of the rate for $\theta = 10$ and $\Delta t = 0.392$ when it is only halved for $\theta = 5$.

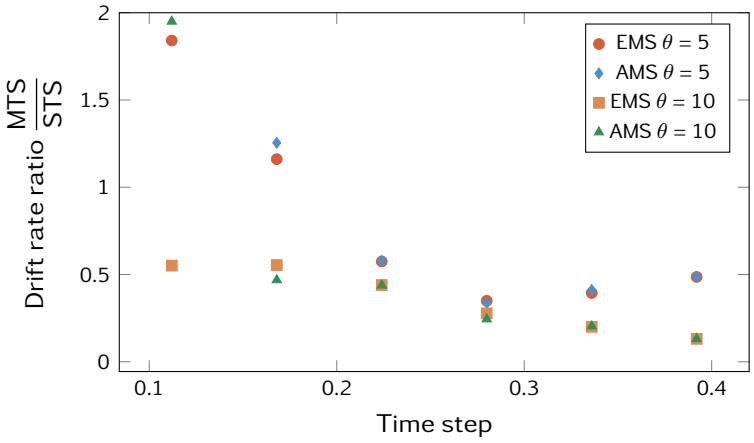


Figure 4.9 | Ratio between the slope of the energy drift for the multiple time steps Metropolized schemes (EMS and AMS) and their STS versions (with $\Delta t = \Delta t_{\mathrm{VV}}$).

Scheme	Time (μs/iter/part)
Verlet	37.66
SSA	49.48
EMS	63.39
AMS	51.07
EMS with MTS	43.57
AMS with MTS	40.92

Table 4.1 | Comparison of the computation time per iteration per particle for the Shardlow-like algorithm and the Metropolis schemes. For the multiple time step implementations, the time steps ratio is set to $\theta = 5$. The time for Velocity Verlet only is given as a reference.

We measure the time per iteration and per particle for the different Metropolis schemes with $\Delta t = 2.24 \times 10^{-2}$ or $\Delta t_{\mathrm{VV}} = 2.24 \times 10^{-2}$ and gather them in Table 4.1 For the multiple time step algorithms, the number of iteration is the number of Verlet steps (which is thus the same than in the STS case). The integration of the fluctuation/dissipation dynamics with SSA represent a fourth of the total computational time. The integration of the fluctuation/dissipation part with the exact Metropolization is about twice as long since we need to compute the reverse move and estimate the Metropolis ratio. This results in an overall increase by 30% of the total simulation time. However, much larger time steps can be chosen with EMS while SSA suffers from stringent stability limitations. There is almost no overhead when resorting to the approximate

Metropolization which also greatly improves the stability and is as good as EMS in terms of energy conservation. With the multiple time step strategy, the time needed for the fluctuation/dissipation is greatly reduced, as expected, by a factor θ. This ultimately results in integration schemes that are faster than SSA that cannot profit from the MTS acceleration due to its stability issues.

Simulation of non-equilibrium systems

While all the previous simulations were carried in an equilibrium situation, the Metropolized schemes we propose are also suited for non-equilibrium. As an example we test them in a shock wave simulation. The system is initialized as previously mentioned but with $N = 23400$ particles organized on $10 \times 10 \times 234$ lattice with periodic boundary conditions in the x- and y-directions. In the z-direction, two walls are located at each end of the system and formed of 3 layers "virtual" SDPD particles, using the same ideas as Bian *et al.* [14]. The positions and momenta of the virtual particles are not updated with the dynamics but are kept fixed within the walls. These virtual particles enable us to evaluate the density of the SDPD particles in the neighborhood of the walls, as well as the conservative forces (2.12) acting on the actual particles. In order to ensure that walls are not permeable, these particles induce a repulsive force deriving from a truncated Lennard-Jones potential:

$$\mathscr{U}_{\mathrm{LJ,rep}}(r) = 4\varepsilon_{\mathrm{rLJ}}\left[\left(\frac{\sigma_{\mathrm{rLJ}}}{r}\right)^{12} - \left(\frac{\sigma_{\mathrm{rLJ}}}{r}\right)^{6} + \frac{1}{4}\right] 1_{r \leq 2^{\frac{1}{6}}\sigma_{\mathrm{rLJ}}}.$$

We set $\varepsilon_{\mathrm{rLJ}} = 1$ and $\sigma_{\mathrm{rLJ}} = 1$ in the reduced units (2.20). After the system equilibration during $\tau_{\mathrm{therm}} = 50$, the lower wall is given a constant velocity $v_{\mathrm{P}} = 1661$ m.s^{-1} in the z-direction.

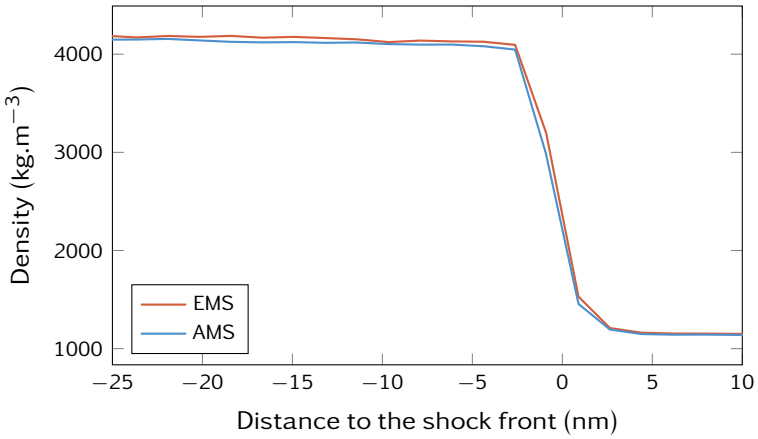


Figure 4.10 | Density profile in the reference frame of the shock front for the exact and approximate Metropolization.

In order to avoid the effects due to the presence of the walls, we only consider the information arising from particles located at a distance larger than 10σ from a wall. Making use of the stationarity of shock waves in the reference frame of the shock front, it is possible to average profiles over time. We split the simulation box into a number of slices $n_{\mathrm{sl}} = 100$ regularly distributed along the z-axis and compute average quantities in the slices. We determine the position of the shock front at every step as the point where the mean particles velocity along the z-axis is the closest to the velocity $\frac{v_P}{2}$. The various profiles are then averaged by setting the position of the shock front as the reference frame ($z = 0$).

We plot in Figure 4.10 the density profile for the Metropolized schemes (EMS and AMS) with $\Delta t = 0.045$. This choice is governed by the piston velocity v_{P} and ensures than the piston does not move by more than 20% of the characteristic distance between two particles. This avoids instabilities in the conservative part of the dynamics. The Rankine-Hugoniot relations make use of the conservation of mass, momentum and energy to predict the thermodynamic properties in the shocked state from the initial thermodynamic conditions and the velocity of the particles in the shocked region. This is explained in more details in Section 6.1. The properties estimated from the SDPD simulations, namely the velocity of the shock wave v_S, the density ρ_s, pressure P_s and temperature T_S in the shocked state, all agree very well with the theoretical predictions as can be seen in Table 4.2. Let us point out that this simulation would not have been possible with SSA

Scheme	v_S (km.s^{-1})	ρ_S (kg.m^{-3})	P_S (GPa)	T_S (K)
EMS	2254	4173	4.50	7816
AMS	2268	4151	4.49	7836
RH	2314	4075	4.58	8244

Table 4.2 | Average observables in the shocked state: SDPD compared to the Rankine-Hugoniot (RH) predictions.

since negative internal energies appear very early in the simulation even for time steps as small as $\Delta t = 10^{-4}$. The Metropolization procedure can thus be particularly useful in non-equilibrium simulations where stability issues are aggravated.

Since they are based on SSA, the Metropolized schemes presented here still suffer from a difficult parallelization. This is particularly problematic to study physical problems that require to simulate large systems. The adaptation of such a stabilization procedure to parallel schemes such as SER would prove a huge improvement in the integration of stochastic dynamics like DPDE or SDPD.

5 A MUTLIPLE RESOLUTION METHOD

One of the main advantages of SDPD is the ability to select the resolution at which the system is described while including consistent thermal fluctuations. This makes it a precious tool to check whether results from microscopic simulations may be extrapolated to larger time and length scales and to validate the scaling laws usually applied in this context. In Section 5.1, we first check that the physical properties computed with SDPD do not depend on the resolution and remain consistent with the atomistic description, prescribed through the equation of state, for a wide range of particle sizes. This size consistency along with the natural ability of the SDPD equations of motion (see Equation (2.18)) to handle multiple masses makes it very appealing to couple different resolutions within the same simulation. This could provide a way to increase the accuracy in specific regions (*e.g.* near the shock front) while avoiding a large overhead. We explore in Section 5.2 a possible concurrent coupling for SDPD at two different resolutions.

5.1 Size consistency for SDPD

In this section, we study how the properties predicted by SDPD are influenced by the choice of the resolution, namely the size of the particles. We first study the size consistency of SDPD at equilibrium for both the ideal gas equation of state (4.7) (see Section 5.1.1) and an equation of state optimized for a Lennard-Jones fluid [90] (see Section 5.1.2). We then consider non-equilibrium situations with the simulation of shock waves in Section 5.1.3.

5.1.1 Ideal gas

We first study a SDPD system with the ideal gas equation of state (4.7) at different masses $m_K = Km_0$ with $m_0 = 10^{-25}$ kg. We run simulations of a system of $N = 1000$ particles initialized according to the method described in Section 4.1.3 at density $\rho = 1150$ kg.m^{-3} and temperature $T = 1000$ K. The number of iterations is fixed to $N_{\text{it}} = 5 \times 10^5$. The timestep is chosen for each K such that the drift in relative energy is less than 0.5% after N_{it} iterations, which gives $\Delta t = 0.13$ for $K = 10$ in reduced units.

Under the invariant measure (2.31), the momenta are distributed according to a normal distribution with mean 0 and variance $K\dfrac{m_0}{\beta}$ (so that the variance of the velocities scale as $\dfrac{1}{K}$), which is well recovered in our simulations. We recall the marginal law for the internal energy for

the ideal gas equation of state, stated in Equation (4.8), is given by

$$\overline{\mu}_{\beta,\varepsilon}(\mathrm{d}\varepsilon) = \frac{\beta^{\frac{C_K}{k_\mathrm{B}}}}{\Gamma\left(\frac{C_K}{k_\mathrm{B}}\right)} \varepsilon^{\frac{C_K}{k_\mathrm{B}}-1} \exp\left(-\beta\varepsilon\right)\, \mathrm{d}\varepsilon,$$

where $C_K = \frac{3}{2}(K-1)k_\mathrm{B}$ is the heat capacity in the equation of state (4.7) and Γ is the Gamma function. We check that we recover this distribution in our simulations for $K = 5$, $K = 10$ and $K = 50$ in Figure 5.1.

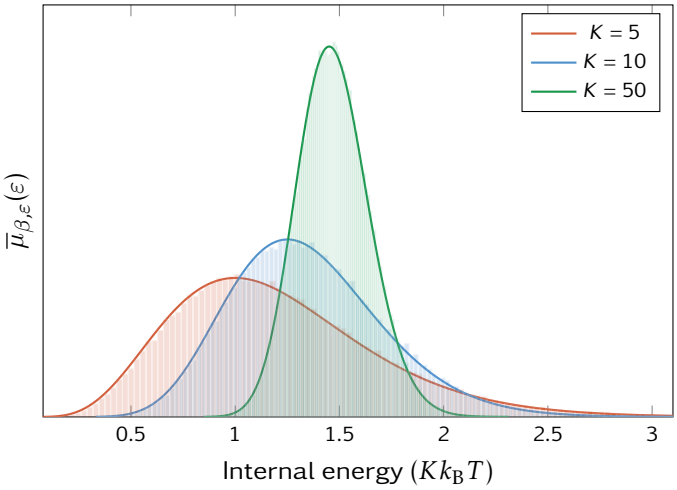


Figure 5.1 | Internal energy distribution for the ideal gas rescaled by the size K of the particles. The simulation results (histograms) are compared to analytic distributions (solid line).

We next study the evolution of the average pressure and temperature with respect to the particle size for the Lucy kernel (1.14) and the cubic kernel (1.15). The pressure is estimated according to Equation (2.37). There are two temperature estimators: the kinetic temperature (2.32) and the internal temperature (2.34). We compare the simulation results to the values given by the equation of state (4.7). Small biases (around 0.1%) are observed for small particle sizes but, as predicted by Equations (2.32) and (2.34), the kinetic and internal temperatures are in excellent agreement with the equation of state as soon as $K \geq 100$. There is no theoretical result predicting a perfect agreement of the pressure obtained by SDPD with the equation of state. However, the results obtained from SDPD simulations with both the Lucy kernel and the cubic kernel match the pressure from the equation of state with a maximum of 5% difference for sizes varying from $K = 5$ to $K = 25000$. The thermodynamic limit for pressure is reached for sizes $K \geq 1000$. Let us however mention that we observe some metastability issues at large masses for the Lucy kernel due to particle clumping [133, 164, 149]. This leads us to prefer the cubic kernel in future computations.

5.1.2 Lennard-Jones fluid

We discuss in this section the size consistency of properties estimated for a more realistic fluid of Lennard-Jones type. In a fully atomistic model, particles interactions can be modeled by a

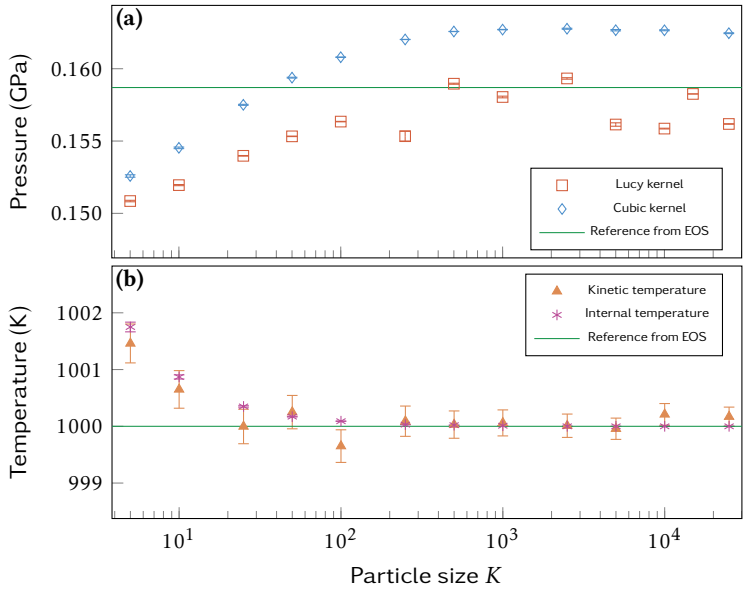


Figure 5.2 | Numerical estimation of (a) the equilibrium pressure, and (b) the kinetic and internal temperatures as a function of the size K of the SDPD particles (displayed with a logarithmic scale) for the ideal gas equation of state. Error bars are computed by integrating in time the autocorrelation as discussed in [109].

pairwise potential of Lennard-Jones type introduced in Equation (1.1) and recalled here:

$$\mathscr{U}_{\mathrm{LJ}}(r) = 4\varepsilon_{\mathrm{LJ}}\left[\left(\frac{\sigma_{\mathrm{LJ}}}{r}\right)^{12} - \left(\frac{\sigma_{\mathrm{LJ}}}{r}\right)^{6}\right].$$

We use the standard parameters for Argon ($\sigma_{\mathrm{LJ}} = 3.405 \times 10^{-10}$ m, $\varepsilon_{\mathrm{LJ}} = 1.657 \times 10^{-21}$ J, $m_0 = 6.64 \times 10^{-25}$ kg). For SDPD, we use the equation of state for Lennard-Jones fluids presented in [90]. It is based on microscopic simulations carried out with MD in the NVT ensemble. The Helmholtz free energy $\mathscr{F}(\rho, T)$ is fitted as a function of density and temperature on a modified form of the Benedict-Webb-Rubin equation of state [87], with 33 parameters. The useful quantities for SDPD, like the internal energy $\mathscr{E}(\rho, T)$, the entropy $\mathscr{S}(\rho, T)$, the pressure $\mathscr{P}(\rho, T)$ and the heat capacity $\mathscr{C}(\rho, T)$, are then deduced from the free energy as

$$\begin{aligned}
\mathscr{E}(\rho, T) &= -T^2 \partial_T \left(\frac{\mathscr{F}(\rho, T)}{T}\right), \\
\mathscr{S}(\rho, T) &= \frac{\mathscr{E}(\rho, T) - \mathscr{F}(\rho, T)}{T}, \\
\mathscr{P}(\rho, T) &= \rho^2 \partial_\rho \mathscr{F}(\rho, T), \\
\mathscr{C}(\rho, T) &= \partial_T \mathscr{E}(\rho, T).
\end{aligned}$$

Since we use the internal energy as our primary variable, we perform a Newton inversion algorithm to find the temperature corresponding to a given internal energy ε_i and density ρ_i whenever we need to compute the associated pressure or temperature. Denoting the temperature at iteration k by T_i^k, we initialize the algorithm with $T_i^0 = T_\beta$, with T_β the thermodynamic temperature, and iterate until the relative residual

$$\frac{\mathscr{E}(\rho_i, T_i^k) - \varepsilon_i}{\varepsilon_i}$$

	Expected value $\mathfrak{m}_K$	Variance $\mathfrak{s}_K$
Energy	$1.266 - \dfrac{0.088}{K} + \dfrac{0.394}{K^2}$	$1.81K^{-1.008}$
Density	$1116 + \dfrac{187}{K} - \dfrac{167}{K^2}$	$2.5 \times 10^4 K^{-0.924}$
Pressure	$0.649 + \dfrac{0.178}{K} + \dfrac{0.612}{K^2}$	$0.114K^{-1.004}$

Table 5.1 | Scaling of the expected values and variances for internal energy, density and pressure with respect to the particle size K.

decreases below a threshold $\kappa_{\text{tol}} = 10^{-9}$. Usually only a few iterations are required for convergence.

The functional form of the equation of state [90] diverges for small temperatures. Since a few particles can, at few occasions, reach this small temperature domain due to fluctuations, we continuously extend the equation of state for $T < T_{\text{low}}$ by choosing the heat capacity to be independent of temperature, *i.e.*:

$$\mathscr{C}(\rho, T) = \mathscr{C}(\rho, T_{\text{low}}), \text{ if } T < T_{\text{low}}.$$

We then write the energy and entropy in the regime $T < T_{\text{low}}$ as

$$\begin{aligned}\mathscr{E}(\rho, T) &= \mathscr{C}(\rho, T_{\text{low}})(T - T_{\text{low}}) + \mathscr{E}(\rho, T_{\text{low}}) \\ \mathscr{S}(\rho, T) &= \mathscr{C}(\rho, T_{\text{low}}) \log\left(\frac{T}{T_{\text{low}}}\right) + \mathscr{S}(\rho, T_{\text{low}}).\end{aligned}$$

This enhances the stability of our simulations. We set in practice $T_{\text{low}} = 100$ K.

We run simulations for systems of $N = 1000$ particles initialized at temperature $T = 1000$ K and density $\rho = 1150$ kg.m^{-3} as in Section 4.1.3. We use the cubic kernel and the reduced units defined in Section 2.3. The number of iterations is fixed to $N_{\text{it}} = 5 \times 10^5$. The timestep is chosen for each K such that the drift in energy is less than 0.5% after N_{it} iterations, which gives $\Delta t = 0.03$ for $K = 10$ in reduced units.

We plot the distributions of normalized internal energies $\dfrac{\varepsilon_i}{K}$, densities ρ_i and pressures P_i for several masses (see Figure 5.3). For each distribution, we find the appropriate scaling of their expected values $\mathfrak{m}_K$ and variances $\mathfrak{s}_K^2$ with respect to the particle size K by fitting $\mathfrak{m}_K$ as a second-order polynomial in $\dfrac{1}{K}$ and $\mathfrak{s}_K^2$ as a power law in K (see Table 5.1).

The distributions are then rescaled as

$$\widetilde{f_K}(x) = \mathfrak{s}_K f_K(\mathfrak{m}_K + \mathfrak{s}_K x),$$

where f_K is the distribution function for some quantity. The rescaled distributions $\widetilde{f_K}$ are represented as an inset in Figure 5.3. We notice that, for $K > 5$, the rescaled distributions $\widetilde{f_K}$ collapse to a single distribution independent of the particle size K. As K increases, the mesoparticles stand for a larger collection of molecules, so that some effective averaging process takes place. The Central Limit Theorem from probability theory suggests that the variances $\mathfrak{s}_K$ scale as $\dfrac{1}{K}$ and

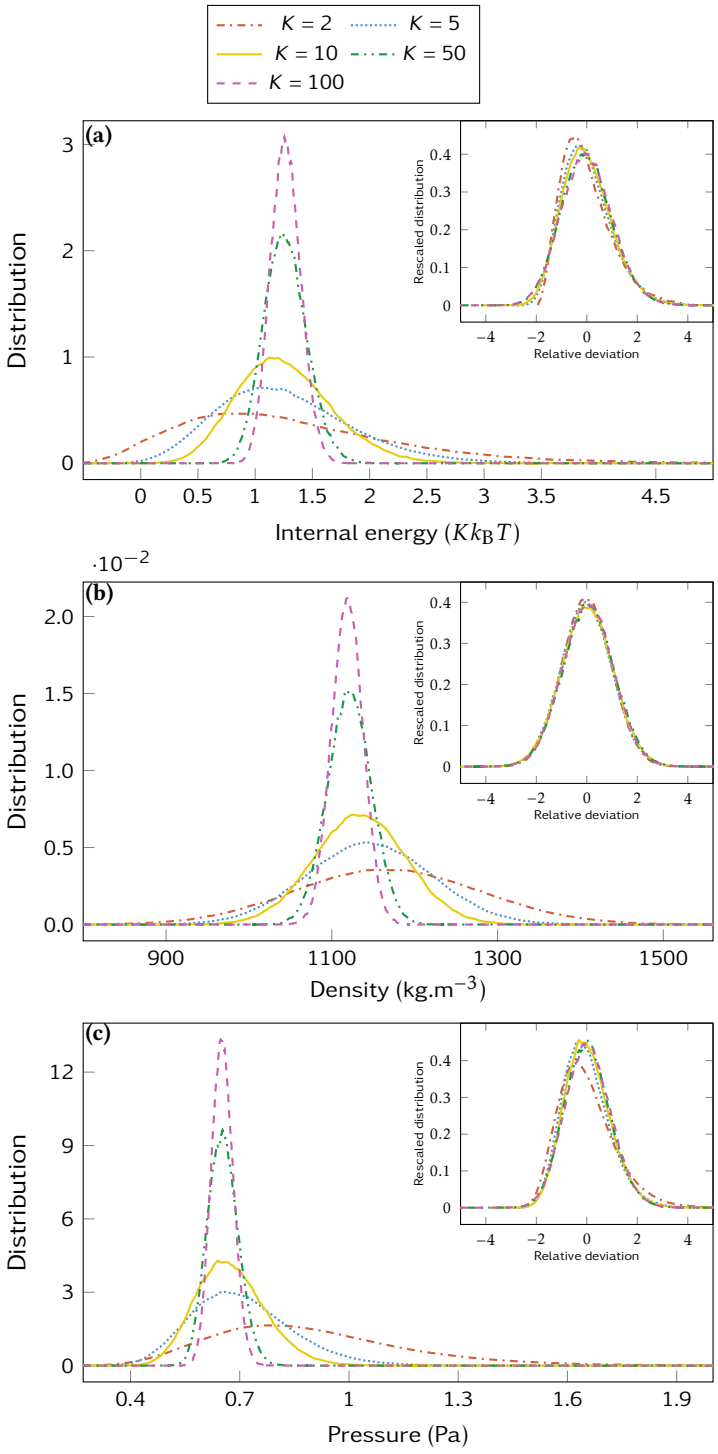


Figure 5.3 | Distributions, for different SDPD masses K, of (a) the normalized internal energy $\frac{\varepsilon_i}{K}$, (b) the density ρ_i and (c) the internal pressure P_i. The rescaled distributions are displayed as insets in these figures.

that the distribution should tend to a normal distribution. Our numerical results are in excellent agreement with this prediction, the distributions becoming more symmetric for larger sizes K with a variance inversely proportional to K.

We check the consistency of the SDPD simulations with the reference equation of state by plotting the average pressure, internal and kinetic temperatures with respect to the mass

of the fluid particles in Figure 5.4. For large masses, the thermal fluctuations included in the

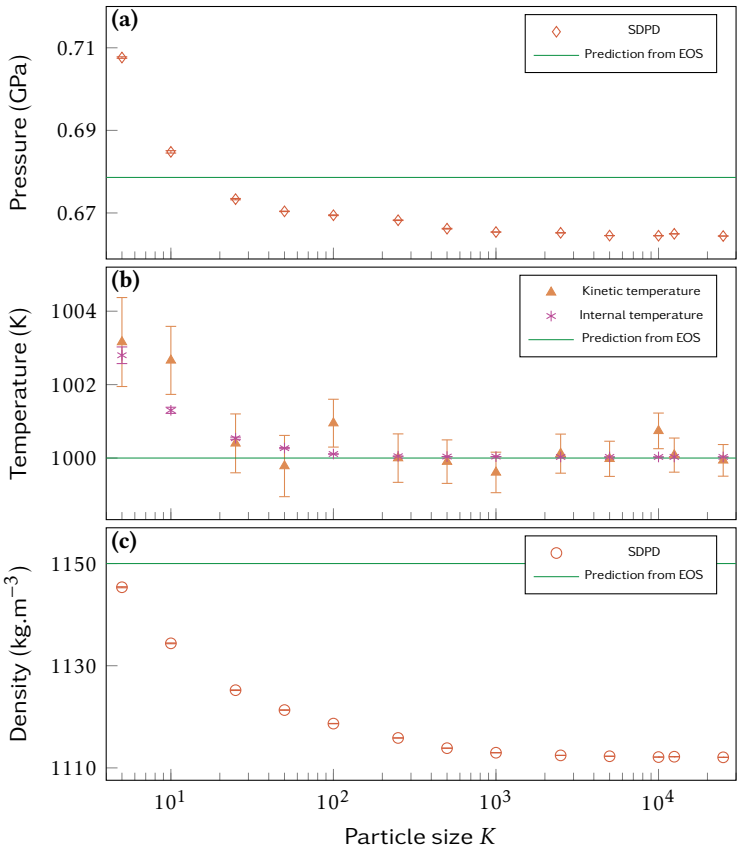


Figure 5.4 | Numerical estimations of (a) the equilibrium pressure, (b) the kinetic and internal temperatures and (c) the density as a function of the size K of the SDPD particles (displayed with a logarithmic scale) for the Lennard-Jones equation of state.

SDPD equations are no longer significant and the estimated pressure converges to some limiting pressure which is 3% lower than the pressure predicted by the equation of state. However, we also note a discrepancy in the estimation of the density as we observe an average mean density of 1112 kg.m^{-3} for $K > 1000$ instead of the expected value 1150 kg.m^{-3}. As the size of the particles decreases, the agreement between the pressure obtained from SDPD simulations and the pressure predicted by the equation of state remains within 5% of difference even for $K = 5$ or $K = 10$, *i.e.* for masses of the order of only a few multiples of m_0.

5.1.3 Shock waves

We turn in this section to the study of the consistency of SDPD in non-equilibrium situations such as shock waves. We consider a system of $N = 54272$ particles initialized on a simple cubic lattice $16 \times 16 \times 212$. We use periodic boundary conditions in the x- and y-directions whereas two walls are located at each end of the system in the z-direction. Each wall is composed of 3 layers of "virtual" SDPD particles arranged in a cubic lattice. These virtual particles interact with the real SDPD particles through the conservative forces (1.27) and a repulsive Lennard-Jones potential that ensures the impermeability of the walls (see Section 4.3.3). We use the Lennard-Jones equation of state [90] in these simulations. The system is initialized at a temperature $T_0 = 500$ K and a density $\rho_0 = 1150$ kg.m^{-3}. To produce a sustained shock wave in the system, the bottom wall is

set in motion at a velocity $v_P = 500$ m.s^{-1} in the z-direction and continues moving at velocity v_P throughout the simulation. We run the simulation with particle sizes varying from $K = 10$ to $K = 10000$.

To obtain the profiles of physical properties at a given time, the simulation box is divided into $n_{\text{sl}} = 100$ slices regularly distributed along the z-axis in which the physical properties are averaged. Since a shock wave is a stationary process in the reference frame of the shock front, we can average profiles over time after shifting the position of the shock front to $z = 0$. We proceed as in Section 4.3.3 and locate the shock front where the particle velocity is $v = \frac{v_P}{2}$.

Table 5.2 summarizes the main physical properties estimated with the simulations: the velocity of the shock front v_S along with the thermodynamic properties in the shocked state (the density ρ_S, the pressure P_S and the internal temperature $T_{\text{int},S}$). They are compared to the corresponding values obtained via direct MD simulation and to the values predicted by the Rankine-Hugoniot relations described in Section 6.1. We find that SDPD gives similar results for all the resolutions which are considered. These results are consistent with the predictions obtained from the Rankine-Hugoniot relations. They also agree with MD within a 5%-difference margin for pressure, density and temperature. While no particular bias is observed for temperature, the density observed in SDPD is slightly higher and the pressure slightly lower than the MD results. The shock velocity is also a bit underestimated and seems to decay for larger particles. Since we consider a bulk material, the viscosity has no effect on the average properties in the shocked state. As such, we obtain quasi identical results when $\eta = 10^{-4}$ Pa.s (as presented in Table 5.2) or $\eta = 2 \times 10^{-3}$ Pa.s

K	v_S (m.s^{-1})	ρ_S (kg.m^{-3})	P_S (GPa)	$T_{\text{int},S}$ (K)
MD	1961	1508	1.45	939
EoS	1975	1540	1.47	969
10	1846	1547	1.37	911
100	1900	1546	1.39	946
500	1897	1547	1.39	946
1000	1886	1545	1.37	938
5000	1870	1552	1.39	935
10000	1864	1551	1.38	929

Table 5.2 | Average observables in the shocked state. The wall velocity is fixed to $v_P = 500$ m.s^{-1} and the viscosity parameter for SDPD is set to $\eta = 10^{-4}$ Pa.s.

Following [77, 76], we compute the one-dimensional Navier-Stokes shock wave profile. In this 1D stationary setting, the Navier-Stokes conservation equations (1.9) simplify to simple differential equations in the reference frame of the shock front:

$$\begin{aligned} \rho(z)v(z) &= \rho_0 v_0, \\ P(z) - \eta v'(z) + \rho_0 v_0 v(z) &= P_0 + \rho_0 v_0^2, \\ u(z) - \frac{1}{2}v(z)^2 + \frac{P_0 + \rho_0 v_0^2}{\rho(z)} &= u_0 + \frac{1}{2}v_0^2 + \frac{P_0}{\rho_0}, \end{aligned} \tag{5.1}$$

where $z \in \mathbb{R}$ is the distance to the shock front (located at $z = 0$). The unknowns are the density

ρ, the velocity v, and the internal energy per unit mass u, while the pressure P is given by the equation of state. We choose the unshocked material to be at $z > 0$ and the shocked fluid at $z < 0$. This determines the velocity in the unshocked state to be $v_0 = -v_S$ and the velocity in the shocked state $v_1 = v_P - v_S$. Equations (5.1) are integrated with a finite differences scheme on a domain $[-L, L]$ and with initial conditions $v(0) = \frac{1}{2}(v_0 + v_S)$. The density $\rho(0)$ and energy $u(0)$ at the origin are then determined thanks to Equation (5.1). We choose here $L = 10^{-8}$ m and a mesh spacing $\Delta x = 10^{-12}$ m.

We also present the results for a MD simulation of the same setting. In MD simulations, the walls are modeled as infinitely massive particles interacting with the other particles through a Lennard-Jones potential. We use a Velocity-Verlet scheme [172] and a timestep $\Delta t = 10^{-15}$ s for the integration of the Hamiltonian dynamics.

The mean profiles for density are given in Figure 5.5 in the corresponding reduced units and in physical units. The reduced length unit for MD and Navier-Stokes is the same as the SDPD reduced length unit for $K = 1$ to allow for a comparison with the other profiles. Figure 5.5 is

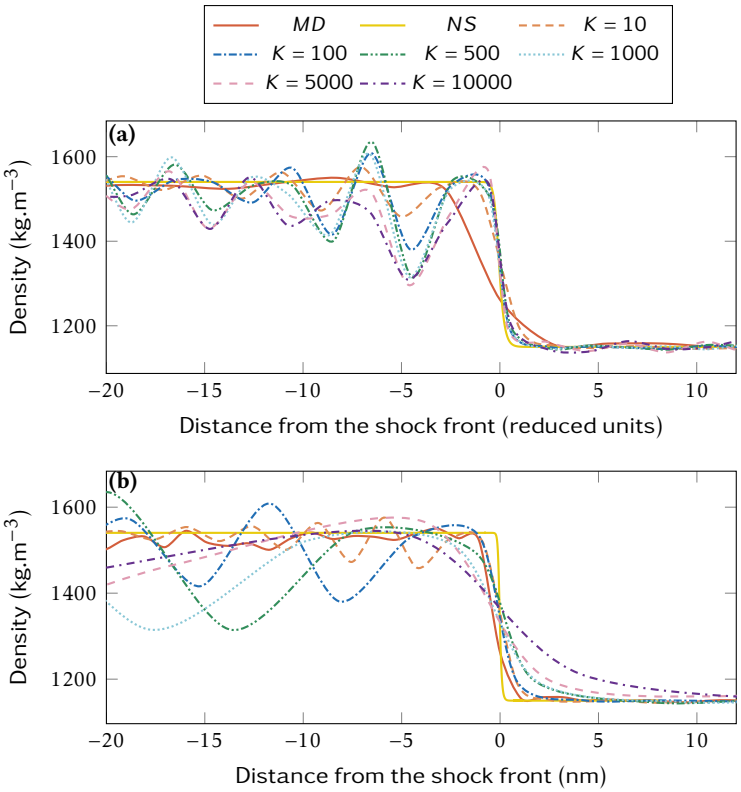


Figure 5.5 | Density profiles in the shock reference frame for $K = 10$ to $K = 10000$ compared to MD and Navier-Stokes (NS). The reduced units are defined by equation (2.20). The viscosity is set to $\eta = 10^{-4}$ Pa.s and the wall velocity to $v_P = 500$ m.s^{-1}.

obtained by using a viscosity $\eta = 10^{-4}$ Pa.s, which is of the same order as the viscosity of the Lennard-Jones fluid, for the SDPD simulations and the Navier-Stokes solution, which allows for a comparison between these methods. While the profile derived from Equation (5.1) is sharper than the MD profile, we observe that we can recover reasonably well the profile from MD for small SDPD particle sizes. When the size of the SDPD particles increases, the shock front widens and no longer agrees with the MD profile. Since the width of the shock front in SDPD seems constant

in reduced units for any of the tested resolutions, the main factor governing the shock width in physical units in this situation appears to be the resolution chosen for SDPD.

The profiles computed with SDPD display strong oscillations in the shocked state due to the small value of the viscosity. Similar issues are encountered in SPH, where an artificial viscosity is introduced to alleviate the oscillations [134]. Figure 5.6 presents the profiles computed with a larger viscosity $\eta = 2 \times 10^{-3}$ Pa.s, which is comparable to water. The oscillations are effectively dampened but the shock front is now quite wide compared to MD and agrees with the Navier-Stokes results. Its width in physical units no longer depends on the particles size for the range of resolution we study. In this situation, it appears that the dominating effect is the viscosity and any of the tested particles sizes is able to accurately resolve the shock front for moderately viscous fluids. We anticipate similar results for higher viscosity fluids. This demonstrates the ability of

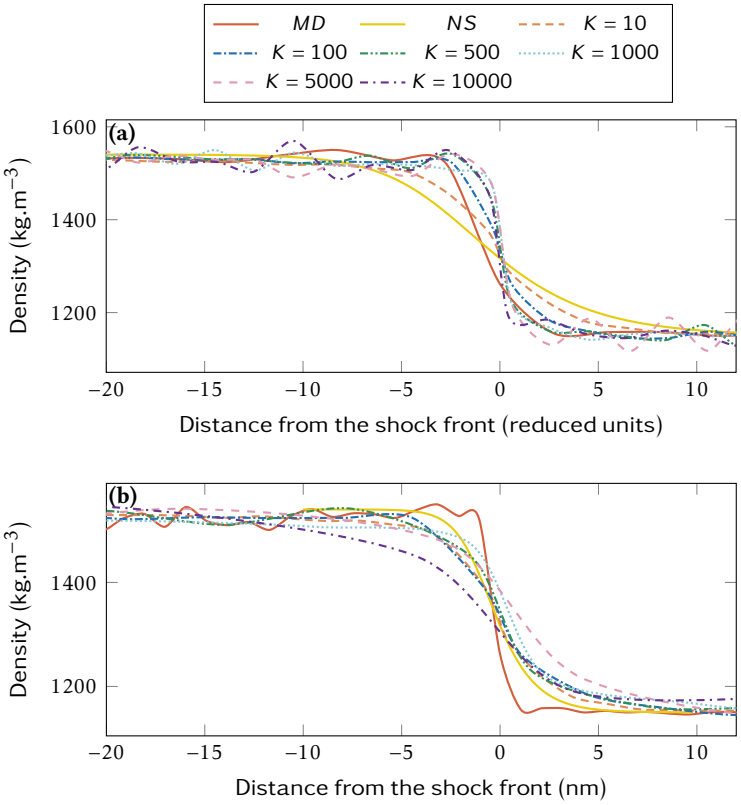


Figure 5.6 | Density profiles in the shock reference frame for $K = 10$ to $K = 10000$ compared to MD and Navier-Stokes (NS). The reduced units are defined by equation (2.20). The viscosity is set to $\eta = 2 \times 10^{-3}$ Pa.s and the wall velocity to $v_P = 500$ m.s^{-1}.

SDPD to consistently describe not only equilibrium simulations but also shock waves.

5.2 Multiscale SDPD

We showed in Section 5.1 that the physical properties could be retrieved with SDPD for a wide range of particle sizes. This consistency is valid for equilibrium thermodynamic properties but also for non equilibrium situations like shock waves. This allows us to envision a concurrent coupling of SDPD at different resolutions.

Many physical problems are indeed multiscale by nature, involving phenomena that occur at different time and length scales in the same system. In the context of shock waves for instance, the shock front is a very small subset of the whole domain. Since it is subject to very strong gradients, it requires a fine description while a much coarser resolution would be sufficient to deal with the remainder of the system, especially the unshocked region which is at equilibrium.

We introduce in Section 5.2.1 a possible multiscale coupling for SDPD where the resolution may vary by splitting or merging particles. This method is illustrated by a multiscale simulation at equilibrium in Section 5.2.2. We pay a particular attention to possible bias between the refined and the coarse region. In Section 5.2.3 we discuss the limits of such couplings and possible improvements for concurrent multiscale simulations.

5.2.1 Splitting and merging particles

In particle methods such as SPH or SDPD, the resolution is governed by the size of the particles (and the smoothing length that should vary consistently with it following Equation (1.17)). In order to increase the accuracy, we thus need to increase the number of particles while decreasing their masses and smoothing lengths. We consider a system that will be described with SDPD at two different resolutions and propose a possible multiscale coupling.

The domain in divided into two main areas Ω_0 and Ω_1 where the resolution is fixed by the particle sizes K_0 and K_1 and a buffer region $\mathscr{B}$ (see Figure 5.7). In the refined region Ω_1, where

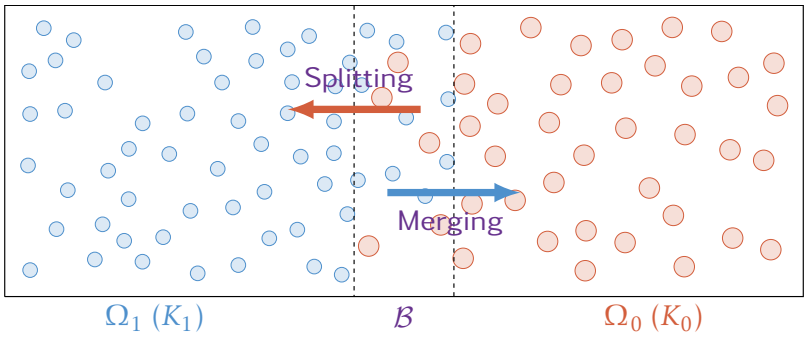


Figure 5.7 | Scheme of the multiscale SDPD.

the accuracy is increased along with the computational cost, we use smaller particles than in the coarse domain Ω_0. The particle size K_1 in Ω_1 is related to the particle size K_0 in Ω_0 by an integer refinement ratio $\mathscr{R} = \frac{K_1}{K_0}$. In order to ensure that the resolution remains fixed in the subdomains Ω_0 and Ω_1, the particles need to change their sizes within the buffer region.

An approach first introduced for SPH (see for instance [95, 51] for the refinement procedure and [170, 8] for refinement and derefinement) and adapted in the context of isothermal SDPD [98, 145] consists in splitting particles to increase the resolution or merging particles for a coarser description. This effectively lets the resolution vary within the simulation and could be viewed as the counterpart for particle methods of Adaptive Mesh Refinement [13, 12].

In this thesis, we propose a multiscale method for the full SDPD inspired by the isothermal version [98]. As the particles move within the domain, their resolution is adapted depending on their positions. When a particle enters the buffer zone, it remains unchanged until it leaves it. However, upon entry in the refined domain, a particle of size K_0 is split into $\mathscr{R}$ smaller particles of size K_1. On the other hand, a particle of size K_1 entering the coarse domain is merged with $\mathscr{R} - 1$

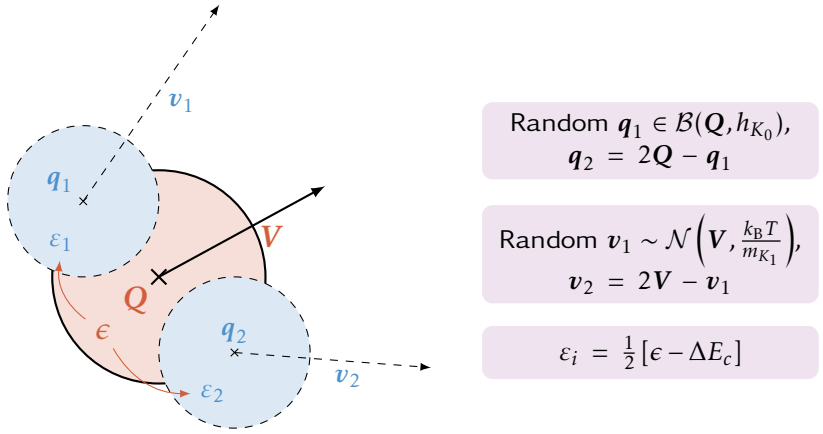


Figure 5.8 | Splitting of a large particle of size K_0 in two smaller particles of size $K_1 = \frac{K_0}{2}$.

neighboring particles of the same size K_1 to form a larger particle of size K_0. This automatically ensures the conservation of mass in the system. It is possible to further preserve the momentum and the energy by assigning the appropriate values to the new particles. We consider in the following only the case when $\mathscr{R} = 2$ and describe the splitting and merging mechanism.

Splitting

Splitting occurs when a large particle, at position $\boldsymbol{Q}$, momentum $\boldsymbol{P}$ and internal energy ϵ leaves the buffer region and enters the refined region. It is then split into $\mathscr{R}$ smaller particles located at positions $\boldsymbol{q}_i$ and with momentum $\boldsymbol{p}_i$ and internal energy ε_i, for $i \in \{1 \dots \mathscr{R}\}$. Since this creates more degrees of freedom, the conservation of the total momentum and the total energy in the system can be easily achieved. In SDPD, the fluctuations scale with the mass of the particles. We thus introduce some additional fluctuation consistent with the size K_1 when splitting large particles of size K_0. In the case $\mathscr{R} = 2$, we first randomly select the position $\boldsymbol{q}_0$ of the first small particles within a radius h_{K_0} of the position $\boldsymbol{Q}$ of the original particle. The position $\boldsymbol{q}_1$ of the second small particles is then determined to keep the center of mass constant as $\boldsymbol{q}_1 = 2\boldsymbol{Q} - \boldsymbol{q}_0$. Similarly, the momentum $\boldsymbol{p}_0$ is chosen randomly with a normal distribution centered around $\frac{\boldsymbol{P}}{2}$ and with the appropriate variance (given by the equilibrium distribution adapted to the particle mass). The choice for the second momentum ensures the conservation of the total momentum with $\boldsymbol{p}_1 = \boldsymbol{P} - \boldsymbol{p}_0$. Finally, the internal energy and the variation of the kinetic energy $\frac{\boldsymbol{p}_1^2 + \boldsymbol{p}_2^2}{2m_{K_1}} - \frac{\boldsymbol{P}^2}{2m_{K_0}}$ are split equally between the new particles. The splitting procedure is summarized in Figure 5.8.

Merging

Merging is the reverse mechanism by which $\mathscr{R}$ small particles are fused into a single large particle. Using the same notation as for the splitting procedure for the particles coordinates, the position $\boldsymbol{Q}$, momentum $\boldsymbol{P}$ and internal energy ϵ of the new particle are fixed solely by the preservation of the center of mass, of the total momentum and of the total energy since we are reducing the number of degrees of freedom. The position and momentum are computed at the center of mass

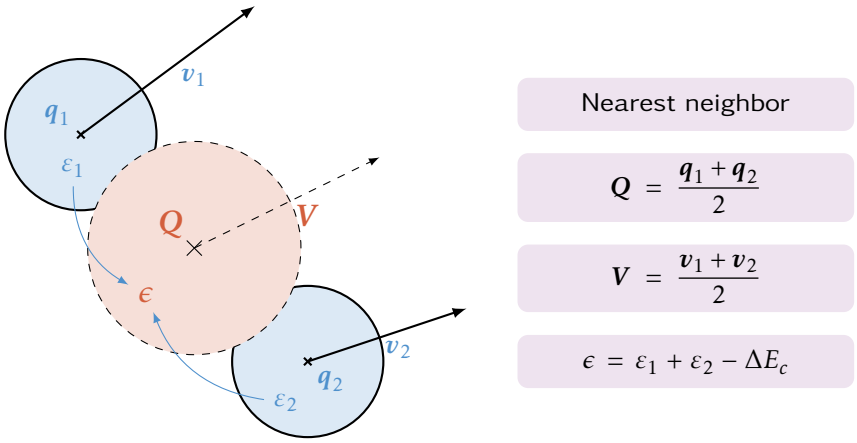


Figure 5.9 | Merging of two small particles of size K_1 in a large particle of size $K_0 = 2K_1$.

as

$$\boldsymbol{Q} = \frac{1}{2}\left(\boldsymbol{q}_0 + \boldsymbol{q}_1\right),$$
$$\boldsymbol{P} = \boldsymbol{p}_0 + \boldsymbol{p}_1.$$

The internal energy is later determined by taking into account the resulting variation in the kinetic energy, hence preserving the total energy with

$$\epsilon = \varepsilon_1 + \varepsilon_2 + \frac{\boldsymbol{p}_1^2 + \boldsymbol{p}_2^2}{2m_{K_1}} - \frac{\boldsymbol{P}^2}{2m_{K_0}}.$$

Note that the condition $\epsilon > 0$ may be violated with such a merging procedure if the internal energies $\varepsilon_1 + \varepsilon_2$ are smaller than the variation of kinetic energy produced by the derefinement. For large particles, it should not be a problem since the internal energies are much larger than the kinetic terms and in practice we have not encountered such a situation in our simulations. As the size of the particles decreases, it would however probably occur considering the stability issues observed in Section 4. This means that the energy and the momentum cannot be preserved together in such a situation.

The key choice in the merging procedure is to decide which particles will be merged. The merging procedure is triggered by a small particle of size K_1 entering the coarse domain Ω_0. The remaining $\mathscr{R} - 1$ particles of the same size K_1 needed to form the new large particle are chosen to be its nearest neighbors. This mechanism is illustrated by Figure 5.9.

5.2.2 Numerical illustration

We illustrate the coupling mechanism between SDPD at different resolutions with an equilibrium simulation using ideal gas equation of state (see Equation (4.7)). The system is initialized with $N_{50} = 40000$ particles of size $K = 50$ organized on a $20\times20\times100$ simple cubic lattice with position $z < 0$ and with $N_{100} = 20000$ particles of size $K = 100$ on a $10\times10\times50$ face centered cubic lattice with position $z > 0$. The lattice parameters are chosen so that the density in the simulation box is $\rho = 1150$ kg.m^{-3} in both subdomains. The initial temperature is set to $T = 1000$ K. We use in the following the reduced units for $K = 50$. Periodic boundary conditions are used in all directions

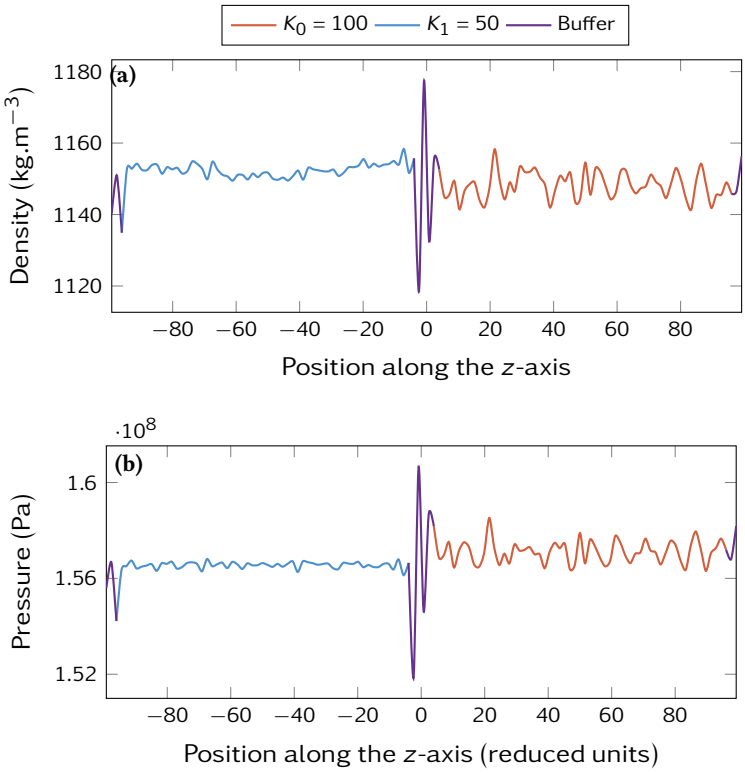


Figure 5.10 | Average profile for (a) density and (b) pressure in multiscale SDPD ($K_0 = 100$ and $K_1 = 50$).

and two buffer regions are defined: at the center of the simulation box ($-3.2 < z < 3.2$) and at its edges ($-100 < z < -96.8$ and $96.8 < z < 100$). A time step $\Delta t = 0.18$ is used. In this multiscale approach, the time step is essentially limited by the finer resolution. For large refinement ratios when the difference between admissible time steps for K_0 and K_1 become significant, a multiple time step approach, where a larger time step would be used for the larger particles, may be relevant to further decrease the computational cost in the coarser region.

After a thermalization time $\tau_{\text{therm}} = 100$, we observe the properties of the multiscale coupling during a total time $\tau_{\text{sim}} = 2000$. Since we are considering an equilibrium situation, the density and pressure in the whole domain should be the same. In order to check whether the multiscale method introduces spatial biases between the two regions Ω_0 and Ω_1, we plot in Figure 5.10 average profiles for density and pressure computed by using $n_{\text{sl}} = 126$ bins regularly distributed along the z-axis. There is a slight discrepancy between the average density (and thus pressure) between the refined and the coarse domain but it is limited to only 0.5%, which is quite satisfying. However, we notice larger peaks in the buffer region of the order of 2.5% both in density and pressure. This probably arises because of the abrupt transition from one resolution to another with the merging or splitting mechanisms. Jumps in the pressure and/or density profiles are quite usual in multiscale coupling for particle methods. Different corrections can be applied so that the same density or pressure is observed in the whole domain (see [146] for a coupling between MD and coarse-grained model). However, these methods are generally not able to ensure the equality of both pressure and density in the two subdomains.

We also measure the average number of particles for each particle size. We counted 20187 particles of size K_0 and hence 39626 particles of size K_1. This represents only a 1% deviation from the initial distribution. Since the domain has been split equally between the refined and

the coarse regions, the initial distribution should be indeed maintained in average during the simulation. Our observations are also consistent with the very small deviation in the density between the two regions (see Figure 5.10).

The time step chosen for this simulation is small enough for the relative energy drift in a single resolution simulation with $K = K_1 = 50$ to be very small, of the order of 5×10^{-7} (see Section 4.1.3). As previously mentioned, the drift if the system was entirely described with particles of size $K_0 = 100$ would be further reduced. In the multiscale simulation, no drift is apparent and it seems that the refinement and derefinement steps do not perturb the energy conservation.

5.2.3 Possible improvements

One of the key factor in the multiscale coupling method we propose is the refinement ratio $\mathscr{R}$. When replacing a large particle $\mathscr{P}_0$ by several smaller ones $(\mathscr{p}_i)_{i\in[\![1,\mathscr{R}]\!]}$, we approximate the long range kernel (with a smoothing length h_{K_0}) centered around $\mathscr{P}_0$ by a sum of smaller range kernels (with a smoothing length h_{K_1}) centered around the particles $\mathscr{p}_i$. This effectively represents the error we make in the SPH interpolation of the density. It is possible to optimize the positions of the inserted particles so as to minimize this error. For the splitting part, we may actually determine the optimized position beforehand and use it in the simulation without extra cost [51]. The more particles we insert to replace the original particles, the more accurate we can hope to be. It is however unclear what effects a large refinement ratio would have in the splitting mechanism, especially for the reverse procedure of merging particles. Furthermore, the coexistence of particles with very different aspect ratios may lead to metastability issues. To highlight this, we run a simulation with $\mathscr{R} = 8$ where particles of size $K_0 = 400$ and $K_1 = 50$ can coexist in the whole domain (*i.e.* the whole domain is composed solely of the buffer region). We observe that smaller particles tend to cluster around the larger ones that are organized on a lattice. Though this situation would be limited to the buffer region in the multiscale coupling, it may lead to exacerbated interface effects there.

An origin of the spurious peaks in the buffer region is probably the brutal transition from refined to derefined particles, or inversely. We may hope that a smoother transition would prevent these oscillations to appear. This could be achieved for instance by letting particles gradually change their refinement state depending on their positions in the buffer zone and indexing it by a transition variable $\lambda \in [0, 1]$. In [8], when a particle is refined, it keeps memory of the small particles that originated from it so that these particles can be merged again if needed. Such a mechanism could be adapted to let the two descriptions coexist in the buffer region. When $\lambda = 0$ or $\lambda = 1$, only the large particle or respectively the refined particles would interact with neighboring particles, which corresponds to the usual SDPD. However, in the buffer region, the interactions would be computed as a weighted average between the coarse and fine particles. A limitation of this technique is that refined particles need to stay close to each other for the dual view to still make sense. This is clearly not ensured, especially with the fluctuations of SDPD for small particle sizes. We should also beware of the additional forces caused by the position-dependent transition variables, which break the momentum conservation and may lead to undesired behaviors. In the MD/coarse-grained coupling [146], this issue was solved by writing the total energy as a mixed resolution Hamiltonian, preserving the energy as well as the total momentum.

In this section, the multiscale method is based on a domain decomposition that does not vary with time. This is mostly adapted to static phenomenon that happens in a determined region of space. The propagation of a shock wave is on the contrary a fast moving process. In order to resort to a multiscale coupling for shock waves, we need to be able to determine the refined region at each step based on physical criteria. For instance, we may detect strong gradients and refine the resolution around their positions. It means that phenomena like shock waves involve a lot of refinements and derefinements, further stressing the need for a stable, accurate and unbiased multiscale coupling to avoid errors to propagated. Furthermore, the cost of the various steps in the multiscale procedure including merging, splitting and detecting the shock front should be taken into account and balanced with the gain in the simulation time due to the coarsening of most of the domain. The method becomes obviously more interesting for large aspect ratios between the finer and the coarser resolutions. This may be achieved with a large refinement ratio $\mathscr{R}$ or with several refinement levels, as for AMR in mesh-based methods, that would allow to smooth out the transition from a fine to a very coarse description of the fluids. An example in particle methods can be found in [25] where the resolution varies from MD to coarse-grained dynamics and finally to hydrodynamics.

6 Applications to shock and detonation waves

This chapter studies the ability of SDPD to simulate complex physical systems at various resolutions. We apply SDPD to shock-induced phenomena for which SDPD is well suited since it preserves the energy and includes correct heat capacity and compressibility through the equation of state. We first give some elements on shock and detonation waves in Section 6.1. In Section 6.2, we focus on the ejection of particles when a shock wave is reflected on a rough free surface resulting in micro-jetting. We also discuss the possible implementation of surface tension effects in SDPD since it plays a major role when interfaces and free surfaces are considered. We then turn our attention, in Section 6.3, to detonation waves, which are shock waves driven by exothermic chemical reactions behind the shock front. To that end, we introduce a reactive mechanism in SDPD, which allows us to take into account chemical reactions. We illustrate the relevance of the reactive SDPD model by simulating a detonation wave in nitromethane.

6.1 Shock and detonation waves

In this section, we give some definitions and important relations in the theory of shock and detonation waves. We refer to [54, 167] for a detailed approach of these phenomena.

A shock wave is a perturbation that is propagated at a velocity v_S higher than the sound velocity c of the material. It is characterized by a sharp transition of the thermodynamic variables, like pressure, temperature and density.

Assuming that the propagation of a planar shock wave can be described in an effective manner by a one-dimensional Euler system (in particular, viscosity effects can be neglected), the Rankine-Hugoniot conditions allow to predict the thermodynamic properties in the shocked state, knowing the velocity v_P of the particles in the shocked region and the initial thermodynamic state, determined by the density ρ_0, specific energy u_0 and pressure $P_0 = \mathscr{P}(u_0, \rho_0)$. These conditions are obtained from the conservation laws for mass, momentum and energy (see Equation (5.1)). The density ρ_1, internal energy per unit mass u_1 and pressure $P_1 = \mathscr{P}(u_1, \rho_1)$ in the shocked state are respectively predicted to be

$$\begin{cases} \rho_1(v_S - v_P) = \rho_0 v_S, \\ P_1 + \rho_0 v_S(v_S - v_P) = P_0 + \rho_0 v_S^2, \\ u_1 - \dfrac{1}{2}(v_S - v_P)^2 + \dfrac{P_0 + \rho_0 v_S^2}{\rho_1} = u_0 + \dfrac{1}{2}v_S^2 + \dfrac{P_0}{\rho_0}. \end{cases}$$

The velocity v_S of the shock wave can be inferred from these relations. Plugging the first two equations in the third one allows to reformulate the Rankine-Hugoniot conditions as

$$u_1 = u_0 + \frac{1}{2}(P_0 + P_1)\left(\frac{1}{\rho_0} - \frac{1}{\rho_1}\right). \tag{6.1}$$

This defines the Hugoniot curve, which is the ensemble of thermodynamic states that can be reached from a reference state by shocks. In order to determine it numerically, a Newton inversion can be performed using the equation of state (1.22) to relate the pressure with the energy and the density.

A detonation wave is formed when exothermic chemical reactions occur behind a shock front. The energy released by the reactions sustains the propagation of the shock wave and establishes a stationary process followed by a self-similar rarefaction wave. This is illustrated in Figure 6.1 where a schematic ideal detonation wave is represented. The thermodynamic states at which the

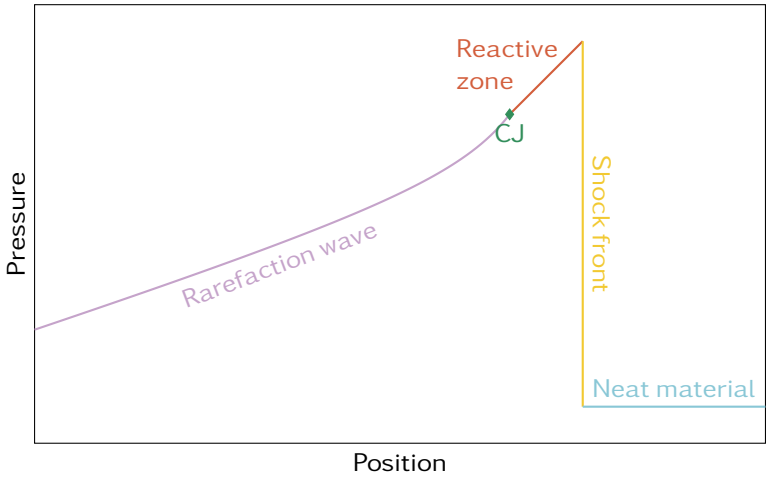


Figure 6.1 | Ideal detonation wave.

reacted material can be found are no longer determined by the unreacted Hugoniot relations (6.1) since the chemical reactions change the equation of state on top of releasing energy with the exothermicity. This needs to be taken into account in the conservation laws and the admissible detonated thermodynamic state (ρ_D,P_D,u_D) are now determined with

$$u_D = u_0 + \frac{1}{2}(P_0 + P_D)\left(\frac{1}{\rho_0} - \frac{1}{\rho_D}\right) + u_{exo},$$

where u_{exo} is the exothermicity per unit mass. Note that the pressure in the detonated state is now related to the energy and density by the equation of state of the reacted material:

$$P_D = \mathscr{P}_{reacted}(u_D, \rho_D).$$

This relation defines the Crussard curve which is the Hugoniot curve of the detonation product. We plot in Figure 6.2 the Hugoniot curve of an unreacted material described by the HZ equation of state (6.10) (see Section 6.3.2) along with the Crussard curve when the JWL equation of state (6.11) (see Section 6.3.2) is used for the product.

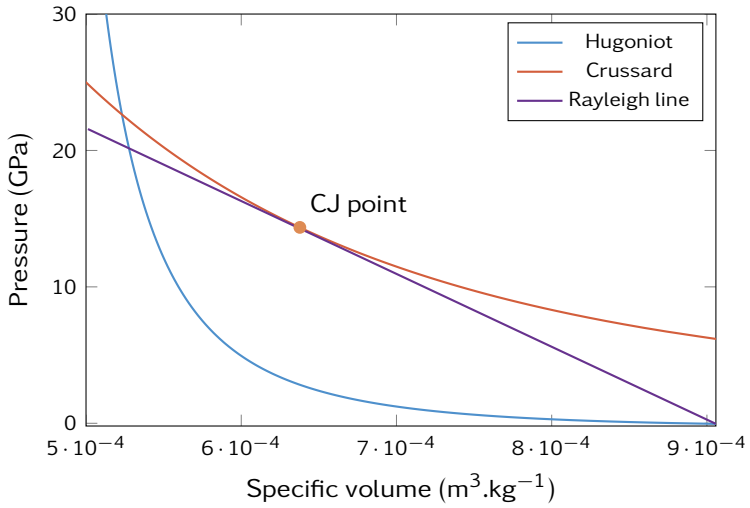


Figure 6.2 | Hugoniot curve for the HZ equation of state and Crussard curve for the JWL equation of state. The Rayleigh line and the Chapman-Jouguet point are also displayed.

The Rayleigh line is defined by the relation

$$P = P_0 + \rho_0^2 v_S^2 \left(\frac{1}{\rho_0} - \frac{1}{\rho} \right).$$

Its intersections with the Hugoniot and Crussard curves give the admissible thermodynamic states when the shock has the velocity v_S. A particularly interesting case is when the Rayleigh line is tangent to the Crussard curve. This characterizes the ideal detonation wave which velocity v_D is the minimum velocity for a detonation. If $v_S < v_D$, the Crussard curve and the Rayleigh line do not intersect. Hence, no detonation is possible. On the contrary if $v_S > v_D$, a detonation wave is unstable and its velocity should decrease until it reaches v_D. Furthermore, the tangent point between the Crussard curve and the Rayleigh line at v_D is the Chapman-Jouguet (CJ) point which determines the end of the out of equilibrium reactive zone (see Figure 6.1) and the beginning of the rarefaction wave. It also coincides with the sonic point where the velocity of the particles is equal to the sound velocity of the material. This means that the rarefaction wave cannot affect the reactive region, allowing the detonation wave to remain stable. Starting from the CJ point, the thermodynamic state of the products evolves along an isentrope (at constant entropy), which is also tangent to the Crussard curve and the Rayleigh line at the CJ point.

6.2 Micro-jetting

The reflection of a shock wave on a rough free surface causes particles to be ejected from the surface. This may cause perturbations that would not be accounted for if we assume that the free surface is perfect. This has spurred many studies, both experimental [159, 143, 114, 153] and numerical, to better understand the phenomenon and in particular to characterize the distribution in size and velocity of the ejecta. Current simulations mainly rely on MD [61, 33, 34, 35, 70, 36] which have shown the importance of thermal fluctuations to explain the size distribution in the ejecta [37]. However in order to compare the results with experimental studies, it is necessary to extrapolate MD simulations up to the experimental time and length scales using postulated scaling

laws. Rather than mesh-based methods like Finite Elements which suffer from the presence of large deformations and the need of a fragmentation model, hydrodynamic simulations of ejecta are performed with SPH [38, 154] that can more naturally take into account these effects. They require the inclusion of several ingredients originating from microscopic properties, in particular surface tension since its absence may lead to discrepancies in the velocity profiles [38].

Since SDPD naturally includes fluctuations and shares with SPH its ability to deal with large deformations, it is a good candidate to simulate micro-jetting at larger time and length scales than MD while retaining fluctuating properties. It could provide a way to check the validity of the scaling laws assumptions. Surface tension effects are however not included in the usual SDPD model of Section 2 and an extra modeling is required to take it into account. Possible methods to recover the surface tension in SDPD are briefly discussed in the following although they are not implemented in the simulations we report.

We present in the following some simulations of micro-jetting for tin. In the absence of surface tension, we restrict ourselves to a qualitative study. We introduce in Section 6.2.1 the equation of state used for tin and the initial geometry of the simulation. The results are then analyzed in Section 6.2.2. Finally we discuss briefly in Section 6.2.3 the possible implementations of surface tension in the context of SDPD.

6.2.1 Simulation setting

In our simulation, tin is modeled by a Mie-Grüneisen equation of state [72] which reads

$$\mathcal{S}_{\mathrm{Tin}}(\varepsilon,\rho) = C_{V_r}\log\left(1+\frac{\varepsilon-\mathfrak{E}_k(\rho)}{C_{V_r}\Theta(\rho)u_r}\right), \tag{6.2}$$

with the reference energy

$$\mathfrak{E}_k(\rho) = \frac{K_s}{\rho_s}\left[\frac{\exp\left((N_s+1)\left[1-\frac{\rho_s}{\rho}\right]\right)}{(N_s+1)^2}-\frac{1-\frac{\rho_s}{\rho}}{N_s+1}\right],$$

and temperature

$$\Theta(\rho) = \Theta_0\left(\frac{\rho}{\rho_0}\right)^{\Gamma_\infty}\exp\left(\frac{\Gamma_0-\Gamma_\infty}{q}\left[1-\left(\frac{\rho_0}{\rho}\right)^q\right]\right).$$

The parameters used for this equation of state are gathered in Table 6.1. In order to enforce a thermodynamic consistency between SDPD and MD, these parameters are obtained by fitting the Mie-Grüneisen equation of state on a Hugoniot curve computed with MD simulations where tin atoms interacted with an EAM potential [22]. The Mie-Grüneisen equation of state is well adapted to model the behavior of liquid metal. While tin is solid at the standard thermodynamic conditions (atmospheric pressure and temperature), it melts under sufficiently strong shock, which is the domain of interest.

The system is constituted of a block of tin with periodic boundary conditions in the x- and y-directions. In the z-direction, a wall made of virtual particles (see Section 4.3.3) is set at one end of the system with an initial velocity $v_{\mathrm{P}} = 1580\ \mathrm{m.s^{-1}}$ while the other end is a free surface. A sinusoidal defect, characterized by a wave length λ and a depth $\mathscr{d}$ is created in the free surface as illustrated in Figure 6.3. The dimension in the y-direction is equal to the defect wave length λ. The length in the x-direction is three times the depth $\mathscr{d}$ of the defect. A larger system would avoid

Parameter	Value	Unit
Γ_0	2.8	-
Γ_∞	0.43	-
ρ_0	7000	$\mathrm{kg.m^{-3}}$
Θ_0	1150	K
u_r	0.172	-
q	1.96	-
C_{V_r}	173	$\mathrm{J.K^{-1}.kg^{-1}}$
ρ_s	6930	$\mathrm{kg.m^{-3}}$
K_s	4.19×10^{10}	Pa
N_s	5.4	-

Table 6.1 | Parameters for the Mie-Grüneisen 6.1 equation of state for tin

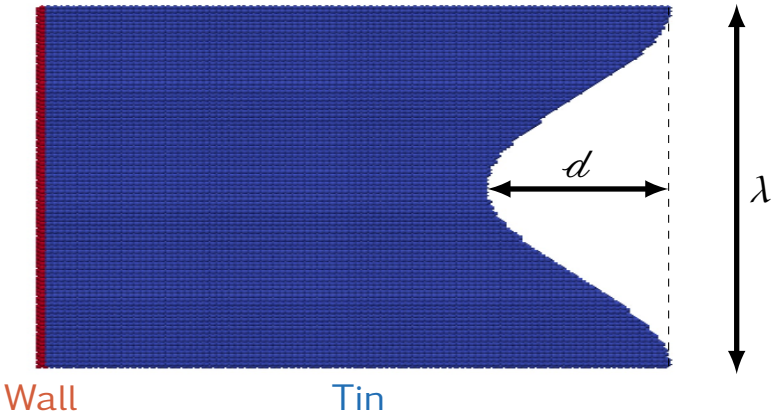


Figure 6.3 | Initial geometry of the ejecta simulations.

perturbations caused by multiple reflections of the shock wave but would obviously increase the cost of the simulation. The system is initialized at density $\rho = 7775$ $\mathrm{kg.m^{-3}}$ and temperature $T = 300$ K in the standard conditions. The simulations have been performed with the parallel code ExaStamp [21] to which SDPD has been added (see Appendix A). We integrate the dynamics with the SER scheme (see Section 4.2) with a time step $\Delta t = 10^{-15}$ s in order to avoid instabilities.

6.2.2 Results

As the shock propagates in the material, it finally reaches the rough free surface where it is reflected. The shock wave first hits the tip of the defect, at a depth d from the free surface, and ejects some particles at a higher velocity than the free surface (see Figure 6.4). An ejecta sheet is thus formed and continues to propagate in the vacuum. The spike head finally reaches a constant velocity. As the sheet is elongated, it gets thinner until it breaks up. The fragmentation of the ejecta then results in clusters of various sizes. However, in the absence of surface tension, we cannot hope to retrieve the correct size distribution or even the correct shape of the ejected clusters.

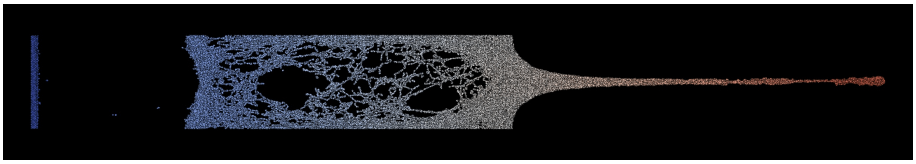


Figure 6.4 | Ejection of matter at the reflection of the shock on the free surface.

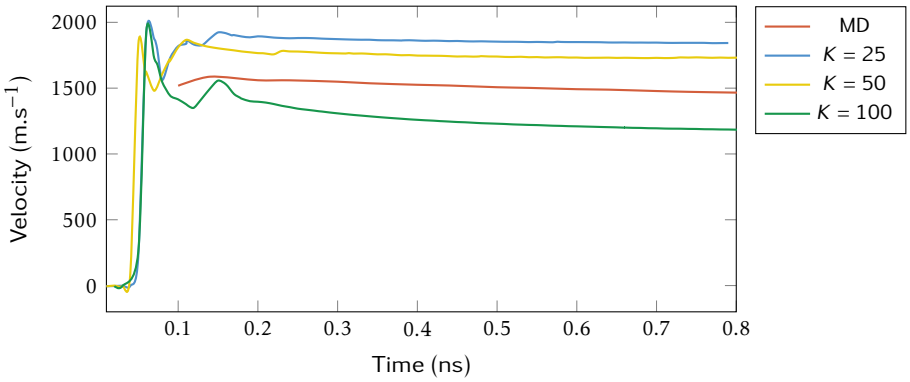


Figure 6.5 | Velocity difference between the spike head and the bubble for SDPD at different resolutions compared to MD results from [35].

In order to evaluate the results obtained from SDPD, we reproduce the MD simulations from [35] for tin. We choose a wavelength $\lambda = 154$ nm with a depth $\mathscr{a} = 50$ nm. At every 5000 time steps, we compute the density and velocity profile along the y-direction by splitting the domain in $n_{\mathrm{sl}} = 1000$ regularly distributed slices and averaging over all particles in these bins. This allows to determine two important regions for the ejecta. The head of the spike is naturally located where the particles are the farthest from the free surface. On the other hand, the bubble is defined as the beginning of the bulk behind the ejecta sheet and we determine its position as the place where the density goes over $\frac{\rho}{2}$. We compute the velocity for both the spike head (v_{sp}) and the bubble (v_{bb}) by averaging other the 5 bins around their location determined as stated above. We plot the difference $v_{\mathrm{sp}} - v_{\mathrm{bb}}$ between the spike velocity and the bubble velocity for the SDPD simulations and compare it to the MD results [35]. We notice about a 20% discrepancy between MD and SDPD. This might be explained by the absence of surface tension in our model since it is known to influence the velocities in the ejecta. The next step would be to add surface tension to SDPD in order to assess this assumption and check whether a much closer agreement can be found with MD. Apart from this expected difference between SDPD and MD, it appears that the velocity profile for $K = 100$ differs considerably from the other resolutions. The origin of this size effect is unclear. However, simulations at coarser resolutions have proved unable to properly describe the geometry used in this work with a visibly poor behavior at the formation of the ejecta. It should indeed be no surprise that a defect of a given size requires enough particle to be accurately described, hence imposing a limit on the admissible resolutions. With this observation in mind, the large discrepancy between $K = 100$ and the other SDPD simulations may indicate that this resolution is also too coarse for the defect studied here. When larger defects are considered, for instance the experimental sizes are of the order of the micrometer or millimeter, the limitations on the resolution in SDPD should allow for much larger particle sizes K.

6.2.3 Surface tension in SDPD

The surface tension plays a fundamental role to accurately simulate micro-jetting. In particular, it influences the velocity in the ejecta and the shapes and sizes of particles during the fragmentation of the spike. More generally, it plays an important role in fluid/fluid or fluid/solid interactions. As such, its inclusion in the SDPD model would represent a great improvement for the modeling of complex systems and geometries.

A number of methods have been developed in the context of SPH. A macroscopic model for the surface tension may be used by introducing a color function [16, 82, 1]. Particles in different phases are assigned a different color and the interfaces are located where the gradient of the color function is significantly different from 0. Alternatively, interfaces may be detected at a given level set of the color function seen as an indicator function for the phases. This allows to determine the surface curvature and subsequently the expression of a surface force modeling the effects of the surface tension at the continuum level. Another approach, which was also extended to SDPD [107], is to introduce additional microscopic attractive potentials that affect all particles [165]. Unlike the previous macroscopic model, it lacks a proper theoretical foundation but is very straightforward to implement. Since surface tension arises at the microscopic scale because of inter-particle attractions, this method is able to create surface tension in the SDPD system. The parameters of the additional potential function may be fitted to obtain the desired value. However the addition of extra forces modifies the pressure and we must make sure that their influence is negligible.

We tested the potential proposed in [107] that consists in the addition of an attractive and a repulsive Gaussian kernels:

$$U_{\mathrm{sf}}(r) = u_0 \left(\exp\left(-\frac{r^2}{2r_b^2} \right) - A \frac{r_a^2}{r_b^2} \exp\left(-\frac{r^2}{2r_a^2} \right) \right).$$

The parameters r_a and r_b governs the width of the attractive and repulsive Gaussian function while A sets the ratio between the two terms. Lastly u_0 fixes the amplitude of the potential. We use this potential, along with the usual SDPD interactions, for tin described by the Mie-Grüneisen equation of state (6.2) at temperature $T = 1000$ K and density $\rho = 7500$ kg.m^{-3}. We run equilibrium simulations with a system made of a slab of $10 \times 10 \times 20$ particles surrounded on each side by the same volume of vacuum. The particles size is fixed to $K = 100$. We integrate the dynamics with the SSA scheme and a time step $\Delta t = 0.2$ during a thermalisation time $\tau_{\mathrm{therm}} = 250$ and a simulation time $\tau_{\mathrm{sim}} = 1000$. In order to evaluate the surface tension γ_{s} in the system, we resort to its thermodynamic definition as the derivative of the free energy with respect to the area $\mathscr{A}$ of the interface. This allows us to derive an analytic expression for surface tension

$$\gamma_{\mathrm{s}} = \frac{1}{\mathscr{A}} \left\langle \sum_{1 \leq i < j \leq N} \boldsymbol{r}_{ij}^T \tilde{\mathfrak{J}} \boldsymbol{\mathscr{F}}_{\mathrm{cons},ij} \right\rangle_{\mu_\beta}, \tag{6.3}$$

with the matrix

$$\tilde{\mathfrak{J}} = \begin{pmatrix} -\frac{1}{2} & 0 & 0 \\ 0 & -\frac{1}{2} & 0 \\ 0 & 0 & 1 \end{pmatrix}.$$

We refer to Section B for a proof of this identity. From our observations, the parameter having the most significant effect on surface tension is the amplitude u_0. The ratio A and the radii r_a and r_b do not seem to greatly impact either the surface tension or the pressure. We use in the following $A = 32$, $r_a = \frac{h_K}{7}$ and $r_b = 2r_a$, which were used in [107]. The remaining parameter u_0 is fitted to reproduce the desired surface tension. The MD simulations that were used to optimize the Mie-Grüneisen equation of state yield a value of the surface tension $\gamma_S = 0.08\,\mathrm{N.m^{-1}}$. We find that $u_0 = 2.45 \times 10^{-3}$ J allows to recover this value. However, the pressure is strongly perturbed by the addition of these potential forces. With pure SDPD, the pressure is measured to be $P = 5.3$ GPa whereas we obtain $P = 4.2$ GPa after the inclusion of the surface tension potential. This huge discrepancy, which was not observed for a model of water in [107], cannot be neglected and we prefer to keep a correct thermodynamic behavior in our simulations. A more thorough optimization on all the parameters may improve the results but there is no guarantee that this method allows to recover both the pressure and the surface tension in the simulation. A safer route is probably to use a more founded model that can correctly describe surface tension at the SDPD scale. The color function method [16, 82, 1] looks promising but is better suited to mixture of two fluids and would need to be adapted to this context.

6.3 Detonation wave

A detonation wave is a shock wave followed by a reactive zone where exothermic chemical reactions occur. The energy generated by these exothermic reactions sustains the propagation of the shock wave that in turns heat the neat material and allows it to react. Detonation waves have been simulated successfully with MD [152, 74, 71], and more recently with a reactive version of DPDE [127, 126] or with SPH [175]

In order to simulate detonation waves with SDPD, we include, in Section 6.3.1, a reactive mechanism that allows to change the equation of state of a particle from the reactant to the products and to liberate energy through the exothermicity. We then apply this reactive SDPD in the context of a detonation wave in nitromethane in Section 6.3.2.

6.3.1 Reactive SDPD

Since chemical reactions modify inter-atomic molecular bonds, the most accurate method to simulate them is to resort to quantum mechanics where it is possible to take into account electronic effects. As mentioned in Section 1.1.1, ab-initio methods are however very limited in terms of accessible time and length scales. In practice, simulations for larger systems are performed with classical MD and complex reactive potentials [166, 171]. At a coarser level, chemical reactions are usually handled in a more statistical sense with macroscopic laws that represent the evolution of the reaction progress by means of a chemical kinetics. This was used to include a reactive mechanism to DPDE [127] and to successfully simulate detonation waves in nitromethane with this reactive DPDE [126]. We adapt it to the context of SDPD and introduce the necessary ingredients to this end: the chemical kinetics, reactive equations of state and exothermicity.

Kinetics of the chemical reaction

In the spirit of [127], we model the progress of chemical reactions by adding a progress variable $\lambda_i \in [0, 1]$ to each mesoparticle. Considering a model chemical reaction

$$A \rightleftharpoons B,$$

we associate $\lambda = 0$ to the reactant A and $\lambda = 1$ to the product B. The progress variable can be seen as the portion of the mesoparticle that has reacted. This statistical point of view gains a clearer meaning as the size of the mesoparticle increases.

The evolution of the progress variable is governed by a kinetics that can be freely chosen to model the chemical reaction. In this work, we adopt second order kinetics where mesoparticles can interact with neighboring particles. We use the smoothing kernel W as a cut-off function to limit the range of the chemical interactions. The progress variable is thus evolved as

$$\frac{\mathrm{d}\lambda_i}{\mathrm{d}t} = \sum_{j \neq i} \mathscr{K}_{0\to1}\left(T_{ij}\right)(1-\lambda_i)(1-\lambda_j)W(r_{ij}) - \mathscr{K}_{1\to0}\left(T_{ij}\right)\lambda_i\lambda_j W(r_{ij}), \tag{6.4}$$

where $\mathscr{K}_{0\to1}$ and $\mathscr{K}_{1\to0}$ are the reaction rates, respectively, for the forward and backward reactions. The reaction rates depend on the mean temperature $T_{ij} = \frac{1}{2}\left(T_i + T_j\right)$ according to some Arrhenius law :

$$\mathscr{K}_{\mathscr{X}}(T) = Z_{\mathscr{X}} \exp\left(-\frac{E_{\mathscr{X}}}{k_{\mathrm{B}}T}\right), \tag{6.5}$$

with an activation energy $E_{\mathscr{X}}$, that represents the energy barrier a molecule needs to overcome during the reaction, and a prefactor $Z_{\mathscr{X}}$ that governs the frequency of the reaction. Extension of this model to several chemical reactions would be straightforward.

Reactive equation of state

Since the equations of state for the reactants and for the product are different, we need to define a mixed equation of state when $0 < \lambda < 1$. In the following, we denote all quantities related to the reactant by a superscript 0 and to the product by a superscript 1. The functions yielding temperature and pressure from the equation of state (2.8) are thus denoted by $\mathscr{T}^0$ and $\mathscr{P}^0$ for the reactant. The internal energy of a mesoparticle, due to its extensivity, can be expressed as

$$\varepsilon_i = \varepsilon_i^0 + \varepsilon_i^1, \tag{6.6}$$

where ε_i^0 and ε_i^1 are the energies, respectively, of the reactant (a $1-\lambda$ portion of mesoparticle i) and the products (a λ portion of the mesoparticle). The density, being an intensive variable, is given as a weighted average of the density of the reactant ρ_i^0 and of the products ρ_i^1:

$$\rho_i = (1-\lambda)\rho_i^0 + \lambda\rho_i^1, \tag{6.7}$$

Note that we only have access to the internal energy ε_i and density ρ_i (through Equation (1.20)) of the whole mesoparticle, along with its progress variable λ_i. In order to obtain the temperature T_i, pressure P_i and heat capacity C_i for each mesoparticle, we need to determine the state of each chemical species (ε_i^0, ρ_i^0 and ε_i^1, ρ_i^1) thanks to a mixing law. If $\lambda_i = 0$ or $\lambda_i = 1$, the mesoparticle is actually composed purely of either A or B. Hence we may use the equation of state for the

pure chemical species. In the other cases ($0 < \lambda_i < 1$), we consider the two components to be at thermal and mechanical equilibrium inside a mesoparticle, which means that

$$\begin{aligned}\mathscr{T}^0(\varepsilon_i^0, \rho_i^0) &= \mathscr{T}^1(\varepsilon_i^1, \rho_i^1),\\ \mathscr{P}^0(\varepsilon_i^0, \rho_i^0) &= \mathscr{P}^1(\varepsilon_i^1, \rho_i^1).\end{aligned}$$

Using relations (6.6) and (6.7) to express ρ_i^1 and ε_i^1 as a function of the global state ε_i, ρ_i and of the state of the other component ε_i^0, ρ_i^0, this amounts to

$$\begin{aligned}\mathscr{T}^0(\varepsilon_i^0, \rho_i^0) - \mathscr{T}^1\left(\varepsilon_i - \varepsilon_i^0, \frac{\rho_i - (1-\lambda)\rho_i^0}{\lambda}\right) &= 0,\\ \mathscr{P}^0(\varepsilon_i^0, \rho_i^0) - \mathscr{P}^1\left(\varepsilon_i - \varepsilon_i^0, \frac{\rho_i - (1-\lambda)\rho_i^0}{\lambda}\right) &= 0.\end{aligned} \tag{6.8}$$

The computation of the energy ε_i^0 and density ρ_i^0 generally requires to resort to a numerical inversion, like the Newton method, so that Equation (6.8) holds. This finally yields the temperature $T_i = \mathscr{T}^0(\varepsilon_i^0, \rho_i^0)$ and pressure $P_i = \mathscr{P}^0(\varepsilon_i^0, \rho_i^0)$ that are used in Equation (6.4) for the chemical reactions and in the usual equations of motion of SDPD (2.18).

Exothermicity

Chemical reactions are called exothermic if they release some chemical energy (or heat) as they occur. It is naturally important to take into account such effects and an exchange between the chemical energy and the other degrees of freedom occurs as the reaction progresses. The exothermicity, which is the energy liberated by the reaction of a single molecule, is given as

$$E_{\text{exo}} = E_{1\to 0} - E_{0\to 1}$$

as illustrated in Figure 6.6. The total energy in our reactive system now reads

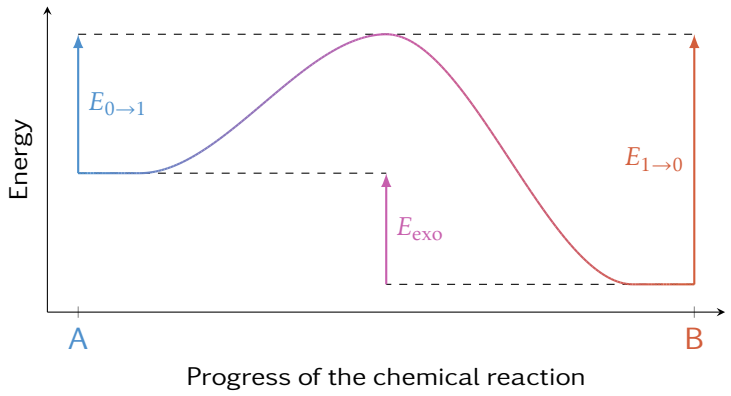


Figure 6.6 | Activation energies and exothermicity

$$E(\boldsymbol{q}, \boldsymbol{p}, \varepsilon, \lambda) = \sum_{i=1}^{N} \varepsilon_i + \frac{\boldsymbol{p}_i^2}{2m} + (1-\lambda_i) KE_{\text{exo}}.$$

Note that the chemical energy scales with the particle size K. Since we request that E is exactly preserved as the reaction progresses, the exothermicity is progressively transferred in the internal energy, inducing an evolution of the internal energy given by

$$\mathrm{d}\varepsilon_i = KE_{\mathrm{exo}}\,\mathrm{d}\lambda_i.$$

It would be possible to also release this energy in the kinetic energy at the cost of the conservation of the total momentum. In practice the exchange of energy between the internal and external degrees of freedom quickly leads to an equilibration between the kinetic and internal energy.

This reactive mechanism is coupled with the equations of motion of SDPD (2.18). Consequently, the dynamics for the reactive SDPD allows to evolve the positions, momenta, internal energies and progress variables as:

$$\begin{cases} \mathrm{d}\boldsymbol{q}_i = \dfrac{\boldsymbol{p}_i}{m_i}\,\mathrm{d}t, \\ \mathrm{d}\boldsymbol{p}_i = \displaystyle\sum_{j\neq i} m_i m_j \left(\frac{P_i}{\rho_i^2} + \frac{P_j}{\rho_j^2}\right) F_{ij}\boldsymbol{r}_{ij}\,\mathrm{d}t - \boldsymbol{\Gamma}_{ij}\boldsymbol{v}_{ij}\,\mathrm{d}t + \Sigma_{ij}\mathrm{d}\boldsymbol{B}_{ij}, \\ \mathrm{d}\varepsilon_i = \displaystyle\sum_{j\neq i} -\frac{m_i m_j P_i}{\rho_i^2} F_{ij}\boldsymbol{r}_{ij}^T\boldsymbol{v}_{ij}\,\mathrm{d}t + \frac{1}{2}\left[\boldsymbol{v}_{ij}^T\Sigma_{ij}\boldsymbol{v}_{ij} - \frac{1}{m_{ij}}\mathrm{Tr}(\Sigma_{ij}\Sigma_{ij}^T)\right]\mathrm{d}t - \frac{1}{2}\boldsymbol{v}_{ij}^T\Sigma_{ij}\mathrm{d}\boldsymbol{B}_{ij}, \\ \dfrac{\mathrm{d}\lambda_i}{\mathrm{d}t} = \displaystyle\sum_{j\neq i} \mathscr{K}_{0\to 1}\left(T_{ij}\right)(1-\lambda_i)(1-\lambda_j)W(r_{ij}) - \mathscr{K}_{1\to 0}\left(T_{ij}\right)\lambda_i\lambda_j W(r_{ij}), \end{cases} \tag{6.9}$$

The integration schemes described in Chapter 4 are therefore modified as follows:

1. Integration of the conservative part with the Velocity-Verlet scheme (see Section 4.1.1),
2. Integration of the fluctuation/dissipation (see Sections 4.1, 4.2 and 4.3),
3. Evolution of the chemical reactions.

In step 3, the kinetics (6.4) is discretized with an explicit Euler scheme. After the update of the progress variables, the internal energies are evolved by taking into account the exothermicity with

$$\varepsilon_i^{n+1} = \varepsilon_i^n + (\lambda_i^{n+1} - \lambda_i^n)KE_{\mathrm{exo}}.$$

This ensures that the total energy is preserved when integrating the reactive part of the dynamics.

6.3.2 Simulation of a detonation wave for nitromethane

We assess the validity of the reactive SDPD model by simulating the propagation of a detonation wave in nitromethane. Nitromethane (CH_3NO_2) is a high explosive that is liquid at standard pressure and temperature. We model the decomposition of nitromethane by a single irreversible exothermic reaction :

$$\mathrm{NiMe} \to \mathrm{products}.$$

Compared to the more generic framework of Section 6.3.1 for reversible reactions, the irreversibility of the reaction is achieved by taking $Z_{1\to 0} = 0$. The reaction rate follows the Arrhenius law specified in (6.5). The activation energy is $E_a = 3\times 10^{-19}$ J/molecule and the exothermicity

$E_{\text{exo}} = 4.78 \times 10^{-19}$ J/molecule as in [126]. The influence of the prefactor Z will be investigated below.

Inert nitromethane is represented by an equation of state obtained from Monte Carlo molecular simulations [28] with a force field optimized to reproduce the properties of nitromethane under shock [27]. The analytic form of the equation of state is given by

$$\mathcal{S}_{\text{NiMe}}(\varepsilon, \rho) = C_V \log\left[\frac{\varepsilon - \mathscr{E}_{\text{ref}}(\rho)}{C_V} + \theta(\rho)\right] + C_V \Gamma_0 \frac{\rho_0}{\rho}, \tag{6.10}$$

with

$$\theta(\rho) = (T_0 - T_{00}) \exp\left[\Gamma_0 \left(1 - \frac{\rho_0}{\rho}\right)\right],$$

and

$$\mathscr{E}_{\text{ref}}(\rho) = \frac{1}{2}\frac{c_0^2 x^2}{1 - sx} \times \begin{cases} 1 + \dfrac{sx}{3} - s\,(\Gamma_0 - s)\,\dfrac{x^2}{6} & \text{if } x \geq 0, \\ 1 & \text{if } x < 0, \end{cases}$$

where $x = 1 - \dfrac{\rho_0}{\rho}$, and T_0 and T_{00} are two constants defined as the standard temperature $T_0 = 298.13$ K and the temperature T_{00} on the reference curve $\mathscr{E}_{\text{ref}}$. This constant is determined as $T_{00} = \frac{E_0}{C_V}$ where E_0 is the energy in standard conditions (density ρ_0 and pressure $P_0 = 10^5$ Pa). The parameters of (6.10) are summarized in Table 6.2.

Parameter	Value	Unit
Γ_0	1	-
ρ_0	1140	kg.m^{-3}
c_0	1358.47	m.s^{-1}
C_V	1211	J.K^{-1}.kg^{-1}
s	2.000184	-

Table 6.2 | Parameters of the equation of state (6.10) for nitromethane.

The products of the reaction are modeled by a Jones-Wilkins-Lee (JWL) equation of state, introduced in [105] for reaction products. It reads

$$\mathcal{S}_{\text{JWL}}(\varepsilon, \rho) = C_V \log\left[\frac{\varepsilon - \mathscr{E}_k(\rho)}{C_V}\right] - C_V \Gamma_0 \log(\rho), \tag{6.11}$$

with

$$\mathscr{E}_k(\rho) = \frac{a}{\rho_0 R_1} \exp\left[-R_1 \frac{\rho_0}{\rho}\right] + \frac{b}{\rho_0 R_2} \exp\left[-R_2 \frac{\rho_0}{\rho}\right] + \frac{\mathfrak{K}}{\rho_0 \Gamma_0} \left(\frac{\rho_0}{\rho}\right)^{-\Gamma_0} + C_{\text{ek}},$$

using the parameters from [31], which are gathered in Table 6.3. In order to define the constants

Parameter	Value	Unit
Γ_0	0.3	-
ρ_0	1128	$\mathrm{kg.m^{-3}}$
E_0	0	J
D_{CJ}	6280	$\mathrm{m.s^{-1}}$
P_{CJ}	1.25×10^{10}	Pa
T_{CJ}	3000	K
C_V	2764.23	$\mathrm{J.K^{-1}.kg^{-1}}$
a	2.092×10^{11}	Pa
b	5.689×10^{9}	Pa
R_1	4.4	-
R_2	1.2	-

Table 6.3 | Parameters of the JWL equation of state (6.11) for reacted nitromethane (products).

$\mathfrak{K}$ and C_{ek}, we first introduce

$$\begin{cases} \rho_{\mathrm{CJ}} = \rho_0 \dfrac{\rho_0 D_{\mathrm{CJ}}^2}{\rho_0 D_{\mathrm{CJ}}^2 - P_{\mathrm{CJ}}}, \\ E_{\mathrm{CJ}} = E_0 + \dfrac{1}{2} P_{\mathrm{CJ}} \left(\dfrac{1}{\rho_0} - \dfrac{1}{\rho_{\mathrm{CJ}}} \right), \\ P_{\mathrm{k1CJ}} = a \exp\left(-R_1 \dfrac{\rho_0}{\rho_{\mathrm{CJ}}} \right) + b \exp\left(-R_2 \dfrac{\rho_0}{\rho_{\mathrm{CJ}}} \right). \end{cases}$$

Then,

$$\mathfrak{K} = \left(P_{\mathrm{CJ}} - P_{K1\mathrm{CJ}} - \frac{1}{m} C_v \Gamma_0 T_{\mathrm{CJ}} \rho_{\mathrm{CJ}} \right) \left(\frac{\rho_0}{\rho_{\mathrm{CJ}}} \right)^{\Gamma_0 + 1},$$

and

$$C_{\mathrm{ek}} = E_{\mathrm{CJ}} - \frac{a}{\rho_0 R_1} \exp\left(-R_1 \frac{\rho_0}{\rho_{\mathrm{CJ}}} \right) - \frac{b}{\rho_0 R_2} \exp\left(-R_2 \frac{\rho_0}{\rho_{\mathrm{CJ}}} \right) - \frac{P_{\mathrm{CJ}} - P_{\mathrm{k1CJ}}}{\rho_{\mathrm{CJ}} \Gamma_0}.$$

In order to observe a detonation wave in our simulations, we first create a shock wave in the neat nitromethane that transforms to a detonation wave provided the shock velocity is high enough. The time step Δt is chosen such that the particle after the initial shock wave do not move by more than 10% of the characteristic inter-particle distance during one step. We first study the transition from a shock wave to a detonation wave before turning to the analysis of the stationary behavior of the detonation wave. We conclude by studying the influence of the Arrhenius prefactor.

Shock to detonation transition

The system we consider is formed of $N = 86400$ particles initially distributed on a $12 \times 12 \times 594$ grid at the nitromethane equilibrium density $\rho = 1104\ \mathrm{kg.m^{-3}}$. The initial velocities and internal energies are chosen so that the initial temperature in the system is 300 K. Periodic boundary

conditions are used in the x- and y-directions. In the z-direction, two walls, formed of "virtual" SDPD particles as described in [14] and Section 4.3.3, are located at each end of the system. These virtual particles interact with the real SDPD particles through the conservative forces (1.27) and a repulsive Lennard-Jones potential that ensures the impermeability of the walls. After the system equilibration during $\tau_{\text{therm}} = 100$ ps, the lower wall is given a constant velocity $v_{\text{P}} = 1764$ m.s^{-1} in the z-direction. We choose the viscosity parameter $\eta = 2 \times 10^{-3}$ Pa.s so that the shock profile is smooth and no spurious oscillations are observed after the shock front. We first use a prefactor $Z = 10^{15}$ s^{-1} that is large enough to observe the shock-to-detonation transition in the spatio-temporal window of the simulation.

We carry several simulations for different particle sizes K. Since we keep the dimensions of the system constant in reduced units, the overall size in physical units increases with the particle size. Due to the different time and length scales, the time step is also dependent on K: for instance, we take $\Delta t = 1.3 \times 10^{-13}$ s for $K = 10$ and $\Delta t = 6.0 \times 10^{-13}$ s for $K = 1000$. At each step, the spatial domain is split into $n_{\text{sl}} = 450$ slices along the z-direction over which the thermodynamic variables are averaged in order to estimate instantaneous profiles. Their evolution along time is

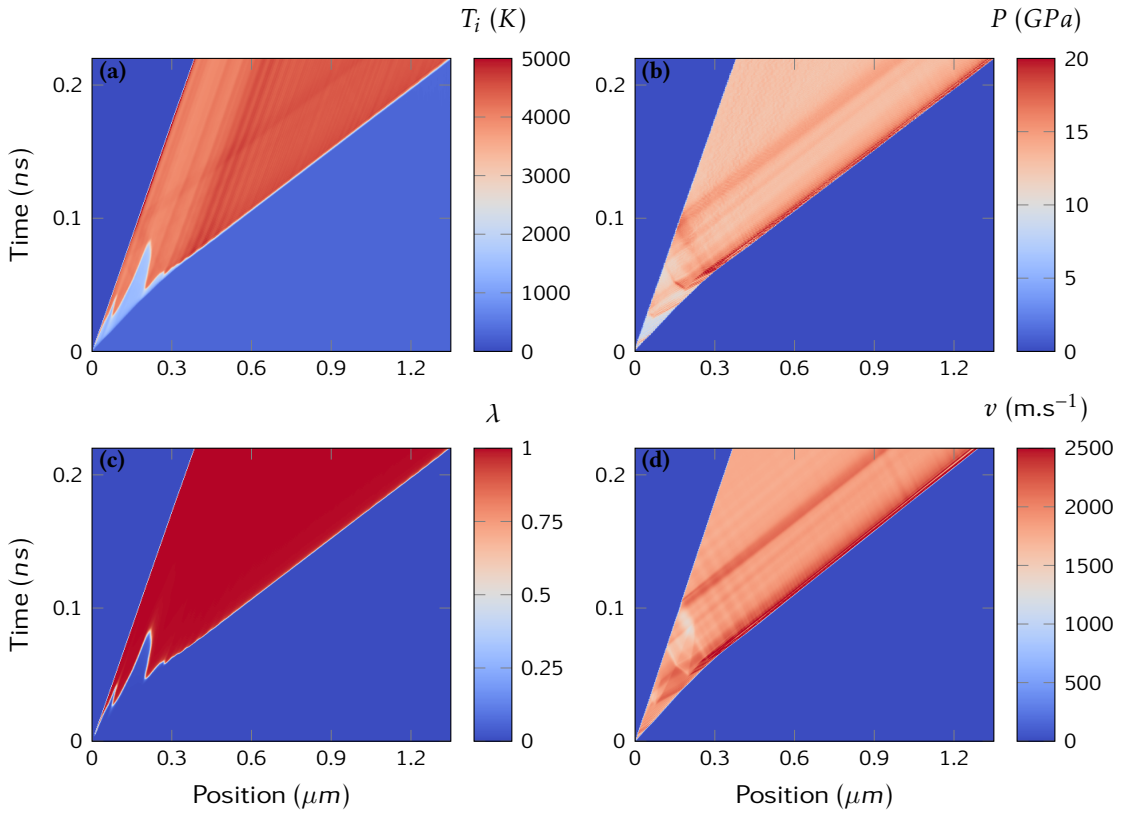


Figure 6.7 | Space-time diagram of (a) temperature, (b) pressure, (c) chemical progress and (d) material velocity for $K = 100$.

plotted in time-space diagrams (see Figure 6.7). Two distinct domains can be distinguished. First, a shock wave is formed thanks to the piston movement. While it propagates in the material, the high temperature leads to the ignition of chemical reactions in the shocked nitromethane. These reactions create compressive waves in the shocked material, leading to the appearance of new ignitions points, forward in the neat shocked nitromethane. Finally as the new ignition points

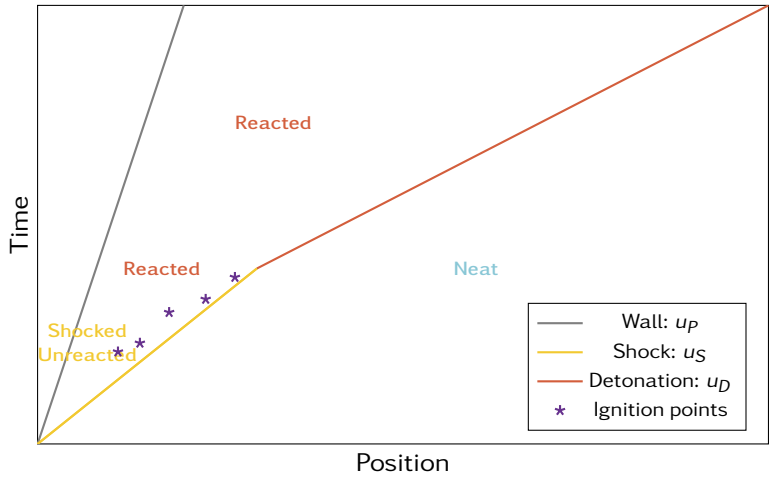


Figure 6.8 | Schematic representation of the shock-to-detonation transition in a time-space diagram

get closer to the shock front, they catch up with the shock front and begin to drive the shock at a larger velocity, hence forming a detonation wave which propagates at a constant velocity $v_{\mathrm{D}} = 6646$ m.s^{-1}. This is in good agreement with the theoretical hydrodynamic prediction which reads $D_{\mathrm{CJ}} = 6620$ m.s^{-1}. This shock-to-detonation transition mechanism is very similar to previous computations carried at a more microscopic scale with reactive DPDE [126] where the same discontinuous process, with successive ignition points in the shocked material, was observed. This mechanism is illustrated in Figure 6.8 with a schematic representation of the time-space diagrams 6.7. However this differs from hydrodynamic simulations where a reactive wave, first ignited close to the wall, catches up with the shock front, forming a so-called super-detonation propagating at a velocity higher than D_{CJ} [130]. It is still not clear what is the origin of this discrepancy. It may be an effect of the large prefactor used in [126] and in our simulations which accelerate the chemical kinetics and change its time scale compared to the hydrodynamic time scale.

We compare in Figure 6.9 the space-time diagram for particle sizes ranging from $K = 10$ to $K = 10000$. We observe the same mechanism, with ignition points catching up with the shock front, at any resolution. Moreover it seems that the shock-to-detonation transition occurs in the same physical time and length scales. A more quantitative measurement of the invariance of the transition is to track the position of the shock front during its propagation (see Figure 6.10). Inside the two domains (the non reactive shock wave and the detonation wave), the shock front propagates with a constant velocity: u_{S} for the shock wave and u_{D} for the detonation wave. The time to detonation is evaluated by extrapolating the linear evolution of the shock front in the detonation phase down to $t = 0$. The intercept of these linear interpolations with the time axis yields very close values for all particle sizes with a maximum 10% difference between $K = 10$ ($t_{\mathrm{D}}(z = 0) = 0.0157$ ns) and $K = 10000$ ($t_{\mathrm{D}}(z = 0) = 0.0140$ ns).

Steady detonation wave

We now slightly modify our setup to study steady detonation waves. The system is still formed of $N = 86400$ nitromethane particles on a $12 \times 12 \times 594$ grid at $\rho = 1104$ kg.m^{-3} and $T = 300$ K. A wall made of virtual SDPD particles is placed at one end of the system. At the other end, we insert a 50 nm layer of nitromethane particles initialized at $\rho = 1869$ kg.m^{-3} and $T = 2330$ K,

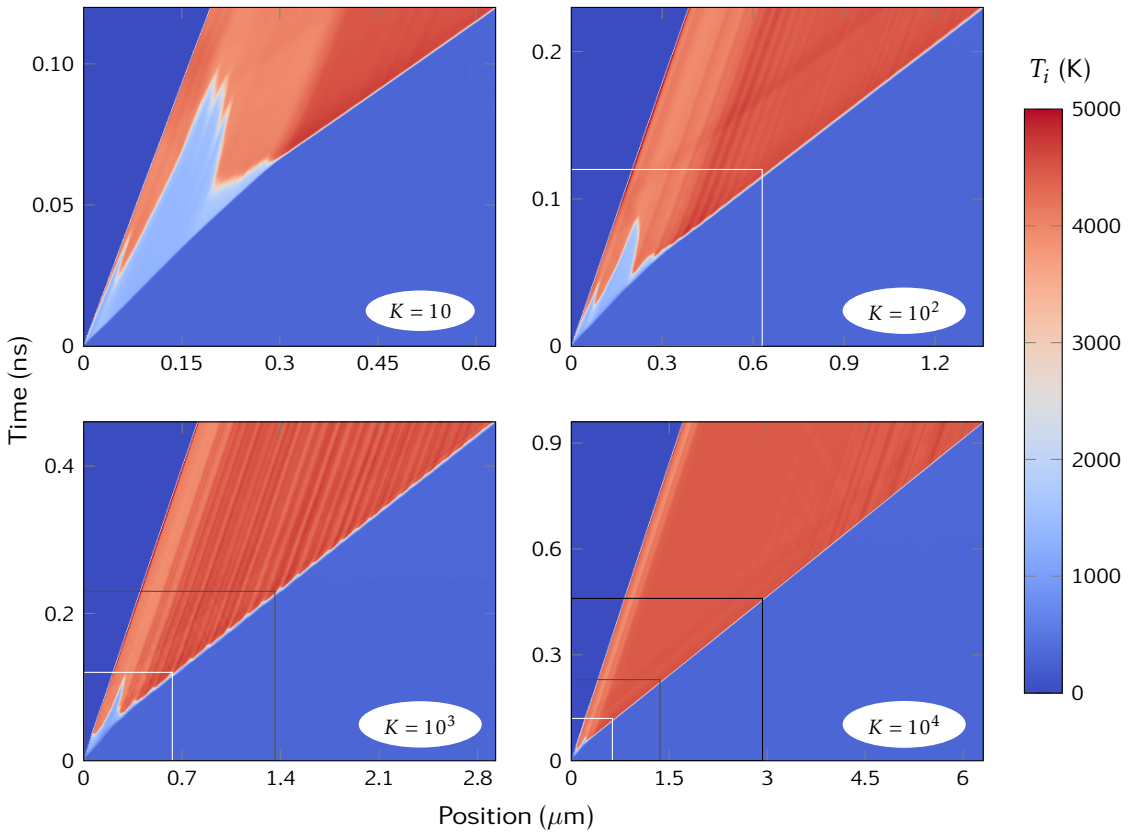


Figure 6.9 | Space-time diagram of the temperature for several particle sizes: from $K = 10$ to $K = 10000$. The size of the space-time domain explored for each resolution is displayed in the diagram of the coarser simulations with a white ($K = 10$), gray ($K = 100$) or black ($K = 1000$) frame.

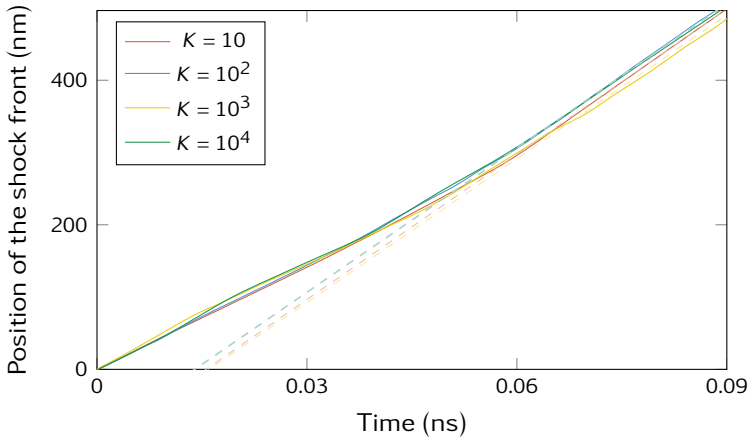


Figure 6.10 | Position of the shock front with respect to time for different particle sizes. The linear interpolation during the detonation phase is plotted in dashed lines.

which corresponds to the thermodynamic state obtained on the unreacted Hugoniot with a shock at $v_P = 2500$ m.s^{-1}. We observe a fast transition to a detonation wave that is followed by a rarefaction wave.

We check that we have reached the stationary regime with a reactive wave propagating at a constant velocity and a self-similar rarefaction wave . Figure 6.11 shows instantaneous profiles

in the reference frame of the shock front for $K = 100$. The reactive zone, where the progress

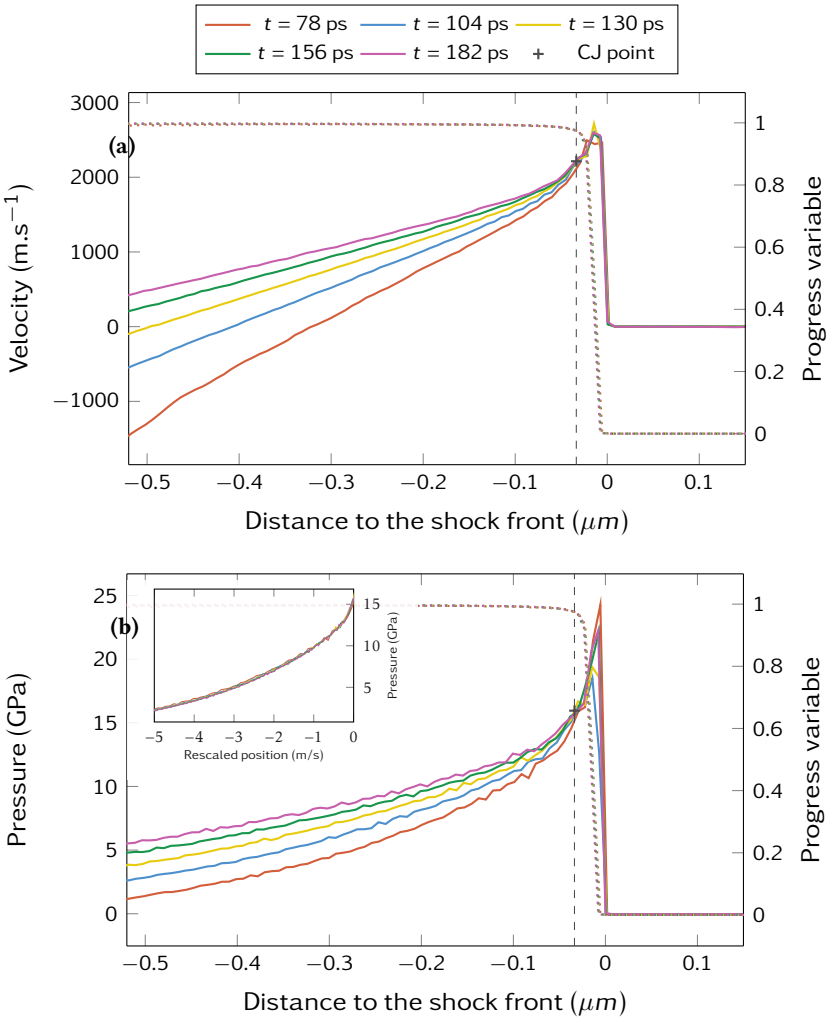


Figure 6.11 | Instantaneous profiles of (a) velocity and (b) pressure in the reference frame of the shock front. The profile of the progress variable is also displayed in dotted line on both figures. The inset in (b) is obtained by rescaling the positions as $\frac{z - z_{\mathrm{CJ}}}{t}$.

variable evolves from 0 to 1, is delimited by the pressure peak, just behind the shock front, and the CJ point determined in the pressure volume diagram (see Figure 6.12) as the tangent point between the Rayleigh line and the Crussard curve. The rarefaction wave begins after the CJ point (located at position z_{CJ}). Upon rescaling the positions z as $\frac{z - z_{\mathrm{CJ}}}{t}$ for each time t, the profiles coincide for $z < z_{\mathrm{CJ}}$, highlighting the self-similarity of the rarefaction wave.

In order to compare our results with theoretical predictions, we plot the instantaneous values of slice-averaged thermodynamic quantities in a pressure-volume diagram (see Figure 6.12) at time $t = 130$ ps for $K = 100$. Up to the thermal fluctuations present in SDPD, the thermodynamic states observed in the rarefaction wave agree very well with the isentrope computed from the equation of state (6.11). We summarize in Table 6.4 the detonation velocity for different particle sizes and compare them to the theoretical prediction obtained from the Rayleigh line in a simplified model that in particular does not account for viscosity effects. The detonation velocities in SDPD are very close to the theoretical value. It seems to be decreasing with the particle size. This is

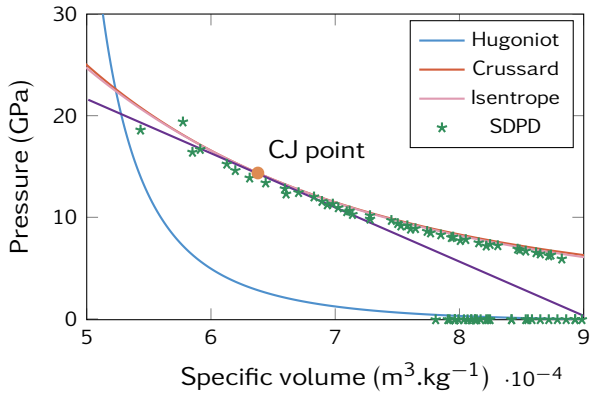


Figure 6.12 | Hugoniot, Crussard and isentrope curve of nitromethane computed from the equations of state (solid lines) and the thermodynamic states observed in the SDPD simulations with $K = 100$ (points). The Rayleigh line is also shown.

Size	Detonation velocity (m.s^{-1})
Rayleigh	6620
10	6709
100	6591
1000	6549

Table 6.4 | Detonation velocity for different particle sizes compared to the theoretical hydrodynamic prediction.

consistent with previous observations for shock waves, see Table 5.2 in Section 5.1.3.

Influence of the Arrhenius prefactor

All these results have been obtained with an arbitrarily chosen prefactor in the Arrhenius law (6.5), namely $Z = 10^{15}$ s^{-1}. We study in the following the influence of the prefactor on the properties of the detonation wave. We first turn our attention to the shock-to-detonation transition and perform the simulations reported in Section 6.3.2 for $K = 100$ and prefactors $Z = 5 \times 10^{14}$ s^{-1}, $Z = 10^{15}$ s^{-1} and $Z = 2 \times 10^{15}$ s^{-1}. All the dimensions along the z-axis are scaled by a factor $\varkappa = \dfrac{Z}{10^{15}}$. In all these settings the same mechanism is observed and we check whether a simple scaling law can predict the time to transition. In Figure 6.13, we plot the position of shock front with respect to time for several prefactors. The positions and times are rescaled by the factor $\varkappa$. Since we have taken $Z = 10^{15}$ s^{-1} as the reference, the scaling factor is $\varkappa = 1$ for the prefactor $Z = 10^{15}$ s^{-1} and its profile remains unchanged in Figure 6.13 compared to Figure 6.10. It appears that, upon a simple rescaling, the trajectories of the shock front match reasonably well for the prefactors considered here, although the one associated with the smallest prefactor ($Z = 5 \times 10^{14}$ s^{-1}) somewhat deviates from the others.

We also study the influence of the Arrhenius prefactor on the stationary properties of the detonation wave and perform the simulations described in Section 6.3.2 for $K = 100$ and prefactors $Z = 5 \times 10^{14}$ s^{-1}, $Z = 10^{15}$ s^{-1} and $Z = 2 \times 10^{15}$ s^{-1}. As for the STD transition, all the dimensions along the z-axis are scaled by the factor $\varkappa$. We compare in Figure 6.14 the pressure profile at time $\varkappa \times 130$ ps for several prefactors. The distances are also rescaled by the factor $\varkappa$. The profiles

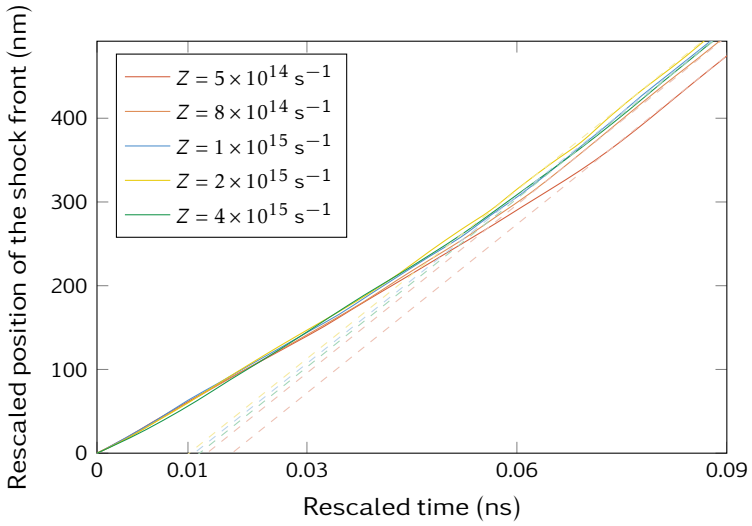


Figure 6.13 | Position of the shock front with respect to time for different prefactors.

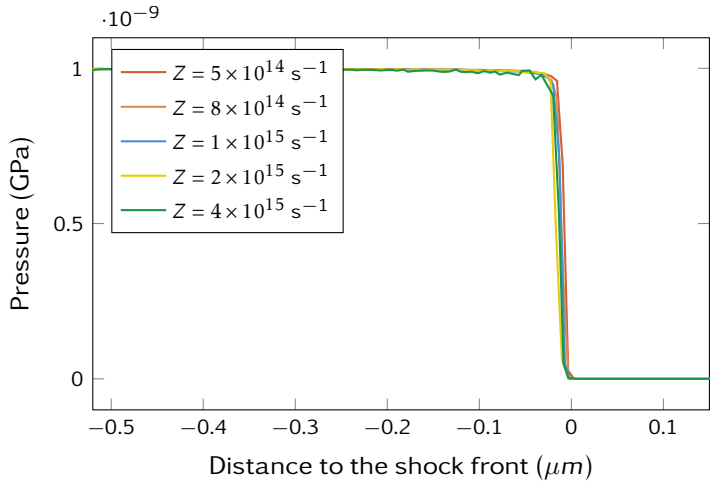


Figure 6.14 | Pressure profiles for several prefactors at time $t = \dfrac{Z}{10^{15}} \times 130$ ps. The positions are rescaled with the same factor.

agree very well with each other after the rescaling. We notice however that as the prefactor increases higher pressures are observed at the shock front. This can result in oscillations in the relaxation zone as clearly visible for $Z = 4 \times 10^{15}$ s^{-1}.

In order to study the width of the reactive zone, we average the profiles of the progress variable over time. We determine the reactive zone to be the region where the progress variable λ is significantly different from 0 or 1, that is $0.02 \leq \lambda \leq 0.98$. The widths for all tested prefactors along with the detonation velocity are gathered in Table 6.5. As expected, the detonation velocity remains very similar and close to the theoretical prediction which does not depend on the chemical kinetics. As for the reactive region, its width roughly scales as $\varkappa^{-1}$, further suggesting that the prefactor simply involves a rescaling of the domain.

In Table 6.5, it is manifest that the previous conclusions do not hold for $Z = 4 \times 10^{15}$ s^{-1} for which even the detonation velocity is off by 15%. Coupled with the observation in Figure 6.14, this suggests that a finer resolution is required to deal with fast chemical reactions. To confirm

Prefactor (s^{-1})	Width of the reactive zone (nm)	Detonation velocity ($m.s^{-1}$)
5×10^{14}	61.9	6604
8×10^{14}	39.9	6599
1×10^{15}	31.5	6591
2×10^{15}	15.6	6622
4×10^{15}	14.2	7314

Table 6.5 | Width of the reaction zone and detonation velocity for several Arrhenius prefactors.

this, we run a simulation with the prefactor $Z = 4 \times 10^{15}$ s^{-1} at a smaller particle size ($K = 10$). The detonation velocity determined with this setting, namely $u_D = 6777$ $m.s^{-1}$, is much closer to the theoretical prediction.

While the change of prefactor in the regime explored by our simulations mainly amounts to rescaling the time and length scales, it appears that we should be careful to choose a sufficiently fine resolution. As the kinetics are accelerated, with a larger prefactor, the reactive mechanism described in Section 6.3.1 in which the chemical reactions are averaged inside each mesoparticle, becomes unable to properly handle fast reactions for large particles. Except for this limitation, SDPD has proved to be able to simulate detonation waves with a much coarser resolution than MD or DPDE and still recover not only the stationary properties but also the STD transition mechanism observed in [127, 126].

Conclusion

In this thesis, we have considered mesoscopic methods that could bridge the gap between microscopic and macroscopic models for the simulation of fluid dynamics. This means that, on one hand, they include the appropriate atomistic ingredients that enhance the accuracy and allow it to deal with complex phenomena and, on the other hand, that they offer a consistent way to change their resolution from a microscopic scale to a macroscopic one. This effectively increases the accessible time and length scales that can be simulated with a good accuracy and enable the simulation of complex phenomena such as wave collision, large deformation or reactive materials. Furthermore, while MD allows for an accurate simulation of a material behavior, scaling laws often need to be assumed in order to compare MD results with experimental observations. Mesoscopic methods can provide a way to validate these postulated scaling laws by studying systems on par with the experimental time and length scales. Another possibility that a model consistent at several resolutions lets us envision is to devise a concurrent multiscale coupling. This should be particularly helpful for shock waves where a fine description is required at the shock front while a much coarser one can capture the physics in the rest of the domain.

This thesis has mainly focused on a mesoscopic model called Smoothed Dissipative Particle Dynamics (SDPD) that couples a particle discretization of the Navier-Stokes equation and thermal fluctuations scaling consistently with the resolution. These two foundations, respectively from macroscopic and microscopic origins, provides SDPD with the means to consistently simulate fluids over a wide range of resolutions. In Chapter 3, we have also validated the key assumption that allowed the derivation of the coarse-grained model Dissipative Particle Dynamics with Energy conservation (DPDE) from first principles. This provided a way to parametrize the equation of state in DPDE by using the entropy of a single isolated molecule.

In SDPD the fluid particles are characterized by the positions and momenta of their centers of mass along with an internal variable that takes into account the coarse-grained degrees of freedom. From the original formulation where the internal degrees of freedom were represented by the entropy, we have reformulated the equations of SDPD in terms of internal energies in Chapter 2. This has the advantage to increase the structural similarity with DPDE. We have determined the form of some invariant measures for the energy reformulation of SDPD, which has allowed us to establish estimators for temperature and pressure.

Thanks to the reformulation of the equations of SDPD and the increased structural similarity with DPDE, numerical schemes devoted to the integration of DPDE have been adapted in the context of SDPD in Chapter 4. These integration algorithms focus on ensuring a good conservation

of the energy, the SSA scheme being the most accurate while SER's main advantage relies in its straightforward parallelization. The stability of SSA has been greatly enhanced by the addition of a Metropolis procedure that prevent internal energies to become negative.

In Chapter 5, we have shown that SDPD yields consistent results for a wide range of resolutions both at equilibrium and in non-equilibrium situations, namely shock waves. The size consistency demonstrated for SDPD enticed us to propose a concurrent multiscale coupling between SDPD at two different resolutions that would allow to concentrate the computation power only where a fine resolution is needed. It gives satisfying results at equilibrium with very limited bias in the average properties for both resolutions.

The ability of SDPD to provide physical insight, in particular to probe the validity of scaling laws, for real systems was demonstrated by simulating micro-jetting and detonation wave in Chapter 6. The thermodynamic consistency with the microscopic description of matter was ensured by fitting the SDPD equations of state from MD simulations. Micro-jetting simulations have been carried and are in a qualitative agreement with MD provided the resolution is fine enough compared to the defect size. A reactive mechanism has also been included to extend SDPD to reactive materials. This has allowed us to simulate detonation waves and observe the same mechanism for the shock to detonation transition that was previously observed with reactive DPDE.

During this thesis, particle mesoscopic methods, namely DPD, DPDE and SDPD, have been implemented within the massively parallel MD code ExaStamp [21, 20] developed at CEA/DAM to take full advantage of the next generation of supercomputers. This allows to efficiently simulate matter at the mesoscopic scale and should prove most useful to further increase the time and length scales these methods can reach.

Outlook and perspectives

The enhanced structural similarity between SDPD and DPDE has allowed us to propose several integration schemes for SDPD. However, due to the pairwise nature of the fluctuation/dissipation interactions in these mesoscopic methods, most of the numerical schemes devoted to their integration are not easily parallelized. While this latter property is satisfied by the SER scheme, this scheme suffers from significantly larger energy drifts and increased stability issues compared to the SSA scheme that handles pairs sequentially. It would be most beneficial to increase the accuracy and stability of the SER scheme, for instance by increasing its order or adapting the Metropolization procedure that has greatly enhanced the stability of the SSA scheme in this context. This a major challenge to further extend the spatial and temporal range of these mesoscopic methods thanks to an efficient and accurate integration algorithm.

Since SDPD has proved to remain consistent with its equation of state over a large range of resolution, we have proposed a multiscale coupling between SDPD at different resolutions. This proof of concept can be improved, especially to avoid the spurious peaks that have been observed at the interfaces between the coarse and fine resolutions. It is very appealing for shock related problems since the shock front, which is a small part of the domain, concentrates most of the accuracy needs. However, it requires to decide on the fly which region should be refined as the shock front propagates within the material and its location thus cannot be determined a priori. A possible way to do this is to detect large gradients in quantities like density or velocity. Moreover, an extension to a multiscale coupling with other mesoscopic models, *e.g.* DPDE, would

allow to use a microscopic and accurate model where it is needed (for instance near the shock front). As the distance with the region of interest increases, the description of matter could then be progressively coarsened by successive couplings between SDPD at different resolutions.

Finally the physical relevance of the method can be enhanced by further modeling efforts to include important physical microscopic features. In particular, adding surface tension effects in SDPD would allow to properly describe free surface or interfaces between several fluids. Surface tension plays a major role in simulations like micro-jetting and would allow for a more quantitative comparison of SDPD with MD simulations and experimental observations.

A ExaStamp

ExaStamp [21, 20] is a MD code developed at CEA/DAM written in the C++ language. It aims at taking full advantage of the highly parallel architecture of current and future supercomputers. In order to reach the exaflop, that is 10^{18} floating point operations per second, processors now include multiple processing units, or cores, on the same chip. While different processors must resort to costly communications to exchange information, cores on the same processors are connected to the same memory which grants them a faster access to the data residing on their processors. Modern cores are also equipped with vectorized processing units, also called Single Instruction Multiple Data (SIMD). As the name suggests, it allows to perform the same operation on several data elements organized in a contiguous vector at the same time.

These three levels of parallelism have guided the design and implementation of ExaStamp in [21, 20]. We present in Section A.1 the main elements constituting ExaStamp architecture. In Section A.2 we focus on our implementation of mesoscopic methods (DPD, DPDE and SDPD) in ExaStamp.

A.1 The architecture

The main structure in ExaStamp relies on four objects: the `Node`, which implements high level functions at the level of a MPI process, the `Domain`, which represents a part of the physical domain Ω, the `Grid`, which consists in a domain decomposition into cells (see Section 1.1.1), and the `CellList` where the particle data is stored and the computations actually done. This architecture is summarized in Figure A.1.

The `Node` corresponds to the first level of parallelism where the work is split on a distributed memory system thanks to the MPI library [131]. Each MPI process is associated to a single Node which contains one or several `Domains`. The `Node` is responsible for handling inputs and outputs as well as the communications between MPI processes thanks to a communication manager (`CommManager`). The computation of the potential interactions may indeed involve particles located in different `Domains`. In such cases, the domain responsible for updating the particle positions need to transmit the information to neighboring `Domains` at each step. Communications may also occur when a particle moves out of a `Domain` and is affected to another one. The time loop involved for physical computations is also managed by the `Node` through an `IntegrationScheme` that interacts with the `Domain` with high level instructions, *e.g.* computing the forces or updating the positions of the particles.

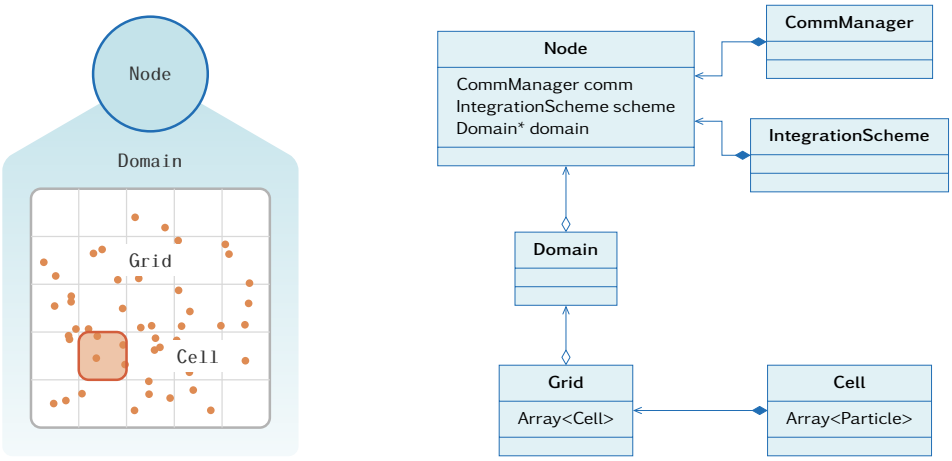


Figure A.1 | Overview of the ExaStamp architecture (from [20]).

The `Domain` breaks these high-level tasks into elementary functions which are passed on to the `Grid`. This latter object contains an array of `CellLists`. As mentioned in Section 1.1.1, this spatial decomposition is useful to limit the cost of neighbor search. Here it is also where the second level of parallelism intervenes and distributes the work in a shared memory system. Most functions in the `Grid` indeed consist in looping over `CellLists` to call the instruction required by the `Domain`. Thanks to the TBB library [84], this loop is split among several threads that can work concurrently on different `CellLists`. The work within the `CellLists` is indeed mostly independent from the others. When computations involve several particles, typically for forces evaluation, and provided that the input data (*e.g.* the positions for potentials) does not change, the only interactions between threads occur when the output data (*e.g.* the forces) are updated in the `CellLists`. A system of locks avoid the modification of the same `CellList` at the same time by different threads.

Finally the `CellList` contains the particles data organized in arrays, in particular for each coordinate of the positions and momenta. It also implements all the low level elementary functions which need to access the particles information. An explicit vectorization library (Libevi) was developed to take advantage of the vectorized processing units. It wraps the vectorized instructions, which are processor-specific, so that ExaStamp can use them almost transparently and provides vectorized versions of the functions demanding a lot of computations, for example the evaluation of the potential forces. In order to fully accelerate the computational work, this requires a good management of the memory by stacking data in contiguous arrays.

A particularly interesting feature for the mesoscopic methods we consider in this thesis is the parallel random number generator implemented in ExaStamp. The SARU pseudo-random generator [2] actually works as a deterministic function that, given three input variables, yields a pseudo-random number with good statistical properties. This allows to reproduce the same random number on every processor when needed. For instance, for a pair of particles (i, j), using $i + j$ and $i \times j$ along with the iteration number n as the input of the SARU generator ensures that the resulting number is equal on every processor. This is crucial when interactions between particles located on different processors are considered.

A.2 Implementation of mesoscopic models

During this thesis, we implemented several mesoscopic models, namely DPD, DPDE and SDPD, in ExaStamp. Since they require not only specific functions but also to store additional data, *e.g* internal energy or density, we separated their implementation from the one dedicated to classic MD by adding specific `CellLists`. We now denote the original `CellList` handling MD by `CellListAtom`.

The new `CellList` for DPD and DPDE, called `CellListMesoparticle`, inherits from `CellListAtom`. This enables it to take advantage of all the already implemented tasks like neighbor search or potential force computation that are shared by all methods. A storage for internal energy was added to `CellListMesoparticle`, along with some convenient variables: the fluctuation/dissipation forces and the internal temperature. In DPDE, the internal temperature is related to the internal energy by an equation of state. A generic member function in `CellListMesoparticle` allows to call a dedicated SIMD kernel to evaluate the equation of state associated with each type of mesoparticle. The main additions to the `CellList` are related to the computation of the fluctuation/dissipation forces for DPD and DPDE and their integration with splitting schemes (see Section 1.1.3). For DPD an explicit Euler scheme is used for the fluctuation/dissipation part while we resort to SER [79] for DPDE. Both of them are well adapted for parallelism compared to Shardlow-like schemes which requires to handle the pairs successively. The total fluctuation/dissipation forces for each particle are first computed with a first parallel loop on the `CellLists`. While the explicit Euler scheme for DPD then simply consists in updating the velocities, SER for DPDE requires the knowledge of the pairwise fluctuation/dissipation forces to integrate the internal energy equation. In order to avoid an expensive storage of all pair interactions, the fluctuation/dissipation forces are recomputed during the energy update thanks to the reproducibility of the random number generated by SARU. Vectorized versions using the Libevi library allow to further accelerate the force computations.

A specific `CellListSmoothparticle` has been implemented to handle SDPD. It inherits from `CellListMesoparticle` to reuse the computation of fluctuation/dissipation forces and their integration with SER. Additional variables are stored to described the thermodynamic state of the particles: density, entropy, pressure and heat capacity. The functions introduced for the equations of state in DPDE are extended to take the density as well as the energy or the entropy as input and vectorized equations of state are provided to evaluate the thermodynamic variables. The main difference with the other methods implemented in ExaStamp reside in the SDPD conservative forces which depend on the density of a particle and its neighbors. Two loops on particles pairs are thus needed: the first one to evaluate the density and the second one to compute the conservative forces after all thermodynamic quantities have been updated. In between a communication allows neighboring `Nodes` to exchange information and update the densities in the ghost cells.

A reactive mechanism has been included at the level of `CellListMesoparticle` by means of an additional progress variable and the functions allowing to evolve it along time. While the full implementation of reactive DPDE still requires reactive potentials that may change as the reaction progresses, a generic framework allows to switch the SDPD equations of state from the product to the reactant, hence enabling simulations with reactive SDPD in ExaStamp. We have also added virtual SDPD particles that move at a constant velocity in order to simulate walls as described in Section 4.3.3.

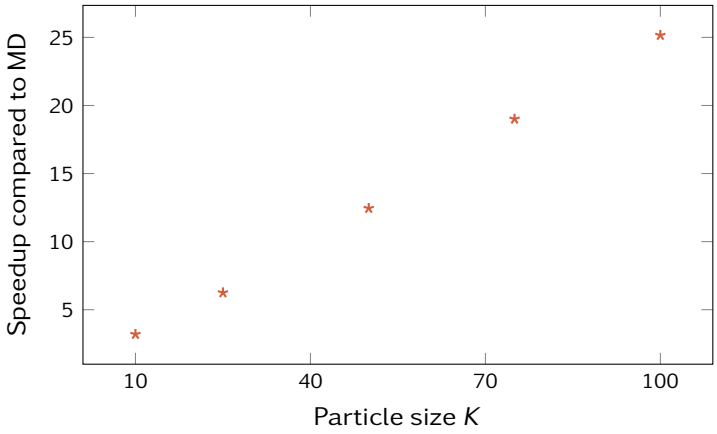


Figure A.2 | Speedup as a function of the particle size in SDPD compared to MD. The MD potential is of EAM type while a Mie-Grüneisen equation of state is used for SDPD. All simulations are carried for the same physical spatial and temporal domain.

We provide in Figure A.2 a comparison between the computational cost of MD and SDPD at different resolutions and plot the speedup evaluated as the ratio between the computation times for MD and for SDPD. MD simulations are performed with an EAM potential optimized for tin while we resort to the Mie-Grüneisen equation of state (6.2) for tin in SDPD. For all simulations, which are carried out with ExaStamp, the system is constituted of 2×10^6 tin atoms at density $\rho = 7775$ kg.m^{-3} and temperature $T = 600\ K$. The time step is fixed to $\Delta t = 10^{-15}$ s and the total time to $1000\Delta t$. This means that the same physical spatial and temporal domain is used for all particle sizes. MD is integrated with the Velocity-Verlet scheme and SDPD with SER. The speedup varies linearly with a slope $\frac{K}{4}$. The linear behavior simply accounts for the diminution of the number of particles as their size increases. A further acceleration should be observed for larger particle sizes if we adapt the time step to the resolution. As seen in Chapter 4, a coarse resolution indeed allows for larger time steps to be used in terms of both energy conservation and stability. The factor $\frac{1}{4}$ comes from the respective cost of an iteration of MD and SDPD for an equal number of particles. The increased cost of a time step with SDPD is however largely compensated by the reduction of the degrees of freedom and effectively allows to simulate larger systems at a reduced cost with SDPD.

B Surface tension

We check in this section that the identity (6.3) provides an estimator for the surface tension in a SDPD system.

The surface tension γ_s is defined as the derivative of the free energy $\mathscr{F}$ with respect to the surface area $\mathscr{A}$ at constant volume $\mathscr{V} = |\Omega|$:

$$\gamma_s = \partial_{\mathscr{A}} \mathscr{F}.$$

Since the free energy $\mathscr{F}(\beta, \mathscr{V})$ is related to the partition function Z_β as

$$\mathscr{F}(\beta, \mathscr{V}) = -\frac{1}{\beta} \log Z_\beta(\beta, \mathscr{V}),$$

we may also write the surface tension as

$$\gamma_s = -\frac{1}{\beta} \frac{\partial_{\mathscr{A}} Z_\beta}{Z_\beta}. \tag{B.1}$$

In the following we find a more explicit formulation of the surface tension in SDPD. Considering a system with periodic boundary conditions made of a slab of material for z-coordinates $z^- < z < z^+$ and of vacuum for $z_{\min} < z < z^-$ and $z^+ < z < z_{\max}$, *i.e.* with planar interfaces orthogonal to the z-axis (see Figure B.1), the area of the free surfaces is

$$\mathscr{A} = 2\delta_x \delta_y,$$

where δ_x and δ_y are the extension of the domain in the x-and y-directions.

In order to evaluate the variation of the free energy with respect to the surface area, we follow the same ideas as for pressure (see Section 2.4.3) and introduce a spatial dilation $\tilde{\boldsymbol{q}} = \boldsymbol{J}_\lambda \boldsymbol{q}$ that will change the surface area but keep the total volume constant. For instance

$$\boldsymbol{J}_\lambda = \begin{pmatrix} \frac{1}{\sqrt{1+\lambda}} & 0 & 0 \\ 0 & \frac{1}{\sqrt{1+\lambda}} & 0 \\ 0 & 0 & 1+\lambda \end{pmatrix}$$

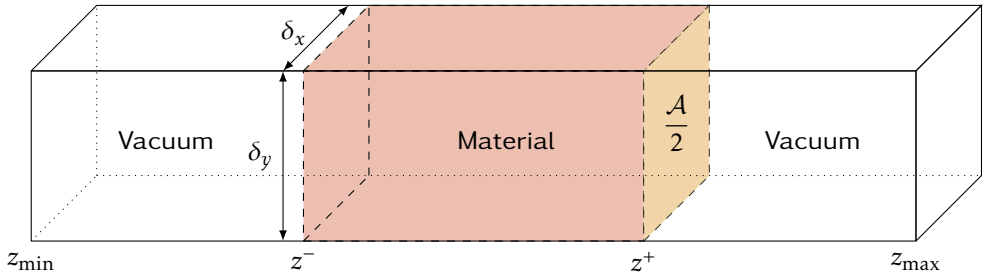


Figure B.1 | Planar interfaces for the estimation of surface tension.

for $\lambda > -1$. With this dilation, the area of the free surfaces is now given by

$$\mathscr{A}(\lambda) = \frac{2\delta_x \delta_y}{1+\lambda}, \tag{B.2}$$

while the volume remains constant $|\boldsymbol{J}_\lambda \Omega| = |\Omega|$. In order to compute the derivatives of Z_β with respect to the surface area, we consider the partition function associated with the domain $\boldsymbol{J}_\lambda \Omega$. From Section 2.4.3, it reads

$$\mathscr{Z}(\lambda) = \mathscr{Z}_\beta \int_{[\boldsymbol{J}_\lambda \Omega]^N} \prod_{i=1}^N \left[\int_{\mathbb{R}_+} \exp\left(\frac{S_i(\varepsilon_i, \tilde{\boldsymbol{q}})}{k_\mathrm{B}} - \beta \varepsilon_i \right) \mathrm{d}\varepsilon_i \right] \mathrm{d}\tilde{\boldsymbol{q}},$$

where the normalization constant $\mathscr{Z}_\beta = k_\mathrm{B}^N \beta^{5N/2} (2\pi)^{-3N/2} \left(\prod_{i=1}^N m_i \right)^{-3/2}$ does not depend on the surface area $\mathscr{A}$. We map back the integration domain to Ω^N thanks to a change of variables and obtain

$$\mathscr{Z}(\lambda) = \mathscr{Z}_\beta \times \int_{\Omega^N} \prod_{i=1}^N \left[\int_{\mathbb{R}_+} \exp\left(-\beta \varepsilon_i + \frac{S_i(\varepsilon_i, \boldsymbol{J}_\lambda \boldsymbol{q})}{k_\mathrm{B}} \right) \mathrm{d}\varepsilon_i \right] \mathrm{d}\boldsymbol{q}.$$

Note that $\lambda = 0$ corresponds to no dilation and thus $\mathscr{Z}(0) = Z_\beta$. Using Equation (B.2), it holds $\mathscr{A}'(0) = -\mathscr{A}(0)$. The derivative of the partition function Z_β with respect to the surface area $\mathscr{A}$ can then be written as

$$\partial_{\mathscr{A}} Z_\beta = \frac{\mathscr{Z}'(0)}{\mathscr{A}'(0)} = -\frac{\mathscr{Z}'(0)}{\mathscr{A}(0)}.$$

We now need to derive $\log(\mathscr{Z}(\lambda))$ with respect to λ at $\lambda = 0$ as

$$\frac{\mathscr{Z}'(0)}{\mathscr{Z}(0)} = \frac{\mathscr{Z}_\beta}{Z_\beta} \int_{\Omega^N \times \mathbb{R}_+^N} \partial_\lambda \left(\sum_{i=1}^N \frac{S_i(\varepsilon_i, \boldsymbol{J}_\lambda \boldsymbol{q})}{k_\mathrm{B}} \right) \Bigg|_{\lambda=0} \exp\left(\sum_{i=1}^N -\beta \varepsilon_i + \frac{S_i(\varepsilon_i, \boldsymbol{q})}{k_\mathrm{B}} \right) \mathrm{d}\varepsilon \, \mathrm{d}\boldsymbol{q}. \tag{B.3}$$

In order to evaluate (B.3), we first need to compute the derivatives of the density ρ_i and of the entropy S_i with respect to λ. We have, by deriving Equation (1.20),

$$\partial_\lambda \left[\rho_i \left(\boldsymbol{J}_\lambda \boldsymbol{q} \right) \right] = \sum_{j \neq i} m_j \partial_\lambda [W(\boldsymbol{J}_\lambda \boldsymbol{r}_{ij})] = -\sum_{j \neq i} m_j F(\boldsymbol{J}_\lambda \boldsymbol{r}_{ij}) \boldsymbol{r}_{ij}^T \partial_\lambda \boldsymbol{J}_\lambda \boldsymbol{r}_{ij},$$

where

$$\partial_\lambda \boldsymbol{J}_\lambda = \begin{pmatrix} -\frac{1}{2}(1+\lambda)^{-\frac{3}{2}} & 0 & 0 \\ 0 & -\frac{1}{2}(1+\lambda)^{-\frac{3}{2}} & 0 \\ 0 & 0 & 1 \end{pmatrix}.$$

With this result and the equation of state (2.8), we can compute the derivative of the entropies as

$$\partial_\lambda [S_i\left(\varepsilon_i, \boldsymbol{J}_\lambda \boldsymbol{q}\right)] = \partial_\lambda [\rho_i(\boldsymbol{J}_\lambda \boldsymbol{q})] \partial_{\rho_i} S_i = \sum_{j \neq i} \frac{m_i m_j P_i}{\rho_i^2 T_i} F(\boldsymbol{J}_\lambda \boldsymbol{r}_{ij}) \boldsymbol{r}_{ij}^T \partial_\lambda \boldsymbol{J}_\lambda \boldsymbol{r}_{ij}.$$

Finally, plugging these expressions evaluated at $\lambda = 0$ in equation (B.3) leads to

$$\begin{aligned} \frac{\mathscr{Z}'(0)}{\mathscr{Z}(0)} &= \frac{\mathscr{Z}_\beta}{Z_\beta} \int_{\Omega^N \times \mathbb{R}_+^N} \left[\sum_{i=1}^N \sum_{j \neq i} m_i m_j F_{ij} \frac{P_i}{\rho_i^2 T_i} \boldsymbol{r}_{ij}^T \partial_\lambda \boldsymbol{J}_1 \boldsymbol{r}_{ij} \right] \prod_{k=1}^N \exp\left(-\beta \varepsilon_k + \frac{S_k(\varepsilon_k, \boldsymbol{q})}{k_\mathrm{B}} \right) \mathrm{d}\varepsilon \, \mathrm{d}\boldsymbol{q} \\ &= \sum_{i=1}^N \beta Z_\beta^{-1} \int_{\mathscr{E}} \left[\frac{P_i}{\rho_i^2} \sum_{j \neq i} m_i m_j F_{ij} \boldsymbol{r}_{ij}^T \partial_\lambda \boldsymbol{J}_1 \boldsymbol{r}_{ij} \right] \exp\left(-\beta \sum_{k=1}^N \left[\frac{\boldsymbol{p}_k^2}{2m_k} + \varepsilon_k \right] \right) \frac{\exp\left(\frac{S_i}{k_\mathrm{B}}\right)}{T_i} \\ &\qquad \times \prod_{k \neq i} \frac{\exp\left(\frac{S_k}{k_\mathrm{B}}\right)}{T_\beta} \, \mathrm{d}\boldsymbol{q} \, \mathrm{d}\boldsymbol{p} \, \mathrm{d}\varepsilon. \end{aligned}$$

In each term of the sum, we use the relation (2.36) for all variables ε_k with $k \neq i$, which gives

$$\frac{\mathscr{Z}'(0)}{\mathscr{Z}(0)} = \beta \int_{\mathscr{E}} \left[\sum_{i=1}^N \sum_{j \neq i} m^2 F_{ij} \boldsymbol{r}_{ij}^T \mathfrak{J} \boldsymbol{r}_{ij} \frac{P_i}{\rho_i^2} \right] \mu_\beta(\mathrm{d}\boldsymbol{q} \, \mathrm{d}\boldsymbol{p} \, \mathrm{d}\varepsilon),$$

with

$$\mathfrak{J} = \partial_\lambda \boldsymbol{J}_0 = \begin{pmatrix} -\frac{1}{2} & 0 & 0 \\ 0 & -\frac{1}{2} & 0 \\ 0 & 0 & 1 \end{pmatrix}.$$

We can finally compute the surface tension in a SDPD system using (B.1):

$$\gamma_\mathrm{s} = \frac{1}{\beta \mathscr{A}(0)} \frac{\mathscr{Z}'(0)}{\mathscr{Z}(0)} = \frac{1}{\mathscr{A}(0)} \left\langle \sum_{1 \leq i < j \leq N} \boldsymbol{r}_{ij}^T \mathfrak{J} \boldsymbol{\mathcal{F}}_{\mathrm{cons},ij} \right\rangle_{\mu_\beta},$$

with the forces $\boldsymbol{\mathcal{F}}_{\mathrm{cons},ij}$ defined in Equation (1.27).

Bibliography

[1] S. Adami, X. Hu, and N. Adams. A new surface-tension formulation for multi-phase SPH using a reproducing divergence approximation. *J. Comput. Phys.*, 229(13):5011 – 5021, 2010.
➢ Cited on pages 107 and 108.

[2] Y. Afshar, F. Schmid, A. Pishevar, and S. Worley. Exploiting seeding of random number generators for efficient domain decomposition parallelization of dissipative particle dynamics. *Comput. Phys. Commun.*, 184(4):1119 – 1128, 2013.
➢ Cited on pages 72 and 126.

[3] R. L. C. Akkermans and W. J. Briels. Coarse-grained dynamics of one chain in a polymer melt. *J. Chem. Phys.*, 113(15):6409–6422, 2000.
➢ Cited on pages 11 and 49.

[4] B. J. Alder and T. E. Wainwright. Phase transition for a hard sphere system. *J. Chem. Phys.*, 27(5):1208–1209, 1957.
➢ Cited on page 1.

[5] M. Allen and D. Tildesley. *Computer Simulation of Liquids*. Oxford Science Publ. Clarendon Press, 1989.
➢ Cited on pages 6 and 7.

[6] J. Anderson. *Computational Fluid Dynamics*. Computational Fluid Dynamics: The Basics with Applications. McGraw-Hill Education, 1995.
➢ Cited on pages 2 and 15.

[7] J. B. Avalos and A. D. Mackie. Dissipative particle dynamics with energy conservation. *Europhys. Lett.*, 40(2):141, 1997.
➢ Cited on pages vii, 2, 11, 12, 30, and 40.

[8] D. Barcarolo, D. L. Touzé, G. Oger, and F. de Vuyst. Adaptive particle refinement and derefinement applied to the smoothed particle hydrodynamics method. *J. Comput. Phys.*, 273:640 – 657, 2014.
➢ Cited on pages 94 and 98.

[9] A. P. Bartók, M. C. Payne, R. Kondor, and G. Csányi. Gaussian approximation potentials: The accuracy of quantum mechanics, without the electrons. *Phys. Rev. Lett.*, 104:136403, 2010.
➢ Cited on page 62.

[10] A. Bartòk-Pártay. *The Gaussian Approximation Potential*. PhD thesis, University of Cambridge, 2010.
➢ Cited on page 62.

[11] M. I. Baskes. Modified embedded-atom potentials for cubic materials and impurities. *Phys. Rev. B*, 46:2727–2742, 1992.
➢ Cited on page 7.

[12] M. Berger and P. Colella. Local adaptive mesh refinement for shock hydrodynamics. *J. Comput. Phys.*, 82(1):64 – 84, 1989.
➢ Cited on pages 2, 15, and 94.

[13] M. J. Berger and J. Oliger. Adaptive mesh refinement for hyperbolic partial differential equations. *J. Comput. Phys.*, 53(3):484 – 512, 1984.
➢ Cited on pages 2, 15, and 94.

[14] X. Bian, S. Litvinov, R. Qian, M. Ellero, and N. A. Adams. Multiscale modeling of particle in suspension with smoothed dissipative particle dynamics. *Phys. Fluids*, 24(1):012002, 2012.
➢ Cited on pages 25, 82, and 114.

[15] H. Bock, K. E. Gubbins, and S. H. L. Klapp. Coarse graining of nonbonded degrees of freedom. *Phys. Rev. Lett.*, 98:267801, 2007.
➢ Cited on page 14.

[16] J. Brackbill, D. Kothe, and C. Zemach. A continuum method for modeling surface tension. *J. Comput. Phys.*, 100(2):335 – 354, 1992.
➢ Cited on pages 107 and 108.

[17] J. K. Brennan, M. Lísal, J. D. Moore, S. Izvekov, I. V. Schweigert, and J. P. Larentzos. Coarse-grain

model simulations of nonequilibrium dynamics in heterogeneous materials. *J. Phys. Chem. Lett.*, 5(12):2144–2149, 2014.
➢ Cited on page 12.

[18] R. Car and M. Parrinello. Unified approach for molecular dynamics and density-functional theory. *Phys. Rev. Lett.*, 55:2471–2474, 1985.
➢ Cited on page 6.

[19] S.-H. Cha and A. P. Whitworth. Implementations and tests of Godunov-type particle hydrodynamics. *Mon. Not. R. Astron. Soc.*, 340:73–90, 2003.
➢ Cited on page 24.

[20] E. Cieren. *Molecular Dynamics for Exascale Supercomputers.* PhD thesis, Université de Bordeaux, 2015.
➢ Cited on pages 2, 122, 125, and 126.

[21] E. Cieren, L. Colombet, S. Pitoiset, and R. Namyst. Exastamp: A parallel framework for molecular dynamics on heterogeneous clusters. *Euro-Par 2014: Parallel Processing Workshops*, pages 121–132, 2014.
➢ Cited on pages 2, 3, 105, 122, and 125.

[22] M. S. Daw and M. I. Baskes. Embedded-atom method: Derivation and application to impurities, surfaces, and other defects in metals. *Phys. Rev. B*, 29:6443–6453, 1984.
➢ Cited on pages 7 and 104.

[23] G. De Fabritiis, R. Delgado-Buscalioni, and P. V. Coveney. Multiscale modeling of liquids with molecular specificity. *Phys. Rev. Lett.*, 97:134501, 2006.
➢ Cited on page 3.

[24] R. Delgado-Buscalioni and G. De Fabritiis. Embedding molecular dynamics within fluctuating hydrodynamics in multiscale simulations of liquids. *Phys. Rev. E*, 76:036709, 2007.
➢ Cited on page 3.

[25] R. Delgado-Buscalioni, K. Kremer, and M. Praprotnik. Concurrent triple-scale simulation of molecular liquids. *J. Chem. Phys.*, 128(11), 2008.
➢ Cited on pages 3 and 99.

[26] A. Dequidt and J. G. S. Canchaya. Bayesian parametrization of coarse-grain dissipative dynamics models. *J. Chem. Phys*, 143:084122, 2015.
➢ Cited on pages 62 and 63.

[27] N. Desbiens, E. Bourasseau, and J.-B. Maillet. Potential optimization for the calculation of shocked liquid nitromethane properties. *Mol. Simulat.*, 33(13):1061–1070, 2007.
➢ Cited on page 112.

[28] N. Desbiens, E. Bourasseau, J.-B. Maillet, and L. Soulard. Molecular based equation of state for shocked liquid nitromethane. *J. Hazard. Mater.*, 166(2):1120 – 1126, 2009.
➢ Cited on page 112.

[29] G. A. Dilts. Moving-least-squares-particle hydrodynamics–i. consistency and stability. *Int. J. Numer. Meth. Eng.*, 44(8):1115–1155, 1999.
➢ Cited on page 24.

[30] C. Diu, B. nad Guthmann, L. D., and R. B. *Physique Statistique.* Hermann, 1996.
➢ Cited on page 8.

[31] B. M. Dobratz and P. C. Crawford. *LLNL explosives handbook: properties of chemical explosives and explosive simulants.* Lawrence Livermore National Laboratory, CA (US), 1985.
➢ Cited on pages 15 and 112.

[32] J. Donea, P. Fasoli-Stella, and S. Giulani. Lagrangian and eulerian finite element techniques for transient fluid-structure interaction problems. *Trans. Int. Conf. Struct. Mech. Reactor Tech.*, 1977.
➢ Cited on page 15.

[33] O. Durand and L. Soulard. Large-scale molecular dynamics study of jet breakup and ejecta production from shock-loaded copper with a hybrid method. *J. Appl. Phys.*, 111(4):044901, 2012.
➢ Cited on page 103.

[34] O. Durand and L. Soulard. Power law and exponential ejecta size distributions from the dynamic fragmentation of shock-loaded Cu and Sn metals under melt conditions. *J. Appl. Phys.*, 114(19):194902, 2013.
➢ Cited on page 103.

[35] O. Durand and L. Soulard. Mass-velocity and size-velocity distributions of ejecta cloud from shock-loaded tin surface using atomistic simulations. *J. Appl. Phys.*, 117(16):165903, 2015.
➢ Cited on pages xvii, 103, and 106.

[36] O. Durand and L. Soulard. Modeling from molecular dynamics simulations of ejecta production induced by shock-loaded metallic surfaces. *J. Dyn. Behavior Mater.*, pages 1–11, 2017.
➢ Cited on page 103.

[37] O. Durand, L. Soulard, E. Bourasseau, and G. Filippini. Investigation of the static and dynamic fragmentation of metallic liquid sheets induced by random surface fluctuations. *J. Appl. Phys.*, 120(4):045306, 2016.
➢ Cited on page 103.

[38] S. A. Dyachkov, A. N. Parshikov, and V. V. Zhakhovsky. Shock-produced ejecta from tin: Comparative study by molecular dynamics and smoothed particle hydrodynamics methods. *J. Phys. Conf. Ser.*, 653(1):012043, 2015.
➢ Cited on page 104.

[39] F. Ercolessi and J. B. Adams. Interatomic potentials from first-principles calculations: The force-matching method. *Europhys. Lett.*, 26(8):583, 1994.
➢ Cited on page 62.

[40] P. Español and M. Revenga. Smoothed dissipative particle dynamics. *Phys. Rev. E*, 67:026705, 2003.
➢ Cited on pages vii, ix, 3, 20, 22, 23, 25, 26, 29, and 66.

[41] P. Espanol, M. Serrano, I. Pagonabarraga, and I. Zuniga. Energy-conserving coarse-graining of complex molecules. *Soft Matter*, pages –, 2016.
➢ Cited on pages x, xi, 13, 14, 49, 51, 61, and 63.

[42] P. Español and I. Zúñiga. Obtaining fully dynamic coarse-grained models from MD. *Phys. Chem. Chem. Phys.*, 13(22):10538–45, 2011.
➢ Cited on pages 62 and 63.

[43] P. Español. Dissipative particle dynamics with energy conservation. *Europhys. Lett.*, 40(6):631, 1997.
➢ Cited on pages vii, 2, 11, 12, 30, and 40.

[44] P. Español and P. Warren. Statistical mechanics of dissipative particle dynamics. *Europhys. Lett.*, 30(4):191, 1995.
➢ Cited on pages vii and 12.

[45] R. Eymard, T. Gallouët, and R. Herbin. Finite volume methods. *Handbook of Numerical Analysis*, 7:713 – 1018, 2000.
➢ Cited on page 15.

[46] G. Faure, R. Delgado-Buscalioni, and P. Español. The entropy of a complex molecule. *J. Chem. Phys.*, 146(22):224106, 2017.
➢ Cited on page 4.

[47] G. Faure and J.-B. Maillet. Simulation of detonation waves with smoothed dissipative particle dynamics. *Submitted to Phys. Rev. E.*
➢ Cited on page 4.

[48] G. Faure, J.-B. Maillet, J. Roussel, and G. Stoltz. Size consistency in smoothed dissipative particle dynamics. *Phys. Rev. E*, 94:043305, 2016.
➢ Cited on page 4.

[49] G. Faure, J.-B. Maillet, and G. Stoltz. Local density dependent potential for compressible mesoparticles. *J. Chem. Phys.*, 140(11), 2014.
➢ Cited on page 63.

[50] G. Faure and G. Stoltz. Stable and accuracte schemes for smoothed dissipative particle dynamics. *Submitted to Appl. Math. Mech.*
➢ Cited on page 4.

[51] J. Feldman and J. Bonet. Dynamic refinement and boundary contact forces in SPH with applications in fluid flow problems. *Int. J. Numer. Meth. Eng.*, 72(3):295–324, 2007.
➢ Cited on pages 94 and 98.

[52] G. Ferré, J.-B. Maillet, and G. Stoltz. Permutation-invariant distance between atomic configurations. *J. Chem. Phys.*, 143(10):104114, 2015.
➢ Cited on page 62.

[53] J. Ferziger and M. Peric. *Computational Methods for Fluid Dynamics*. Springer Berlin Heidelberg, 2001.
➢ Cited on page 2.

[54] W. Fickett. *Introduction to Detonation Theory*. Basic and Applied Science. University of California Press, 1985.
➢ Cited on page 101.

[55] R. Franck. Mixed Eulerian-Lagrangian method. *Methods in Computational Physics*, pages 47–67, 1964.
➢ Cited on page 15.

[56] D. Frenkel and B. Smit. *Understanding Molecular Simulation: From Algorithms to Applications*. Computational science series. Academic Press, 2001.
➢ Cited on pages 6 and 7.

[57] D. A. Fulk. *A Numerical Analysis of Smoothed Particle Hydrodynamics*. PhD thesis, Air Force Institute of Technology, 1994.
➢ Cited on page 24.

[58] D. A. Fulk and D. W. Quinn. An analysis of 1-d smoothed particle hydrodynamics kernels. *J. Comput. Phys.*, 126(1):165 – 180, 1996.
➢ Cited on page 18.

[59] G. C. Ganzenmüller, S. Hiermaier, and M. O. Steinhauser. Energy-based coupling of smooth particle hydrodynamics and molecular dynamics with thermal fluctuations. *Eur. Phys. J. Spec. Top.*, 206(1):51–60, 2012.
➢ Cited on page 3.

[60] N. A. Gatsonis, R. Potami, and J. Yang. A smooth dissipative particle dynamics method for domains with arbitrary-geometry solid boundaries. *J. Comput. Phys.*, 256(0):441 – 464, 2014.
➢ Cited on page 65.

[61] T. C. Germann, J. E. Hammerberg, and B. L. Holian. Large-scale molecular dynamics simulations of ejecta formation in copper. *AIP Conf. Proc.*, 706(1):285–288, 2004.
➢ Cited on pages xvii and 103.

[62] R. A. Gingold and J. J. Monaghan. Smoothed particle hydrodynamics - Theory and application to non-spherical stars. *Mon. Not. R. Astron. Soc.*, 181:375–389, 1977.
➢ Cited on pages viii, ix, 2, 16, and 19.

[63] V. Girault and P. Raviart. *Finite Element Methods for Navier-Stokes Equations: Theory and Algorithms*. Springer Series in Computational Mathematics. Springer-Verlag, 1986.
➢ Cited on page 15.

[64] J. N. Glosli, D. F. Richards, K. J. Caspersen, R. E. Rudd, J. A. Gunnels, and F. H. Streitz. Extending stability beyond cpu millennium: a micron-scale atomistic simulation of kelvin-helmholtz instability. In *Supercomp. Proc.*, pages 1–11, 2007.
➢ Cited on page 1.

[65] M. S. Green. Markoff random processes and the statistical mechanics of time-dependent phenomena. *J. Chem. Phys.*, 20(8):1281–1295, 1952.
➢ Cited on pages 11 and 49.

[66] M. Grmela and H. C. Öttinger. Dynamics and thermodynamics of complex fluids. I. Development of a general formalism. *Phys. Rev. E*, 56:6620–6632, 1997.
➢ Cited on pages 25 and 29.

[67] E. Hairer, C. Lubich, and G. Wanner. Geometric numerical integration illustrated by the Störmer-Verlet method. *Acta Numer.*, 12:399–450, 2003.
➢ Cited on pages xii, 9, and 66.

[68] E. Hairer, C. Lubich, and G. Wanner. *Geometric numerical integration: Structure-preserving algorithms for Ordinary Differential Equations*, volume 31 of *Springer Series in Computational Mathematics*. Springer, 2006.
➢ Cited on pages 9 and 66.

[69] W. K. Hastings. Monte Carlo sampling methods using Markov chains and their applications. *Biometrika*, 57(1):97–109, 1970.
➢ Cited on page 8.

[70] A.-M. He, P. Wang, and J.-L. Shao. Molecular dynamics simulations of ejecta size distributions for shock-loaded cu with a wedged surface groove. *Comput. Mater. Sci.*, 98:271 – 277, 2015.
➢ Cited on pages xvii and 103.

[71] A. J. Heim, N. Grønbech-Jensen, T. C. Germann, B. L. Holian, E. M. Kober, and P. S. Lomdahl. Influence of interatomic bonding potentials on detonation properties. *Phys. Rev. E*, 76:026318, 2007.
➢ Cited on page 108.

[72] O. Heuzé. General form of the mie-grüneisen equation of state. *CR Mecanique*, 340(10):679 – 687, 2012.
➢ Cited on pages 15 and 104.

[73] C. Hijón, P. Español, E. Vanden-Eijnden, and R. Delgado-Buscalioni. Mori-Zwanzig formalism as a practical computational tool. *Faraday Discuss.*, 144(1):301–22; discussion 323–45, 467–81, 2010.
➢ Cited on pages 11, 14, 49, 50, 52, and 63.

[74] B. L. Holian, T. C. Germann, J.-B. Maillet, and C. T. White. Atomistic mechanism for hot spot initiation. *Phys. Rev. Lett.*, 89:285501, 2002.
➢ Cited on page 108.

[75] B. L. Holian, W. G. Hoover, B. Moran, and G. K. Straub. Shock-wave structure via nonequilibrium molecular dynamics and navier-stokes continuum mechanics. *Phys. Rev. A*, 22:2798–2808, 1980.
➢ Cited on pages 1 and 2.

[76] B. L. Holian, M. Mareschal, and R. Ravelo. Test of a new heat-flow equation for dense-fluid shock waves. *J. Chem. Phys.*, 133(11), 2010.
➢ Cited on page 91.

[77] B. L. Holian, C. W. Patterson, M. Mareschal, and E. Salomons. Modeling shock waves in an ideal gas: Going beyond the navier-stokes level. *Phys. Rev. E*, 47:R24–R27, 1993.
➢ Cited on page 91.

[78] A. Homman. *Development of new numerical integration schemes of multiscale coarse-graining methods*. PhD thesis, Université Paris-Est, 2016.
➢ Cited on pages 65 and 69.

[79] A.-A. Homman, J.-B. Maillet, J. Roussel, and G. Stoltz. New parallelizable schemes for integrating the dissipative particle dynamics with energy conservation. *J. Chem. Phys.*, 144(2):024112, 2016.
➢ Cited on pages xiii, xiv, 4, 14, 43, 65, 69, 71, 72, 79, and 127.

[80] J. Hongbin and D. Xin. On criterions for smoothed particle hydrodynamics kernels in stable field. *J. Comput. Phys.*, 202(2):699–709, 2005.
➢ Cited on page 18.

[81] P. J. Hoogerbrugge and J. M. V. A. Koelman. Simulating microscopic hydrodynamic phenomena with dissipative particle dynamics. *Europhys. Lett.*, 19(3):155, 1992.
➢ Cited on pages vii and 11.

[82] X. Hu and N. Adams. A multi-phase SPH method for macroscopic and mesoscopic flows. *J. Comput. Phys.*, 213(2):844 – 861, 2006.
➢ Cited on pages 107 and 108.

[83] S. ichiro Inutsuka. Reformulation of smoothed particle hydrodynamics with riemann solver. *J. Comput. Phys.*, 179(1):238 – 267, 2002.
➢ Cited on page 24.

[84] Intel Corporation. Intel® Threading Building Blocks. *https://www.threadingbuildingblocks.org/*.
➢ Cited on page 126.

[85] S. Izvekov, P. W. Chung, and B. M. Rice. Particle-based multiscale coarse graining with density-dependent potentials: Application to molecular

crystals (hexahydro-1,3,5-trinitro-s-triazine). *J. Chem. Phys.*, 135(4):044112, 2011.
➢ Cited on page 63.

[86] S. Izvekov and G. A. Voth. Multiscale coarse graining of liquid-state systems. *J. Chem. Phys.*, 123(13):134105, 2005.
➢ Cited on page 62.

[87] R. T. Jacobsen and R. B. Stewart. Thermodynamic properties of nitrogen including liquid and vapor phases from 63k to 2000k with pressures to 10,000 bar. *J. Phys. Chem. Ref. Data*, 2(4):757–922, 1973.
➢ Cited on page 87.

[88] S. John. *Many-Body Coarse-Grained Interactions using Gaussian Approximation Potentials.* PhD thesis, University of Cambridge, 2016.
➢ Cited on page 62.

[89] G. R. Johnson and S. R. Beissel. Normalized smoothing functions for sph impact computations. *International Journal for Numerical Methods in Engineering*, 39(16):2725–2741, 1996.
➢ Cited on page 18.

[90] J. K. Johnson, J. A. Zollweg, and K. E. Gubbins. The lennard-jones equation of state revisited. *Mol. Phys.*, 78(3):591–618, 1993.
➢ Cited on pages xiv, 85, 87, 88, and 90.

[91] M. E. Johnson, T. Head-Gordon, and A. A. Louis. Representability problems for coarse-grained water potentials. *J. Chem. Phys.*, 126(14):144509, 2007.
➢ Cited on page 62.

[92] J. E. Jones. On the determination of molecular fields. ii. from the equation of state of a gas. *Proceedings of the Royal Society of London A: Mathematical, Physical and Engineering Sciences*, 106(738):463–477, 1924.
➢ Cited on page 6.

[93] K. Kadau, J. L. Barber, T. C. Germann, B. L. Holian, and B. J. Alder. Atomistic methods in fluid simulation. *Philos. T. R. Soc. A*, 368(1916):1547–1560, 2010.
➢ Cited on page 1.

[94] K. Kadau, C. Rosenblatt, J. L. Barber, T. C. Germann, Z. Huang, P. Carlès, and B. J. Alder. The importance of fluctuations in fluid mixing. *P. Natl. Acad. Sci. USA*, 104(19):7741–7745, 2007.
➢ Cited on page 24.

[95] S. Kitsionas and A. Whitworth. Smoothed particle hydrodynamics with particle splitting, applied to self-gravitating collapse. *Mon. Not. R. Astron. Soc.*, 330(1):129–136, 2002.
➢ Cited on page 94.

[96] W. Kliemann. Recurrence and invariant measures for degenerate diffusions. *Ann. Probab.*, 15(2):690–707, 04 1987.
➢ Cited on page 10.

[97] M. P. Kroonblawd, T. D. Sewell, and J.-B. Maillet. Characteristics of energy exchange between inter- and intramolecular degrees of freedom in crystalline 1,3,5-triamino-2,4,6-trinitrobenzene (tatb) with implications for coarse-grained simulations of shock waves in polyatomic molecular crystals. *J. Chem. Phys.*, 144(6), 2016.
➢ Cited on page 14.

[98] P. M. Kulkarni, C.-C. Fu, M. S. Shell, and L. Gary Leal. Multiscale modeling with smoothed dissipative particle dynamics. *J. Chem. Phys.*, 138, 2013.
➢ Cited on pages xv, 3, and 94.

[99] L. Landau and E. Lifshits. *Fluid Mechanics*, volume 6 of *Course of Theroretical Physics.* Pergamon Press, 1959.
➢ Cited on page 2.

[100] M. Langenberg and M. Müller. eMC: A Monte Carlo scheme with energy conservation. *Europhys. Lett.*, 114(2):20001, 2016.
➢ Cited on page 73.

[101] P. Langevin. Sur la théorie du mouvement Brownien. *Comptes Rendus de l'Académie des Sciences*, 1908.
➢ Cited on page 10.

[102] N. Lanson and J.-P. Vila. Renormalized meshfree schemes i: Consistency, stability, and hybrid methods for conservation laws. *SIAM J. Numer. Anal.*, 46(4):1912–1934, 2008.
➢ Cited on page 18.

[103] N. Lanson and J.-P. Vila. Renormalized meshfree schemes ii: Convergence for scalar conservation laws. *SIAM J. Numer. Anal.*, 46(4):1935–1964, 2008.
➢ Cited on page 18.

[104] J. P. Larentzos, J. K. Brennan, J. D. Moore, M. Lísal, and W. D. Mattson. Parallel implementation of isothermal and isoenergetic Dissipative Particle Dynamics using Shardlow-like splitting algorithms. *Comput. Phys. Commun.*, 185(7):1987 – 1998, 2014.
➢ Cited on pages xiv, 14, 65, and 69.

[105] E. L. Lee, H. C. Hornig, and J. W. Kury. *Adiabatic Expansion Of High Explosive Detonation Products.* Lawrence Livermore National Laboratory, CA (US), 1968.
➢ Cited on page 112.

[106] C. Leforestier. Classical trajectories using the full ab initio potential energy surface H-+CH4-

>CH4+H-. *J. Chem. Phys.*, 68(10):4406–4410, 1978.
➢ Cited on page 6.

[107] H. Lei, C. J. Mundy, G. K. Schenter, and N. K. Voulgarakis. Modeling nanoscale hydrodynamics by smoothed dissipative particle dynamics. *J. Chem. Phys.*, 142(19), 2015.
➢ Cited on pages 107 and 108.

[108] T. Lelièvre, G. Stoltz, and M. Rousset. *Free Energy Computations: A Mathematical Perspective.* Imperial College Press, 2010.
➢ Cited on pages 10 and 35.

[109] T. Lelièvre and G. Stoltz. Partial differential equations and stochastic methods in molecular dynamics. *Acta Numer.*, 25:681–880, 2016.
➢ Cited on page 87.

[110] C. A. Lemarchand, M. Couty, and B. Rousseau. Coarse-grained simulations of cis - and trans - polybutadiene: A bottom-up approach. *J. Chem. Phys.*, 146(7):074904, 2017.
➢ Cited on page 63.

[111] D. S. Lemons and C. M. Lund. Thermodynamics of high temperature, mie-gruneisen solids. *American Journal of Physics*, 67(12):1105–1108, 1999.
➢ Cited on page 15.

[112] R. LeVeque. *Finite Volume Methods for Hyperbolic Problems.* Cambridge Texts in Applied Mathematics. Cambridge University Press, 2002.
➢ Cited on page 15.

[113] Z. Li, X. Bian, B. Caswell, and G. E. Karniadakis. Construction of dissipative particle dynamics models for complex fluids via the mori-zwanzig formulation. *Soft Matter*, 10:8659–8672, 2014.
➢ Cited on page 63.

[114] Z. Li, Z. Luo, Z. Liu, Y. Ye, Z. Li, J. Zhong, and J. Li. High-speed microjet particles measurement using in-line pulsed holography. *J. Appl. Phys.*, 108(11):113110, 2010.
➢ Cited on page 103.

[115] K.-H. Lin, B. L. Holian, T. C. Germann, and A. Strachan. Mesodynamics with implicit degrees of freedom. *J. Chem. Phys.*, 141(6):064107, 2014.
➢ Cited on page 12.

[116] R. D. Lisio, E. Grenier, and M. Pulvirenti. The convergence of the sph method. *Comput. Math. Appl.*, 35(1):95 – 102, 1998.
➢ Cited on page 24.

[117] S. Litvinov, M. Ellero, X. Hu, and N. Adams. A splitting scheme for highly dissipative smoothed particle dynamics. *J. Comput. Phys.*, 229(15):5457 – 5464, 2010.
➢ Cited on page 65.

[118] S. Litvinov, M. Ellero, X. Hu, and N. A. Adams. Smoothed dissipative particle dynamics model for polymer molecules in suspension. *Phys. Rev. E*, 77:066703, 2008.
➢ Cited on page 25.

[119] G. R. Liu and M. B. Liu. *Smoothed Particle Hydrodynamics, a meshfree particle method.* World scientific publishing, 2003.
➢ Cited on pages 16 and 21.

[120] M. Liu, G. Liu, and K. Lam. Constructing smoothing functions in smoothed particle hydrodynamics with applications. *J. Comput. Appl. Math.*, 155(2):263 – 284, 2003.
➢ Cited on pages 17 and 35.

[121] W. K. Liu, S. Jun, and Y. F. Zhang. Reproducing kernel particle methods. *Int. J. Numer. Meth. Fl.*, 20(8-9):1081–1106, 1995.
➢ Cited on page 18.

[122] A. A. Louis. Beware of density dependent pair potentials. *J. Phys. Condens. Matter*, 14(40):9187, 2002.
➢ Cited on page 62.

[123] L. B. Lucy. A numerical approach to the testing of the fission hypothesis. *Astron. J.*, 82:1013–1024, 1977.
➢ Cited on pages viii, ix, 2, 16, and 19.

[124] A. P. Lyubartsev and A. Laaksonen. Calculation of effective interaction potentials from radial distribution functions: A reverse monte carlo approach. *Phys. Rev. E*, 52:3730–3737, 1995.
➢ Cited on page 62.

[125] M. Lísal, J. K. Brennan, and J. B. Avalos. Dissipative particle dynamics at isothermal, isobaric, isoenergetic, and isoenthalpic conditions using Shardlow-like splitting algorithms. *J. Chem. Phys.*, 135(20):204105, 2011.
➢ Cited on pages xiii, 13, 65, 69, and 79.

[126] J. B. Maillet, E. Bourasseau, N. Desbiens, G. Vallverdu, and G. Stoltz. Mesoscopic simulations of shock-to-detonation transition in reactive liquid high explosive. *Europhys. Lett.*, 96(6):68007, 2011.
➢ Cited on pages xviii, 2, 12, 108, 112, 115, and 120.

[127] J. B. Maillet, L. Soulard, and G. Stoltz. A reduced model for shock and detonation waves. II. the reactive case. *Europhys. Lett.*, 78(6):68001, 2007.
➢ Cited on pages xvii, 2, 3, 12, 108, 109, and 120.

[128] C. Marsh. *Theoretical aspects of Dissipative Particle Dynamics.* PhD thesis, University of Oxford, 1998.
➢ Cited on page 68.

[129] S. Mas-Gallic and P. A. Raviart. A particle method for first-order symmetric systems. *Numerische*

Mathematik, 51(3):323–352, 1987.
➢ Cited on page 24.

[130] R. Menikoff and M. S. Shaw. Modeling detonation waves in nitromethane. *Combustion and Flame*, 158(12):2549 – 2558, 2011.
➢ Cited on page 115.

[131] Message Passing Interace Forum. *MPI: A Message-Passing Interface Standard.* University of Tennessee, 1994.
➢ Cited on page 125.

[132] N. Metropolis, A. W. Rosenbluth, M. N. Rosenbluth, A. H. Teller, and E. Teller. Equation of state calculations by fast computing machines. *J. Chem. Phys.*, 21(6):1087–1092, 1953.
➢ Cited on page 8.

[133] J. Monaghan. SPH without a tensile instability. *J. Comput. Phys.*, 159(2):290 – 311, 2000.
➢ Cited on pages 18 and 86.

[134] J. Monaghan and R. Gingold. Shock simulation by the particle method SPH. *J. Comput. Phys.*, 52(2):374 – 389, 1983.
➢ Cited on page 93.

[135] J. D. Moore, B. C. Barnes, S. Izvekov, M. Lisal, M. S. Sellers, D. E. Taylor, and J. K. Brennan. A coarse-grain force field for RDX: Density dependent and energy conserving. *J. Chem. Phys.*, 144:104501, 2016.
➢ Cited on page 63.

[136] T. C. Moore, C. R. Iacovella, and C. McCabe. Derivation of coarse-grained potentials via multistate iterative boltzmann inversion. *J. Chem. Phys.*, 140(22):224104, 2014.
➢ Cited on page 62.

[137] N. Moreno, P. Vignal, J. Li, and V. M. Calo. Multiscale modeling of blood flow: Coupling finite elements with smoothed dissipative particle dynamics. *Procedia Comput. Sci.*, 18:2565 – 2574, 2013. 2013 International Conference on Computational Science.
➢ Cited on page 3.

[138] H. Mori. Transport, collective motion, and Brownian motion. *Prog. Theor. Phys.*, 33(3):423–455, 1965.
➢ Cited on pages 11 and 49.

[139] B. B. Moussa and J. P. Vila. Convergence of sph method for scalar nonlinear conservation laws. *SIAM J. Numer. Anal.*, 37(3):863–887, 2000.
➢ Cited on page 24.

[140] A. M. N. Niklasson, C. J. Tymczak, and M. Challacombe. Time-reversible born-oppenheimer molecular dynamics. *Phys. Rev. Lett.*, 97:123001, 2006.
➢ Cited on page 6.

[141] W. Noh. CEL: a time-dependent, two-space-dimensional, coupled Eulerian-Lagrange code. *Methods in Computational Physics*, pages 117–179, 1964.
➢ Cited on page 15.

[142] W. G. Noid, J.-W. Chu, G. S. Ayton, V. Krishna, S. Izvekov, G. A. Voth, A. Das, and H. C. Andersen. The multiscale coarse-graining method. i. a rigorous bridge between atomistic and coarse-grained models. *J. Chem. Phys.*, 128(24):244114, 2008.
➢ Cited on page 61.

[143] V. A. Ogorodnikov, A. L. Mikhaĭlov, V. V. Burtsev, S. A. Lobastov, S. V. Erunov, A. V. Romanov, A. V. Rudnev, E. V. Kulakov, Y. B. Bazarov, V. V. Glushikhin, I. A. Kalashnik, V. A. Tsyganov, and B. I. Tkachenko. Detecting the ejection of particles from the free surface of a shock-loaded sample. *J. Exp. Theor. Phys.*, 109(3):530, 2009.
➢ Cited on page 103.

[144] N. D. Petsev, L. G. Leal, and M. S. Shell. Hybrid molecular-continuum simulations using smoothed dissipative particle dynamics. *J. Chem. Phys.*, 142(4), 2015.
➢ Cited on page 3.

[145] N. D. Petsev, L. G. Leal, and M. S. Shell. Multiscale simulation of ideal mixtures using smoothed dissipative particle dynamics. *J. Chem. Phys.*, 144(8), 2016.
➢ Cited on pages xv, 3, and 94.

[146] R. Potestio, S. Fritsch, P. Español, R. Delgado-Buscalioni, K. Kremer, R. Everaers, and D. Donadio. Hamiltonian adaptive resolution simulation for molecular liquids. *Phys. Rev. Lett.*, 110:108301, 2013.
➢ Cited on pages 3, 97, and 98.

[147] M. Praprotnik, L. D. Site, and K. Kremer. Adaptive resolution molecular-dynamics simulation: Changing the degrees of freedom on the fly. *J. Chem. Phys.*, 123(22):224106, 2005.
➢ Cited on page 3.

[148] A. Rahman. Correlations in the motion of atoms in liquid argon. *Phys. Rev.*, 136:A405–A411, Oct 1964.
➢ Cited on page 1.

[149] J. I. Read, T. Hayfield, and O. Agertz. Resolving mixing in smoothed particle hydrodynamics. *Mon. Not. R. Astron. Soc.*, 405(3):1513–1530, 2010.
➢ Cited on pages 18 and 86.

[150] D. Reith, M. Pütz, and F. Müller-Plathe. Deriving effective mesoscale potentials from atomistic simulations. *J. Comput. Chem.*, 24(13):1624–1636, 2003.
➢ Cited on page 62.

[151] L. Rey-Bellet. Ergodic properties of markov processes. *Open Quantum Systems II: The Markovian Approach*, pages 1–39, 2006.
➢ Cited on page 10.

[152] B. M. Rice, W. Mattson, J. Grosh, and S. F. Trevino. Molecular-dynamics study of detonation. i. a comparison with hydrodynamic predictions. *Phys. Rev. E*, 53:611–622, 1996.
➢ Cited on page 108.

[153] C. Roland, T. de Rességuier, A. Sollier, E. Lescoute, D. Loison, and L. Soulard. Ejection of micron-scale fragments from triangular grooves in laser shock-loaded copper samples. *J. Dyn. Behavior Mater.*, pages 1–8, 2016.
➢ Cited on page 103.

[154] C. Roland, T. de Rességuier, A. Sollier, E. Lescoute, L. Soulard, and D. Loison. Hydrodynamic simulations of microjetting from shock-loaded grooves. *AIP Conf. Proc.*, 1793(1):100027, 2017.
➢ Cited on page 104.

[155] D. Ruelle. *Statisical Physics: Rigorous Results*. Benjamin, 1969.
➢ Cited on page 10.

[156] T. Shardlow. Splitting for dissipative particle dynamics. *SIAM J. Sci. Comput.*, 24(4):1267–1282, 2003.
➢ Cited on pages xiii, 12, 13, 65, 66, and 67.

[157] T. Shardlow and Y. Yan. Geometric ergodicity for dissipative particle dynamics. *Stoch. Dynam.*, 6(01):123–154, 2006.
➢ Cited on page 43.

[158] M. S. Shell. The relative entropy is fundamental to multiscale and inverse thermodynamic problems. *J. Chem. Phys.*, 129(14):144108, 2008.
➢ Cited on page 62.

[159] D. S. Sorenson, R. W. Minich, J. L. Romero, T. W. Tunnell, and R. M. Malone. Ejecta particle size distributions for shock loaded sn and al metals. *J. Appl. Phys.*, 92(10):5830–5836, 2002.
➢ Cited on page 103.

[160] G. Stoltz. A reduced model for shock and detonation waves. I. The inert case. *Europhys. Lett.*, 76(5):849, 2006.
➢ Cited on pages xiii, 2, 3, 4, 12, 13, 44, 65, 66, 67, and 68.

[161] G. Stoltz. Stable schemes for dissipative particle dynamics with conserved energy. *J. Comput. Phys.*, 340:451 – 469, 2017.
➢ Cited on pages xiv, 4, 14, 65, 73, and 80.

[162] A. Strachan and B. L. Holian. Energy exchange between mesoparticles and their internal degrees of freedom. *Phys. Rev. Lett.*, 94:014301, 2005.
➢ Cited on pages 11 and 12.

[163] G. Strang. On the construction and comparison of difference schemes. *SIAM J. Numer. Anal.*, 5:506–517, 1968.
➢ Cited on pages xi, 9, and 66.

[164] J. Swegle, D. Hicks, and S. Attaway. Smoothed particle hydrodynamics stability analysis. *J. Comput. Phys.*, 116(1):123 – 134, 1995.
➢ Cited on pages 18, 24, and 86.

[165] A. Tartakovsky and P. Meakin. Modeling of surface tension and contact angles with smoothed particle hydrodynamics. *Phys. Rev. E*, 72:026301, 2005.
➢ Cited on page 107.

[166] J. Tersoff. New empirical approach for the structure and energy of covalent systems. *Phys. Rev. B*, 37:6991–7000, 1988.
➢ Cited on pages 7 and 108.

[167] J. Thouvenin. *Détonique*. CEA Editions, 1998.
➢ Cited on page 101.

[168] H. F. Trotter. On the product of semi-groups of operators. *Proc. Amer. Math. Soc.*, 10:545–551, 1959.
➢ Cited on pages xi, 10, and 66.

[169] M. Tuckerman. *Statistical Mechanics: Theory and Molecular Simulation*. Oxford Graduate Texts. OUP Oxford, 2010.
➢ Cited on page 8.

[170] R. Vacondio, B. Rogers, P. Stansby, P. Mignosa, and J. Feldman. Variable resolution for sph: A dynamic particle coalescing and splitting scheme. *Comput. Methods Appl. Mech. Eng.*, 256:132 – 148, 2013.
➢ Cited on page 94.

[171] A. C. T. van Duin, S. Dasgupta, F. Lorant, and W. A. Goddard. Reaxff: A reactive force field for hydrocarbons. *J. Phys. Chem. A*, 105(41):9396–9409, 2001.
➢ Cited on pages 7 and 108.

[172] L. Verlet. Computer "experiments" on classical fluids. I. Thermodynamical properties of Lennard-Jones molecules. *Phys. Rev.*, 159:98–103, 1967.
➢ Cited on pages xii, 7, 9, 66, and 92.

[173] A. Vázquez-Quesada, M. Ellero, and P. Español. Consistent scaling of thermal fluctuations in smoothed dissipative particle dynamics. *J. Chem. Phys*, 130(3):034901, 2009.
➢ Cited on page 25.

[174] H. Wang, C. Junghans, and K. Kremer. Comparative atomistic and coarse-grained study of water: What do we lose by coarse-graining? *Eur. Phys. J. E*, 28(2):221–229, 2009.
➢ Cited on page 62.

[175] G. Yang, Y. Fu, D. Hu, and X. Han. Feasibility analysis of SPH method in the simulation of condensed explosives detonation with ignition and growth model. *Comput. Fluids*, 88(0):51 – 59, 2013.
➢ Cited on page 108.

[176] R. Zwanzig. Memory effects in irreversible thermodynamics. *Phys. Rev.*, 124:983–992, 1961.
➢ Cited on pages 11 and 49.